

Many-particle entanglement, Einstein-Podolsky-Rosen steering and Bell correlations in Bose-Einstein condensates

Inauguraldissertation

zur
Erlangung der Würde eines Doktors der Philosophie
vorgelegt der
Philosophisch-Naturwissenschaftlichen Fakultät
der Universität Basel

von

Matteo Fadel
aus Italien

Basel, 2019

This work is licensed under a Creative Commons
Attribution-NonCommercial-NoDerivatives 4.0 International License.



Originaldokument gespeichert auf dem Dokumentserver der Universität Basel
edoc.unibas.ch

Genehmigt von der Philosophisch-Naturwissenschaftlichen Fakultät
auf Antrag von
Prof. Dr. Philipp Treutlein
Prof. Dr. Nicolas Brunner

Basel, den 18 September 2018

Prof. Dr. Martin Spiess
Dekan

Abstract

According to quantum mechanics, the results of measurements performed on different systems can show correlations that are stronger than what is classically possible. Three important types of nonclassical correlations that have been identified are entanglement (nonseparability), Einstein-Podolsky-Rosen correlations (steering) and Bell correlations (nonlocality). Apart from shedding light on the foundations of quantum theory and on how nature behaves, they represent different resources for applications that are inaccessible by classical means. While such correlations have been extensively investigated in systems composed of a few particles, their role in many-body systems is much less explored.

In this thesis I present both experimental and theoretical results on quantum correlations in many-body systems. Specifically, I report experiments where we prepare a Bose-Einstein condensate of approximately 600 Rubidium-87 atoms on an atom chip in a spin squeezed state, and analyze the correlations between the constituent atoms. First, I show state-of-the-art detection of entanglement, and of its depth, using collective measurements. For a state with a Wineland spin squeezing parameter of -6.8 dB we conclude an entanglement depth of ≈ 56 particles. Then, I describe the first detection of Bell correlations in a many-body system. This result was enabled by deriving a witness for Bell correlations which involves only collective measurements on the atomic ensemble. Moreover, we present a sufficient criterion to close the statistics loop-hole, derive additional multi-partite inequalities and witnesses detecting Bell correlations in a larger class of states, and report ways to quantify their depth. Applying these to our experimental data, we conclude the presence of at least 6-partite Bell correlations. As a new tool, we provide a method to detect Bell correlations in experimental data by running a computer algorithm consisting in a hierarchy of semi-definite programs bounding the set of classical correlations. Finally, I present the first observation of Einstein-Podolsky-Rosen steering between spatially separated regions in an ensemble of massive particles. This result was obtained by high resolution imaging of an expanded spin-squeezed Bose-Einstein condensate in order to measure spin correlations between spatially separated parts.

Our experimental and theoretical studies of quantum correlations in many-body systems are an important step towards exploring the predictions of quantum mechanics in

macroscopic systems, and could enable a variety of quantum information tasks. Our experiments show that Bose-Einstein condensates on atom chips are an ideal platform for the implementation and investigation of such many-body quantum correlations.

Contents

1	Introduction	11
2	Bose-Einstein condensates: Theory	15
2.1	Bose-Einstein condensation	15
2.1.1	Elementary concepts	16
2.1.2	Critical temperature for condensation	17
2.1.3	BEC on atom chips	18
2.2	Zero-temperature BEC	18
2.2.1	The Gross-Pitaevskii equation	18
2.2.2	Stationary solutions to the GPE	20
2.2.3	Multi-component BEC	22
2.2.4	Collective spin Hamiltonian	24
2.2.5	BEC lifetime	32
2.2.6	BEC coherence time	34
3	Bose-Einstein condensates: Experiments	39
3.1	Experimental apparatus	39
3.1.1	Overview of the setup	39
3.1.2	Typical experimental sequence	45
3.1.3	Details of the experiment traps	46
3.1.4	Characterization of the imaging system	47
3.2	BEC manipulation	53
3.2.1	Spin state manipulation	53
3.3	Ramsey interferometry	54
3.3.1	Motional state manipulation	56
4	Quantum correlations: Theory	59
4.1	History and philosophy	59
4.1.1	Elements of reality and the completeness of physical theories	60
4.1.2	Heisenberg uncertainty principle	60
4.1.3	Einstein-Podolsky-Rosen paradox	62

CONTENTS

4.1.4	Schrödinger's entanglement and nonseparability	64
4.1.5	Bell nonlocality	65
4.2	Technical definitions of quantum correlations	66
4.2.1	Correlations as resources for tasks	66
4.2.2	Inequivalence of entanglement, steering and nonlocality	70
4.2.3	Constraints on physical models	71
4.2.4	Multi-partite scenarios	72
4.3	Entanglement detection and characterization	75
4.3.1	Entanglement criteria	75
4.3.2	Entanglement depth	78
4.4	EPR steering	80
4.4.1	EPR steering criteria	80
4.5	Detection of Bell correlations	83
4.5.1	Multipartite permutationally-invariant Bell inequalities	83
4.5.2	Bounding the set of classical correlations	85
4.5.3	Bell correlations depth	91
4.5.4	Witnessing Bell correlations and their depth	95
4.5.5	Finite statistics loophole	100
5	Quantum correlations: Experiments	103
5.1	Spin-squeezing and entanglement in Bose-Einstein condensates	103
5.1.1	Experimental preparation of spin-squeezed states	104
5.1.2	Squeezing sequence with spin echo	104
5.1.3	Experimental characterization of spin-squeezed states	106
5.1.4	Entanglement in spin-squeezed states	107
5.1.5	Conclusions and outlook	108
5.2	Bell correlations in a BEC	110
5.2.1	Violation of a Bell correlation witness	110
5.2.2	Connection with entanglement	112
5.2.3	Many settings witnesses	113
5.2.4	Statistical analysis	114
5.2.5	Nonlocality depth	117
5.2.6	Towards a Bell test with a many-body system	117
5.2.7	Conclusions and outlook	119
5.3	Spatial entanglement patterns and EPR steering in a BEC	121
5.3.1	From indistinguishable particles to distinguishable modes	122
5.3.2	Local collective spins	123
5.3.3	Spatial entanglement patterns	124
5.3.4	Einstein-Podolsky-Rosen steering	127
5.3.5	Crosstalk	128
5.3.6	Coherent state measurements	130
5.3.7	Conclusions and outlook	131

6 Summary and outlook	133
6.1 Summary	133
6.2 Outlook	134
6.2.1 Nonclassical correlations between two BECs	134
6.2.2 Schrödinger kitten states	135
6.2.3 More multipartite Bell inequalities	136
 Appendices	 137
A BEC ground state	137
A.1 Derivation of the Gross-Pitaevskii equation	137
A.2 ϵ as the chemical potential	140
B Derivation of phase noise due to losses	141
C Local collective spins	143
C.1 Definition of local collective spins	143
C.2 Naive definition	143
C.3 Proper definition	145
C.4 Imaging noise subtraction	146
C.5 Unbiased sample estimate of inferred variances	147
D Derivation of the Sørensen entanglement criterion	149
D.1 Original derivation	149
D.2 Derivation from the spin uncertainty relation	153
E Correlations in systems with fluctuating number of particles	155
E.1 Theoretical framework	155
E.2 Entanglement criterion	158
E.3 Bell correlation witness	158
F Spin expectation values	161
F.1 One-axis twisting	161
F.2 Squeezing and splitting	162
G Convex optimization	163
G.1 Linear program	163
G.2 Integer program	164
G.3 Semidefinite program	165
 Bibliography	 167

Introduction

Nonclassical correlations between the constituent particles of a many-body system are particularly interesting for both fundamental research and practical applications. On the one hand they allow to investigate the validity range of quantum mechanics, by testing its predictions in ever larger systems, while, on the other hand, they are a resource allowing a system to perform better than with classical correlations in certain tasks.

Different classes of nonclassical correlations have been identified [1], namely entanglement (or non-separability) [2, 3], Einstein-Podolsky-Rosen (EPR) correlations (or steering) [4], and Bell (or nonlocal) correlations [5]. Each of these is a resource for specific tasks such as parameter estimation [6], quantum teleportation [7], secure communication [8], and certified randomness generation [9]. Moreover, their detection put strong constraints on the possible physical models describing nature.

For systems composed of a few (usually two) parties, nonclassical correlations have been extensively investigated [2, 4, 5]. In particular, in the case of individually addressable massive particles, EPR correlations were observed between two atoms [10], and Bell correlations in up to fourteen ions [11]. However, preparing and observing such correlations in many-body systems is challenging. Some of the difficulties lie in the fragility of such correlations to uncontrolled noise, in the complexity of manipulating many-body quantum systems, and in the need of addressing and detecting their constituent particles individually.

In experiments with cold and ultracold atomic ensembles, a variety of spin-squeezed and other nonclassical states are routinely prepared using different schemes. For a comprehensive list of such states and techniques we refer the reader to the recent review Ref. [12]. The main techniques adopted in the field rely on collisional interactions in Bose-Einstein condensates (BECs), on the backaction of quantum non-demolition measurements (either in free space or in a cavity), or on the interaction between atoms mediated by a cavity mode. These allow the preparation of spin squeezed/over-squeezed states, Dicke states and small Schrödinger cat states.

Nonclassical states of atomic ensembles find applications in *e.g.* quantum metrology [6, 13], where they allow for interferometry with a precision beyond classical limits [14–17]. Besides their usefulness for applications, it is of fundamental interest to characterize the correlations between the constituent atoms.

1. Introduction

The usual strategies to study correlations in few-body systems require to control and perform measurements on the individual particles. In many-body systems, such as ensembles with hundreds of atoms, this is impossible to be achieved in practice. Moreover, in the special case of Bose-Einstein condensates (BECs) this is even impossible in principle: the atoms in a BEC are identical particles that occupy the same spatial mode. The limited access to the particles of a many-body system can be circumvented by investigating collective observables, shifting the difficulty from a technical level to a conceptual one: it requires to connect global properties of a system to the underlying properties of its constituents [2, 3, 18].

An extensive theoretical research resulted in a number of practical witnesses to reveal the presence of nonclassical correlations with collective measurements on the entire ensemble [2, 3]. Following this approach, experimental studies confirmed the presence of entanglement [14, 19] and of EPR correlations [20] in BECs. However, collective witnesses suited to detect quantum correlations stronger than these, namely Bell correlations, were lacking. Only recently [21], further theoretical investigations provided such tools, which we developed further and tested experimentally in our BECs. In this thesis, we will show experimentally that also Bell correlations can be prepared in a many-body system and witnessed with collective observables.

On the one hand, observing correlations with collective measurements has shown to be extremely practical for large systems, but, on the other hand, it can pose additional conceptual challenges. In fact, already the idea of correlation implicitly assumes that there are distinct components that are individually resolved. Because of this, the concept of entanglement in ensembles of indistinguishable particles has been discussed controversially, and its usefulness for quantum technologies other than metrology has been questioned (for a brief review of the debate, see [22]). In this thesis, we will show experimentally how correlations in a system of indistinguishable particles can be extracted into spatially separated regions and used to demonstrate EPR steering.

This thesis

In this thesis I present the experimental investigation of quantum correlations in a many-body system. Specifically, we use Bose-Einstein condensates (BECs) of approximately 600 Rubidium-87 atoms, prepared and manipulated on an atom chip [23]. We use microwave near-field gradients, generated with an on-chip coplanar waveguide, to control the collisions between the atoms [19,24]. This nonlinear interaction allows us to prepare spin-squeezed states [25], where particles share correlations which we want to characterize. By taking high-resolution images of the atomic density distribution, we are able to access collective or local observables, whose measurement results show nonclassical statistics. In this way, we present the first observation of Bell correlations and of EPR-steering in a many-body system. These results have been published in references [26,27].

Moreover, in this thesis I also present further theoretical developments in the study of Bell correlations in many-body systems. In particular, we derived a new method, based on a hierarchy of semi-definite programs, to prove that the observed measurement statistics arise from Bell-correlated particles and to derive new multi-partite Bell inequalities. Then, we investigate the statistics loop-hole, originating from the necessarily finite number of experimental measurements, which might lead to an artificial violation of some inequality. Finally, to provide a characterization for the observed Bell correlations, we developed a strategy to quantify their depth by using collective measurements. These results have been published in references [28–30].

Outline

Chapter 2 gives a general introduction to BECs, and it presents the theoretical models used for their description. Chapter 3 discusses the experimental setup we use to prepare BECs. Chapter 4 gives a theoretical description of entanglement, EPR-steering and Bell correlations, introducing the criteria suited to their detection. These are then used in the experiments presented in chapter 5, where we investigate the correlations among the atoms of spin-squeezed BECs. Finally, chapter 6 summarizes the conclusions of this thesis, and it gives an outlook on future ideas and research directions.

1. Introduction

Publications of thesis work

- “*Split spin-squeezed Bose-Einstein Condensates*”
Y. Jing, M. Fadel, V. Ivannikov and T. Byrnes
preprint at arXiv:1808.10679
- “*Bell correlations at finite temperature*”
M. Fadel and J. Tura
preprint at arXiv:1805.00449
- “*Spatial entanglement patterns and Einstein-Podolsky-Rosen steering in Bose-Einstein condensates*”
M. Fadel, B. Décamps, T. Zibold and P. Treutlein
Science **360**, 409 (2018)
- “*Bell correlations depth in many-body systems*”
F. Baccari, J. Tura, M. Fadel, A. Aloy, J.-D. Bancal, N. Sangouard, M. Lewenstein, A. Acín and R. Augusiak
preprint at arXiv:1802.09516
- “*Bounding the set of classical correlations of a many-body system*”
M. Fadel and J. Tura
Phys. Rev. Lett. **119**, 230402 (2017)
- “*Bell correlations in a many-body system with finite statistics*”
S. Wagner, R. Schmied, M. Fadel, P. Treutlein, N. Sangouard, J.-D. Bancal
Phys. Rev. Lett. **119**, 170403 (2017)
- “*Mesoscopic quantum superpositions in bimodal Bose-Einstein condensates: decoherence and strategies to counteract it*”
K. Pawłowski, M. Fadel, P. Treutlein, Y. Castin and A. Sinatra
Phys. Rev. A. **95**, 063609 (2017)
- “*Bell correlations in a Bose-Einstein condensate*”
R. Schmied, J.-D. Bancal, B. Allard, M. Fadel, V. Scarani, P. Treutlein and N. Sangouard
Science **352**, 441 (2016)

Publications not included in this thesis work

- “*Sideband Rabi spectroscopy of finite-temperature trapped Bose gases*”
B. Allard, M. Fadel, R. Schmied and P. Treutlein
Phys. Rev. A. **93**, 043624 (2016)

Bose-Einstein condensates: Theory

In this chapter we briefly introduce the concept of Bose-Einstein condensates and give an overview of theoretical models describing their dynamics. Moreover, we explain how particle losses and decoherence limit the practical applications of such systems. Furthermore, we present the derivation of theoretical models describing the excitation spectrum of BECs at both zero and finite temperatures. For further theoretical details excellent references are [31, 32], while an experimental perspective of the field is given in [33].

2.1 Bose-Einstein condensation

In 1924-25 Bose and Einstein [34, 35] realized that, when cooled to very low temperatures, an ideal gas of non-interacting bosons can undergo a peculiar phase transition, later called Bose-Einstein condensation. The resulting state of matter is characterized by a macroscopic population of the lowest energy state of the system, and it is a genuinely quantum phenomenon arising due to the indistinguishability of the bosonic particles.

For decades Bose-Einstein condensates (BECs) were just a curious theoretical result, without any experimental evidence. Moreover, as the original idea involved non-interacting bosons, it was never really clear what role could have played interactions between the particles, almost always present in nature. For example, intuition would tell us that at low temperatures atoms just form a solid.

After many years of attempts, involving different systems and techniques, the first experimental realizations of BECs in dilute gases were observed in 1995 [36–38]. Since then, a vast number of further theoretical and experimental investigations appeared, constituting an entirely new field of physics.

In our experiments we use BECs as a tool. Important features making such many-body quantum systems especially suited for our investigations are the exceptional coherence properties, and the practical state manipulation. Moreover, the fact that all atoms in a BEC occupy the same spatial quantum state results in a magnification of quantum phenomena to the macroscopic scale, making them easier to observe. Also for these reasons, BECs found numerous applications in the fields of *e.g.* quantum metrology and quantum information.

2. Bose-Einstein condensates: Theory

2.1.1 Elementary concepts

A first, intuitive, understanding of Bose-Einstein condensation can be obtained from the following simple argument [33]. According to quantum mechanics, particles can be described by wavepackets, which have a spatial extent on the order of the thermal de Broglie wavelength $\lambda_{\text{dB}} = (2\pi\hbar^2/mk_B T)^{1/2}$, where T is the temperature and m the mass of the particle. This wavelength can be seen as a position uncertainty, and its dependence on temperature is related to the uncertainty relation. At low temperatures the momentum uncertainty decreases, which requires λ_{dB} to increase, while at high temperatures the converse applies.

Whether particles are indistinguishable or not is irrelevant at high temperatures, because their small spatial extent allows to distinguish them according to their position. On the contrary, if temperature is low enough λ_{dB} becomes comparable to the separation among the particles, and the individual wavepackets start to overlap. Particle indistinguishability plays now an important role. In the case of indistinguishable bosons a phase transition occurs, called Bose-Einstein condensation, characterized by a significant fraction of the particles occupying the same spatial quantum state. Decreasing the temperature even further increases this fraction, in the ideal case until all particles occupy the same state.

Even if this explanation is rather qualitative, it gives an intuitive understanding of Bose-Einstein condensation. A more refined description can be formulated from simple combinatorial arguments, which highlight the crucial role of bosonic statistics [32].

Consider a quantum system characterized by p energy levels, among which N particles are distributed. In the special case where there are $N = p$ distinguishable particles, there are $N!$ configurations with one particle per state, but only N configurations with all the particles in the same state. Therefore, even for small N , it is extremely unlikely to find a large population of any state. However, if particles are indistinguishable, there is only 1 configuration with one particle per state, but still N configurations where all particles are in the same state. This shows how for indistinguishable particles (that are all allowed to occupy the same state, such as bosons in quantum mechanics), there is a much higher probability of finding a large population of one of the states.

In practical situations, observing a large population in a single state is hindered by the fact that the number of accessible states is typically $p \gg N$. Intuitively, we can understand that the probability for such configurations to occur is negligible compared to the one where there is one particle per state, independently of whether the particles are indistinguishable or not. To enter in a regime where $p \lesssim N$, one needs to limit the number of states accessible by the particles, which is achieved experimentally by lowering the temperature T of the system.

It is important to emphasize that Bose-Einstein condensation is due to quantum statistics, and not to the interaction between the particles as for other phase transitions. In fact, condensation can occur for non-interacting particles, and interactions with finite strength result only in a shift of the BEC transition temperature.

2.1.2 Critical temperature for condensation

To be observed, Bose-Einstein condensation requires to cool the particles below the critical temperature T_c associated to the system. Whether or not $T_c > 0$ depends entirely on the density of states, and on how they are distributed in energy. These properties are directly related to the dimensionality of the system, to the interactions present among the particles, and on the geometry of the confining potential. In the particular cases where $T_c = 0$ condensation will never occur in practice, as experiments are always performed at finite temperature. For example, in a uniform gas of massive non-interacting bosons condensation occurs at finite temperature only in more than two dimensions.

For our experiments we use atoms of Rubidium-87, which can be described as massive bosons with (weak) s -wave repulsive interactions, confined in a three-dimensional harmonic potential $V = m(\omega_x^2 x^2 + \omega_y^2 y^2 + \omega_z^2 z^2)/2$. Under the approximation of large N and no interactions, the transition temperature is

$$T_c^0 = \left(\frac{N}{\zeta(3)} \right)^{1/3} \frac{\hbar \bar{\omega}_g}{k_B}, \quad (2.1)$$

where $\bar{\omega}_g = (\omega_x \omega_y \omega_z)^{1/3}$ is the geometric mean of the trapping frequencies. Finite number of atoms, and interactions, result in a shift of this temperature. A more accurate transition temperature for our experimental situation is given by introducing correction terms taking into account these effects, which results in the expression [39]

$$T_c \simeq \left(1 - 0.73 \frac{\bar{\omega}_a}{\bar{\omega}_g} N^{-1/3} - 1.33 \frac{a_s}{a_{\text{HO}}} N^{1/6} \right) T_c^0, \quad (2.2)$$

where $\bar{\omega}_a = (\omega_x + \omega_y + \omega_z)/3$ is the arithmetic mean of the trapping frequencies, a_s the scattering length characterizing the s -wave interaction strength, and $a_{\text{HO}} = (\hbar/m\bar{\omega}_g)^{1/2}$ is the harmonic oscillator length scale. In Eq. (2.2) the term proportional to $N^{-1/3}$ corrects for finite number of atoms, while the term proportional to $N^{1/6}$ takes into account the effect of interactions. As an example for our typical experimental parameters, $N = 500$ atoms in a trap of frequencies (110, 730, 730) Hz, we find for Eq. (2.2) $T_c \simeq (1 - 0.124 - 0.036) 139.166 \text{ nK} \approx 117 \text{ nK}$. From this we note that the finite-size correction is approximately three times larger than the interaction corrections, and together they result in a reduction of the transition temperature by $\approx 16\%$.

When $T < T_c$, the ratio between the number of particles in the condensate and the total number of particles is given by

$$\frac{N_0}{N} = 1 - \left(\frac{T}{T_c} \right)^3. \quad (2.3)$$

This expression shows that the condensed fraction increases rapidly for $T < T_c$, *e.g.* it is already $\approx 85\%$ for $T = T_c/2$.

2. Bose-Einstein condensates: Theory

2.1.3 BEC on atom chips

Among the several experimental setups conceived to achieve Bose-Einstein condensations, atom chips [23] constitute a compact platform to prepare, confine and manipulate ultracold atomic ensembles. Such chips, placed inside ultra-high vacuum chambers, are devices with micro-fabricated wire structures, that allow to magnetically confine neutral atoms. In addition, the versatility in the design and in the fabrication techniques permit to embed additional components, to couple atoms with magnetic, radio-frequency (RF), microwave, or optical fields.

As for the case of optical traps, on-chip magnetic traps are loaded from atomic ensembles previously laser cooled with standard techniques. Then, Bose-Einstein condensations is reached by further evaporative cooling stages [40]. By controlling the currents flowing through the chip's wires a variety of magnetic trapping potentials can be tailored, and precise control and coherent manipulation of the atomic motional state has been demonstrated [24, 41]. Sending RF or microwave currents creates additional strong near-field gradients at the atoms' position, which can couple on- or off-resonantly to the atomic transitions, and be used for internal-state manipulations or to produce state-selective potentials [24].

Apart from the flexibility in their design, atom chips have the advantage of relying on DC, RF and microwave currents for trapping and manipulating the atomic ensemble. The electronics required to generate such currents with high stability is well developed, and result in good reproducibility of the experimental sequence. This is in contrast to setups relying on optical traps, since intensities of the laser lights are more difficult to stabilize. Furthermore, atom chips allow for relatively small experimental setups. This enables to find a number of practical applications for BECs, from portable atomic clocks to sensors for metrology, which rely on compact devices [42, 43].

2.2 Zero-temperature BEC

Throughout this work, by “zero temperature” we actually refer to the regime where the number of non-condensed particles is much smaller than the number of condensed particles, so that they can be neglected. This requires the temperature to be low enough with respect to the critical temperature, to avoid thermal depletion, but also the interaction strength must be sufficiently small. In fact, even at $T = 0$, collision between condensed particles can scatter them outside the condensate (quantum depletion). For our typical experimental parameters the fraction of non-condensed atoms due to quantum depletion can be roughly estimated to be $\frac{N-N_0}{N} \approx \sqrt{a_s^3 n} \sim 10^{-3}$ [44], where n is the density, indicating that it can be neglected.

2.2.1 The Gross-Pitaevskii equation

An accurate description for the quantum state of a BEC is given by the many-body ground-state wavefunction $\Phi_0(\mathbf{x}_1, \dots, \mathbf{x}_N, t)$ solving the Schrödinger equation of the

system. However, finding such solution is in general extremely complicated, because of interactions. To circumvent this problem, one can derive an approximate description for the state of the BEC, with the assumptions that (1) the many-body wavefunction $\Phi(\mathbf{x}_1, \dots, \mathbf{x}_N, t) = \prod_{i=1}^N \phi(\mathbf{x}_i, t)$ is the product of identical single-particle wavefunctions $\phi(\mathbf{x}_i, t)$, and that (2) particles interact pairwise through the contact potential $g\delta(\mathbf{x} - \mathbf{x}')$ characterized by the interaction strength g . These two assumptions are remarkably good for dilute gases of weakly interacting particles, as in our case.

Time-independent description

In the stationary case the quantum state of a BEC is associated to a time-independent single-particle wavefunction $\phi(\mathbf{x}_i)$. The latter is defined as the solution to the Gross-Pitaevskii equation (GPE)

$$\left[h(\mathbf{x}) + g(N-1)|\phi(\mathbf{x})|^2 \right] \phi(\mathbf{x}) = \mu \phi(\mathbf{x}), \quad (2.4)$$

where μ is the chemical potential, $g(N-1)|\phi(\mathbf{x})|^2$ is an effective interaction potential, and $h(\mathbf{x})$ is the Hamiltonian for a single particle in the confining potential $V(\mathbf{x})$

$$h(\mathbf{x}) = -\frac{\hbar^2}{2m} \nabla_{\mathbf{x}}^2 + V(\mathbf{x}). \quad (2.5)$$

Eq. (2.4) is derived from the time-independent Schrödinger equation of the system, as it is shown in Appendix A.1.

For dilute gases where s -wave scattering gives a good approximation of the interaction process among atoms, the strength of the contact potential can be expressed in terms of the scattering length a_s by

$$g = \frac{4\pi\hbar^2 a_s}{m}. \quad (2.6)$$

The chemical potential μ appearing in Eq. (2.4) can be thought of as “the energy needed to add one particle to the system”, and importantly it is not the mean energy per particle. For a detailed discussion of these concepts, see Appendix A.1.

Apart from the stationary many-body wavefunction $\Phi(\mathbf{x}_1, \dots, \mathbf{x}_N) = \prod_{i=1}^N \phi(\mathbf{x}_i)$, it is common to define the condensate order parameter as $\Psi(\mathbf{x}) = \sqrt{N}\phi(\mathbf{x})$. A rigorous (and physical) understanding of this quantity needs a treatment of the problem in the second quantization formalism, where its connection with the bosonic field operator $\hat{\Psi}$ becomes evident.

Time-dependent description

To describe dynamical problems we consider the wavefunction $\Phi(\mathbf{x}_1, \dots, \mathbf{x}_N, t) = \prod_{i=1}^N \phi(\mathbf{x}_i, t)$, where the time-dependent single-particle wavefunction $\phi(\mathbf{x}_i, t)$ is defined as the solution to the time-dependent GPE (TDGPE)

$$i\hbar \frac{\partial}{\partial t} \phi(\mathbf{x}, t) = \left[h(\mathbf{x}) + g(N-1)|\phi(\mathbf{x}, t)|^2 \right] \phi(\mathbf{x}, t). \quad (2.7)$$

2. Bose-Einstein condensates: Theory

Similarly to the time-independent GPE, Eq. (2.7) may be derived from the time-dependent Schrödinger equation describing the many-body system.

From the fact that the time evolution of the stationary wavefunction is $\phi(\mathbf{x}, t) = \phi(\mathbf{x})e^{i\theta(t)}$, inserting this expression into Eq. (2.7), and making use of Eq. (2.4), we obtain

$$\frac{d\theta(t)}{dt} = -\frac{\mu}{\hbar}. \quad (2.8)$$

Therefore, under stationary conditions the BEC wavefunction evolves in time as

$$\phi(\mathbf{x}, t) = \phi(\mathbf{x})e^{-i\mu t/\hbar}. \quad (2.9)$$

It is interesting to note that the phase evolution is given by the chemical potential μ , and not by the single particle energy. This reflects the fact that interactions, which are included in μ by the GPE mean-field description, influence the time evolution of the phase.

While Eq. (2.7) conserves the total number of particles, $N(t) = N$, we will see that in practical situations atoms are lost from the BEC. To describe the dynamics for long times, where losses cannot be neglected, it is possible to introduce complex terms on the right hand side of Eq. (2.7), effectively resulting in a decay of $N(t)$. As an example, a term $-i\frac{\hbar}{2}\gamma_1\phi(\mathbf{x}, t)$ mimics (1-body) losses at a rate γ_1 , while a term $-i\frac{\hbar}{2}\gamma_2|\phi(\mathbf{x}, t)|^2\phi(\mathbf{x}, t)$ mimics (2-body) density-dependent losses at a rate $\gamma_2|\phi(\mathbf{x}, t)|^2$.

2.2.2 Stationary solutions to the GPE

The GPE is a nonlinear differential equation, which in general has no analytic solution. However, for particular cases analytic solution are known. These cases are *e.g.* for no interactions, $g = 0$ (harmonic oscillator limit), and for strong interactions, where the kinetic energy is negligible in comparison to the interaction energy (Thomas-Fermi limit).

To have an indication of the regime of the system, it is convenient to consider the ratio between interaction and kinetic energy. The parameter

$$\eta = \frac{N|a_s|}{a_{\text{HO}}} \quad (2.10)$$

expresses the importance of particle interactions compared to their kinetic energy. For $\eta < 1$, the system is described with reasonable accuracy by the harmonic oscillator approximation, while for $\eta \gg 1$ by the Thomas-Fermi approximation.

Harmonic oscillator limit, $\eta = 0$

If the particles are not interacting, *i.e.* $g = 0$, or if the interaction energy is negligible compared to the kinetic energy, then the non-linear (interaction) term in the GPE can be neglected, leaving a linear Schrödinger equation.

2.2 Zero-temperature BEC

In the case of a 3D harmonic trapping potential, $V(\mathbf{x}) = \frac{1}{2}m(\omega_x^2 x^2 + \omega_y^2 y^2 + \omega_z^2 z^2)$, the ground state single-particle wavefunction is

$$\phi(\mathbf{x}) = \left(\frac{m\bar{\omega}g}{\pi\hbar}\right)^{3/4} \exp\left(-\frac{m}{2\hbar}(\omega_x x^2 + \omega_y y^2 + \omega_z z^2)\right), \quad (2.11)$$

and the chemical potential becomes simply the ground state energy

$$\mu = \frac{\hbar(\omega_x + \omega_y + \omega_z)}{2}. \quad (2.12)$$

The spatial extension of the ground state $\phi(\mathbf{x})$ is given by $\langle x^2 \rangle = a_{\text{HO}}^2/2$, with similar expressions for $\langle y^2 \rangle$ and $\langle z^2 \rangle$, independent of N .

Perturbation theory, $\eta \approx 0$

If the interaction energy is small compared to the kinetic energy, but not negligible, it is possible to use perturbation theory to obtain corrections beyond the harmonic oscillator limit.

For example, to first order in perturbation theory the ground state of the system is still the one of the harmonic oscillator limit, but the chemical potential becomes

$$\begin{aligned} \mu &= \frac{\hbar(\omega_x + \omega_y + \omega_z)}{2} + (N-1)g \int d\mathbf{x} |\phi(\mathbf{x})|^4 \\ &= \frac{\hbar(\omega_x + \omega_y + \omega_z)}{2} + (N-1)g \left(\frac{m\bar{\omega}g}{2\pi\hbar}\right)^{3/2}. \end{aligned} \quad (2.13)$$

To second and higher order also the wavefunction is modified, and the expressions become more complicated.

Thomas-Fermi limit, $\eta \gg 1$

If the interaction energy is very large compared to the kinetic energy, the latter can be neglected. In this regime the GPE equation can be approximated by the expression (which is not a differential equation)

$$\left[V(\mathbf{x}) + g(N-1)|\phi(\mathbf{x})|^2 \right] \phi(\mathbf{x}) = \mu \phi(\mathbf{x}). \quad (2.14)$$

Multiplying both sides by $\phi(\mathbf{x})^*$, and integrating over space, gives the atomic density distribution $|\phi(\mathbf{x})|^2 = (\mu - V(\mathbf{x})) / g(N-1)$, where μ is such that $\int d\mathbf{x} |\phi(\mathbf{x})|^2 = 1$. The wavefunction for the ground state of the system can therefore be expressed as the real function

$$\phi(\mathbf{x}) = \begin{cases} \sqrt{\frac{\mu - V(\mathbf{x})}{g(N-1)}} & V(\mathbf{x}) < \mu \\ 0 & V(\mathbf{x}) \geq \mu \end{cases} \quad (2.15)$$

2. Bose-Einstein condensates: Theory

In the case of a harmonic trapping potential the BEC has a parabolic density profile (see Fig. 2.1)

$$|\phi(\mathbf{x})|^2 = \frac{15}{8\pi} N \left(\frac{m\bar{\omega}g}{2\mu} \right)^{3/2} \max \left[1 - \left(\frac{x^2}{R_{\text{TF},x}^2} + \frac{y^2}{R_{\text{TF},y}^2} + \frac{z^2}{R_{\text{TF},z}^2} \right), 0 \right], \quad (2.16)$$

with $R_{\text{TF},i}$ the Thomas-Fermi radius along $i \in \{x, y, z\}$, where the condensate density goes to zero. These are defined as

$$R_{\text{TF},x} = \sqrt{\frac{2\mu}{m\omega_x^2}} = \left(\frac{15\hbar^2 a_s \omega_y \omega_z}{m^2 \omega_x^4} \right)^{1/5} (N-1)^{2/5}, \quad (2.17)$$

where we used $g = \frac{4\pi\hbar^2 a_s}{m}$. Similar expressions are found for $R_{\text{TF},y}$ and $R_{\text{TF},z}$.

The chemical potential is found by integrating the density over the ellipsoid $\left(\frac{x}{R_{\text{TF},x}} \right)^2 + \left(\frac{y}{R_{\text{TF},y}} \right)^2 + \left(\frac{z}{R_{\text{TF},z}} \right)^2 \leq 1$, and requiring normalization. This gives

$$\mu = \frac{\hbar\bar{\omega}g}{2} \left(15 \frac{(N-1)a_s}{a_{\text{HO}}} \right)^{2/5}. \quad (2.18)$$

The total energy of the system is $E_{\text{TF}} = \frac{5}{7}\mu$, and $\langle x^2 \rangle = \frac{1}{7}R_{\text{TF},x}^2$, with similar expressions for $\langle y^2 \rangle$ and $\langle z^2 \rangle$.

Intermediate regimes, η

For the typical parameters of our experiments, $N = 500$ atoms in a trap of frequencies (110, 730, 730) Hz, we find $\eta \approx 5$. This means that we are neither in the harmonic oscillator limit nor in the Thomas-Fermi limit. In these intermediate regimes there are known analytical expressions for $\phi(\mathbf{x})$ interpolating between the two extreme cases, which can be found in [45, 46]. However, for practical purposes, it is often more convenient to solve numerically the GPE, see Fig. 2.1. As an example, for the experimental parameters quoted before we find numerically a chemical potential of $\mu_{\text{GPE}}/h = 1373$ Hz, while the approximations $\mu_{\text{HO}}/h = 785$ Hz (Eq. (2.12)), $\mu_{\text{PT}}/h = 2289.7$ Hz (Eq. (2.13)) and $\mu_{\text{TF}}/h = 1079.5$ Hz (Eq. (2.18)) would give significantly different estimates.

2.2.3 Multi-component BEC

Until now, we considered the case where the condensed bosons do not have any internal degree of freedom. If this additional property exists, particles in different internal states can be distinguished, and for this reason they can be described as distinct condensates constituting together a multi-component BEC [32]. In this situation, Eq. (2.4) can be generalized to a system of coupled GPEs

$$\left[\hbar_i(\mathbf{x}) + g_{ii}(N_i - 1)|\phi_i(\mathbf{x})|^2 + \sum_{j \neq i} g_{ij} N_j |\phi_j(\mathbf{x})|^2 \right] \phi_i(\mathbf{x}) = \mu_i \phi_i(\mathbf{x}), \quad (2.19)$$

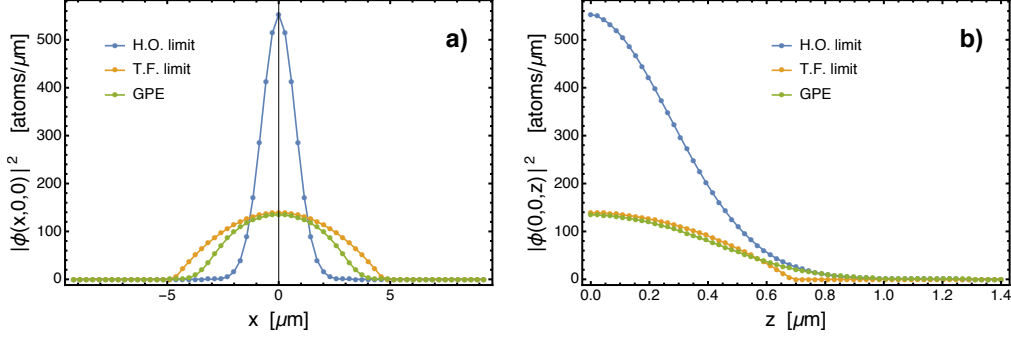


Figure 2.1: BEC wavefunction for different regimes. Simulation for $N = 500$ particles in the harmonic oscillator regime (blue line), Thomas-Fermi regime (orange line), and for our experimental situation (green line). The trap has frequencies 2π (110, 730, 730) Hz. **a)** Axial (x -direction) density profiles. **b)** Radial (z -direction) density profiles. Note that for our experimental parameters the BEC wavefunction is not reproduced correctly by the two limiting cases.

where the indexes i and j label the different components, g_{ii} and g_{ij} are the strength of interactions between particles with respectively equal and different internal states, and $h_i(\boldsymbol{x})$ is the single-particle Hamiltonian. For the time-dependent case, a similar generalization holds for Eq. (2.7).

In the case of s -wave scattering, the interaction strengths in Eq. (2.19) can be written as $g_{ij} = \frac{4\pi\hbar^2 a_{ij}}{m}$, where the scattering length a_{ij} in general depends on the internal states i and j of the interacting particles. For the hyperfine states $|1\rangle = |F = 1, m_F = -1\rangle$ and $|2\rangle = |F = 2, m_F = 1\rangle$ of the ^{87}Rb electronic ground state, the scattering lengths are [47]

$$\begin{aligned} a_{11} &= 100.40 a_0 \\ a_{12} &= 98.01 a_0 \\ a_{22} &= 95.44 a_0 \end{aligned}$$

where a_0 is the Bohr radius. Even if their difference is only $\approx 5\%$, the effect of this asymmetry is reflected on the shape of the different components. For equal superposition of the two states, the component $|2\rangle$ tends to form a core surrounded by a condensate of atoms in state $|1\rangle$ of lower density, Fig. 2.2. In the case of large BEC atom numbers ($N \gg 1000$) one can even observe a complete separation of the two components [48].

Eq. (2.19) describes a stationary situation with constant populations in the wavefunctions $\phi_i(\boldsymbol{x})$ of the different components, N_i . In the presence of *e.g.* spin-exchanging collisions or external fields coupling the different components, these populations might vary in time. To describe these scenarios, additional terms need to be added to the multi-component time-dependent GPE.

For the two-component situation we are interested in, we can consider the system of

2. Bose-Einstein condensates: Theory

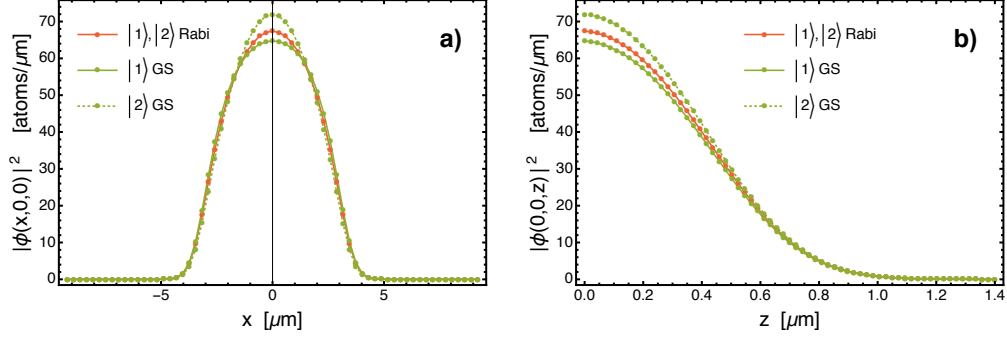


Figure 2.2: Two-component BEC wavefunctions. Simulation for $N = 500$ particles equally distributed among the two internal components assuming the system to be prepared by a $\pi/2$ Rabi pulse (red line), or in the ground state (green lines). The trap has frequencies 2π (110, 730, 730) Hz. **a)** Axial (x -direction) density profiles. **b)** Radial (z -direction) density profiles. Note that in the ground state (green lines) the wavefunctions of the two components have slightly different shapes due to the different scattering cross sections. On the contrary, if the system is initially prepared with all the particles in state $|1\rangle$, and then a $\pi/2$ Rabi pulse is sent to transfer half of its population in state $|2\rangle$, immediately afterwards the wavefunctions are identical for the two components (assuming an instantaneous transfer, red lines). This result in a situation different from the ground state, and therefore of non-equilibrium, where the wavefunctions will change in time.

two coupled GPEs

$$i\hbar \frac{\partial}{\partial t} \phi_1 = [h_1 + g_{11}(N_1 - 1)|\phi_1|^2 + g_{12}N_2|\phi_2|^2] \phi_1 + \frac{\hbar\Omega_R}{2} e^{-i\delta t} \phi_2 - i\frac{\hbar}{2}\gamma_1\phi_1$$

$$i\hbar \frac{\partial}{\partial t} \phi_2 = [h_2 + g_{22}(N_2 - 1)|\phi_2|^2 + g_{12}N_1|\phi_1|^2] \phi_2 + \frac{\hbar\Omega_R}{2} e^{i\delta t} \phi_1 - i\frac{\hbar}{2}\gamma_2\phi_2$$

where Ω_R is the Rabi frequency, δ is the detuning of the Rabi pulse with respect to the $|1\rangle$ to $|2\rangle$ transition and γ_i is the 1-body loss rate for state i . Higher order loss process can be introduced by adding further imaginary terms, *e.g.* a term $-i\frac{\hbar}{2}\gamma_{11}|\phi_1|^2\phi_1$ would mimic (2-body) density-dependent losses in state $|1\rangle$, at a rate $\gamma_{11}|\phi_1|^2$.

2.2.4 Collective spin Hamiltonian

The multi-component GPE provides a mean-field description of the spatial mode functions into which the atoms are condensed. To focus on the description of the BEC internal state, it is convenient to express the Hamiltonian of the system in terms of a collective spin [12]. The idea relies on the fact that a boson with internal states can be equivalently described as an effective spin, and therefore that the entire system can be seen as the (usually symmetric) composition of all such spins. Interestingly, this same description is used also for the internal state of thermal atoms that couple identically to the same light field and are thus indistinguishable with respect to this interaction [12], highlight-

ing the fact that a collective spin can be defined independently on whether particles are indistinguishable or occupying the same spatial mode.

To derive the collective spin description of a two-component BEC, we follow the approach of Ref. [49]. First, we consider the Hamiltonian of the system in the second quantization formalism,

$$\hat{H} = \int d\mathbf{x} \sum_{i=1,2} \left[\hat{\Psi}_i^\dagger(\mathbf{x}) h_i \hat{\Psi}_i(\mathbf{x}) + \frac{1}{2} g_{ii} \hat{\Psi}_i^\dagger(\mathbf{x}) \hat{\Psi}_i^\dagger(\mathbf{x}) \hat{\Psi}_i(\mathbf{x}) \hat{\Psi}_i(\mathbf{x}) \right] + g_{12} \hat{\Psi}_1^\dagger(\mathbf{x}) \hat{\Psi}_2^\dagger(\mathbf{x}) \hat{\Psi}_2(\mathbf{x}) \hat{\Psi}_1(\mathbf{x}), \quad (2.22)$$

where $\hat{\Psi}_i$ is the bosonic field operator associated to the i -th component. Then, we define the operator

$$\hat{a}_i = \int d\mathbf{x} \bar{\phi}_i^*(\mathbf{x}) \hat{\Psi}_i(\mathbf{x}) \quad (2.23)$$

where $\bar{\phi}_i$ is the stationary wavefunction for the i -th component, found as a solution to the coupled GPEs Eq. (2.19) with $\bar{N}_i = \langle \hat{N}_i \rangle$ particles. This so-called two-mode approximation assumes that the field operator can be decomposed as $\hat{\Psi}_i(\mathbf{x}) = \hat{a}_i \bar{\phi}_i$, where the spin and the spatial degrees of freedom factorize. In other words, this means that there are only two spatial modes, ϕ_1 and ϕ_2 , that can be occupied by the atoms (note that in our case, since $g_{11} \approx g_{22}$, we have $\phi_1 \approx \phi_2$).

From Eq. (2.23) we define the components of the collective spin operator

$$\hat{S}_x = \frac{1}{2} (\hat{a}_1^\dagger \hat{a}_2 + \hat{a}_2^\dagger \hat{a}_1) \quad (2.24a)$$

$$\hat{S}_y = \frac{1}{2i} (\hat{a}_1^\dagger \hat{a}_2 - \hat{a}_2^\dagger \hat{a}_1) \quad (2.24b)$$

$$\hat{S}_z = \frac{1}{2} (\hat{a}_1^\dagger \hat{a}_1 - \hat{a}_2^\dagger \hat{a}_2) \quad (2.24c)$$

together with the atom number operators $\hat{N}_i = \hat{a}_i^\dagger \hat{a}_i$ and $\hat{N} = \hat{N}_1 + \hat{N}_2$. From Eqs. (2.24) we see that \hat{S}_z is equal to half the atom number difference between the two components, while $\hat{S}_x = \Re \left[\hat{a}_1^\dagger \hat{a}_2 \right]$ and $\hat{S}_y = \Im \left[\hat{a}_1^\dagger \hat{a}_2 \right]$ are related to their relative phase.

At this point, we expand the Hamiltonian \hat{H} of the system around the mean number of atoms in the two components, \bar{N}_i . To second order this gives

$$\hat{H} \simeq E(\bar{N}_1, \bar{N}_2) + \sum_j (\mu_j)_{\bar{N}_1, \bar{N}_2} (\hat{N}_j - \bar{N}_j) + \frac{1}{2} \sum_j \left(\frac{\partial \mu_j}{\partial N_j} \right)_{\bar{N}_1, \bar{N}_2} (\hat{N}_j - \bar{N}_j)^2 + \frac{1}{2} \left(\frac{\partial \mu_1}{\partial N_2} + \frac{\partial \mu_2}{\partial N_1} \right)_{\bar{N}_1, \bar{N}_2} (\hat{N}_1 - \bar{N}_1)(\hat{N}_2 - \bar{N}_2), \quad (2.25)$$

where $E(\bar{N}_1, \bar{N}_2)$ is the mean energy, and the chemical potentials (for $(N_i - 1) \approx N_i$)

2. Bose-Einstein condensates: Theory

are defined as

$$\begin{aligned}\mu_j &= \frac{\partial H}{\partial N_j} \\ &= \int d\mathbf{x} \phi_i^* h_i \phi_i + \sum_{j=1,2} g_{ij} N_j \int d\mathbf{x} |\phi_i|^2 |\phi_j|^2 .\end{aligned}\quad (2.26)$$

The Hamiltonian for the collective spin operator is now formulated by rewriting Eq. (2.25) in the form

$$\hat{H} = \left((\mu_1 - \mu_2) - 2\hbar\chi \langle \hat{S}_z \rangle + \hbar\tilde{\chi}(\hat{N} - \bar{N}) \right) \hat{S}_z + \hbar\chi \hat{S}_z^2 , \quad (2.27)$$

where we omitted the irrelevant constant term proportional to the total number of particles \hat{N} , and we introduced the coefficients

$$\tilde{\chi} = \frac{1}{2\hbar} \left(\frac{\partial \mu_1}{\partial N_1} - \frac{\partial \mu_2}{\partial N_2} \right)_{\bar{N}_1, \bar{N}_2} , \quad (2.28a)$$

$$\chi = \frac{1}{2\hbar} \left(\frac{\partial \mu_1}{\partial N_1} + \frac{\partial \mu_2}{\partial N_2} - \frac{\partial \mu_1}{\partial N_2} - \frac{\partial \mu_2}{\partial N_1} \right)_{\bar{N}_1, \bar{N}_2} . \quad (2.28b)$$

In Eq. (2.27), the term proportional to \hat{S}_z gives a rotation around z which depends on $\langle \hat{S}_z \rangle$ and on \hat{N} , while the term proportional to \hat{S}_z^2 gives rise to a nonlinear evolution, and it can be identified with the one-axis twisting Hamiltonian of Ref. [25].

In practice, Eqs. (2.28) can be evaluated by discretizing the derivatives as *e.g.* $\partial \mu_1 / \partial N_1 = [\mu_1(N_1 + \epsilon/2, N_2) - \mu_1(N_1 - \epsilon/2, N_2)] / \epsilon$, and then computing numerically each chemical potential from a system of coupled GPEs. This approach implicitly assumes the system to be prepared in its stationary ground state, which is close to but not precisely the situation occurring experimentally where the population in the two components is set by a Rabi pulse: this changes the internal state of the atoms without adapting their state-dependent spatial wavefunction, see Fig. 2.2. For typical parameters used in our experiments we find the values of χ and $\tilde{\chi}$ reported in Tab. 2.1.

In Fig. 2.3 we show the dependence of χ and $\tilde{\chi}$ on experimentally controllable parameters such as the variation in the relative longitudinal trapping frequency (Fig. 2.3a) and in the spatial separation between the two trap centers (Fig. 2.3b). The former parameter changes both χ and $\tilde{\chi}$, because all terms $\partial \mu_i / \partial N_j$ are affected. On the contrary, changing the spatial separation between the trap centers affects the density overlap between the two components, effectively changing only $\partial \mu_i / \partial N_{j \neq i}$ and therefore χ but not $\tilde{\chi}$. This approach is used in our experiment, where we make use of state-dependent potentials to tune the strength of χ by several orders of magnitude [19].

If the mode functions in Eq. (2.26) are independent on N_i , *i.e.* in the harmonic oscillator limit, then the derivatives in Eqs. (2.28) take the simple expressions

$$\tilde{\chi} = \frac{1}{2\hbar} \left(g_{11} \int d\mathbf{x} |\phi_1|^4 - g_{22} \int d\mathbf{x} |\phi_2|^4 \right) \quad (2.29a)$$

$$\chi = \frac{1}{2\hbar} \left(g_{11} \int d\mathbf{x} |\phi_1|^4 + g_{22} \int d\mathbf{x} |\phi_2|^4 - 2g_{12} \int d\mathbf{x} |\phi_1|^2 |\phi_2|^2 \right) . \quad (2.29b)$$

2.2 Zero-temperature BEC

N	(f_x, f_y, f_z)	$\tilde{\chi}/h$	χ/h
500	(27, 130, 130) Hz	1.8×10^{-3} Hz	-1.5×10^{-4} Hz
1000	(27, 130, 130) Hz	1.2×10^{-3} Hz	-0.8×10^{-4} Hz
500	(110, 540, 540) Hz	10.2×10^{-3} Hz	-6.7×10^{-4} Hz
1000	(110, 540, 540) Hz	6.8×10^{-3} Hz	-3.9×10^{-4} Hz
500	(110, 730, 730) Hz	13.0×10^{-3} Hz	-7.5×10^{-4} Hz
1000	(110, 730, 730) Hz	8.8×10^{-3} Hz	-6.7×10^{-4} Hz

Table 2.1: Values of $\tilde{\chi}$ and χ for some typical experimental parameters. The number of atoms in the two components is $N_1 = N_2 = N/2$. The calculation is based on discretizing the derivatives appearing in Eqs. (2.28), and then computing numerically each chemical potential from a system of coupled GPEs.

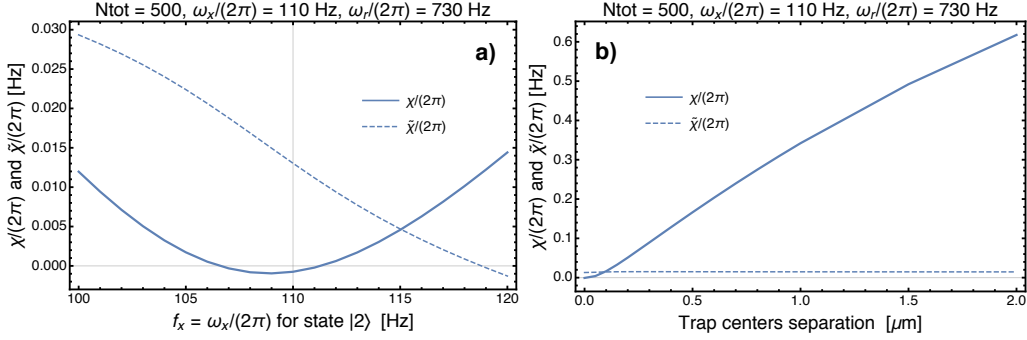


Figure 2.3: Dependence of χ and $\tilde{\chi}$ on experimentally controllable parameters. Simulation for $N = 500$ particles equally distributed among the two internal components, and assumes the system to be in the ground state. The trap for state $|1\rangle$ has always frequencies 2π (110, 730, 730) Hz. **a)** Dependence of χ and $\tilde{\chi}$ on the longitudinal trapping frequency for state $|2\rangle$, *i.e.* for 2π (f_x , 730, 730) Hz. Spatially, the traps are considered to be concentric. **b)** Dependence of χ and $\tilde{\chi}$ on the longitudinal separation between the traps, both with frequencies 2π (110, 730, 730) Hz.

The latter expression makes evident how χ depends both on the scattering lengths g_{ij} , and on the density overlaps $\int d\mathbf{x} |\phi_i|^2 |\phi_j|^2$. Therefore, this parameter can be controlled experimentally by modifying the scattering lengths, for example via Feshbach resonances, or by varying the density overlap between the two components, as we do in our experiments. For the internal states we use, the interaction strengths differ by at most 5%. Because of this, χ is small for overlapping atomic densities, but it can be increased by three orders of magnitude by separating completely the two components [19].

Relevant collective spin states

Some collective spin states are of particular importance because of their properties. In this section we define Dicke states, coherent spin states, squeezed states and Schrödinger

2. Bose-Einstein condensates: Theory

cat states, which are the ones that will be encountered again in the following chapters.

The simultaneous eigenstates of the \hat{S}_z and $\hat{S}^2 = \hat{S}_x^2 + \hat{S}_y^2 + \hat{S}_z^2$ operators are called Dicke states, and they are characterized by a specific relative atom number between the two components, and a completely undetermined relative phase. They are denoted with the symbol $|S, m\rangle$, where $S(S+1) = \langle \hat{S}^2 \rangle$ and $m = \langle \hat{S}_z \rangle$, and they form a complete basis. Fully symmetric states have $S = N/2$ and $m = -N/2, -N/2 + 1, \dots, N/2$. Dicke states with $|m| < N/2$ are entangled, and they are not trivial to be created experimentally. For example, they could be prepared by performing a non-destructive measurement of \hat{S}_z (to project the system in a state with definite m), or by controlling particular dynamics of the system. For example, with Rubidium-87 the spin-exchanging collisions $|F = 1, m_F = 0\rangle + |F = 1, m_F = 0\rangle \rightarrow |F = 1, m_F = -1\rangle + |F = 1, m_F = +1\rangle$ can be used to prepare an identical atom number in the two $m_F = \pm 1$ Zeeman levels, corresponding to the Dicke state $|N/2, 0\rangle$ (now for the two-level system formed by states $|F = 1, m_F = -1\rangle, |F = 1, m_F = +1\rangle$) also called “twin-Fock state” [50].

Of simple experimental preparation are coherent spin states, which are the tensor product of N identical and independent spin-1/2 states. In some sense, these can be thought of as the “most classical” pure quantum states, as all spins point on average along a specific direction (θ, ϕ) , so that the collective spin resembles a classical spin. Still, contrary to a classical spin, a coherent state has an uncertainty in the pointing direction due to quantum fluctuations (projection noise). Along any quadrature perpendicular to the mean spin direction the noise is always $\text{Var}[\hat{S}_\perp] = S/2$, while along the z -axis it is $\text{Var}[\hat{S}_z] = S \sin^2(\theta)/2$. A coherent spin state can be expressed as the binomial distribution of Dicke states

$$|\text{CSS}; \theta, \phi\rangle = \sum_{m=-S}^S \left[\binom{N}{x} p^x (1-p)^{N-x} \right]^{\frac{1}{2}} e^{-im\phi} |S, m\rangle, \quad (2.30)$$

with $N = 2S$, $x = S + m$ and $p = \cos^2 \frac{\theta}{2}$. From Eq. (2.30) we notice that the stretched spin states (or extremal Dicke states) $|S, \pm S\rangle$ are coherent spin states, *i.e.* $|\text{CSS}; 0, \phi\rangle = |S, S\rangle$ and $|\text{CSS}; \pi, \phi\rangle = |S, -S\rangle$, which are independent of ϕ . Experimentally, any coherent spin state $|\text{CSS}; \theta, \phi\rangle$ can be prepared from a stretched state by a single Rabi pulse. For example,

$$\begin{aligned} |\text{CSS}; \theta, \phi\rangle &= e^{-i\theta \hat{S}_{(\phi+\frac{\pi}{2})}} |S, S\rangle \\ &= e^{-i(\pi-\theta) \hat{S}_{(\phi-\frac{\pi}{2})}} |S, -S\rangle. \end{aligned} \quad (2.31)$$

Interesting states for metrology are spin squeezed states. Such states are polarized states (*i.e.* they have a mean spin length $\sqrt{\langle \hat{S}_x \rangle^2 + \langle \hat{S}_y \rangle^2 + \langle \hat{S}_z \rangle^2} \approx N/2$) characterized by a spin projection noise lower than than the one of a coherent state along a certain axis (squeezed direction). This noise reduction is compensated by a higher noise along the perpendicular axis (anti-squeezed direction), in order to keep the uncertainty relation satisfied. The metrological advantage is evident for the squeezed direction, along which

perturbations to the state can be resolved with a precision beyond the classical limit, which is the one given by a coherent state. Moreover, the robustness of squeezed states against particle losses makes them especially suited for practical applications. Experimentally, such states can be prepared by evolving a coherent spin state on the equator, $|\text{CSS}:\pi/2, \phi\rangle$, with the one-axis twisting Hamiltonian $\chi\hat{S}_z^2$ for a time $t \lesssim N^{-2/3}/\chi$ [25]. Because of their central role in our experiments, they will be discussed in detail later.

Finally, relevant highly entangled states are Schrödinger cat states, which are the coherent superposition of two (or more) coherent states. They highlight a counterintuitive feature of quantum mechanics which is the possibility of a superposition of macroscopically distinct states as, for example, in the cat state $\frac{1}{\sqrt{2}}(|S, -S\rangle + |S, +S\rangle)$ all spins are pointing simultaneously both up and down. Furthermore, in interferometric schemes such states allow to reach the Heisenberg limit for phase estimation, *i.e.* $\Delta^2\phi = 1/N^2$ which is the best allowed by quantum mechanics. Unfortunately, cat states are extremely fragile against noise and particle losses: losing even a single particle would completely destroy the state. Experimentally, such states can be prepared by evolving a coherent spin state on the equator, $|\text{CSS}:\pi/2, \phi\rangle$, with the one-axis twisting Hamiltonian $\chi\hat{S}_z^2$ for a time $t = \pi/(2\chi)$. Also these states will be discussed later in more detail.

Collective spin representations

The state of a two-level system can be equivalently interpreted as the state of a spin-1/2 particle, as their associated Hilbert spaces are identical. Pure states, $c_1|1\rangle + c_2|2\rangle$, are characterized by complex amplitudes c_i satisfying the normalization condition $|c_1|^2 + |c_2|^2 = 1$, where $|c_1|^2$ is the population of the i th level. Note that of the four real parameters defining c_1 and c_2 , one is constrained by normalization and another by the fact that global phases are irrelevant in the state description, so that only two independent parameters are left. This is made explicit with the parametrization $c_1 = \cos(\frac{\theta}{2})$, $c_2 = \sin(\frac{\theta}{2})e^{i\phi}$, where $0 \leq \theta \leq \pi$ determines the relative population between the two levels and $0 \leq \phi \leq 2\pi$ the relative phase. In this way, the state of the system can be represented graphically as the point with polar coordinates (θ, ϕ) on the surface of a sphere called Bloch sphere. It is advantageous to set the radius of this sphere to 1/2, such that the Cartesian coordinates of the point, $(\frac{1}{2}\cos(\phi)\sin(\theta), \frac{1}{2}\sin(\phi)\sin(\theta), \frac{1}{2}\cos(\theta))$, coincides with the spin expectation values $(\hat{s}_x, \hat{s}_y, \hat{s}_z) = \frac{\hat{\sigma}}{2}$, where $\hat{\sigma}$ is the vector of the Pauli matrices.

In the same spirit, the state of the collective spin introduced in Eqs. (2.24) has a convenient graphical representation as a point on the surface of a Bloch sphere with radius $N/2$, as the two accessible modes are now populated by N particles. The components

2. Bose-Einstein condensates: Theory

of the collective spin operator have expectation values

$$\langle \hat{S}_x \rangle = \left\langle \frac{1}{2} \left(\hat{a}_1^\dagger \hat{a}_2 + \hat{a}_2^\dagger \hat{a}_1 \right) \right\rangle = \frac{N}{2} \cos(\phi) \sin(\theta) \quad (2.32a)$$

$$\langle \hat{S}_y \rangle = \left\langle \frac{1}{2i} \left(\hat{a}_1^\dagger \hat{a}_2 - \hat{a}_2^\dagger \hat{a}_1 \right) \right\rangle = \frac{N}{2} \sin(\phi) \sin(\theta) \quad (2.32b)$$

$$\langle \hat{S}_z \rangle = \left\langle \frac{1}{2} \left(\hat{a}_1^\dagger \hat{a}_1 - \hat{a}_2^\dagger \hat{a}_2 \right) \right\rangle = \frac{N}{2} \cos(\theta) . \quad (2.32c)$$

Experimentally, the inevitable presence of noise prevents the preparation of pure states. For this reason the state of a physical system is better described by a statistical mixture of pure states, called mixed state. The most general expression for the state of a system is thus given by the density matrix

$$\hat{\rho} = \sum_i p_i |\psi_i\rangle \langle \psi_i| , \quad (2.33)$$

where $0 \leq p_i \leq 1$ is the statistical weight of the i th pure state $|\psi_i\rangle$, and $\sum_i p_i = 1$. For N spins the density matrix has dimension $2^N \times 2^N$. If we restrict to states that are symmetric under permutation of the parties the dimension is significantly reduced to $(N+1) \times (N+1)$.

Even if $\hat{\rho}$ gives a complete description of the state of the system, a graphical representation of its matrix elements does not give an intuitive understanding of such state. A more convenient (and still complete) description is given by the Wigner function, whose spherical version is defined as [51, 52]

$$W(\theta, \phi) = \sum_{k=0}^{2S} \sum_{q=-k}^k \rho_{kq} Y_{kq}(\theta, \phi) , \quad (2.34)$$

where Y_{kq} are the spherical harmonics and

$$\rho_{kq} = \sum_{m=-S}^S \sum_{m'=-S}^S t_{kq}^{Smm'} \langle S, m | \hat{\rho} | S, m' \rangle . \quad (2.35)$$

In the expression above we introduced the transformation coefficients

$$t_{kq}^{Smm'} = (-1)^{S-m} \sqrt{2k+1} \begin{pmatrix} S & k & S \\ -m & q & m' \end{pmatrix} \quad (2.36)$$

where the last term in parentheses is the Wigner $3j$ symbol.

The function $W(\theta, \phi)$ is a quasi-probability distribution which can be conveniently plotted on a generalized Bloch sphere of radius $N/2$, Fig. 2.4. The ‘‘center of mass’’ of W corresponds to the expectation value of $\hat{\mathbf{S}}$. Even if the marginals of W do not directly represent the probability distribution of an observable, the projection of W along a general spin direction $\hat{S}_{\vec{n}}$ can be related to the probability distribution of measuring $\hat{S}_{\vec{n}}$.

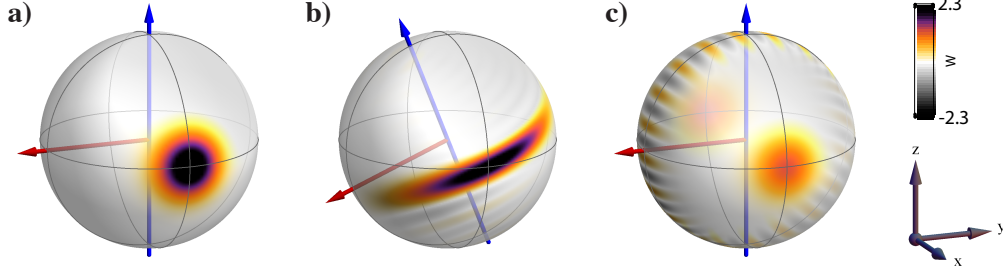


Figure 2.4: One-axis twisting dynamics. Simulation of the Hamiltonian $\chi\hat{S}_z^2$ for $N = 20$ particles. States are illustrated as spherical Wigner functions on Bloch spheres. **a)** Coherent spin state at time $t = 0$. **b)** Spin squeezed state obtained after a time $t = 0.13/\chi$. **c)** Schrödinger cat state obtained after a time $t = \pi/(2\chi)$. Figure adapted from Ref. [53].

Collective spin dynamics

Now that we have a graphical representation for the state of the collective spin describing the two-component BEC, we can easily illustrate the dynamics generated by the Hamiltonian Eq. (2.27). The typical initial condition to observe a non-trivial dynamics is a coherent state on the equator, Fig. 2.4a. As in the ideal case this state has $\langle \hat{S}_z \rangle = 0$ and a fixed number of atoms N , the only relevant term in the Hamiltonian Eq. (2.27) is $\hbar\chi\hat{S}_z^2$. After a time $t \lesssim N^{-2/3}/\chi$, the coherent state has evolved into a spin-squeezed state, Fig. 2.4b. Waiting for longer time results in a state which is wrapped around the sphere, up to the point when, at $t = \pi/(2\chi)$, a Schrödinger cat state is obtained, Fig. 2.4c. For even longer evolution times the dynamics appears reversed as at $t = \pi/(2\chi)$ a coherent spin state is obtained again, and from this time on the evolution repeats periodically in the same way.

In real experiments the total number of atoms fluctuates from shot to shot, and atoms are lost during the evolution. Both these effects result in a dynamics which deviates from the ideal case described by the one-axis twisting Hamiltonian, giving origin to noise in the final state. Total atom number fluctuations produce additional rotations around the z -axis, also called collisional clock shift, as described by the term $\hbar\tilde{\chi}(\hat{N} - \bar{N})\hat{S}_z$ in Eq. (2.27). Therefore, at time $t > 0$ one observes an incoherent superposition (statistical mixture) of states with different orientations. Note that this effect is deterministic, and in could be exactly corrected if the measured atom number at the end of the sequence corresponds to the initial atom number, meaning the absence of losses. Atom losses during the evolution change $\langle \hat{S}_z \rangle$, and for this reason the state acquires an additional rotation around the z -axis, as described by the term $2\hbar\chi\langle \hat{S}_z \rangle \hat{S}_z$ in Eq. (2.27). Again, after a time $t > 0$ this result in an incoherent superposition of states with different orientations. Note here that, as losses occur randomly in time, this noise cannot be canceled. These two effects will be discussed in more detail at the end of this chapter.

2. Bose-Einstein condensates: Theory

2.2.5 BEC lifetime

In any practical situation, potentials used to confine atomic ensembles have always a finite depth. For this reason particles can escape from the trap, thus limiting the lifetime of the atomic system. The main mechanism leading to losses consists in collisions whose final states are not trapped anymore. These scattering processes occur either among particles of the ensemble, or between particles of the background gas and of the ensemble. While the former process depends on the specific choice of internal states and trapping parameters, the background gas pressure is always finite, and therefore constitutes an unavoidable loss channel. The finite lifetime of trapped atomic systems imposes limitations on the possible duration of an experimental run and, for this reason, also on their practical applications. Apart from causing a depletion of the system over time, losses are also responsible for additional noise, which is discussed in more detail in the next section.

For a single ensemble composed by particles all in the same internal state, the mean atom number evolves according to the rate equation

$$\frac{dN}{dt} = - \sum_{m=1} k_m N^m . \quad (2.37)$$

Here, $k_m = \kappa_m \int d\mathbf{x} |\phi(\mathbf{x}, t)|^{2m}$ is the m -body loss rate, which depends on the time-dependent density profile and on the loss constants κ_m . When the time dependence of the density can be neglected, k_m is a constant and Eq. (2.37) can be solved analytically [53].

If the ensemble is composed of particles in more than one internal state they can collide among each other, constituting additional loss channels. The number of particles in each state is described by a system of coupled differential equations, whose solution can be found by numerical integration. For our experiments, involving ^{87}Rb atoms in the two states $|1\rangle \equiv |F = 1, m_F = -1\rangle$ and $|2\rangle \equiv |F = 2, m_F = -1\rangle$, we consider the two coupled rate equations

$$\frac{dN_1}{dt} = -k_1 N_1 - k_{2,1} N_1^2 - k_{2,i} N_1 N_2 - k_{3,1} N_1^3 \quad (2.38a)$$

$$\frac{dN_2}{dt} = -k_1 N_2 - k_{2,2} N_2^2 - k_{2,i} N_1 N_2 - k_{3,2} N_2^3 \quad (2.38b)$$

where we kept terms only up to the relevant three-body loss processes.

One-body losses result from collisions between the atoms of the ensemble and the molecules of the residual gas in the vacuum chamber. Since these molecules are at room temperature, they can kick atoms out of the trap. This process is proportional to the pressure of the background gas, but it is independent on the density of the ensemble, therefore leading to an exponential decay of its atom number over time, at a rate k_1 .

Two-body losses result from inelastic collisions between two particles of the ensemble. For ^{87}Rb atoms in state $|F = 2, m_F = 1\rangle$, the spin-exchanging process $|2, 1\rangle + |2, 1\rangle \rightarrow |2, 0\rangle + |2, 2\rangle$, which conserves m_F , leads to final states that escape from the trapping potential, resulting in particle losses at a rate $k_{2,2}$. For state

$|F = 1, m_F = -1\rangle$ spin-exchanging collisions are forbidden by angular momentum and energy conservation. Other inelastic two-body processes (spin-dipole mechanism) are extremely weak also compared to one-body losses, and therefore they can be neglected, giving $k_{2,1} = 0$. In multi-component ensembles collisions can occur also between atoms in different internal states, therefore leading to additional loss channels. For ^{87}Rb atoms, the process $|1, -1\rangle + |2, 1\rangle \rightarrow |1, 0\rangle + |2, 0\rangle$ is possible, resulting in particle losses at a rate $k_{2,i}$.

Three-body losses result from inelastic collisions between three particles of the ensemble. While energy-momentum conservation prevents the formation of molecules in two-body inelastic collisions, the presence of a third particle allows this process. The energy released when two particles form a bound state is converted into kinetic energy of both the molecule and the third particle, which escape from the trapping potential. For ^{87}Rb atoms this process occurs in both state $F = 1$ and $F = 2$, resulting in particle losses at the rates $k_{3,1}$ and $k_{3,2}$, respectively.

The loss constants κ_m appearing in k_m depend on the atomic species and on the internal state. The one of our interest have been measured for ^{87}Rb BECs in several experiments

One-body losses:	$\kappa_1 \approx 0.13 \text{ s}^{-1}$	
Two-body losses, $F = 1$:	$\kappa_{2,1} = 0$	[47]
Two-body losses, $F = 2$:	$\kappa_{2,2} = 8.1(3) \times 10^{-20} \text{ m}^3/\text{s}$	[47]
Two-body losses, interstate:	$\kappa_{2,i} = 1.5(2) \times 10^{-20} \text{ m}^3/\text{s}$	[47]
Three-body losses, $F = 1$:	$\kappa_{3,1} = 5.8 \times 10^{-42} \text{ m}^6/\text{s}$	[54]
Three-body losses ¹ , $F = 2$:	$\kappa_{3,2} = 18(5) \times 10^{-42} \text{ m}^6/\text{s}$	[55]

Contrary to the other rates, the one-body loss rate is not a fundamental constant, as it depends on the specific background pressure inside the vacuum chamber used for the experiments. The value we quote is chosen to match the atom number decay of our experimental data [53].

Note that in the case of a thermal ensemble, the loss coefficients reported above are modified due to particle distinguishability. Two-body loss rates are increased by a factor $2!$, while three-body loss rates by a factor $3!$.

To simplify Eqs. (2.38) it is often possible to consider the constant loss rate approximation

$$\frac{dN_1}{dt} = -\gamma_1 N_1 \quad (2.39a)$$

$$\frac{dN_2}{dt} = -\gamma_2 N_2 \quad (2.39b)$$

¹The value used for $\kappa_{3,2}$ was measured for the $|F = 2, m_F = 2\rangle$ state. An accurate value for $|F = 2, m_F = 1\rangle$ is not available, since the two-body loss dominates at typical experimental densities, including in the present experiment.

2. Bose-Einstein condensates: Theory

where γ_i is an effective loss rate for the i -th component, including contributions from one- two- and three-body loss processes. In practice, these constants are extracted by fitting the experimentally observed atom number decay with the exponential function $N_i(t) = N_i(t = 0)e^{-\gamma_i t}$. The constant loss rate approximation assumes *e.g.* that the atomic density does not change significantly during the losses, and it is therefore valid especially for short times where the fraction of lost atoms is small.

2.2.6 BEC coherence time

According to the time-dependent Gross-Pitaevskii equation Eq. (2.7), the global phase of a stationary BEC evolves deterministically as $\theta(t) = -\mu t/\hbar$, as expressed by Eq. (2.8). The generalization of this result holds for multi-component BECs as well, where the relative phase between different components become easily observable from interference measurements. In practical situations BECs are never closed systems, and for this reason phase evolution is affected by stochastic processes (*e.g.* losses, collisions) causing decoherence. Phase coherence is of primary importance to perform experiments in the quantum regime, and its finite duration poses also stringent limitations on the possible practical applications for such systems. For these reasons, investigating the fundamental limits of this property is of crucial interest.

The typical experimental procedure used to characterize decoherence is the following Ramsey sequence. First, one prepares a BEC in a single internal state. Then, a Rabi pulse is sent to transfer part of the population to a second internal state, thus setting a well-defined relative phase between the two BEC's components (*i.e.* preparing a coherent spin state). Finally, after a time T_R during which the condensate evolves in the trapping potential, a second Rabi pulse is sent, which allows to measure the relative phase between the components from their relative atom number. By repeating this experimental sequence a number of times, one has access to the distribution of the relative phase after an evolution time T_R , so that phase coherence as function of time can be investigated. More precisely, by varying the phase of the second Rabi pulse an interference fringe in the relative atom number is recorded, which carries information about the spreading of the relative phase distribution. The interference contrast is in fact [56]

$$C(t) \simeq e^{-\frac{1}{2} \text{Var}[\delta\theta(t)]}, \quad (2.40)$$

where $\delta\theta(t)$ is the relative phase under investigation and $\text{Var}[\delta\theta(t)]$ is its variance. This variance results from the sum of different contributions (*e.g.* atom number fluctuations, losses, finite temperature, technical noise), some of which are discussed here in detail. In practice, each contribution can be estimated by studying the dependence of $C(t)$ on experimental parameters and on time. For small noise (*e.g.* at small times T_R) where $C(t) \approx 1$ it is better to measure $\text{Var}[\delta\theta(t)]$ directly on the slope of a Ramsey fringe.

In the following, we will denote with N the atom number in a single shot of the experiment, \bar{N} its mean value, and ΔN its standard deviation, typically assumed to be $\Delta N \ll \bar{N}$.

Phase diffusion

Already at zero-temperature, *i.e.* when the non-condensed fraction can be neglected, and without losses, a decaying interference contrast can be observed due to a phenomenon called phase diffusion. This arises from the fact that the relative number of atoms and the relative phase between the different components of a BEC are conjugate non-commuting variables. Therefore, the typical state preparation consisting in setting a well-defined relative phase results in an uncertainty in the relative atom number. Because interaction energy depends on the populations of the components, uncertainty in the relative atom number directly translates into an uncertainty in the phase evolution, which causes a decay of $C(t)$. For two-component condensates at zero-temperature this phase noise is generated by the evolution of a coherent spin state with the term $\chi \hat{S}_z^2$ in Eq. (2.27). In other words, it corresponds to the anti-squeezing resulting from the one-axis twisting dynamics. For a coherent spin state with equal superposition, where $\text{Var} [\hat{S}_z] = \bar{N}/4$, the phase noise after a time t is [57]

$$\text{Var} [\delta\theta(t)] = \bar{N} \chi^2 t^2, \quad (2.41)$$

where χ is given in Eq. (2.28b). The resulting characteristic time (*i.e.* the time such that $C(t)$ is reduced by $e^{-1/2}$) for phase diffusion is

$$t_{\text{PD}} = \frac{1}{\chi \sqrt{\bar{N}}}. \quad (2.42)$$

For an estimate, consider the parameters of our experiments with $\bar{N} = 400$ atoms in a trap of frequencies (110, 730, 730) Hz. If the two components are spatially overlapping, $g_{11} \approx g_{22} \approx g_{12}$, which gives $\chi = 2\pi (-8.7 \times 10^{-4} \text{ Hz})$. This would imply $t_{\text{PD}} \approx 9$ s, which is of the same order of magnitude as the BEC lifetime (~ 10 s) and two orders of magnitude larger than the duration of a typical BEC experimental sequence (~ 100 ms).

Fluctuations in total N

Repeated preparations of BECs are characterized by fluctuations of the total number of atoms, which constitutes an additional source of phase noise because interaction energy depends on particle number, reducing $C(t)$. In principle this shift could be completely canceled in the data analysis, as it depends deterministically on the initial number of atoms. However, in practice this is only partially possible because what is measured is the atom number at the end of the experimental sequence, which is affected by random losses during the evolution and finite detection resolution. For two-component condensates at zero-temperature this phase noise is described by the term $\tilde{\chi}(\hat{N} - \bar{N})$ in Eq. (2.27) and, considering shot-to-shot fluctuations on the total number of particles with standard deviation $\Delta N \ll \bar{N}$, it gives [57]

$$\text{Var} [\delta\theta(t)] = (\Delta N)^2 \tilde{\chi}^2 t^2, \quad (2.43)$$

2. Bose-Einstein condensates: Theory

where $\tilde{\chi}$ is given in Eq. (2.28a). The resulting characteristic time for the decay of the contrast is

$$t_{\text{PS}} = \frac{1}{\tilde{\chi}\Delta N} . \quad (2.44)$$

For an estimate, consider again the parameters of our experiments with $\Delta N = 10$ *e.g.* set by post-selection. If the two components are spatially overlapping we find $\tilde{\chi} = 2\pi (14.7 \times 10^{-3} \text{ Hz})$. This would imply $t_{\text{PS}} \approx 1$ s, which is only one order of magnitude larger than the duration of a typical BEC experimental sequence (~ 100 ms).

As mentioned before, if fluctuations in the BEC atom number were the only uncontrolled parameter, the resulting dephasing could be completely canceled. To understand this, notice the following. In an experimental shot with N different from \bar{N} , the term $\tilde{\chi}(\bar{N} - \hat{N})\hat{S}_z$ in Eq. (2.27) gives an additional deterministic rotation around the z -axis by an angle $\tilde{\chi}(\bar{N} - N)t$. From its definition, Eq. (2.28a), $\tilde{\chi}$ is a constant when the fluctuations in N are small enough. In this regime, measurements of any spin quadrature will show a linear dependence on N because of the N -dependent rotation (only for measurements of \hat{S}_z the slope of this linear dependence is zero, *i.e.* there is no dependence). For this reason, by knowing N we can extract the slope of this linear dependence by fitting the data as a function of N , and subtract it from the measurements. In this way, post-processing of the data would allow to completely cancel phase shifts due to fluctuations in the atom number. This is similar to the clock-shift correction adopted in atomic clocks [42]. Clearly, in practical situations the initial atom number N is unknown, because what is measured is the atom number at the end of an evolution with losses, and because of the noise on the atom counting. This results in a cancellation of the mentioned phase shift which is only partial. A practical example of this correction is given in the next chapter.

Particle losses

When losses are also considered the phase evolution complicates significantly. Removing one particle from the condensate results in a change of the interaction energy, which is translated into a jump of the phase evolution. As losses are stochastic, these phase jumps occur randomly over time, giving origin to phase noise. This problem has been considered in [49], where expressions for the interference contrast in several scenarios are given. In the case of two-component BECs at zero-temperature, with Poissonian fluctuations in the total number of particles and losses described (in the constant loss rate approximation, see Eqs. (2.39)) by the effective one-body loss rates γ_1 and γ_2 , we find (see Appendix B for the derivation)

$$\text{Var} [\delta\theta(t)] \simeq 2 \Re \epsilon \left[\bar{N} (1 - e^{-i\tilde{\chi}t} L) \right] , \quad (2.45)$$

where we defined the function

$$L = \frac{1/2}{\gamma_1 + i(\chi + \tilde{\chi})} \left[\gamma_1 e^{i\tilde{\chi}t} + i(\chi + \tilde{\chi}) e^{-(\gamma_1 + i\chi)t} \right] + \frac{1/2}{\gamma_2 - i(\chi - \tilde{\chi})} \left[\gamma_2 e^{i\tilde{\chi}t} - i(\chi - \tilde{\chi}) e^{-(\gamma_2 - i\chi)t} \right]. \quad (2.46)$$

It is important to remark that Eq. (2.45) is valid under the assumption that χ and $\tilde{\chi}$ do not vary significantly during the evolution, meaning that the lost fraction has to be small. Including two- and three-body losses results in much more complicated expressions, which are related to the results presented in Appendix F of Ref. [49].

It is worth mentioning that an equivalent description of the phenomenon can be reproduced in a classical Monte-Carlo simulation. First, the total number of atoms N is drawn from a Poissonian distribution, which is then partitioned into the two components according to a Binomial distribution. Then, the relative phase of the system evolves according to the Hamiltonian Eq. (2.27) until a random time τ_1 , when the first particle is lost. From this time on, the evolution occurs in a system with $N - 1$ particles until time τ_2 , when a second particle is lost. This process continues until the chosen total evolution time T_R . By averaging over many simulated trajectories of the phase evolution, we obtain an estimation for the phase noise at time T_R .

Finite temperature

As experimental realizations of BECs are inevitably at finite temperature, a fraction of non-condensed particles is always present. This thermal component interacts with the condensate, and for this reason it is also expected to influence its coherence properties. Theoretical studies, which consider for simplicity a uniform single-component condensate, make different predictions for the phase spreading over time, depending on how the system is initially prepared [56, 58]. In the presence of shot-to-shot fluctuations of either total particle number or total energy, the phase spreading is ballistic (*i.e.* $\sim t^2$). Conversely, when both particle number and energy are fixed, the phase spreading is diffusive (*i.e.* $\sim t$). For other statistical ensembles, *e.g.* fixed particle number and general energy fluctuations, contributions from both ballistic and diffusive terms are expected. Experimentally, these different statistical ensembles could be accessed by different state preparations or different post-selections of the measurements.

To summarize, in the absence of other dephasing mechanisms, the following predictions have been derived [56].

- If the initial state is characterized by fluctuations only in the total atom number, then the phase spreads ballistically as

$$\text{Var} [\delta\theta(t)] \simeq \left(\frac{t}{\hbar} \right)^2 \left(\frac{d\mu(N)}{dN} \right)^2 \text{Var} [N]. \quad (2.47)$$

Correspondingly, the temporal coherence function decays as a Gaussian over time.

2. Bose-Einstein condensates: Theory

- If the initial state is characterized by fluctuations only in energy, for example because it is prepared with fixed N and in equilibrium at temperature T , then at long times the phase spreads ballistically as

$$\text{Var} [\delta\theta(t)] \simeq \left(\frac{t}{\hbar}\right)^2 \left(\frac{d\mu_{\text{mc}}(E)}{dE}\right)_{E=\bar{E}}^2 \text{Var} [H] . \quad (2.48)$$

Here, $\mu_{\text{mc}}(E)$ is the chemical potential of the microcanonical ensemble of energy E , and it is linearized around \bar{E} . For the case of harmonic trapping potentials, the ballistic coefficient of condensate phase spreading at finite temperature has also been evaluated [59]. For long times and $k_B T \gg \mu$ this is

$$\text{Var} [\delta\theta(t)] \simeq \left(\frac{k_B T}{\hbar\omega}\right)^3 \chi^2 t^2 , \quad (2.49)$$

Correspondingly, also in this case the temporal coherence function decays as a Gaussian over time.

- If the initial state is prepared with fixed total atom number and energy, then the phase-change spreads diffusively as

$$\text{Var} [\delta\theta(t)] \simeq 2Dt . \quad (2.50)$$

At low temperatures, and for $k_B T/ng \rightarrow 0$, the diffusion coefficient takes the form

$$\mathcal{D} \approx \frac{0.3036g}{\hbar V} \left(\frac{k_B T}{ng}\right)^4 , \quad (2.51)$$

where V is the volume of the system and n the condensate density. Correspondingly the temporal coherence function decays as an exponential over time.

Interestingly, the effect of phase spreading due to finite temperature has never been measured in three-dimensional BECs. The investigation of such effects would however be of primary importance to understand the fundamental limits on the coherence of these systems.

Technical noise

In experiments, it is important to keep in mind that technical noise also contributes to decoherence and is often dominant. This originates mainly from the unavoidable shot-to-shot fluctuations in the trapping potential and in the control fields, and from the phase noise already present in the local oscillator. All these effects directly result in additional phase noise for the BEC, typically characterized by a ballistic spreading because the relevant technical noise processes are slow.

Bose-Einstein condensates: Experiments

In this chapter we give an overview of our experimental setup, with a special emphasis on the imaging system, which will play an important role in the main experiments presented in this thesis. Moreover, we summarize the procedures adopted for the preparation and characterization of BECs, presenting the tools for the manipulation of their internal and external degrees of freedom, together with measurements of their phase coherence.

3.1 Experimental apparatus

The experiments described in this thesis have been performed with the apparatus built in the group of Prof. Philipp Treutlein at the University of Basel. This setup has been developed during more than ten years, and all its components have been described in the publications and thesis written during this time [53, 60–62]. In particular, no major changes have been brought to the experimental setup with respect to what is already described in the theses by Caspar Ockeloen [53]. For this reason, we are not going to present here the details of the apparatus, but we will just give an overview, sometimes emphasizing the small improvements recently made, or planned for the future.

3.1.1 Overview of the setup

The core of the experiment is a glass cell, constituting the science chamber, whose top wall is formed by our atom chip, see Fig. 3.1b. This cell is connected via a six-way stainless-steel cross to: (1) the ion pump maintaining the ultra-high vacuum of approximately 10^{-10} mbar, (2) the Titanium-sublimation pump, (3) the ion pressure gauge and (4) the electrical feed-throughs for the Rubidium dispensers.

Around the glass cell there is a water-cooled coil cage which provides the approximately homogeneous static magnetic fields needed in the experiments, Fig. 3.1a. To the back of the atom chip a water-cooled copper block is attached, which contains a U-shaped wire used to create the large-volume quadrupolar magnetic field needed in the magneto-optical trapping (MOT) stage of the experimental sequence, Fig. 3.1a. All these water-cooled elements are connected in series to a chiller stabilizing the water temperature to 19° C.

3. Bose-Einstein condensates: Experiments

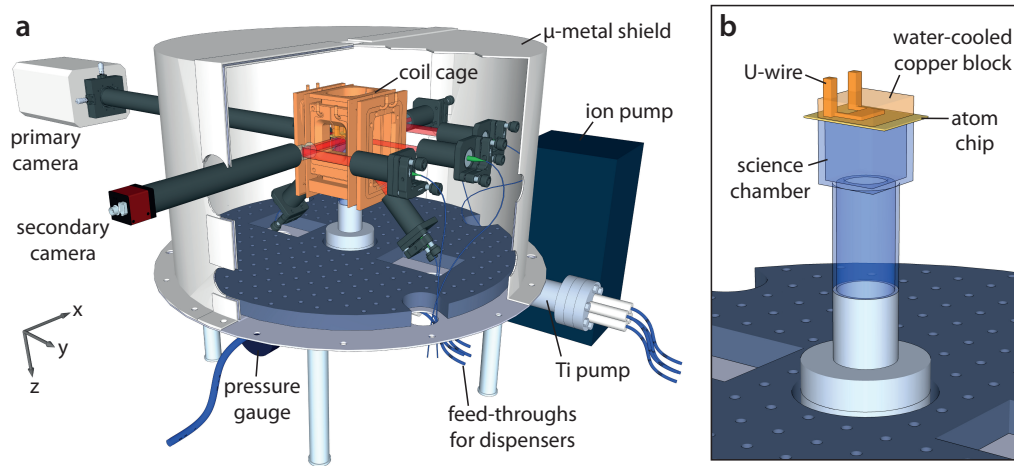


Figure 3.1: Central elements of the experimental setup. **a)** Schematic view of the vacuum system, imaging cameras and inside of the μ -metal shield showing the arrangement of the coil cage and of the fiber output couplers. The microwave horn is not shown. **b)** Detailed view of the science chamber showing the atom chip with copper cooling block and U -wire used for the magneto-optical trap. Figure taken from Ref. [53].

Outside the glass cell there are also a microwave horn and an RF antenna (for the manipulation of the internal state of the atoms), the fiber output couplers (for illuminating the atoms with all required laser beams), and the imaging optics (for imaging the atoms along two orthogonal directions). All these elements are enclosed in a μ -metal shield, to isolate the atoms from the surrounding fluctuations of the magnetic field, see Fig. 3.1a.

On, and around, the optical table hosting the vacuum chamber are situated: the laser system producing the required light, the current sources, the microwave and RF electronics, the imaging cameras, and some other components, see Fig. 3.2. These will be individually discussed in the next paragraphs.

Atom chip

The atom chip used in our experiments is the one described and fabricated in Ref. [60]. It is a multilayer chip, consisting of a base chip on top of which the science chip is glued and wire bonded, see Fig. 3.3a. The base chip is a 0.8 mm thick AlN ceramic substrate, constituting the top wall of the glass cell. It provides mechanical support for large DC wires and for the science chip, and serves as vacuum feed-through for all electric (DC, MW) connections. The science chip consists of gold wires arranged in a two-layer structure, designed to carry DC and MW currents needed to realize static and state-dependent (dressed-state) magnetic trapping potentials.

The outermost layer of the science chip (facing downward inside the glass cell) hosts two sets of wire structures, with five and six wires respectively, see Fig. 3.3b. In the five-wire structure, the three central wires constitute a MW coplanar waveguide, while the

3.1 Experimental apparatus

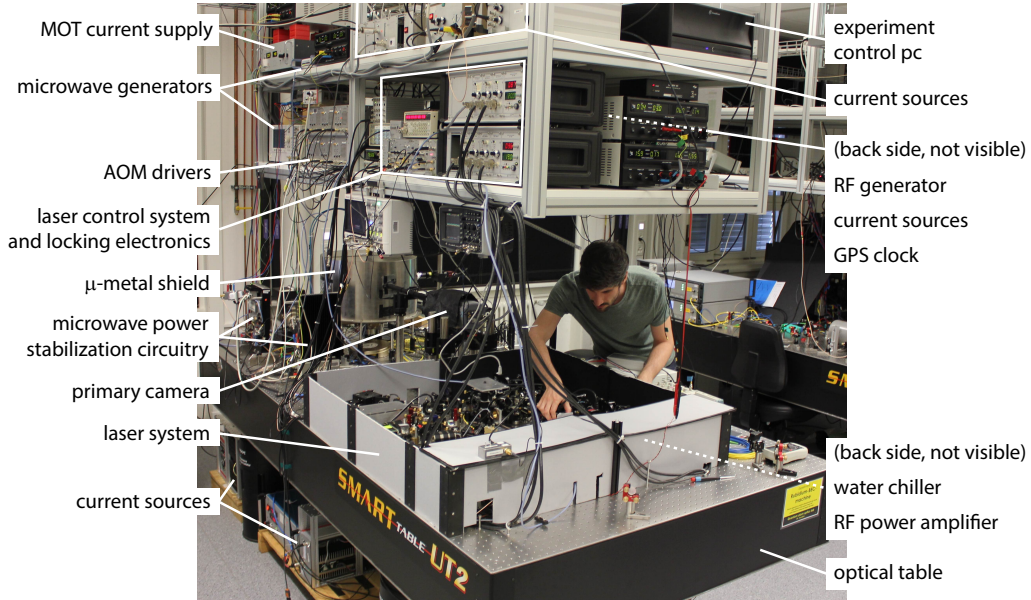


Figure 3.2: Photograph of the optical table with the surrounding devices. Relevant devices composing our experimental apparatus and discussed in the main text are labeled. Some of them are on the back side and therefore they are not visible here.

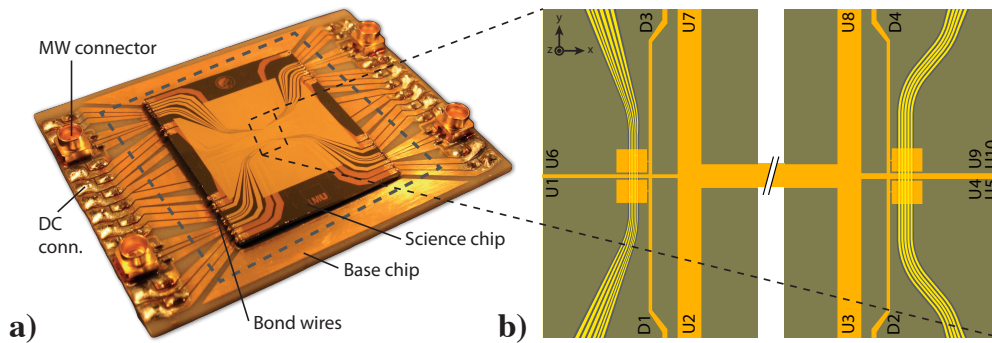


Figure 3.3: Photograph of the atom chip assembly and drawing of the wire structures. **a)** Photograph of the chip with outer dimensions 38×50 mm. The gray dashed line indicates the approximate position where the glass cell is glued. **b)** Drawing of the six- and five-wire structures, left and right respectively, at the chip center. A detailed illustration of the five-wire structure is given in Fig. 3.6. Figures adapted from Ref. [53].

3. Bose-Einstein condensates: Experiments

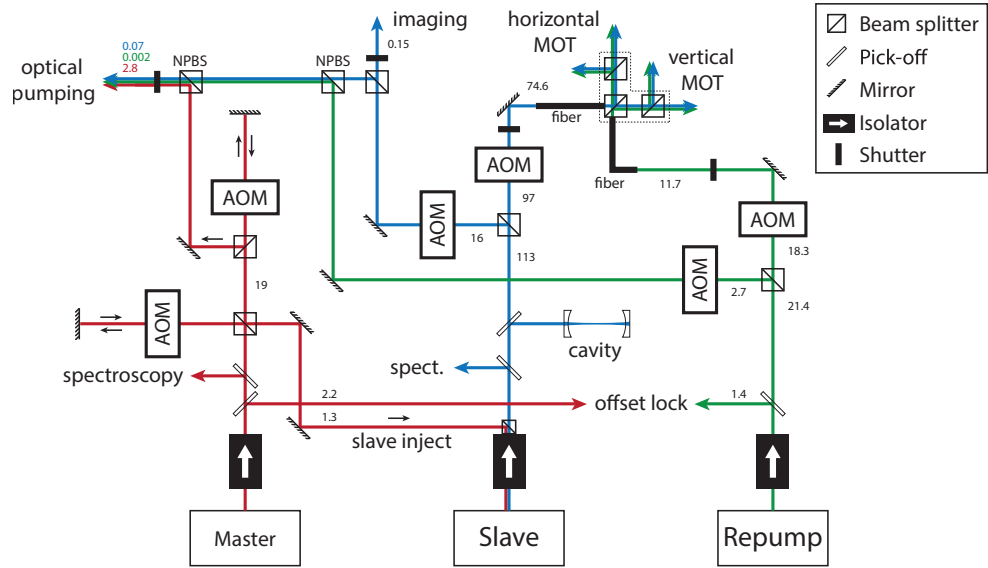


Figure 3.4: Simplified schematic of the laser system, excluding wave plates and several other components. The master laser frequency is locked via saturation spectroscopy. The slave laser is injection-locked to the frequency-shifted output from the master laser. The repump laser frequency is locked to the output from the master via an offset-lock scheme, where the beating signal between the two lasers is kept constant. A confocal cavity and a spectroscopy setup are used to diagnose the injection locking. All output beams are coupled to polarization maintaining single-mode optical fibers. NPBS = non-polarizing beam splitter. Numbers are the laser powers in milliWatt as measured at relevant points on 20 Aug 2018. Figure adapted from Ref. [53].

two surrounding wires are wires for DC currents. In the six-wire structure there are two MW waveguides, each ending with a short between the signal and the ground. A crucial feature is that DC currents are also supplied to the MW wires, by using on-chip and external bias tees. For the experiments presented here, only the three central wires of the five-wire structure are used.

A numerical model of the wire patterns allows us to simulate accurately the static and state-dependent magnetic potentials resulting from the DC and MW currents. This code was originally developed in [60], and it is an indispensable tool to tailor the trapping potentials experienced by the atoms. We use it to estimate parameters of fundamental importance such as the position of the trap, its curvature, and its depth.

On the outermost surface of the science chip, the space surrounding the wire structures is covered by a gold layer which serves as a mirror for the magneto-optical trapping stage of the experiment.

Laser system

The laser light required in our experiments for cooling, optical pumping and imaging of the atoms (see Fig. 3.5a) is prepared on an optical table with three home built lasers

3.1 Experimental apparatus

and commercial free-space optical elements, Fig. 3.2. The details of this laser system are presented extensively in [53, 60, 62], while an up to date schematic is illustrated in Fig. 3.4. We give here a general overview, mentioning the small changes on the locking scheme with respect to the previous presentations.

All the light is generated by three laser diodes, operating at a wavelength of ≈ 780 nm, close to resonance with the Rubidium-87 D_2 line, see Fig. 3.5a. The first (interference-filter stabilized) laser serves as a master, and it is locked via saturated absorption spectroscopy to the cross-over peak between the $F = 2 \rightarrow F' = (2, 3)$ transition. The frequency of the output light is adjusted by an acousto-optic modulator (AOM) in double-pass configuration, and injected into the slave laser diode which acts as an amplifier. Apart from controlling the frequency of the AOM driving RF, we also control its power, to ensure that the intensity of the injected light stays constant. This is important when doing large frequency jumps, as we noticed that the locking of the slave is sensitive to this parameter. The light coming from the slave laser is mostly used as cooling light during the MOT stage, and in a small part for absorption imaging and optical pumping.

The third (interference-filter stabilized) laser is locked to the master via an offset-lock scheme, in which the beating signal between the two lights is used to keep their frequency difference fixed. The details of this locking scheme are presented in [63]. The light coming from this laser is used as repump light during the MOT stage, and as pumping light.

The different laser beams, after passing through AOMs, beam shaping optics, wave plates, mechanical shutters, and other elements, are coupled to single-mode polarization-maintaining fibers, which bring them inside the μ -metal shield to the vacuum chamber. For typical powers of the individual laser beams see Fig. 3.4.

One disadvantage of free-space optics is the sensitivity to mechanical disturbances. Vibrations or temperature fluctuations may cause misalignments of the optical elements, resulting in fluctuations of the light intensity at the fiber outputs, and therefore to unstable BEC preparation. Also for this reason, together with Menlo Systems we developed a new Rubidium-Cooling-Laser (RUCOLA) system, based on fiber lasers and optics. This device is composed of three compact rack modules, containing all the optics and the electronics needed to generate the required lights. A key difference is that the laser units, and their frequency stabilization and control, operates at the convenient telecom wavelength of 1560 nm. Only before the outputs the light is frequency-doubled to 780 nm, with a nonlinear crystal for second harmonic generation. An additional module contains electro-mechanical and optical switches used to turn on and off the lights. These RUCOLA modules are currently under test, and they have not been used for the experiments presented here.

Microwave and Radio-Frequency sources

In our experiments we make use of microwave (MW) and radio frequency (RF) currents to create state-dependent potentials and to manipulate the internal states of the atoms.

3. Bose-Einstein condensates: Experiments

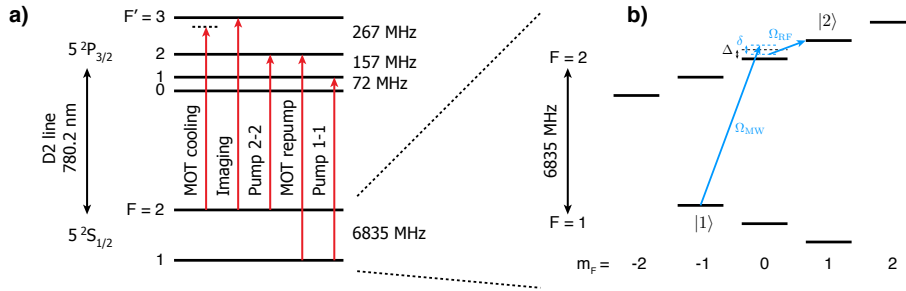


Figure 3.5: Schematics of the Rubidium-87 level structure we address. **a)** Level scheme of the D2 line and laser frequencies used in our experiment. **b)** Hyperfine level structure of the ground state and two-photon transition. The figure shows the MW and RF couplings with Rabi frequencies Ω_{MW} and Ω_{RF} , respectively, and the definitions of the intermediate-state detuning Δ and the two-photon detuning δ .

For the state-dependent potentials we send a MW current of frequency ≈ 6.8 GHz through the on-chip coplanar waveguide. This is provided by a signal generator, and power stabilized by a home-built feedback circuit [53].

To manipulate the internal state of the atoms we use two-photon Rabi pulses, composed of a MW and a RF tone, see Fig. 3.5b. The MW tone of ≈ 6.8 GHz is provided by a second MW signal generator, and it is power stabilized before going to the antenna (horn) pointing towards the atoms. The RF tone of ≈ 1.7 MHz is provided by a programmable signal generator, and it is power amplified before going to the antenna (square coil) pointing towards the atoms. Even if these two fields are emitted far away (≈ 5 cm) from the atoms to minimize the spatial inhomogeneity of their field strength, we experience gradients that are likely caused by a coupling to the chip wire structures. Gradients in the Rabi fields are unwanted as they result in a coupling between internal state (spin) and position, which directly translates to a decrease in the fidelity of the Rabi rotations. To overcome this problem we tweak the position of the MW horn until ≈ 10 Rabi oscillations can be seen with a contrast of at least 98%, indicating that the atoms are situated in a region where fields are nearly uniform.

Good phase coherence is also crucial in these MW and RF fields, in order to coherently manipulate the atoms. For this reason, we use as a phase reference (local oscillator) for all our signal generators a high-quality GPS-disciplined quartz clock.

Current sources

Electric currents are another crucial ingredient for our experiments. During the MOT-stage there is the need for large currents, of up to ≈ 50 A, to create a large-volume quadrupole field. During the experimental sequence there is the need for currents of few Amperes, to supply the coils generating the bias fields, and of small currents of few milliamperes, to supply the chip wires generating the static trapping potentials. These cur-

rents are required to have an extremely low noise level (relative stability of $\approx 1 \times 10^{-5}$), since they are being used for the experimental trap where uncontrolled fluctuations affects the coherence properties of the atomic ensemble. We use both commercial and home-built sources, depending on the requirements. For a detailed description of these devices see [53, 61, 62].

Imaging optics

At the end of each run of our experiment the number of atoms is counted via absorption imaging. The basic idea is that laser light resonant to a cycling transition passes through the atomic cloud, casting a shadow which is recorded by a camera.

The probe light coming from a dedicated optical fiber is collimated by a two-lens telescope, which, at the same time, images an aperture onto the position of the atoms. This aperture ensures that the light does not reach the chip surface, reducing diffraction and therefore inhomogeneities in the illumination. The imaging objective is a $4f$ -telescope with $10\times$ magnification. The images of the atomic density distribution are captured by a CCD camera (Andor Ikon-M) with a 1024×1024 pixels area. Further details of the imaging optics are given in Ref. [53], while its characterization is presented later in this Chapter.

Experiment control

The entire experiment is controlled by a computer equipped with I/O cards, providing digital and analog outputs. The analog outputs modulate the DC and MW currents, as well as the light powers (by controlling the power of the RF signal driving the AOMs), while the digital outputs are used for different switching and triggering.

The experimental sequence is written using the customized editor called *goodTime* [61]. It interprets a simple programming language, and compiles it into a table of times and voltages which is sent to the I/O cards. Moreover, at the beginning of each sequence it communicates with other devices (*e.g.* MW and RF generators, data acquisition computer), connected via GPIB, USB or Ethernet, to initialize their operation.

The data acquisition is handled by a second computer to which the camera is connected. The initialization, control and readout of the camera, and the processing of the images, is done by the customized *MatCam* program [53] that is triggered from the experiment control computer. Even if *MatCam* allows to extract the atomic densities from the images, for the definitive data analysis we use a more accurate program implementing a fringe-removal algorithm [53].

3.1.2 Typical experimental sequence

The detailed steps we follow in the typical experimental sequences are presented in [53, 62]. We start loading the main MOT for approximately ten seconds, after which the atoms are transferred to a compressed MOT. The latter is closer to the chip surface, as its quadrupolar field is generated by one of the base chip wires. Subsequently, magnetic

3. Bose-Einstein condensates: Experiments

field gradients are switched off, and the cooling lasers are detuned further for the optical molasses stage. At this point in the sequence we observe $\approx 1.0 \times 10^6$ atoms at a temperature of $\approx 10 \mu\text{K}$.

The next step consist in transferring the atoms to the first magnetic trap. To this end, we optically pump them in the magnetic trappable state $|F = 1, m_F = -1\rangle$, and then ramp up the currents needed to generate the (Ioffe) trap. What follows is a transfer of the atoms through a series of other Ioffe traps, where each next trap is further compressed and closer to the chip surface. The compression raises the temperature, but this heating is partially compensated by self-evaporative cooling, where atoms that are too hot escape from the trap. To further decrease the temperature, we perform two RF evaporative cooling ramps. The second ramp occurs in a dimple trap, which uses the same set of wires as the experiment trap, and allows to achieve Bose-Einstein condensation of ≈ 2000 atoms. Details of these traps are given in Ref. [53].

Finally, we vary the currents in the wires to transfer the BEC to the trap used in the experiment, of frequencies $f_x = 110 \text{ Hz}$ and $f_y = f_z = 729 \text{ Hz}$, and apply a RF evaporation pulse to set precisely the final atom number. What follows is the main part of the sequence, usually consisting entirely in RF and MW pulses, which is programmed to prepare and measure the state of the BEC according to the specific experiment to be performed (see chapter 5).

At the end of this manipulation of the BEC, we ramp down the trapping field in such a way that the atoms are accelerated away from the chip, in the downward direction. This allows the atomic cloud to expand, without colliding with the chip surface. After a time-of-flight of few milliseconds, the absorption images of the atomic density distributions are taken (see Fig. 5.9c), concluding the run. Further details for specific experimental sequences are given in chapter 5.

During imaging the atoms scatter photons, which destroys the BEC. For this reason, the whole experimental sequence is repeated many times, until enough data have been accumulated. To investigate the dynamics of an observable, stroboscopic measurements are taken, while to access variances statistics is collected.

3.1.3 Details of the experiment traps

The main trap used for the experiments presented here is a static dimple trap [60]. The transverse confinement comes from a wire in the lower gold layer carrying $I_L = 180 \text{ mA}$ in the x -direction plus a static field of $B_y = 7.2 \text{ G}$ in the y -direction. For the longitudinal confinement, we use the three central wires of the five-wire structure, carrying $I_D = 2 \text{ mA}$ each. In two of the wires the current flows in the $-y$ -direction, while in the third in the $+y$ -direction, as shown in Fig.3.6A. The asymmetry in the currents is chosen to position the trap on one side of the coplanar waveguide, in this way the atoms experience a gradient when MW are sent through the central wire. The static field in the x -direction is fine tuned to ensures that the trap bottom is near the “magic” field of 3.23 G . To this aim we perform one-photon spectroscopy of the $|1, -1\rangle \leftrightarrow |2, 0\rangle$ transition by fixing the MW frequency to the theoretical value expected from the level splitting at the magic

3.1 Experimental apparatus

field and counting the atom number N_1 while scanning B_x . On resonance we observe a drop in N_1 from which we conclude $B_x = 3.36$ G, where the offset comes mostly from the fact that the magnetic field produced by the wires has to be compensated.

The simulated trapping frequencies are $(f_x, f_y, f_z) = (112, 728, 729)$ Hz, and the trap minimum is located at $(x_0, y_0, z_0) = (-13.0, -1.7, 41.2)$ μm with respect to the origin chosen to be at the central wire crossing and on the chip surface.

Apart from this static state-independent trap, our experiments make use of a state-dependent trapping potential. This originates from sending a MW current of $I_{\text{mw}} = 21$ mA amplitude through the coplanar waveguide. The frequency of this current is blue-detuned by $\Delta = 2\pi 12$ MHz with respect to the $|1, 0\rangle \leftrightarrow |2, 0\rangle$ transition. The atoms are situated in the near-field of the waveguide, and therefore they experience a MW field gradient, Fig.3.6B. For this reason, the differential level shift occurring between state $|1\rangle$ and $|2\rangle$ is spatially dependent, giving rise to a state-dependent potential. For our parameters, the combination of the static fields with the MW field result in a separation of the trap minima for the two states of ≈ 150 nm, which is used to prepare a spin squeezed state (see sections 5.1.1 and 5.1.2).

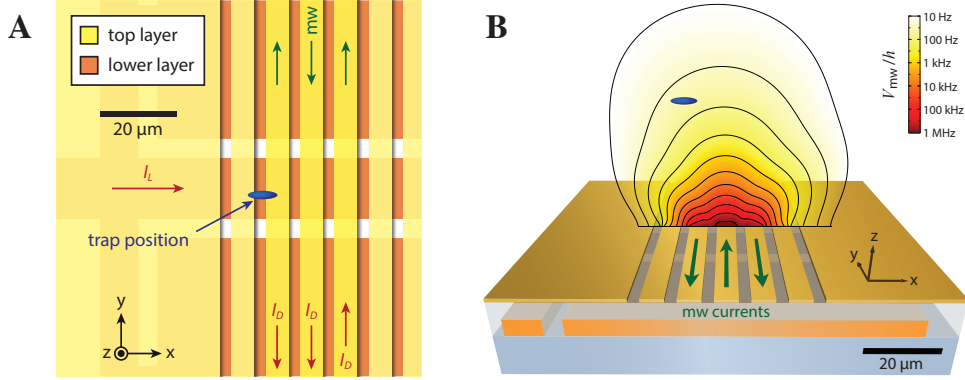


Figure 3.6: Schematics of the chip wires around the trap position. The illustrations are a magnification of the right region in Fig. 3.3b. **(A)** Top view of the central region of the five-wire structure. The arrows indicate the flows of the DC and MW currents used to create the static and state-dependent trapping potentials. **(B)** Angled view of the chip region shown in panel A. The microwave near-field potential V_{mw} for $I_{\text{mw}} \approx 5$ mA and $\Delta_{\text{mw}} = 2\pi 12$ MHz (blue detuning) is drawn for illustration. In both panels the position and shape (Thomas-Fermi radii) of the BEC is shown to scale in blue. The displacement in the trap bottom for the two internal states is too small to be visible at this scale. Figures adapted from Ref. [53].

3.1.4 Characterization of the imaging system

The idea behind absorption imaging is that the atomic density distribution can be reconstructed by observing the attenuation of a light beam passing through it. For a cloud of two-level atoms, the two-dimensional distribution n_{2D} is reconstructed from the beam

3. Bose-Einstein condensates: Experiments

intensities before and after the atoms, I_i and I_f , from the Beer-Lambert law [64]

$$n_{2D} = -\frac{1}{\sigma_0} \left(\ln \left(\frac{I_f}{I_i} \right) - \frac{I_i}{I_{\text{sat}}} \left(1 - \frac{I_f}{I_i} \right) \right). \quad (3.1)$$

In this expression, $\sigma_0 = 3\lambda^2/2\pi$ is the resonant absorption cross section of the imaging transition with wavelength $\lambda = 2\pi c/\omega_0$, and $I_{\text{sat}} = \hbar\Gamma\omega_0^3/12\pi c^2$ is the saturation intensity of the transition.

In practice, the light beam is imaged with a camera, and its intensity needs to be derived from the electrons counted on the CCD pixels. A direct conversion is difficult, as it requires to know the quantum efficiency of the imaging system. For this reason, we replace I_{sat} by an effective saturation intensity I'_{sat} , which we calibrate experimentally. We scan I_i and set I'_{sat} such that the total atom number is independent of the imaging probe intensity [64].

Similarly, the absorption cross-section needs to be corrected to take into account the presence of additional energy levels, their residual populations originating from imperfect optical pumping, and errors in the probe polarization or frequency. For this reason, we replace σ_0 by an effective saturation intensity σ'_0 , which we also calibrate experimentally as explained later.

Image acquisition

At the end of each experimental sequence, we take absorption images of the BEC. Since we want to reconstruct the atomic density distributions for both state $|F = 1, m_F = -1\rangle = |1\rangle$ and $|F = 2, m_F = 1\rangle = |2\rangle$, we adopt the following strategy. First, we image the atoms in state $|2\rangle$ by illuminating them with a probe laser resonant to the $F = 2$ to $F' = 3$ transition. During this process, they are blown away due to photon recoil, leaving in the field of view only atoms in state $|1\rangle$. The latter are optically pumped from $F = 1$ to $F = 2$, and then imaged in the same way as before. Each of these two images give information about the light intensity after the atoms, I_f , entering in Eq. (3.1). However, to evaluate n_{2D} it is necessary to know the light intensity before the atoms, I_i . For this reason, immediately after the first two absorption images, a third image with no atoms is recorded, called reference image. Because photon shot noise results in different images for the same probe light intensity, which in real situations even fluctuates over time due to technical noise, care must be taken to infer I_i from the reference image. For this reason we developed an algorithm to construct an optimal reference image from linear combinations of reference images, which is described in the next paragraph.

Due to the finite speed of the camera, the two absorption images are taken with a delay of 1.33 ms. This means that the cloud of atoms in state $|1\rangle$ expands and falls longer than the cloud of atoms in state $|2\rangle$, leading to an increased rms size of $\sim 2\%$ (0.06 pixel) horizontally and $\sim 25\%$ (0.8 pixel) vertically (see Fig. 5.9c), and to a center position which is $\sim 150 \mu\text{m}$ lower. As a consequence of its larger size, the image of the atoms in state $|1\rangle$ is typically associated with a larger noise with respect to the one for state $|2\rangle$ (see the following paragraph).

Note that already after the first image the spin state of the atoms is projected. However, after the first image only atoms in $|2\rangle$ are spatially localized, while atoms in $|1\rangle$ are still completely delocalized until the second image is taken.

Post-processing of the images

Imperfections in the optical elements, and their finite sizes, inevitably cause intensity fringes in the light field shined onto the atoms. Crucially, the reference image taken immediately after the image of the atomic distribution is used to account for this effect. However, mechanical vibrations result in fringe patterns that vary in time, complicating their subtraction. Moreover, the reference image is affected by photon shot noise, which is the primary source of imaging noise in our setup.

To reduce photon shot noise, we apply the fringe removal algorithm presented in [65]. The idea consists in subdividing the absorption and reference images in blocks of $i_{\max} = 100$ consecutive shots, and then to construct for each absorption image an optimal reference image R_{opt} as a linear combination of the reference images R_i available in the block, namely

$$R_{\text{opt}} = \sum_{i=1}^{i_{\max}} c_i R_i . \quad (3.2)$$

The coefficients $c_i \in \mathbb{R}$ of the linear combination are optimized to minimize the mean squared residuals between the absorption and the optimal reference image, in a region where no atoms are present. Moreover, the linear combination of reference images also suppresses the photon shot noise of the optimal reference image, as the uncorrelated fluctuations add in quadrature as

$$\Delta R_{\text{opt}} = \sqrt{\sum_{i=1}^{i_{\max}} c_i^2 (\Delta R_i)^2} . \quad (3.3)$$

The algorithm corrects also for intensity fluctuations between the absorption image and the reference image, which would cause systematic offsets in the atom number.

Atom number counting and imaging noise

From the fringe removal algorithm, we obtain a reconstruction of the two-dimensional density distributions of atoms in state $|1\rangle$ and $|2\rangle$. The integration of these densities gives the total atom number in each state, N_1 and N_2 . Alternatively, we can integrate the densities only over parts of space, resulting in a measurement of the number of atoms contained in specific regions.

To estimate the error on the atom numbers determined in this way, we make again use of the absorption images. From the imaging light intensity we extrapolate per each pixel the expected photon shot noise, which we convert into fluctuations of the number of atoms. In the experiments presented here, we observe atom number noise levels of $\sigma_{N_2, \text{det}} \lesssim \sigma_{N_1, \text{det}} \approx 3 - 5$ atoms for rectangular regions of interest containing the entire

3. Bose-Einstein condensates: Experiments

cloud (see chapter 5). The noise on the atom number we derive with this method assumes pure photon shot noise. For this reason, this noise is always less than the one extracted by counting atom number fluctuations in images with no atoms, as the latter includes technical noise.

Calibration of the imaging system

The imaging system needs to be calibrated in order to extract the correct atom number. As we are imaging atoms in two different internal states, $i = 1, 2$, the corresponding density distributions are calculated from Eq. (3.1) with the experimentally determined parameters $\sigma'_{0,i}$ and $I'_{\text{sat},i}$. First, each $I'_{\text{sat},i}$ is fixed by ensuring that the detected total atom number in state i is independent on the probe light intensity [64]. We find $I'_{\text{sat},1} = I_{\text{sat}}/0.63$ and $I'_{\text{sat},2} = I_{\text{sat}}/0.59$. Then, to calibrate the absolute atom number we take two set of measurements determining $\sigma'_{0,i}$. One consists in characterizing the differential detectivity of the two states, for which we perform Rabi oscillations with high contrast and ensure that the detected total atom number is independent of the relative population between the two states. This fixes the ratio $\sigma'_{0,2}/\sigma'_{0,1} = 1.11$, which deviates from unity mostly because of the different densities of the two components. The other consists in measuring the scaling of the projection noise with the total atom number (usually for BECs with N between 200 and 1400). For a coherent state with equal population in $|1\rangle$ and $|2\rangle$, we calculate the variance of the relative atom number. We find that the projection noise dominates our measurements, as the scaling is purely linear. The deviation from unity of the fitted slope is then corrected for in our analysis by fixing $\sigma'_{0,1}$ accordingly.

Optical resolution of the imaging system

For the experiments we are going to perform, high spatial resolution images of the atomic density distributions are required. To obtain an upper bound for the optical resolution of our imaging system, we image a small atomic cloud. To this end, we prepare atoms in a trap which is approximately $300 \mu\text{m}$ below the chip surface, such that the atoms are trapped at a position close to where the falling atomic cloud is in the actual experiments. We image the atomic cloud $10 \mu\text{s}$ after switching off this trap, meaning that the atom density corresponds to a good approximation to the in-situ density. Note that even if the magnetic fields do not vanish immediately, their effect leads to an off-resonant image which does not affect the resolution. By using short laser pulses of $10 \mu\text{s}$ for imaging (such that blurring is negligible, see next paragraph), and averaging several absorption images of this small cloud, we obtain an upper estimate of the size of the point spread function of our optical system. From the averaged absorption images, Fig. 3.7, a Gaussian fit gives an upper bound of the size of the optical point spread function of our imaging system. We find rms sizes of $\sigma_{\text{hor}} = 1.1 \text{ pixel} = 1.43 \mu\text{m}$ and $\sigma_{\text{vert}} = 1.2 \text{ pixel} = 1.56 \mu\text{m}$.

3.1 Experimental apparatus

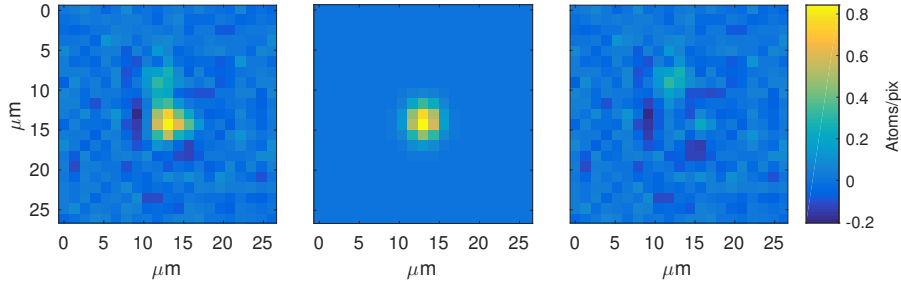


Figure 3.7: Imaging of small BECs. The left panel shows an averaged absorption image of a small atomic cloud, taken a very short time after release from the trap. The gaussian fit (center panel) gives an upper bound of the size of the optical point spread function of our imaging system. In the right panel the fit residuals are shown. The colorbar applies to all three panels.

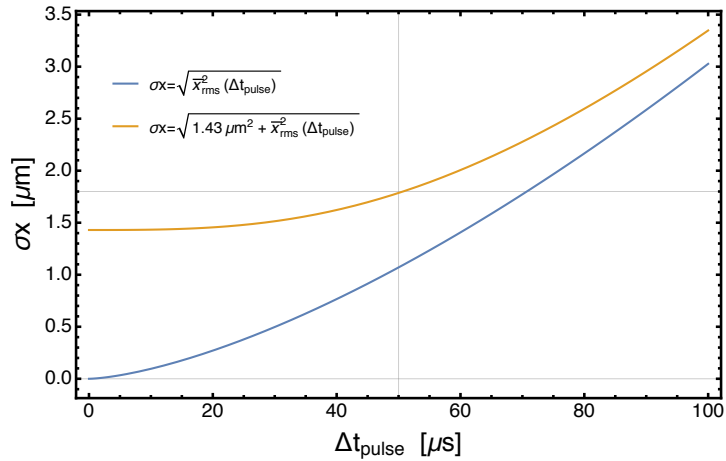


Figure 3.8: Blurring due to photon scattering. The blue line shows the blurring expected from Eq. (3.4) with $s = 1$. The orange line includes the horizontal resolution of our imaging system, $\sigma_{\text{hor}} = 1.43 \mu\text{m}$.

3. Bose-Einstein condensates: Experiments

Image blurring due to random photon scattering during absorption imaging

During the resonant imaging pulse the atoms scatter photons, which leads to a random velocity and position during the pulse. This blurring leads to a reduction of the effective optical resolution. In our experiment the pulse is very well described by a pulse of duration Δt_{pulse} with constant intensity. We derive here a conservative estimate of the blurring. Since the atoms are mostly scattering photons on a cycling transition, we assume here a two-level model for the atomic transition. We further assume that the light is resonant during the whole imaging pulse. These assumptions overestimate the actual spread in position, since the real scattering cross section is smaller and the scattering rate is also reduced due to the longitudinal acceleration Doppler-shifting the atoms out of resonance during the pulse. These two effects are relatively small for our parameters ($\Delta t_{\text{pulse}} < 100 \mu\text{s}$), such that our estimate, although conservative, should still give reasonably good agreement with the experiment.

We are interested in the transverse spread of position due to the random scattering. As derived by Joffe *et al.* [66], the mean squared transverse position at time t is given by

$$x_{\text{rms}}^2(t) = \frac{1}{9} N_p(t) v_{\text{rec}}^2 t^2 = \frac{\Gamma}{18} \frac{s}{1+s} v_{\text{rec}}^2 t^3,$$

where $N_p(t)$ is the number of photons scattered between time 0 and t , $v_{\text{rec}} = 5.8845 \text{ mm/s}$ is the recoil velocity, and $\Gamma = 2\pi \cdot 6.065 \text{ MHz}$ and $s = \frac{I}{I_{\text{sat}}}$ are the decay rate and saturation parameter of the transition, respectively. This size is however only giving the rms transverse size of the atomic cloud at a given time. To estimate the rms size as observed on the image, we have to time-average the spatial distribution over the pulse length. To estimate this quantity, we consider a large number M of atomic trajectories $x_j(t)$, $j = 1 \dots M$. Then, the time averaged mean squared transverse position is

$$\bar{x}_{\text{rms}}^2(\Delta t_{\text{pulse}}) = \frac{1}{M} \sum_{j=1}^M \left[\frac{1}{\Delta t_{\text{pulse}}} \int_0^{\Delta t_{\text{pulse}}} x_j(t) dt \right]^2 \leq \frac{1}{M} \sum_{j=1}^M \frac{1}{\Delta t_{\text{pulse}}} \int_0^{\Delta t_{\text{pulse}}} x_j^2(t) dt.$$

In the last expression we can exchange the order of integral and sum and use the rms transverse size at time t to estimate the expectation value of the set of trajectories. In this way we obtain

$$\bar{x}_{\text{rms}}^2(\Delta t_{\text{pulse}}) \leq \frac{1}{\Delta t_{\text{pulse}}} \int_0^{\Delta t_{\text{pulse}}} x_{\text{rms}}^2(t) dt = \frac{\Gamma}{72} \frac{s}{1+s} v_{\text{rec}}^2 (\Delta t_{\text{pulse}})^3. \quad (3.4)$$

If we take the estimate of the size obtained from in-situ absorption images (see above) into account and the blurring due to resonant absorption during a $50 \mu\text{s}$ long imaging pulses (as for the EPR experiment presented in chapter 5), we obtain a total rms size of the blurred cloud on the camera of $\sigma_{\text{blur}} = 1.4 \text{ pixel} = 1.8 \mu\text{m}$, see Fig. 3.8. We want to emphasize here that our estimation is conservative in the sense that it gives an upper bound for the blurring, overestimating the actual effect.

Resolution asymmetry due to atomic motion during probe pulse

As the absorption images are taken during time of flight, the previously described imaging resolution and blurring, which describes the effective resolution in case of stationary atoms, needs to be averaged over the mean atomic trajectory during the imaging pulse. We do not detect any motion in the horizontal direction but observe that atoms fall with a velocity in the vertical direction of $0.114(1) \mu\text{m}/\mu\text{s}$ for the $F = 2$ state and $0.129(1) \mu\text{m}/\mu\text{s}$ for the $F = 1$ state, the difference being compatible with gravitational acceleration between the two images. Integrated over the atom's trajectory during the imaging pulse, the total effective resolution keeps its Gaussian shape in the horizontal direction with a rms size of $\sigma_{\text{hor}} = 1.4 \text{ pixel} = 1.8 \mu\text{m}$. In the vertical direction, it can still be well approximated by a Gaussian function as long as the falling distance during the imaging pulse is less than the full width at half maximum of the static blurred image. This results in state dependent effective rms sizes of the imaged cloud of $\sigma_{\text{vert},F=2} = 2.0 \text{ pixel} = 2.5 \mu\text{m}$ and $\sigma_{\text{vert},F=1} = 2.1 \text{ pixel} = 2.7 \mu\text{m}$ along the vertical direction.

3.2 BEC manipulation

Necessary for our experiments is the ability to manipulate the BEC internal (spin) an external (motional) degrees of freedom. As explained in the previous section, these are controlled by two-photon Rabi fields and by microwave-dressed potentials, respectively. In this section we report experimental results illustrating the coherent manipulation of different degrees of freedom of the BEC.

3.2.1 Spin state manipulation

To manipulate the internal state of the atoms we apply a two-photon drive [radio-frequency (RF) and microwave (MW)] to induce resonant Rabi rotations, with a two-photon Rabi frequency of $\approx 400 \text{ Hz}$. The mw field is blue-detuned by $\approx 500 \text{ kHz}$ from the intermediate state $|F = 2, m_F = 0\rangle$, see Fig. 3.5. Such Rabi pulses drive the transition from state $|1\rangle$ to $|2\rangle$, achieving coherent population transfers with very high fidelities ($>99\%$). In particular, we are not able to detect any atoms transferred to other states of the ground-state manifold. This allows us to focus entirely on the effective two-level system of states $|1\rangle$ and $|2\rangle$, described by a pseudo-spin $1/2$ for each atom. For the entire BEC, this allows a description of the internal state in terms of a collective spin \hat{S} , as defined in Eqs. (2.24).

Rabi oscillations

To calibrate the frequency of the Rabi field, we start with all atoms in state $|1\rangle$ and then record Rabi oscillations for different detunings $\Delta_{\text{RF},i}$ of the RF field with respect to its current uncalibrated frequency. Note that the time dependence of N_{rel} follows the

3. Bose-Einstein condensates: Experiments

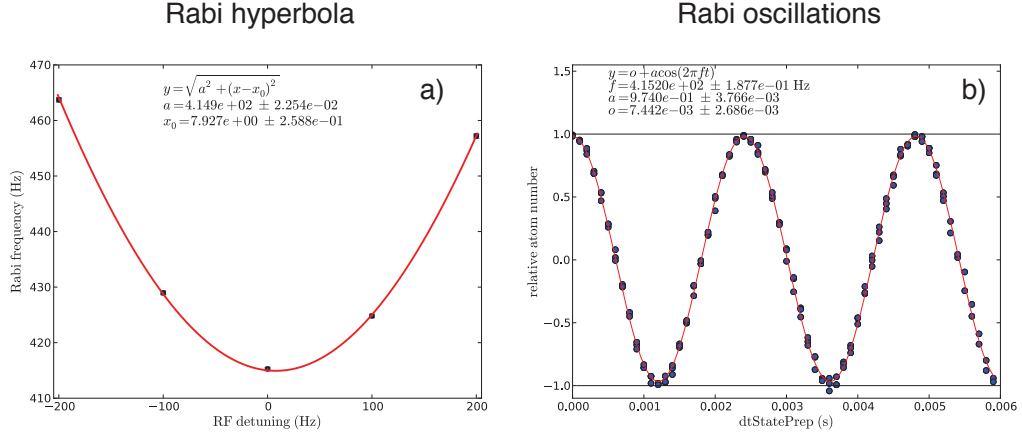


Figure 3.9: Rabi hyperbola and Rabi oscillations. **a:** Rabi frequency as a function of the RF detuning. Fitting the experimentally measured Rabi frequencies (black dots) with an hyperbola (red line) gives the frequency to drive resonant Rabi rotations. **b:** To measure accurately the resonant Rabi frequency we drive Rabi oscillations. Fitting the experimentally measured oscillations (black dots) with a sine (red line) gives the resonant Rabi frequency.

relation

$$N_{\text{rel}} = 1 - \frac{\Omega_R^2}{\Omega_R^2 + \delta^2} \left(1 - \cos \left(\sqrt{\Omega_R^2 + \delta^2} t \right) \right), \quad (3.5)$$

where Ω_R is the resonant Rabi frequency, and δ the (two-photon) detuning between the two-level transition and the driving Rabi fields. The latter being related to the RF detuning by an unknown constant offset δ' as $\delta_i = \Delta_{\text{RF},i} + \delta'$.

Fitting the observed detuned Rabi oscillations gives the frequencies $\Omega_i = \sqrt{\Omega_R^2 + \delta_i^2} = \sqrt{\Omega_R^2 + (\Delta_{\text{RF},i} + \delta')^2}$. Therefore, by further fitting the dependence of Ω_i as a function of $\Delta_{\text{RF},i}$ we are able to extract the unknowns Ω_R and δ' , see Fig. 3.9a. Note that the same idea can be applied to the dependence of the detuned Rabi oscillations amplitude, $\frac{\Omega_R^2}{\Omega_R^2 + \delta^2}$, as a function of $\Delta_{\text{RF},i}$. The obtained δ' is used to calibrate the frequency of the Rabi field, such that it is on resonance with the two-level transition.

To measure accurately the Rabi frequency, and to ensure that resonant oscillations have a high contrast, we record several fringes, Fig. 3.9b. From a sinusoidal fit we directly obtain Ω_R , which is then needed to set the areas of the Rabi pulses used in the experiment.

3.3 Ramsey interferometry

To study the coherence properties of our BECs, we perform Ramsey sequences in the phase domain, for different interrogation times. First, a $\pi/2$ Rabi pulse prepares the BEC in an equal superposition of $|1\rangle$ and $|2\rangle$. Then, after a Ramsey interrogation time T_R , a

3.3 Ramsey interferometry

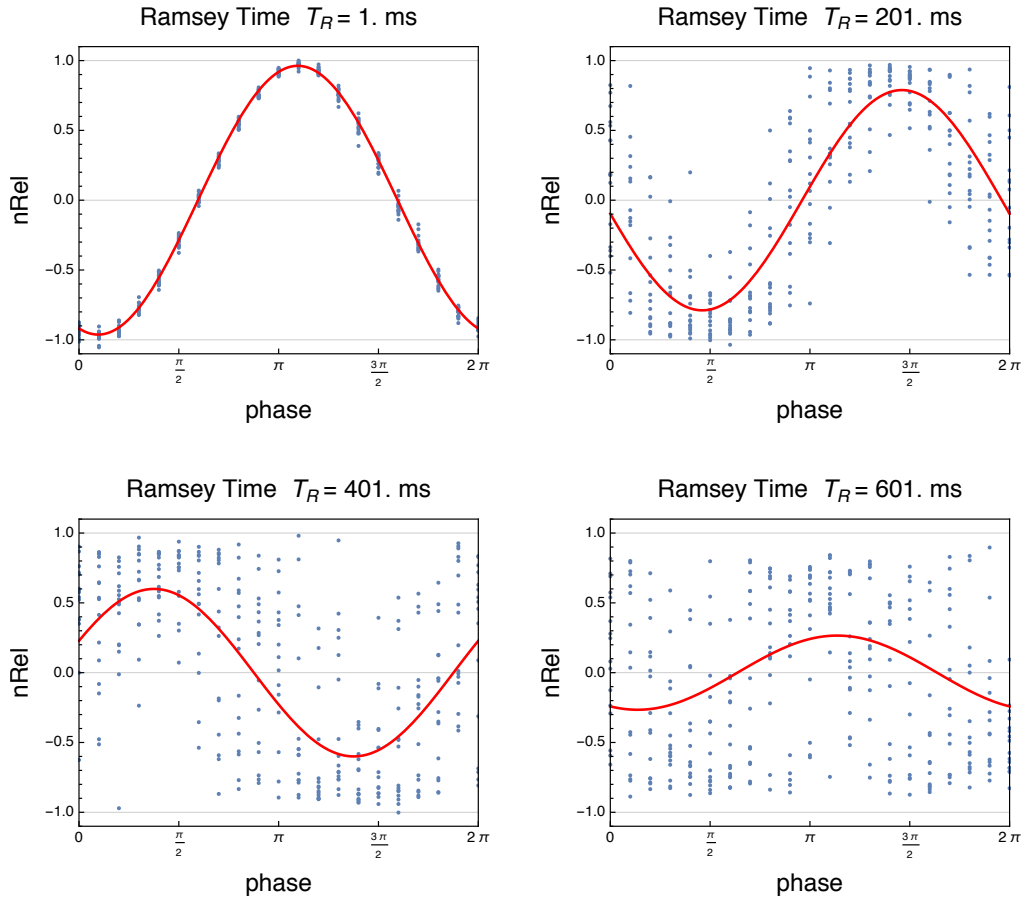


Figure 3.10: BEC coherence measurement. Ramsey measurement in the phase domain for four different Ramsey interrogation times T_R . Shown are experimental data (blue) and sinusoidal fit (red). The fit results in the contrasts (0.962, 0.789, 0.600, 0.266), respectively.

second $\pi/2$ Rabi pulse with phase ϕ_R is sent and the atom number populations are read out. For a fixed T_R we accumulate a number of shots for different Ramsey phases ϕ_R , to record interference fringes.

Figure 3.10 shows Ramsey phase measurements for increasing interrogation times. Note that the shot-to-shot visibility of the fringes stays always relatively high ($\geq 89\%$), while the fitted contrast gets significantly reduced down to even 27%, because of phase noise (see Eq. (2.40)). By fitting with the function $e^{-(\lambda t)^2}$ the contrast as a function of T_R we find $\lambda = 1.9 \text{ s}^{-1}$. This implies a $e^{-1/2}$ reduction in the contrast in ≈ 372 ms, significantly longer than the typical sequences used for the experiments presented here lasting ≈ 60 ms. A detailed study of the limitation posed by this noise is currently ongoing, and the results will be presented in a future work.

3. Bose-Einstein condensates: Experiments

3.3.1 Motional state manipulation

To manipulate the motional state of the atoms we control the trapping potential. Of particular interest is the case where the motional state of each BEC component is independently manipulated, which in our experiment is achieved by state-dependent microwave-dresses potentials.

Because of mean-field interactions, the BEC motional state dynamics is non-trivial. As an example, even a separation between the two trapping potentials much smaller than the extent of the BEC can result in an almost complete separation of the BEC wavefunctions. This “dynamic” splitting and recombination technique is used in our experiments to induce a demixing-remixing of the two components. We split the two potential minima by $\Delta x_0 \approx 150$ nm (much less than the extension of the BEC size of $R_{\text{TF},x} \approx 4$ μm), and observe a modulation in the overlap between the two components [19]. Note that the resulting oscillation frequency is slower than the trap frequency because of interactions.

To show that the demixing-remixing dynamics is coherent, we perform the following Ramsey sequence in the time domain. First, a $\pi/2$ Rabi pulse prepares the BEC in an equal superposition of $|1\rangle$ and $|2\rangle$. Then, we turn on the coplanar MW with a smooth ramp taking 350 μs (slow enough to allow for adiabatic microwave dressing of the potential, but much faster than the motional dynamics of the atoms). This creates a state-dependent MW potential which is left on for the entire Ramsey interrogation time T_R , before a turn-off ramp of 350 μs . Finally, a second $\pi/2$ Rabi pulse is sent and the atom number populations are read out.

The result of this measurement sequence, as a function of T_R is shown in Figure 3.11. We observe fast oscillations, which are the typical interference fringes of a Ramsey sequence, but modulated in amplitude by $\approx 60\%$. This contrast scales with the wave function overlap, and its periodic collapse and revival indicates that the demixing-remixing dynamics of the two components is coherent. For longer times, atom losses during this process results in a reduction of the mean-field interactions, which make this dynamic faster.

To estimate the optimal times T_R where the contrast has a revival, we fit the experimental data with a modulated oscillation, see Fig. 3.11. At these revival times we can obtain a better estimate of the contrast by performing a Ramsey sequence in the phase domain. This consists in fixing T_R to one of the revival times, and then scan the phase of the second $\pi/2$ Rabi pulse. The results of this type of measurement at the three revivals visible in Fig. 3.11 are given in Fig. 3.12. The fact that the contrast gets reduced from one revival to the next is also associated to phase spreading (squeezing) of the condensate, as it is also visible from the increasing noise on the fringes. For the first three revivals we typically find a contrast in the range of 95% – 99%.

The ability to spatially separate the two BEC components allows us to control the collisional interactions between them, effectively controlling the coefficient χ of the nonlinear dynamics described by the Hamiltonian Eq. (2.27). In fact, as it can be most easily seen from the approximated Eq. (2.29), the parameter χ depends on the wave-

3.3 Ramsey interferometry

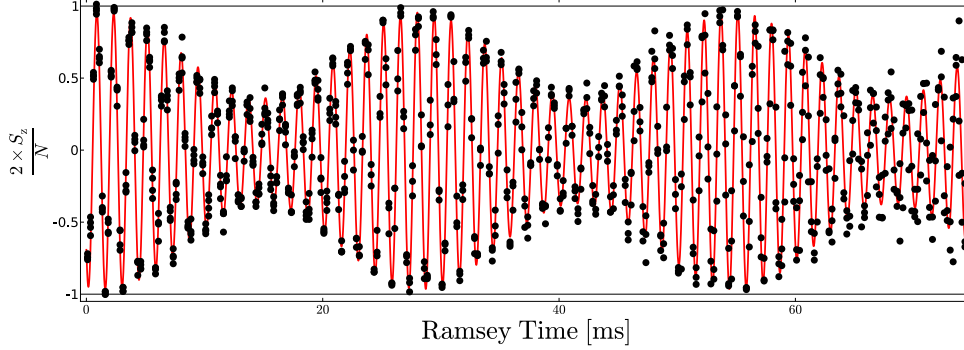


Figure 3.11: Demixing-remixing dynamics. Black dots are measurements of the Ramsey fringes in the time domain as a function of the interrogation time T_R , for a BEC with $N \approx 850$ atoms. During during T_R the microwave near-field is applied, which causes the two components to oscillate in their traps, as it can be seen from a modulation in the contrast. The fit with $O + (A(1 + B(\cos(\omega_{\text{fast}}T_R + \phi_0)))) \cos(\omega_{\text{slow}}T_R + \phi_1)$ (red line) gives for the first three revivals the times $T_{1\text{st}} = 28.2$ ms, $T_{2\text{nd}} = 54.8$ ms and $T_{3\text{rd}} = 81.4$ ms, respectively.

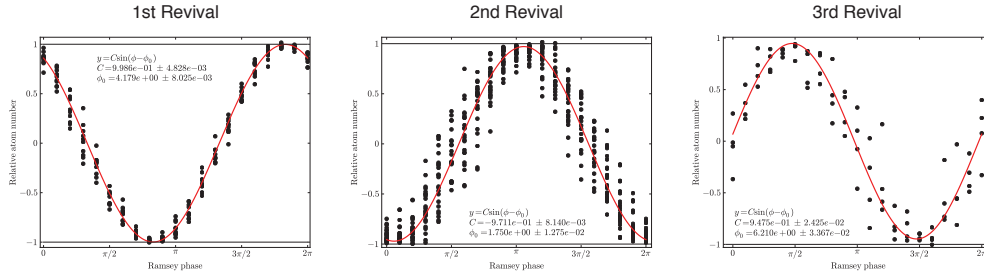


Figure 3.12: Ramsey phase measurements at the recombination times. Ramsey phase measurements at the first three revivals expected from the measurement in Fig. 3.11. The experimental points (black dots) are fitted with the model $C \sin(\phi - \phi_0)$, from which we extracted the Ramsey interference contrast C . Observe the typical decay of this quantity due to imperfect re-overlap between the two wavefunctions.

function overlap of the two states. It is nearly zero for identical and overlapping components, while it increases by several orders of magnitude for completely separated components [19]. For this reason, we use this demixing-remixing dynamics to prepare BECs in spin squeezed states, as we will explain in section 5.1.1.

Quantum correlations: Theory

In this chapter we introduce three main types of correlations arising from quantum mechanics: entanglement [2], Einstein-Podolsky-Rosen correlations [4] and Bell correlations [5]. Starting from an historical overview of their development, we briefly discuss the revolutionary aspects as well as the philosophical implications of these concepts. We then continue with the formulation of rigorous mathematical definitions for these three types of correlations, which allow us to derive practical criteria to reveal them experimentally. Moreover, we introduce approaches to characterize multipartite states based on the properties of the correlations among the constituent parties.

4.1 History and philosophy

During the formulation of quantum mechanics, it was soon realized that a characteristic trait are its probabilistic predictions of measurement results. From this observation, it might look as if it was an incomplete description of the physical world, which cannot give deterministic predictions because it does not consider all existing degrees of freedom. A classical analogy could be the case of thermodynamics, where macroscopic properties (such as temperature, pressure, ...) arise from more fundamental microscopic quantities not included in the theory (such as the speed of each particle in the system). Therefore, as an example, knowing the temperature of a gas gives us information only about the probability of one of its molecule to have a certain speed. Is this also the case for quantum theory, where knowing the wavefunction gives us only probabilistic predictions?

Einstein, Podolsky and Rosen (EPR) addressed this question and, by conceiving a hypothetical experiment, they apparently managed to answer it. In their 1935 paper “Can quantum-mechanical description of physical reality be considered complete?” [67] they proved the incompleteness of quantum mechanics, under the assumption that physical properties exist (are real) independent of their observation. This work raised a lot of discussions and further analyses, in particular by Bohr [68] and Schrödinger [69, 70], but, more crucially, it led to the realization that quantum mechanics predicts correlations among physical systems that are in conflict with the classical world.

4. Quantum correlations: Theory

The question of whether the quantum mechanical description of the world could be “completed” by introducing new variables into the theory, therefore finding an even more fundamental theory, culminated in 1964 with the work of Bell [71]. Remarkably, he proposed an experiment able to rule out such a possibility, which has since already been performed in several forms [5, 72–77], leading to the conclusion that a local realist description of the world is impossible.

4.1.1 Elements of reality and the completeness of physical theories

Following our everyday experience, we are brought up to believe that the universe is an ensemble of objects with associated properties. These properties are called by EPR the “elements of physical reality” and, importantly, they are empiric features, in the sense that they are defined upon what can be predicted by a model and measured by experiments. In general, EPR say that, “If, without in any way disturbing a system, we can predict with certainty (i.e., with probability equal to unity) the value of a physical quantity, then there exists an element of physical reality corresponding to this physical quantity” [67].

According to their definition, elements of reality are objective, *i.e.* independent from *who* observes them, and their reality is rooted in the idea that they exist independently of *whether* someone observes them or not. The collection of all such elements constitutes an objective reality, which is how we perceive the world in our everyday lives.

Ideally, a scientific theory aims to give an accurate description of (at least a portion of) the world, allowing us to predict with certainty the result of the measurements of its elements of reality. According to EPR, a physical theory can be called “complete” if every element of the physical reality has a counterpart in the physical theory. It was the case of quantum mechanics, where measurement results are intrinsically random, that lead EPR to ask whether such a theoretical description of the world is complete. As we will see, this thought developed up to the point of questioning the validity of assigning elements of reality to the observable properties of the quantum realm, like the direction of a spin. Is the result of an experiment revealing a property embedded in the system under study, or is this property made real at the time of observation?

4.1.2 Heisenberg uncertainty principle

A surprising result of quantum mechanics is that it predicts a limit on the precision with which certain physical quantities can be known. This is counterintuitive because, in the classical world, we expect to be able to measure different elements of reality to arbitrarily small precision, bounded only by our experimental apparatus¹. It is important to underline that the limit imposed by quantum mechanics is a fundamental one, independent of our ability to perform the measurements, but which in principle could arise from an incompleteness of the theory in describing the actual world.

¹Actually, as the resources (energy, time, space, ...) available in our Universe are believed to be finite, a measurement with arbitrarily small precision is never possible.

In a practical situation, an observer has to estimate the value of some physical properties, say A and B , and for this he performs repeated measurements. Each time he prepares the system (and the experimental apparatus) in the same initial state, he chooses whether to look either at property A or B , and finally he performs the measurement. The uncertainty relation states that (a rigorous definition is given below), if A and B are some “special pair of properties”, *e.g.* $A = \text{position}$ $B = \text{velocity}$, then the errors of their estimated values can not simultaneously be arbitrarily small, no matter how precise the experimental apparatus or the state preparation are.

At this point, we might ask the question: why during the experiment the observer has to decide whether to look at *either* A or B , can't he look at both? The fact is that, in quantum mechanics, the act of measuring alters the state of the system. Therefore, after the first measurement is performed, any subsequent measurement will be on a state different than the original one, possibly giving a different result. In other words, this means that measuring B after A might be different from measuring A after B . In this case, A and B are called incompatible observables, because they cannot be determined at the same time.

To give a rigorous definition, in quantum mechanics the physical observables A and B are associated to operators, \hat{A} and \hat{B} , and they are incompatible if $\hat{A}\hat{B} \neq \hat{B}\hat{A}$. The uncertainty relations tells that, for any pair of observables

$$\text{Var}[\hat{A}]\text{Var}[\hat{B}] \geq \frac{1}{4} | \langle [\hat{A}, \hat{B}] \rangle |^2, \quad (4.1)$$

where $\text{Var}[\hat{X}] = \langle \hat{X}^2 \rangle - \langle \hat{X} \rangle^2$ is the variance of the operator \hat{X} , and $[\hat{A}, \hat{B}] = \hat{A}\hat{B} - \hat{B}\hat{A}$ is the commutator. If $[\hat{A}, \hat{B}] \neq 0$ then the observables are incompatible (they do not commute), and Eq. (4.1) shows that they cannot be measured and known with arbitrary precision simultaneously. If we know property A precisely, $\text{Var}[\hat{A}] \approx 0$, then we are uncertain about the value of property B , $\text{Var}[\hat{B}] \gg 1$ (in some units), and vice versa. Only in the case $[\hat{A}, \hat{B}] = 0$ can both observables be measured and known simultaneously with arbitrary precision.

EPR made a crucial observation, expressing a conceptual, instead of practical, implication of the uncertainty principle. They write, “[...] it is shown in quantum mechanics that, if the operators corresponding to two physical quantities, say A and B , do not commute, that is, if $\hat{A}\hat{B} \neq \hat{B}\hat{A}$, then the precise knowledge of one of them precludes such a knowledge of the other. Furthermore, any attempt to determine the latter experimentally will alter the state of the system in such a way as to destroy the knowledge of the first. From this follows that either (1) the quantum-mechanical description of reality given by the wave function is not complete or (2) when the operators corresponding to two physical quantities do not commute the two quantities cannot have simultaneous reality.” [67]. These alternatives arise from the consideration that, if ($\bar{1} = \text{not } 1$) quantum mechanics is a complete theory and ($\bar{2} = \text{not } 2$) both quantities have simultaneous reality, then these quantities should enter into the theory which would allow predicting their value with certainty. Since in quantum mechanics this is forbidden by the uncertainty principle, we have to conclude that either ($\bar{1}$) or ($\bar{2}$) (or both) are wrong assumptions.

4. Quantum correlations: Theory

According to the postulates of quantum mechanics, the wavefunction contains the complete description of the state of a system. In this framework, we are therefore only left with the option that the statement $(\bar{2})$ above is wrong (or equivalently that (2) is true), meaning that pairs of observables might not have simultaneous reality, and that Nature has an intrinsic fundamental unpredictability. Einstein could not accept this possibility [78]. Like many others he believed in an objective reality which can be described deterministically in a mathematical language, and for this reason he tried to prove instead that quantum mechanics is incomplete. In their work, EPR analyzed a thought experiment allowing to predict the values of pairs of incompatible observables with certainty, apparently violating the uncertainty principle.

4.1.3 Einstein-Podolsky-Rosen paradox

The thought experiment devised by EPR is the following. Consider two particles, labeled A and B , produced at $x = 0$ by a physical process such that their momenta (velocities) are always the same, $p^A = p^B$, and their positions are opposite with respect to the origin, $x^A = -x^B$. Particle A is sent to observer “Alice”, and B to “Bob”, who perform experiments on them.

When Alice measures the position of particle A , she will obtain the result x_A , which is a random number she cannot predict. However, independently of the specific result, after her measurement she will always be able to predict with certainty the position of particle B that Bob will measure: it must be $x^B = -x^A$. Similarly, if Alice were measuring the momentum of particle A , she would have obtained the (random) result p_A , and she could have predicted with certainty the momentum of particle B that Bob would have measured: $p^B = p^A$. To summarize, regardless of which property Alice decides to measure, her (random) result allows her to predict with certainty Bob’s result for the same property. Measurement outcomes are perfectly (anti-)correlated.

At this point, the difference from a classical scenario might not be apparent. Suppose we pick two coins of identical shape and material, and we give one of them to Alice and the other of Bob. Independently of whether Alice decides to look at the shape or at the material, and independently of her result, she will always be able to predict with certainty the result of Bob’s observation of the same property: he will see the same. Also in this case, there is perfect correlation between the measurement results. Even more, Alice could actually observe simultaneously shape and material of the coin, since these properties are both elements of reality. So, where is the complication arising from?

Contrary to the classical example of the coin, quantum measurements of position and momentum do not commute, and therefore the uncertainty principle applies and they can not be observed simultaneously with arbitrary precision. According to Eq. (4.1), we must have

$$\text{Var} [x^B] \text{Var} [p^B] \geq \frac{1}{4} |\langle [x^B, p^B] \rangle|^2 = \frac{\hbar^2}{4} > 0, \quad (4.2)$$

where \hbar is the reduced Planck constant. This relation implies that measurement uncertainties for position and momentum cannot be both zero: their product is bounded to

a non-zero constant and therefore position and momentum cannot be both determined with certainty. As pointed out by EPR, under the assumption that quantum mechanics is a complete theory, the fact that $[x^B, p^B] \neq 0$ implies that position and momentum are not (simultaneous) elements of reality. Nevertheless, we have seen that there are situations in which a measurement on A allows to predict with certainty the result of a measurement in B , without interacting with it. Unless the act of measuring one particle instantaneously affects the other, which would involve information being transmitted faster than light (“spooky action at a distance”), as forbidden by the theory of relativity, this result forces us to conclude that both position and momentum are elements of reality! We reached opposite conclusions, clearly raising a paradox. The only possible solution seems to be that our assumption of the completeness of quantum mechanics is wrong.

To summarize, using EPR’s words, “Previously we proved that either (1) the quantum-mechanical description of reality given by the wave function is not complete or (2) when the operators corresponding to two physical quantities do not commute the two quantities cannot have simultaneous reality. Starting then with the assumption that the wave function does give a complete description of the physical reality, we arrived at the conclusion that two physical quantities, with non-commuting operators, can have simultaneous reality. Thus the negation of (1) leads to the negation of the other alternative (2). We are thus forced to conclude that the quantum-mechanical description of physical reality given by wave functions is not complete.” [67].

In more generality, the EPR paradox appears whenever the inconsistency between the completeness of quantum mechanics and local realism is observed. According to the postulate of the collapse of the wavefunction, after the first measurement has been performed, the system will be left in the eigenstate of the observable associated to the observed eigenvalue. In other words, depending on what measurement Alice decides to perform, collapse in a different basis (*e.g.* x or p) occurs, and therefore particle B could be left in states with different eigenfunctions. If the two particles cannot interact with each other (*e.g.* because they are far away) we must conclude that no real changes can happen to B after Alice’s measurement choice, and therefore that the different states in which B could be left are just a different description of the same reality (if any). The difficulty arises when these different states are eigenstates of operators that do not commute, as we have just seen. Apart from the conclusion on the completeness of quantum mechanics, one could also raise the observations that the uncertainty relation is not a fundamental principle but just a consequence of this incompleteness, and that the description of physical reality given by quantum mechanics is redundant, since the different quantum states in which a system can collapse upon the measurement on an other distant system, must describe the same physical state.

As we can deduce from the claim, “While we have thus shown that the wave function does not provide a complete description of the physical reality, we left open the question of whether or not such a description exists. We believe, however, that such a theory is possible.” [67], EPR believed they managed to demonstrate that the wavefunction does not provide a complete description of physical reality, and hence that the Copenhagen

4. Quantum correlations: Theory

interpretation of quantum mechanics is unsatisfactory. We will see later how the work of Bell proved this conclusion to be incorrect, and that quantum theory cannot be “completed”. Therefore, which idea or concept upon which the EPR argument is based do we have to reject?

4.1.4 Schrödinger’s entanglement and nonseparability

Using the words of Schrödinger [69, 70], the work by EPR brought the attention to the “very disconcerting fact” that “the current interpretation of quantum mechanics obliges us to admit not only that by suitable measurements, taken on one of the two parts only, the state of the other part can be determined without interfering with it, but also that, in spite of this non-interference, the state arrived at depends quite decidedly on what measurements one chooses to take - not only on the results they yield.” This feature is in drastic conflict with our intuition, “It is rather discomfoting that the theory should allow a system to be steered or piloted into one or the other type of state at the experimenter’s mercy in spite of his having no access to it.” The term “steering” introduced in this sentence has then been used to describe the EPR paradox.

A number of further investigation were driven by the EPR paper, especially among the founders of quantum mechanics like Bohr [68] and Schrödinger [69, 70]. The latter even generalized the original EPR idea, uncovering a peculiar feature of the theory of quantum mechanics. He realized that “the best possible knowledge of a whole does not necessarily include the best possible knowledge of all its parts, even though they may be entirely separated and therefore virtually capable of being ‘best possibly known’, i.e. of possessing, each of them, a representative of its own.” [69]. Schrödinger named this feature “entanglement” of the wavefunctions, to reflect the non-separability of certain composite quantum systems where constituents cannot be fully described without considering the others. This holistic feature is a completely new concept that he claimed to be “[not] *one* but rather *the* characteristic trait of quantum mechanics, the one that enforces its entire departure from classical lines of thought.” [69].

Invoking quantum nonseparability is somehow inconsistent with EPR’s definition of elements of reality, which are a local concept, and it could therefore offer a possible solution for the paradox. The necessity of considering the system as a whole directly implies that a measurement performed on one of its particles will affect all its other particles, no matter how far apart they are. This point of view indicates that EPR’s analysis of their hypothetical experiment has a flaw exactly in the assumption that particle B is not affected by the measurement operation performed in A , a possibility which, for spatially separated parties, seems in clear conflict with causality. For many physicists like Einstein and Schrödinger, entanglement was a concept leading to conclusions so disturbing and counterintuitive that they could not believe it occurs in reality. Some unknown principle should have prevented such entanglement (with its consequent “spooky action at a distance”) predicted by quantum theory, and violating a local realist view of causality. The possibility of an incomplete description of the physical world was still open.

Bohr even had another point of view concerning EPR’s definition of the elements

of reality. In his famous reply, published few months after the EPR article (and with the same title), he writes explicitly, “The wording of the above mentioned criterion [the EPR criterion for elements of reality] ... contains an ambiguity as regards the expression ‘without in any way disturbing a system’.” [68]. In what follows he presents his point of view according to which physical reality cannot be properly defined without referencing to a well-defined experiment including both the entire system and all the measurement apparatuses, “these [experimental] conditions must be considered as an inherent element of any phenomenon to which the term physical reality can be unambiguously applied”. As a consequence, the measurement choice and result of one observer change the physical reality of the whole physical system, which of course includes the other particles. This leads Bohr to reject the EPR assumption according to which the physical reality contained locally at Bob’s position is independent of measurements performed by Alice on an other arbitrarily remote region, and with that the EPR conclusion as well. Bohr summarized his point of view a decade later by writing, “Recapitulating, the impossibility of subdividing the individual quantum effects and of separating a behavior of the objects from their interaction with the measuring instrument serving to define the conditions under which the phenomena appear implies an ambiguity in assigning conventional attributes to atomic objects which calls for a reconsideration of our attitude towards the problem of physical explanation.” [79].

4.1.5 Bell nonlocality

Bell decided to further investigate the results of EPR with a rigorous mathematical approach [80]. His idea consists of assuming the existence of hidden variables, to then formulate a criterion which measurement results must fulfill according to local realism (LR). More precisely, he was able to derive an experimentally measurable quantity S , such that

$$S \stackrel{\text{LR}}{\leq} 2, \quad (4.3)$$

when the measurements are performed on a system which can be described by a local realist theory. Remarkably, Bell’s inequality Eq. (4.3) comes from a completely general treatment of the problem, which does not make any assumption on the type of measurements that are performed, nor on the state of the system.

The key result consists in the observation that according to quantum mechanics (QM)

$$S \stackrel{\text{QM}}{\leq} 2\sqrt{2}, \quad (4.4)$$

and therefore that measurements on a quantum system can violate the criterion Eq. (4.3). This shows that quantum theory cannot be “completed” (made fully deterministic) by adding local properties (elements of reality, hidden variables) to the individual components of the system, as believed by EPR.

We have to keep in mind that, if quantum mechanics cannot be based on a more fundamental local realist theory, this does not mean that the same must be true for Nature. There was still the possibility that quantum mechanics was just an inaccurate model for

4. Quantum correlations: Theory

the physical reality, and that such possibilities predicted by the theory do not actually occur. For this reason, experimental tests were needed to reach a conclusive statement.

The availability of a concrete and practical criterion, Eq. (4.3), motivated several physicists to test it in their laboratories. Nevertheless, a strict test of it was such a challenging task that it took around fifty years. Starting from the pioneering experiments by Clauser in 1972 [81] and Aspect in 1982 [82], until the most recent (loophole-free) experiments by four different groups in 2015-2017 [72–75], considered to be definitive, the measurement results violated Bell’s inequality, as predicted by quantum mechanics.

The expression Eq. (4.3) (as any other Bell inequality) is based on the assumption that there exist, independently of whether they are observed or not, a list of properties for the system (realism), and that measurements performed on one part of the system do not influence its other parts (locality). Remarkably, the experimental violation of a Bell inequality demonstrates that Nature cannot be described by any local realist theory. We have to give up the idea of either reality, or locality, or both.

4.2 Technical definitions of quantum correlations

So far we have seen the historical development of the understanding of quantum correlations. We used terms like entanglement (non-separability), EPR-steering and Bell correlations (nonlocality), without highlighting the conceptual differences between them. Also to this end, we now give a formal definition of these types of correlations.

4.2.1 Correlations as resources for tasks

It is intuitive that the power of correlations lies in enabling better performance in some tasks. Imagine, as a trivial example, any team game: players have a higher probability to win if they agree on a common strategy, rather than if they were playing individually or by taking random decisions. This illustrates how correlations can be seen as a resource to perform a certain task. Interestingly, we may also adopt the following inverse logic: we first define a task (*i.e.* a “game”), and we claim that a certain type of correlations exists among the parties involved (*i.e.* the “players”) if the game is won with certainty. In this way, by constructing specific tasks, we are able to classify correlations, or even to quantify their strength.

Note that, from now on, we will use the words entanglement and non-separability interchangeably. Similarly, Bell correlation and nonlocality are used with the same meaning, as well as EPR correlations and steering.

Bell nonlocality

In this scenario, a source prepares a state which is then shared among two observers, Alice and Bob, Fig. 4.1. These two do not trust that quantum mechanics gives a correct description of their experiments, and they have to convince themselves that their state

4.2 Technical definitions of quantum correlations

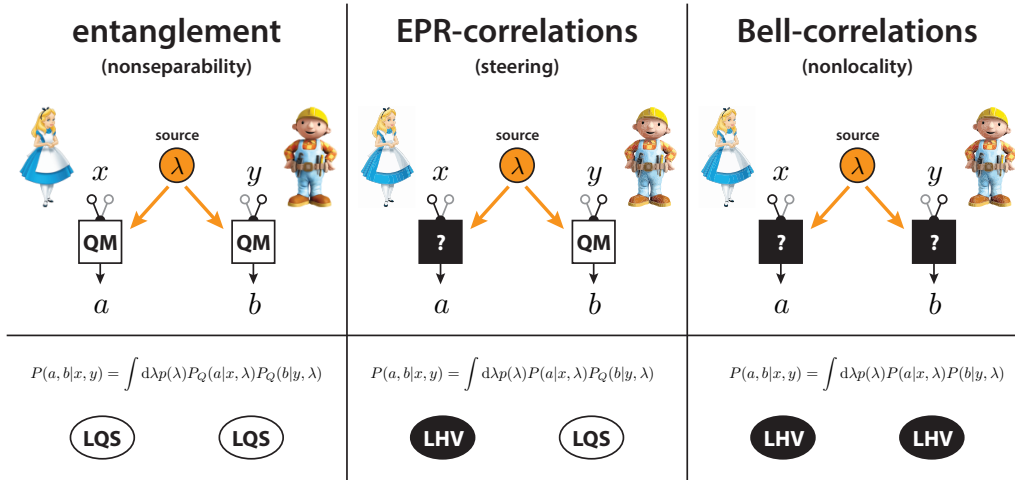


Figure 4.1: Technical definitions of entanglement, EPR-steering and nonlocality. In each scenario, a source prepares a state which is then shared among two observers, Alice and Bob. The state can have some hidden property λ . Alice performs measurement x on her share of the state, and she obtains the result a . Similarly, Bob measures y and he obtains b . After repeating such measurements on many copies of the state, with different settings for x and y , they estimate the joint probability $P(a, b|x, y)$ and check whether it can be explained by the models in the bottom panels. Entanglement is confirmed if $P(a, b|x, y)$ cannot be reproduced by a pair of local-quantum-states (LQS). On the other extreme, nonlocality is confirmed if $P(a, b|x, y)$ cannot be reproduced by a pair of local-hidden-variables (LHV). EPR-steering lies in between these two, and it is confirmed if $P(a, b|x, y)$ cannot be reproduced by a LHV-LQS model. See the text for further details.

shows correlations that cannot be explained in classical terms. To this end, they take a measurement each, collect the results, and repeat the procedure a number of times.

Alice and Bob will be convinced if and only if the correlations they observe in the measurement results cannot be explained by a classical local hidden variable model. In other words, Alice and Bob will succeed in their task if and only if the state they share is Bell correlated, *i.e.* it allows them to violate a Bell inequality [5].

The general reasoning starts from the assumption that a physical system is fully characterized by a list of properties, called hidden variables, which we denote with λ . These are all the elements of reality that could possibly enter in the description of the system, even if they are not yet known or measurable, and, in this sense, λ would contain all the information necessary to deterministically predict the result of any measurement performed on the system.

Suppose Alice performs a measurement labeled x on her share of the state. According to local realism, the probability of obtaining result a depends on both the chosen measurement, x , and on the hidden variable λ . In symbols, this is expressed as $P(a|x, \lambda)$. The same holds for Bob, who performs measurement y on his share of the state, obtaining outcome b .

For the entire system, we extend this idea by defining the joint probability $P(a, b|x, y, \lambda)$

4. Quantum correlations: Theory

of finding as results a and b when Alice and Bob perform measurements x and y , respectively. Remember here that the hidden variable λ contains all possible information of both particles. Following the idea of Bell, our task is now to find a criterion that joint probabilities satisfy under the assumption of local realism.

The principle of locality corresponds to the existence of a λ such that

$$P(a, b|x, y, \lambda) = P(a|x, \lambda)P(b|y, \lambda) , \quad (4.5)$$

meaning that the joint probability can be expressed as the combination of the individual probabilities for the two systems. This is somehow intuitive, as the idea of locality tell us that *e.g.* the probability of a result for Alice, $P(a|x, \lambda)$, does not depend on the measurement y performed by Bob, or on its result b . In the case of spatially separated objects, it is clearly expected that the result of an experiment in Basel should be independent of the result of an experiment performed simultaneously in *e.g.* Sydney, as if this were not the case it would probably be impossible to do any experimental investigation. Moreover, the theory of relativity predicts that information cannot travel faster than light; therefore events in one region of space-time cannot influence events in space-like separated regions. However it is important to remark that, despite its name, the notion of locality does not necessarily imply that the components of the physical systems are spatially separated. If the two particles A and B are at the same spatial position, but they do not “communicate” (interact), there is no way they could possibly know each others measurement setting and outcome, and we would also expect Eq. (4.5) to hold. From an experimental perspective, it is difficult to prove that no communication at all is happening, because there might be unknown channels, and therefore to invoke relativity by ensuring space-like separation of the particles turns out to be the definitive certificate.

In full generality, the parameter λ might change from one run of the experiment to the other (the fact that it is a hidden variable might imply that it cannot be fully controlled), therefore the most general expression for the joint probability is an average over the probability distribution $p(\lambda)$ of the different λ 's (such that $\int d\lambda p(\lambda) = 1$)

$$P(a, b|x, y) = \int d\lambda p(\lambda) P(a|x, \lambda) P(b|y, \lambda) . \quad (4.6)$$

This expression gives a precise condition for locality of a physical system. If for some a, b, x, y Eq. (4.6) is not satisfied, the state shared by the observers is nonlocal.

Nonseparability

In this scenario, a source prepares a state which is then shared among two observers, Alice and Bob, Fig. 4.1. Now these two trust that quantum mechanics gives a correct description of their experiments, and they just have to convince themselves that their state is nonseparable. To this end, they take a measurement each, collect the results, and repeat the procedure a number of times.

Alice and Bob will be convinced that the state they share is nonseparable if the joint probability distribution of their measurement results cannot be expressed as a product

4.2 Technical definitions of quantum correlations

of probability distributions for separate measurements of each party, *i.e.* it violates a separability criterion [2].

Assuming that Alice is able to describe her local measurement results with quantum mechanics means that the probability $P(a|x, \lambda)$ can be expressed as a probability originating from performing quantum measurements on a quantum state, $P_Q(a|x, \lambda)$. The latter is obtained from Born's rule as

$$P_Q(a|x, \lambda) = \text{Tr} [\Pi_a^X \rho_A(\lambda)] , \quad (4.7)$$

where Π_a^X is the projector (or more generally the POVM) associated with obtaining result a when measuring x on Alice's share of the state, $\rho_A(\lambda)$. A similar definition holds for Bob.

In analogy to the definition for locality, the state shared by Alice and Bob is separable if for any a, b, x, y it holds that

$$P(a, b|x, y) = \int d\lambda p(\lambda) P_Q(a|x, \lambda) P_Q(b|y, \lambda) . \quad (4.8)$$

If for some a, b, x, y Eq. (4.8) is not satisfied, the state shared by the observers is entangled (nonseparable).

At this point it is important to note that, while the probabilities appearing in Eq. (4.6) are not restricted to some physical model, as they must only be proper mathematical probabilities (*i.e.* satisfying the Kolmogorov axioms), the probabilities appearing in Eq. (4.8) are less general, as they must come from a quantum description. For this reason, a violation of Eq. (4.6) is more difficult to observe than a violation of Eq. (4.8), reflecting the fact that demonstrating nonlocality is a stronger claim than nonseparability, or, in other words, that nonlocality is a more powerful correlation than entanglement.

EPR-steering

In this scenario, a source prepares a state which is then shared among two observers, Alice and Bob, Fig. 4.1. Alice has to convince Bob that she is able to predict his measurement results with certainty, in contrast to what he would expect if his experiment was locally compatible with quantum mechanics. Bob, who does not trust Alice, decides the measurement he wants to perform and challenges her to make a prediction for the outcome. He collects the results, and asks to repeat the procedure a number of times.

Alice will manage to convince Bob of her claim if and only if he sees that she can predict measurement results of non-commuting operators, apparently violating the uncertainty principle for system B . In other words, Alice will succeed in her task if and only if the state they share allows EPR steering, *i.e.* it shows an EPR paradox [4].

A mathematical definition of this concept was first formulated by Wiseman *et al.* in Refs. [1, 83], in a form similar to Eq. (4.9) and Eq. (4.8). They state that Alice can steer Bob if for some a, b, x, y there is a violation of

$$P(a, b|x, y) = \int d\lambda p(\lambda) P(a|x, \lambda) P_Q(b|y, \lambda) , \quad (4.9)$$

4. Quantum correlations: Theory

where $P(a|x, \lambda)$ is any valid probability and $P_Q(b|y, \lambda)$ is a quantum probability.

Intuitively, Eq. (4.9) is motivated by the fact that, if Bob believes that quantum mechanics gives a correct description of his system, then his measurement results must come from some $P_Q(b|y, \lambda)$. Moreover, as he does not trust Alice, he believes her predictions for his outcomes to be just “random” numbers originating from some $P(a|x, \lambda)$. Observing steering necessarily falsifies this model.

As we can see, the relation Eq. (4.9) is an intermediate case between Eq. (4.8) and Eq. (4.6), reflecting the fact that concluding steering is a stronger claim than just entanglement, but weaker than nonlocality.

We note here that Eq. (4.9), as well as the above description of this task, makes evident that a crucial aspect of EPR steering is its asymmetry between the roles of the two parties (steering *vs.* steered). The fact that Alice can steer Bob’s state does not necessarily imply that the converse is also possible, *i.e.* there is a directionality in the correlations [84, 85]. If only one of the two parties can steer the other then we speak of one-way steering, otherwise of two-way steering. Importantly, two-way steering is necessary but not sufficient for violating a Bell inequality.

4.2.2 Inequivalence of entanglement, steering and nonlocality

Now that we have a rigorous definition of entanglement, steering and nonlocality, we can better appreciate their differences. From a first look, it already appears that nonlocality is a stronger claim than entanglement, and that EPR steering requires entanglement. The hierarchy of these correlations has been studied in detail in a number of works, and we summarize the results here.

For bipartite pure states the scenario is relatively trivial. Given the fact that all pure bipartite entangled states can violate a Bell inequality [86], we immediately see that such states are correlated in the strongest way allowed by quantum mechanics. Therefore, they also allow for two-way steering. Unfortunately, experiments always deal with mixed states and, therefore, this simple theoretical result cannot be applied to practical situations.

In the case of bipartite mixed states a less trivial scenario appears. Consider for example the Werner state

$$\rho_W(p) = p|\Psi^-\rangle\langle\Psi^-| + (1-p)\frac{\mathbb{I}}{4}, \quad (4.10)$$

where $|\Psi^-\rangle = (|\downarrow\uparrow\rangle - |\uparrow\downarrow\rangle)/\sqrt{2}$ is the singlet state, $0 \leq p \leq 1$, and \mathbb{I} is the four-by-four identity matrix representing an uncorrelated state. The variable p parametrizes the purity of the state, for $p = 0$ we have the completely mixed state, while for $p = 1$ we have the pure state $|\Psi^-\rangle$ which is maximally entangled. By asking for which ranges of p we may violate a Bell inequality [87], perform steering [1], or see nonseparability [88], we end up with different ranges, as shown in Fig. 4.2. Note that while the thresholds for separability and steering are known numbers, the range of p for which a local model for projective measurements exists is related to the Grothendieck constant of order three,

4.2 Technical definitions of quantum correlations

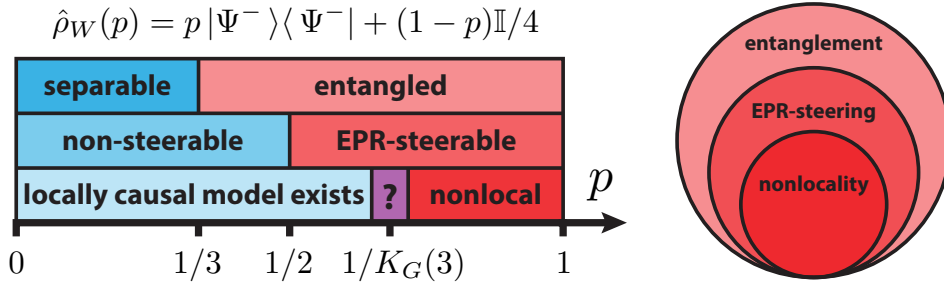


Figure 4.2: Inequivalence of entanglement, EPR-steering and nonlocality. The correlations among the two spins of the Werner state $\hat{\rho}_W(p)$ shows different resources depending on the purity p of the state. Entanglement exists for $p > 1/3$, while EPR-steering for $p > 1/2$. Nonlocality has the strongest requirement, and it exists for $p > 1/K_G(3)$, where $K_G(3)$ is the Grothendieck constant of order three whose exact value is still unknown (see the main text for the known bounds). See text for more details.

$K_G(3)$, whose exact value is remarkably still unknown [87, 89]. Known bounds are $1.5163 \geq K_G(3) \geq 1.4644$, as proven in Ref. [90] and [91] respectively. Figure 4.2 gives a first clear indication of the fact that the three correlations we are considering have different properties, and a specific hierarchy.

The inequivalence of entanglement, steering and nonlocality has been studied in detail also in the field of quantum information. It has been shown that each type of correlation constitutes a different resource for quantum information tasks, therefore finding different practical applications. As an example, entanglement is useful in quantum metrology for parameter estimation beyond the standard quantum limit, steering allows for quantum teleportation and for other one-sided device-independent tasks, while nonlocality is necessary for provably secure quantum key distribution, certified randomness generation and two-sided device-independent tasks.

4.2.3 Constraints on physical models

It is important to mention that an experimental observation of the correlations just presented gives stringent constraints on the structure of any physical theory attempting to describe Nature.

In the specific, observing entanglement corresponds to a violation of a separability criterion (derived from *e.g.* Eq. (4.8)), which rules out the possibility that Alice and Bob could describe their systems by two independent local quantum states (LQs). Still, the possibility remains that Alice could describe her system by a local hidden variable (LHV) state, while Bob by a LQS, as represented by Eq. (4.9). This option is ruled out if Alice is able to steer Bob's state. Similar conclusions hold with the roles of Alice and Bob inverted. Therefore, observing EPR steering rules out local hidden state (LHS) models. A possibility that remains open is the one in which Alice and Bob are able to describe their systems by each considering a LHV model, as in Eq. (4.6). However, this

4. Quantum correlations: Theory

option is also ruled out if Bell correlations are observed.

For these reasons, the observation of a specific type of quantum correlations results in nontrivial limitations on the possible descriptions of a system, Fig. 4.1. In particular, the importance behind the experimental violation of a Bell inequality consists in the fact that it poses a constraint on any physical theory, which is stronger than the one concluded from observing (just) entanglement or steering.

It is worth emphasizing that ruling out LHV models does not mean that quantum mechanics is the ultimate and “best possible” theory to model the microscopic world. The possibility of a more fundamental theory, *e.g.* involving nonlocal hidden variables, is still left open.

4.2.4 Multi-partite scenarios

So far, we considered for simplicity a bipartite system, which is the minimal scenario showing the correlations we presented. However, the generalization of the concepts of entanglement, steering and nonlocality for multipartite systems is of clear interest. On the one hand this throws light on the behavior of quantum systems of large sizes, for example investigating why quantum effects are not commonly observed in the macroscopic world we perceive. On the other hand, for the practical application of these correlations, increasing the number of available particles can increase the usefulness of a state.

Unfortunately, the complexity of detecting quantum correlations in multipartite scenarios increases significantly (often exponentially) with the number of particles. To be more precise, while the generalization of the definitions Eqs. (4.6,4.8,4.9) is straightforward, the derivation of practical criteria to detect the corresponding correlations has a complexity which scales with the system’s size [92–94]. Moreover, from the experimental point of view, it is also more challenging to create and control large quantum systems.

Apart from the generalization of Eqs. (4.6,4.8,4.9), the multipartite case also naturally presents different forms of entanglement, steering and nonlocality. We will discuss these later in more detail, but just to mention an example, consider what could occur already in a tripartite case. Party A can be entangled with B , but together they can be separable from C , while a stronger form of correlation occurs if all three particles are in an entangled state. To distinguish between these two situations, one can associate them with a parameter corresponding to the size of the largest non-separable cluster, called entanglement depth. A similar reasoning applies to steering and nonlocality.

In this thesis we report experimental investigations of such multipartite quantum correlations. Throughout the rest of this chapter we present the criteria that allow us to detect entanglement, steering and nonlocality in an ensemble of N spin-1/2 systems. Moreover, we also show how to characterize multipartite entangled and nonlocal states in terms of their depth.

Scenarios with fluctuating number of parties

Measurements on atomic ensembles are performed either on independently prepared ensembles (*e.g.* for destructive measurements) or on the same ensemble at different times (*e.g.* for weak or non-demolition measurements). In both these situations, subsequent measurements are typically performed on systems with different number of particles, for example because they cannot be set deterministically or because they are lost from the trapping potential. Therefore, one might debate the validity of testing criteria derived to detect correlations in a scenario with definite number of particles N .

For well isolated ensembles of massive particles, the possibility of having a system in a coherent superposition of different number of particles is excluded by ultrafast decoherence processes which give rise to a superselection rule for the total number of particles (see *e.g.* Section III.D.1 of Ref. [32] for BECs). Therefore, we understand that the observed shot-to-shot fluctuations in the total atom number are of statistical, and not quantum, nature.

The set of measurements performed on systems with different particle numbers can be thought of as being performed on a system whose state is a statistical mixture (incoherent superposition) of states each with a definite particle number N (note that, in any case, measurement operators commute with \hat{N} , making the following block-diagonalisation always possible). Using the language of density matrices, this statistical mixture can be written as

$$\hat{\rho} = \bigoplus_{N \geq 1} p_N \hat{\rho}^{(N)}, \quad (4.11)$$

where p_N is the probability of having N particles and $\hat{\rho}^{(N)}$ the density matrix representing the state of a system with N particles.

To analyze the correlations between N particles in a state $\hat{\rho}^{(N)}$, we typically construct a witness operator $\hat{\mathcal{K}}^{(N)}$, such that $\langle \hat{\mathcal{K}}^{(N)} \rangle = \text{Tr}[\hat{\mathcal{K}}^{(N)} \hat{\rho}^{(N)}] \geq 0$ for all states that are not of interest, such that observing $\langle \hat{\mathcal{K}}^{(N)} \rangle < 0$ reveals the correlations under investigation.

Starting from this, the basic idea to detect correlations in a system with fluctuating number of particles consists in constructing a witness operator $\hat{\mathcal{K}}$ such that

$$\langle \hat{\mathcal{K}} \rangle = \text{Tr}[\hat{\mathcal{K}} \hat{\rho}] \geq \sum_{N \geq 1} p_N \text{Tr}[\hat{\mathcal{K}}^{(N)} \hat{\rho}^{(N)}] = \sum_{N \geq 1} p_N \langle \hat{\mathcal{K}}^{(N)} \rangle. \quad (4.12)$$

In this way, if no component $\hat{\rho}^{(N)}$ has the correlations under investigation, then $\langle \hat{\mathcal{K}}^{(N)} \rangle \geq 0$ for all N , and consequently also $\langle \hat{\mathcal{K}} \rangle \geq 0$. Conversely, observing $\langle \hat{\mathcal{K}} \rangle < 0$ proves that at least one component $\hat{\rho}^{(N)}$ of the system's state has the correlations under investigation.

Interestingly, if the witness $\hat{\mathcal{K}}^{(N)}$ is based only on operators that are block-diagonal in the N -basis (*i.e.* that commute with \hat{N} , as in the case of collective spins and their moments) then even if there is coherence between different $\hat{\rho}^{(N)}$ this would play no role as it is not detected [132].

4. Quantum correlations: Theory

We discuss more rigorously these ideas in Appendix E, where we also present specific examples for criteria detecting entanglement and Bell correlations in many-body systems with fluctuating particle number.

4.3 Entanglement detection and characterization

We want to provide experimentally testable criteria allowing to prove the nonseparability of a physical system. Detecting entanglement among two parties can already be a complicated task. In the most general case, where the number of degrees of freedom per party is arbitrary, a (practical) necessary and sufficient condition confirming nonseparability is not known. For specific cases, many relevant and experimentally practical criteria have been proposed, for both discrete and continuous variables. These allowed to experimentally detect entanglement of light and massive particles [2, 12].

In the multipartite scenario the complexity increases significantly. Already from the practical point of view, we understand that individual measurements on the parties become technically challenging or even unfeasible for macroscopic systems. Because of this, criteria witnessing the presence of entanglement that are based on collective observables have been proposed. These allowed to conclude entanglement even between millions of atoms [12, 95, 96].

The multipartite scenario presents naturally also a rich variety of entangled states. As an example, already in the tripartite scenario one can distinguish the case in which the entire system is nonseparable, from the case in which only two of the parties are in a nonseparable state. This raises the question of how to characterize different entangled states, which has been addressed in several ways, see *e.g.* Ref. [2].

In this section we present experimentally practical criteria allowing to conclude entanglement in a bipartite and in a multipartite system, that are known from the literature. Moreover, we present a commonly adopted method to characterize multipartite entangled states in terms of their “depth”, *i.e.* according to the maximum number of parties that are described by a nonseparable state.

4.3.1 Entanglement criteria

Bipartite scenario

The pioneering experiment by Julsgaard *et al.* [95], where two room-temperature macroscopic atomic ensembles showed entanglement, motivated the search for new criteria allowing to investigate other physical systems, states and measurements. In what follows we present a general sufficient criterion which allows to conclude entanglement of arbitrary bipartite systems, originally proven by Giovannetti *et al.* in Ref. [97].

For a bipartite scenario, the two systems A and B are said to be separable if their joint density operator ρ can be expressed as a convex sum of density operators for the two systems

$$\rho = \sum_k p_k \rho_k^A \otimes \rho_k^B, \quad (4.13)$$

where the coefficients p_k satisfy $0 \leq p_k \leq 1$ and $\sum_k p_k = 1$, and where ρ_k^α is a density matrix for the $\alpha \in \{A, B\}$ particle. Entanglement is demonstrated if the separability condition Eq. (4.13) is violated, which is however an experimentally unpractical criterion as it requires the knowledge of the density matrix of the system.

4. Quantum correlations: Theory

To derive a criterion requiring a small number of measurements, we look for a sufficient condition for non-separability when only two measurements are performed per party. On party A either A_1 or A_2 is measured, while on B either B_1 or B_2 is measured. These observables can be of any algebra (*e.g.* spins, continuous variables), and they satisfy the commutation relations

$$[A_i, B_j] = 0 . \quad (4.14)$$

We then define the new observables O_1 and O_2 to be the linear combinations

$$O_1 = a_1 A_1 + b_1 B_1 \quad (4.15a)$$

$$O_2 = a_2 A_2 + b_2 B_2 \quad (4.15b)$$

and look for a criterion that is satisfied for the measurement of these observables on separable states.

The uncertainty relation Eq. (4.1) applied to Eqs. (4.15a) tells us that

$$\text{Var}(O_1) \text{Var}(O_2) \geq \frac{1}{4} |\langle [O_1, O_2] \rangle|^2 = \frac{1}{4} |a_1 a_2 \langle [A_1, A_2] \rangle + b_1 b_2 \langle [B_1, B_2] \rangle|^2 . \quad (4.16)$$

This criterion is completely general, and it cannot be violated in the framework of quantum mechanics. Nevertheless, Giovannetti *et. al.* showed in Ref. [97] that for any separable state a stronger bound exists, namely

$$\text{Var}(O_1) \text{Var}(O_2) \geq \frac{1}{4} (|a_1 a_2| |\langle [A_1, A_2] \rangle| + |b_1 b_2| |\langle [B_1, B_2] \rangle|)^2 . \quad (4.17)$$

If this inequality is violated for some state and measurements, then we must conclude that the physical system under investigation is non-separable. It is important to mention that Eq. (4.17) is a necessary condition for separability or, in other words, that its violation is just a sufficient condition to conclude entanglement. This means that there are entangled states that do not violate Eq. (4.17), and for these other criteria need to be found.

In the experiment we are going to present in chapter 5, the variables of interest are the collective spin operators of two atomic ensembles, S^A and S^B , satisfying the usual spin commutation relations, *e.g.*

$$[S_z^A, S_y^A] = -i S_x^A . \quad (4.18)$$

We then consider $O_1 = g_z S_z^A + S_z^B$ and $O_2 = g_y S_y^A + S_y^B$, which are inserted into Eq. (4.17) together with Eq. (4.18). We obtain the separability criterion for two spins

$$\mathcal{E}_{\text{Ent}} = \frac{4 \text{Var}(g_z S_z^A + S_z^B) \text{Var}(g_y S_y^A + S_y^B)}{(|g_z g_y| |\langle S_x^A \rangle| + |\langle S_x^B \rangle|)^2} \geq 1 . \quad (4.19)$$

Observing $\mathcal{E}_{\text{Ent}} < 1$ is a sufficient condition to certify entanglement (non-separability) between the parties A and B . Note that criterion Eq. (4.19) is valid on separable states

4.3 Entanglement detection and characterization

for arbitrary values of the real parameters g_z and g_y , therefore, we chose them so that \mathcal{E}_{Ent} is minimized.

The criterion Eq. (4.19) deals directly with spin operators and is valid for any spin lengths and states, in contrast to other inequalities relying on the Holstein-Primakoff approximation. Moreover, it is experimentally accessible and well suited to study correlations among two atomic ensembles, as we will show in the next chapter.

Multipartite scenario

Beyond the bipartite scenario, it is of clear interest to detect entanglement among many parties, which requires a generalization of the approach just considered in the previous paragraph. The main complication arises from the fact that the number of measurements required scales with the number of parties, becoming soon unrealistic for many-body systems. Moreover, it is in general the case that when the number of particles involved is $N \gtrsim 100$, individual control and measurement becomes experimentally very challenging, and a complete characterization of the state of the system is impossible. For these reasons, significant efforts have been made to characterize physical systems in terms of their collective properties. In particular, the work by Sørensen *et al.* [98] indicated that entanglement can be detected in a many-body system just by measuring collective observables, as we are going to show.

We are interested in the case where each party is a spin 1/2, associated to the operator $\mathbf{s}^{(i)} = \boldsymbol{\sigma}^{(i)}/2$, with $\boldsymbol{\sigma}^{(i)}$ the vector of Pauli matrices acting on the i th spin. The possible measurements are restricted to projections of the collective spin operator

$$\mathbf{S} = \sum_{i=1}^N \mathbf{s}^{(i)}. \quad (4.20)$$

The variance of one spin component is bound by the uncertainty relation to be *e.g.*

$$\text{Var}[S_z] \geq \frac{1}{4} \frac{|\langle S_x \rangle|^2}{\text{Var}[S_y]}. \quad (4.21)$$

As we did in the previous paragraph, we note that a tighter bound exist for Eq. (4.21) in the case of separable states. To see this, remember that, for a multipartite scenario, the N -body density matrix ρ is separable if it can be expressed in the form

$$\rho = \sum_k p_k \rho_k^{(1)} \otimes \rho_k^{(2)} \otimes \cdots \otimes \rho_k^{(N)}, \quad (4.22)$$

where the coefficients p_k satisfy $0 \leq p_k \leq 1$ and $\sum_k p_k = 1$, and where $\rho_k^{(i)}$ is a density matrix for the i th particle. Thus, for a separable state (see Appendix D for the derivation)

$$\text{Var}[S_z] \geq \frac{\langle S_x \rangle^2}{N}. \quad (4.23)$$

Interestingly, the separability condition Eq. (4.23) is related to a known parameter relevant in the field of quantum metrology. It is known that multi-partite systems can

4. Quantum correlations: Theory

be prepared in states that allow to perform interferometric sequences with a sensitivity beyond the limit set by uncorrelated parties [12]. From this observation, Wineland *et al.* introduced in Ref. [99] a parameter which quantifies the interferometric usefulness of a quantum state, called metrological spin-squeezing parameter

$$\xi^2 = \frac{N \text{Var}[S_a]}{\langle S_x \rangle^2}, \quad (4.24)$$

where \mathbf{a} is the direction perpendicular to x minimizing the spin variance $\text{Var}[S_a]$. If we observe $\xi^2 = 1$ then the state under consideration is, for interferometric purposes, equivalent to an ensemble of uncorrelated particles, *i.e.* it allows to reach the standard quantum limit. On the contrary, if $\xi^2 < 1$ then the interferometric sensitivity is improved by a factor ξ^2 in variance with respect to an ensemble of uncorrelated particles. Intuitively, it can be understood that to observe $\xi^2 < 1$ the particles must be correlated, and therefore that ξ^2 could be used as an indicator for non-separability. This idea was formalized by Sørensen *et al.* in Ref. [98], who proved that observing $\xi^2 < 1$ implies that the particles are entangled. The argument they consider is the following.

From Eq. (4.23) we immediately see that for any separable state the Wineland parameter is $\xi^2 \geq 1$, and hence that any state with $\xi^2 < 1$ is entangled (non-separable). As in the bipartite case, the violation of Eq. (4.23) is only a sufficient condition, and there are entangled states for which $\xi^2 \geq 1$. An obvious example are entangled states with zero mean spin length, for which ξ^2 diverges, which require other criteria.

Apart for the experimental implications, it is conceptually interesting that entanglement in a many-body system can be revealed by measuring collective observables. This opens a number of questions, as whether the same approach can give a characterization of the observed entanglement or whether it allows to detect even stronger correlations (*e.g.* Bell correlations). A positive answer to these question is given in the next paragraphs.

4.3.2 Entanglement depth

Especially in multi-partite systems, entanglement can be of different forms. The interest for classifying these forms led to a number of criteria such as entanglement strength (not discussed in this work) and entanglement depth. We focus here on the latter, which consists in determining the separability of the state with respect to partitions. This depth corresponds to the smallest number of atoms that can be proven to be entangled with one another, but makes no statement about the strength of this entanglement.

Sørensen and Mølmer developed in Ref. [100] a strategy to quantify the depth of entanglement in a many-body system, based on the Wineland parameter Eq. (4.24), and therefore involving collective measurements only. The idea is based on the observation that for a fixed number of spins k , there is a minimum value of ξ^2 that can be achieved. Therefore, reversing this argument, the observation of a ξ^2 below this minimum value implies that there is at least a number k of spins that are entangled. A more formal interpretations of this entanglement depth is given in terms of k -producibility of the state, as given in Ref. [132].

4.3 Entanglement detection and characterization

To convince ourselves that the entanglement criterion Eq. (4.24) has a minimum, it is enough to see the following. For decreasing $\text{Var}[S_a]$, also ξ^2 decreases at first. However, because of the uncertainty principle, $\langle S_x \rangle$ must decrease with $\text{Var}[S_a]$ as well, which increases ξ^2 . The minimum of ξ^2 occurs from a balance between the numerator and the denominator of Eq. (4.24).

In a practical situation, one measures experimentally $\text{Var}[S_a]$ and $\langle S_x \rangle$, and would like to know the entanglement depth k of the state. This k corresponds to the minimum number of particles compatible with the observed measurement results, and indicates that there are at least k entangled particles. We emphasize again that this approach does not make any statement about the strength of the correlations among the parties.

The common strategy to find the entanglement depth k is the following, where we assume that the state is oriented such that $\min_{\mathbf{a} \perp x} = \text{Var}[S_z]$. First, it was noted [100] that for integer spins $S = k/2$ (with even k), the state minimizing $\text{Var}[S_z]$ for a given $\langle S_x \rangle$ has vanishing $\langle S_y \rangle$ and $\langle S_z \rangle$, and therefore is also minimizing the second moment $\langle S_z^2 \rangle$. For this reason, this state can be found by minimizing

$$\mu \langle S_x \rangle + \langle S_z^2 \rangle, \quad (4.25)$$

where μ is the Lagrange multiplier constraining the value of $\langle S_x \rangle$. Numerically the approach consists in diagonalizing the operator $\mu S_x + S_z^2$ for different μ 's. The resulting eigenvector associated to the smallest eigenvalue is the state of interest, which is used to evaluate the mean spin length $\langle S_x \rangle$ and the corresponding bound on the second moment $\langle S_z^2 \rangle$. If the experimentally determined spin variance is smaller than this bound, then there are more than k entangled particles in the system, and the procedure can be iterated with the next integer spins until the measured variance is above the bound. The case of half-integer spins (odd k) is more subtle, since the state minimizing $\langle S_z^2 \rangle$ is not minimizing $\text{Var}[S_z]$, and we will not discuss it here.

In Figure 4.3 we plot the minimum variance $\text{Var}[S_z]$ attainable for different k and $\langle S_x \rangle$, resulting in convex lines. Note that for a given point in the plot there is a minimum $S = k/2$ for which it is allowed. This provides a graphical method to find the entanglement depth of a many-body system, from given experimental data.

For a large spin $N \gg 1$ it is possible to derive [100] an analytical lower bound on $\text{Var}[S_z]$ as a function of $\langle S_x \rangle$, which reads (note there is a typo in Eq. (3) of [100])

$$\text{Var}[S_x] \geq \frac{1}{2} \left[S(S+1) - \langle S_z \rangle^2 - \sqrt{(S^2 - \langle S_z \rangle^2) ((S+1) - \langle S_z \rangle^2)} \right]. \quad (4.26)$$

These lines are also plotted in Fig. 4.3 for comparison with the exact, numerical, bounds. A discrepancy is visible for small values of k .

4. Quantum correlations: Theory

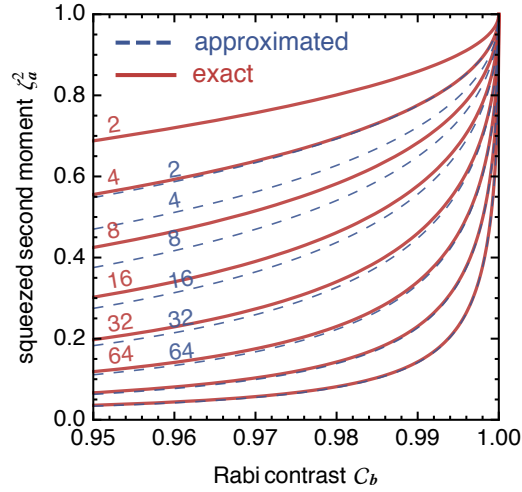


Figure 4.3: Entanglement depth. Exact (red, from Eq. 4.25 as explained in the text) and approximated (dashed blue, Eq. 4.26) k -producibility curves for $k = 2, 2^2, \dots, 2^8$. At least $k + 1$ -partite entanglement is confirmed by observing experimental data below a k -producibility curve.

4.4 EPR steering

As we did for entanglement, we want to provide experimentally testable criteria allowing to prove the steerability of a physical system. Note that in the work by EPR the degrees of freedom under investigation are perfectly (anti)correlated, allowing to predict with certainty the measurement result on one party, based on the result of the other party. In practical situations, observables might not be maximally correlated, resulting in an error on the predicted (inferred) quantity. Nevertheless, steering might still be possible if this error (quantified by the inferred variance) is small enough.

For the bipartite case a number of EPR criteria have been proposed, for both continuous and discrete variable cases [4]. These allowed to observe steering of light quadratures but found (almost) no application in massive particle systems. The multipartite case has also been investigated, but it will not be discussed here.

In this section we present an experimentally practical criterion allowing to conclude EPR steering in a bipartite system, that is known from the literature [4]. We focus on the discrete variable case where steering appears for the components of two macroscopic spins.

4.4.1 EPR steering criteria

The hypothetical experiment proposed by EPR involves the measurements of position and momentum on a pair of particles. Further theoretical investigations devised other possible experiments involving pairs of non-commuting observables, and therefore showing a paradoxical situation equivalent to one obtained by EPR. As an example, Bohm presented a discrete version of the paradox where a pair of spin-1/2 particles is in a state

correlated strongly enough to observe steering [101]. In our case, we are interested in the generalization of this scenario with two macroscopic spins, as discussed in Ref. [4].

We consider measurements of the (collective) spin operators \hat{S}^A and \hat{S}^B , associated to the parties A and B respectively. The underlying algebra imposes a non-trivial commutation relation for the spin components, *e.g.* $[\hat{S}_z^B, \hat{S}_y^B] = -i\hat{S}_x^B$, and therefore the uncertainty relation

$$\text{Var} [S_z^B] \text{Var} [S_y^B] \geq \frac{1}{4} |\langle S_x^B \rangle|^2 . \quad (4.27)$$

According to the EPR reasoning, if $|\langle S_x^B \rangle| \neq 0$ then S_z^B and S_y^B cannot be both associated to elements of reality, because they are non-commuting operators. However, we are going to show that their values could be predicted from a measurement on A , with an uncertainty product lower than the bound given by Eq. 4.27, raising a paradox.

When A and B are correlated, a measurement performed on A could be used to predict the result of a measurement on B . To first order, we may infer the value of (say) S_z^B from S_z^A using the best linear estimator

$$S_z^{B,\text{inf}} = q_z - g_z S_z^A , \quad (4.28)$$

where q_z and g_z are real coefficients. The inferred value deviates from the actual measurement result on B , by a typical error that is estimated with the inferred variance (which is independent of q_z)

$$\text{Var}_{\text{inf}} [S_z^B] = \text{Var} [S_z^{B,\text{inf}} - S_z^B] = \text{Var} [g_z S_z^A + S_z^B] . \quad (4.29)$$

The key idea behind an EPR criterion is that, if we believe that a measurement on B does not depend on a measurement on A , then the uncertainty principle constraints also the product of the inferred variances

$$\text{Var}_{\text{inf}} [S_z^B] \text{Var}_{\text{inf}} [S_y^B] \geq \frac{1}{4} |\langle S_x^B \rangle|^2 . \quad (4.30)$$

If this inequality is violated, *i.e.* if A can predict the measurement results for B better than what would be allowed by Eq. (4.30), then an EPR paradox is observed.

For later convenience, we express Eq. (4.30) as the relation [4, 102]

$$\mathcal{E}_{\text{EPR}}^{A \rightarrow B} = \frac{4 \text{Var}(g_z \hat{S}_z^A + \hat{S}_z^B) \text{Var}(g_y \hat{S}_y^A + \hat{S}_y^B)}{|\langle \hat{S}_x^B \rangle|^2} \geq 1 . \quad (4.31)$$

Comparing this EPR criterion Eq. (4.31) with the entanglement criterion Eq. (4.19) shows that both depend on the same product of inferred variances. The difference lies in the bound to which such product is compared. The fact that, for $|\langle \hat{S}_x^A \rangle| > 0$, the entanglement bound is always bigger than the EPR bound, $\left(|g_z g_y| |\langle \hat{S}_x^A \rangle| + |\langle \hat{S}_x^B \rangle| \right)^2 > |\langle \hat{S}_x^B \rangle|^2$, shows that detecting entanglement is less demanding than EPR steering. In fact, as was mentioned before, these two types of correlations are inequivalent, and entanglement is necessary but not sufficient for steering.

4. Quantum correlations: Theory

From Eq. (4.31) it is also evident that EPR steering is an asymmetric concept: if A can steer B , then not necessarily B can steer A . This shows a rather counterintuitive property of quantum correlations, according to which their strength can be asymmetric. This interesting property has been investigated both theoretically [84, 85, 103] and experimentally [104, 105] in optics.

The criterion Eq. (4.31) can be evaluated experimentally by measuring the collective spins of two distinguishable parties, like two spatially separated atomic ensembles. In the next chapter we will see that local spin measurements on an expanded BEC can violate this criterion (and therefore also the weaker entanglement criterion Eq. (4.31)), demonstrating for the first time EPR steering between two ensembles of massive particles.

4.5 Detection of Bell correlations

We want to provide experimentally testable criteria allowing to prove the nonlocality of a physical system. This task has been investigated in detail for the case of two qubits, and for few other simple systems [5], but it is in general very complicated. The complexity resides mostly in the exponential growth of the problem size as the number of degrees of freedom increases, and becomes soon prohibitive.

For the multipartite scenario we are interested in, the required description of the space of correlations cannot be complete. However, it has been shown that a limited amount of information can be sufficient to conclude the nonclassicality of the observed statistics of measurement outcomes [21]. This is a particularly interesting result because it shows the feasibility of detecting Bell correlations in experiments involving many-body systems.

Similarly to the case of entanglement, the multipartite scenario presents naturally also a rich variety of Bell correlated states. As an example, already in the tripartite scenario one can distinguish the case in which the entire system shares nonlocal correlations, from the case in which only two of the parties are in a nonlocal state. This raises the question of how to characterize different Bell correlated states.

In this section we present experimentally practical criteria allowing to conclude Bell correlations in multipartite systems [26, 28, 29], that have been developed as a part of this thesis based on the ideas of Ref. [21]. Moreover, we present a method to characterize multipartite nonlocal states in terms of their “depth”, *i.e.* according to the maximum number of parties that are described by a nonseparable state. This method was developed in collaboration with the groups of A. Acín and M. Lewenstein at ICFO [30].

4.5.1 Multipartite permutationally-invariant Bell inequalities

Local measurements on different quantum systems can display correlations that cannot be explained by any local hidden variable model (LHVM) [71] or, in other words, that cannot be reproduced by local deterministic strategies (LDS), even if assisted by shared randomness [106]. Bell inequalities bound the space of LHVM or “classical” correlations, and correlations that violate a Bell inequality are termed nonlocal. Beside their fundamental interest, nonlocal correlations are a resource that enables novel quantum information processing tasks [5].

From a geometrical point of view, LHVM correlations form a polytope in the space of correlations (or probabilities), *i.e.* a bounded convex set that can be described as the convex hull of a finite number of vertices, or equivalently as the intersection of a finite number of half-spaces. The vertices of the LHVM polytope correspond to LDS, while the half-spaces in which it is contained are defined by Bell inequalities. For this reason, finding all Bell inequalities gives a necessary and sufficient condition for deciding membership in the LHVM set. However, results in computer science indicate that this search is an extremely demanding problem [107], which is NP-complete even in the bipartite case [108]. Therefore, a complete list of Bell inequalities exists only for the simplest

4. Quantum correlations: Theory

scenarios; *e.g.* only up to 3 parties [109–113].

To characterize correlations in scenarios with a large number of parties, one necessarily has to relax the condition of membership in the LHVM set. This can be done by projecting the LHVM polytope onto the space of observables of a particular form, *e.g.* permutationally invariant (PI) [114], with low-order correlators [21, 115], or translationally invariant [116, 117].

We give here an overview of the approach followed by Tura *et al.* in Refs. [21, 115], to derive multi-partite Bell inequalities involving low-order, permutationally invariant, correlators. Restricting to such observables is particularly interesting for experiments on many-body systems, as they involve a reasonable amount of measurements of collective properties. Their results, based on two measurement per parties, have then been generalized to an arbitrary number of measurements in Ref. [29].

We consider a Bell scenario in which each of N observers (indexed by $i = 1 \dots N$) performs on their share of the system one out of d possible local measurements $\mathcal{M}_{x_i}^{(i)}$, labeled by $x_i = 0 \dots d - 1$. For simplicity, we assume that every measurement is dichotomic, giving as outcome a_i either $+1$ or -1 , keeping the generalization to an arbitrary number of outcomes for later. The correlations that can be observed are represented by the k -body correlators $\langle \mathcal{M}_{x_{i_1}}^{(i_1)} \dots \mathcal{M}_{x_{i_k}}^{(i_k)} \rangle$, with $k = 1, \dots, N$ and $1 \leq i_1 < \dots < i_k \leq N$. In the spirit of Refs. [21, 114, 115], we focus on permutationally invariant (PI) k -body correlators, defined as

$$\mathcal{S}_{x_1 \dots x_k} = \sum_{\substack{i_1, \dots, i_k=1 \\ \text{all } i\text{'s different}}}^N \langle \mathcal{M}_{x_{i_1}}^{(i_1)} \dots \mathcal{M}_{x_{i_k}}^{(i_k)} \rangle. \quad (4.32)$$

If the statistics observed through Eq. (4.32) satisfy a LHVM, it belongs to the so-called (symmetrized) LHVM polytope [114], denoted \mathbb{P}^S . Its vertices correspond to LDS, satisfying

$$\langle \mathcal{M}_{x_{i_1}}^{(i_1)} \dots \mathcal{M}_{x_{i_k}}^{(i_k)} \rangle = \langle \mathcal{M}_{x_{i_1}}^{(i_1)} \rangle \dots \langle \mathcal{M}_{x_{i_k}}^{(i_k)} \rangle \quad (\text{local}), \quad (4.33)$$

$$\langle \mathcal{M}_{x_i}^{(i)} \rangle = \pm 1 \quad \forall i, j \quad (\text{deterministic}). \quad (4.34)$$

As there are $m = 2^d$ possible LDS per party, Eq. (4.34) gives rise to an exponential number of vertices, 2^{dN} . However, the PI condition reduces them to at most $\binom{N+m-1}{m-1}$, a polynomial number in N , because only the amount of parties following the same LDS is relevant [21, 115]. For this reason, it is natural to introduce m variables $\vec{v} = (v_1, \dots, v_m)$, where v_i counts how many parties follow the i -th LDS. Note that the v_i satisfy

$$\sum_{i=1}^m v_i = N, \quad v_i \in \mathbb{Z}_{\geq 0}. \quad (4.35)$$

Using this parameterization, Eq. (4.32) can be written as a polynomial of degree k in m variables with real coefficients, *i.e.* $\mathcal{S}_{x_1 \dots x_k} \in \mathbb{R}[\vec{v}]_k$ [21]. Denoting with $\vec{\mathcal{S}}$ the vector

4.5 Detection of Bell correlations

of all such correlations, we express \mathbb{P}^S as the convex hull (CH) of \vec{S} evaluated on the parameter region defined by Eq. (4.35):

$$\mathbb{P}^S = \text{CH} \left\{ \vec{S}(\vec{v}) \text{ s.t. } \sum_i v_i = N, v_i \in \mathbb{Z}_{\geq 0} \right\}. \quad (4.36)$$

Dedicated algorithms [118, 119] exist to compute the dual description of \mathbb{P}^S , thus obtaining a minimal set of PI Bell inequalities. These inequalities are of the form

$$\sum_k \sum_{x_1 \leq \dots \leq x_k} \alpha_{x_1 \dots x_k} \mathcal{S}_{x_1 \dots x_k} + \beta_C \geq 0, \quad (4.37)$$

where $\alpha_{x_1 \dots x_k} \in \mathbb{R}$, and $\beta_C \in \mathbb{R}$ is the so-called classical bound. If an experiment violates inequality Eq. (4.37), the observed correlations cannot be reproduced by any LHM. In this case, we say that the system is Bell-correlated.

Unfortunately, since the dimension of \mathbb{P}^S scales as $\binom{d+N}{d} - 1$, one in practice cannot obtain a full set of Bell inequalities for $N > 5$ [114]. However, as it was shown in [21, 115], a small subset of the correlators in \vec{S} (namely, one- and two-body PI correlators) suffices to detect Bell correlations for arbitrarily large N . Therefore, we limit the number of components of \vec{S} to contain only up to K -body correlators, effectively projecting \mathbb{P}^S to a polytope \mathbb{P}_K^S living in a subspace of dimension $\binom{d+K}{d} - 1$, independent of N , whose vector of coordinates we denote \vec{S}_K . Still, for small values of K (e.g. 2, 3, ...) finding all PI Bell inequalities only works for few tens of particles in less than a month runtime. Hence, to study the large N regime one has to (i) infer classes of Bell inequalities and generalize them to arbitrary N and (ii) derive a proof of their β_C for each class. This is the approach that has been used in [21, 29], to derive the following inequalities.

In the case $K = 2$ and $d = 2$, a relevant Bell inequality is

$$2\mathcal{S}_0 + \frac{1}{2}\mathcal{S}_{00} + \mathcal{S}_{01} + \frac{1}{2}\mathcal{S}_{11} + 2N \geq 0. \quad (4.38)$$

This expression shows a quantum violation that increases asymptotically with N , relative to the classical bound.

The inequality Eq. (4.38) has also been generalized to the case where each party can perform m different measurements, resulting in the expressions

$$\sum_{x_1=0}^{m-1} (m - 2x_1 - 1) \mathcal{S}_{x_1} + \frac{1}{2} \sum_{x_1, x_2} \mathcal{S}_{x_1 x_2} + \left\lfloor \frac{m^2 N}{2} \right\rfloor \geq 0, \quad (4.39)$$

where $\lfloor x \rfloor$ is the the largest integer smaller or equal to x . Note that when $m = 2$, inequality Eq. (4.39) does not reduce to Eq. (4.38).

4.5.2 Bounding the set of classical correlations

As mentioned before, the study of correlations in many-body scenarios requires to relax the membership condition in the LHM set, which can be done by projecting the

4. Quantum correlations: Theory

LHVM polytope onto a particular space of observables. However, even in these low dimensional spaces, the complexity of the commonly adopted method (going from the vertices description of the polytope, to the dual half-spaces description) [120] still prohibits one to obtain all Bell inequalities for many-body scenarios. Therefore, for large N one has to infer and prove classes of Bell inequalities. This approach was successfully adopted in Refs. [21, 29], allowing to derive Eq. (4.38) and Eq. (4.39). Nevertheless, as more inequalities appear as N increases, this procedure may leave potentially more useful classes unnoticed if they do not show up for sufficiently small N .

In this section, we present a technique to approximate the set of symmetric LHVM correlations, \mathbb{P}_K^S , from the outside, overcoming the above limitations. This technique is based on a hierarchy of semidefinite programs (SdP's), approximating convex hulls of semialgebraic sets [121–124], and it can be seen as checking all Bell inequalities of a specific form with a single test. Contrary to other existing SdP's hierarchies [125, 126], the size of our SdP's are independent of the number of parties, and the hierarchy shows convergence already after few levels. This work, which was carried out as part of this thesis in collaboration with J. Tura, is published in [28].

Our method constitutes an efficient sufficient condition for a set of correlations to be nonlocal, and it naturally provides a Bell inequality that they violate. It is based on two mild relaxations described in the following, yielding a hierarchy of conditions satisfied by all LHVM correlations.

First relaxation

According to Eq. (4.36), \mathbb{P}^S is defined as the convex hull of a finite set of points, therefore not exploiting the inherent algebraic structure present in the polynomials $\vec{S}(\vec{v})$. Similarly, the same observation holds for \mathbb{P}_K^S , the projection of \mathbb{P}^S into the space of at most K -body correlators defined by the coordinates \vec{S}_K . The first relaxation we introduce consists in dropping the condition $v_i \in \mathbb{Z}_{\geq 0}$, and consider instead $v_i \in \mathbb{R}_{\geq 0}$, which gives rise to the set

$$\widetilde{\mathbb{P}}_K^S = \text{CH} \left\{ \vec{S}_K(\vec{v}) \text{ s.t. } \sum_i v_i = N, v_i \in \mathbb{R}_{\geq 0} \right\}. \quad (4.40)$$

Note that $\vec{S}_K(\vec{v})$ with $\vec{v} \in \mathbb{R}^m$ interpolates the vertices of \mathbb{P}_K^S , implying $\mathbb{P}_K^S \subseteq \widetilde{\mathbb{P}}_K^S$. As a consequence, if a set of correlations lies outside $\widetilde{\mathbb{P}}_K^S$, it also lies outside \mathbb{P}_K^S , and therefore it is nonlocal.

Since \vec{v} has $m - 1$ free parameters, and \vec{S}_K has $\binom{d+K}{d} - 1$ components, $\vec{S}_K(\vec{v})$ can be expressed as a set of equations $f_i(\vec{S}_K) = 0$, where $1 \leq i \leq \binom{d+K}{d} - m$. The non-negativity constraints $v_j \geq 0$ can also be expressed as a set of m constraints in \vec{S}_K , by a set of inequalities $g_j(\vec{S}_K) \geq 0$ (see the example). In what follows, we refer to the set of solutions of a system of polynomial equations $f_i(\vec{S}_K) = 0$ as an algebraic set. Moreover, if an algebraic set is further restricted by polynomial non-

negativity constraints $g_j(\vec{\mathcal{S}}_K) \geq 0$, as it is the case for $\widetilde{\mathbb{P}}_K^{\mathcal{S}}$ in Eq. (4.40), we shall call such a set semialgebraic.

Second relaxation

Deciding membership in the CH of a (semi)algebraic set \mathcal{V} is NP-hard [123]. However, there exist efficient approximations for $\text{CH}(\mathcal{V})$ from the outside [121–124]. The idea behind these methods is to reduce the membership problem in $\text{CH}(\mathcal{V})$ to that of a multivariate polynomial being non-negative, which can be relaxed to determining whether such polynomial can be expressed as a sum of squares (s.o.s.)². While the first condition is NP-hard, the second can be efficiently checked using a SdP, as we are going to show.

Following this approach, the main idea behind our method is to construct linear polynomials $l(\vec{\mathcal{S}}_K) \in \mathbb{R}[\vec{\mathcal{S}}_K]_1$ satisfying $l(\vec{\mathcal{S}}_K) \geq 0$ for all $\vec{\mathcal{S}}_K \in \mathcal{V}$, *i.e.* valid Bell inequalities defining half-spaces containing $\text{CH}(\mathcal{V})$.

Starting from the observation that every polynomial of the form $p + \sum_i f_i p_i$, with $p, p_i \in \mathbb{R}[\vec{\mathcal{S}}_K]$, takes the same values when evaluated in \mathcal{V} (because $f_i(\vec{\mathcal{S}}_K) = 0$ for all $\vec{\mathcal{S}}_K \in \mathcal{V}$), we define the ideal I generated by f_i as the set

$$I = \left\{ \sum_i f_i p_i \text{ s.t. } p_i \in \mathbb{R}[\vec{\mathcal{S}}_K] \right\} \subseteq \mathbb{R}[\vec{\mathcal{S}}_K], \quad (4.41)$$

such that every polynomial in $p + I = \{p + q, q \in I\}$ is equivalent when evaluated in \mathcal{V} . Moreover, the ideal I defines the set of equivalence classes $\mathbb{R}[\vec{\mathcal{S}}_K]/I$, where $p, q \in \mathbb{R}[\vec{\mathcal{S}}_K]$ are in the same class if they are equivalent *modulo* I , *i.e.* $p \equiv q \pmod{I}$, meaning that $p - q \in I$.

To express $l(\vec{\mathcal{S}}_K)$ we consider the following *ansatz*:

$$l(\vec{\mathcal{S}}_K) = \sum_{i=0}^m g_i(\vec{\mathcal{S}}_K) \sigma_i(\vec{\mathcal{S}}_K) \pmod{I}, \quad (4.42)$$

where $g_0(\vec{\mathcal{S}}_K) = 1$, and $\sigma_i(\vec{\mathcal{S}}_K)$ are s.o.s. polynomials *modulo* I (*i.e.* there exists a s.o.s. polynomial in $\sigma_i(\vec{\mathcal{S}}_K) + I$). For compactness, let us use the shorthand notation g_i and σ_i . Note that since all $g_i \geq 0$ in \mathcal{V} by definition, and s.o.s. are non-negative, the form of Eq. (4.42) ensures the non-negativity of $l(\vec{\mathcal{S}}_K)$ in \mathcal{V} ,³.

Now, given a point $\vec{\mathcal{S}}_K^*$, our goal is to prove that $l(\vec{\mathcal{S}}_K^*) < 0$ for some σ_i . If we succeed in this proof, then we have to conclude that $\vec{\mathcal{S}}_K^* \notin \text{CH}(\mathcal{V}) \supseteq \mathbb{P}_K^{\mathcal{S}}$, *i.e.* that the statistics in $\vec{\mathcal{S}}_K^*$ come from nonlocal correlations.

For computational reasons, we need to bound the maximum degree of the s.o.s. decomposition allowed in $\sigma_i + I$. The higher the degree, the larger the family of $l(\vec{\mathcal{S}}_K)$ that

²Obviously, every s.o.s. polynomial is non-negative, but the converse is false in general. The textbook counter-example is the Motzkin polynomial, $x^4 y^2 + x^2 y^4 - 3x^2 y^2 + 1$, which is non-negative on \mathbb{R}^2 but it is not a s.o.s. of elements of $\mathbb{R}[x, y]$.

³The *modulo* I in Eq. (4.42) allows to reduce the degree of $l(\vec{\mathcal{S}}_K)$, potentially arriving to a linear polynomial.

4. Quantum correlations: Theory

can be accessed through Eq. (4.42), but the more computationally expensive to produce such s.o.s. representation will be. This naturally yields a hierarchy of outer approximations to $\text{CH}(\mathcal{V})$ by increasing the degree of the s.o.s. decomposition of σ_i . To simplify our exposition, we consider here the special case where all $\sigma_i = \sigma$.

To express all σ that are s.o.s. of degree 2μ , *modulo* I , we adopt the following procedure. First, we select (via a Gröbner basis [127]) a linearly independent set of representatives of $\mathbb{R}[\vec{\mathcal{S}}_K]/I$, and we order them in the vector $\vec{b} = (1, \mathcal{S}_0, \mathcal{S}_1, \dots)^T$. Denoting by \vec{b}_μ the vector of elements of \vec{b} of degree at most μ , we write $\sigma = \sum_j s_j^2 \text{mod } I$, where s_j are linear combinations of the elements of \vec{b}_μ ; *i.e.* $s_j = \vec{b}_\mu^T \vec{a}_j$, with \vec{a}_j real vectors. At this point, by defining the matrix $G = \sum_j \vec{a}_j \vec{a}_j^T$, which is positive semi-definite by construction ($G \succeq 0$), and the moment matrix $\Gamma_i = g_i \vec{b}_\mu \vec{b}_\mu^T \text{mod } I$, we write

$$g_i \sigma = \Gamma_i \cdot G \text{ mod } I, \quad G \succeq 0. \quad (4.43)$$

Here $X \cdot Y = \sum_{ab} X_{ab} Y_{ab}$.

When the elements of Γ_i corresponding to $\vec{\mathcal{S}}_K$ are replaced by $\vec{\mathcal{S}}_K^*$, only some of its entries are constrained. If the remaining free parameters can be tuned to make $\Gamma_i \succeq 0$, Eq. (4.43) ensures that $g_i \sigma \geq 0$ in $\vec{\mathcal{S}}_K^*$ for all σ (that are s.o.s. of degree 2μ , *modulo* I). On the other hand, when $\Gamma_i \not\succeq 0$ for any choice of the free parameters, there exists at least one σ such that $g_i \sigma < 0$ in $\vec{\mathcal{S}}_K^*$ ⁴.

Recall here that our final goal is to prove that there exist a σ such that Eq. (4.42) gives $l(\vec{\mathcal{S}}_K^*) < 0$. To this end, we write Eq. (4.42) as $l(\vec{\mathcal{S}}_K) = \tilde{\Gamma} \cdot \tilde{G} \text{ mod } I$, where $\tilde{\Gamma} = \bigoplus_{i=0}^m \Gamma_i$, and similarly for \tilde{G} . As for Eq. (4.43), we ask whether $\tilde{\Gamma}$ can be made positive semi-definite at the point $\vec{\mathcal{S}}_K^*$. To perform this check with a SdP, we first reduce $\tilde{\Gamma}$ *modulo* I , and then linearize it as

$$\tilde{\Gamma} = \sum_j y_j \tilde{\Gamma}_j, \quad (4.44)$$

where y_j indexes the j -th element of \vec{b} , and $\tilde{\Gamma}_j$ are constant real matrices embodying the constraints among the entries of $\tilde{\Gamma}$. Now, for the point $\vec{\mathcal{S}}_K^*$, we write the SdP

$$\begin{aligned} \max_{y_j \in \mathbb{R}} \quad & 1 \\ \text{s.t.} \quad & \tilde{\Gamma} \succeq 0 \\ & y_0 = 1 \\ & y_j = (\vec{\mathcal{S}}_K^*)_j \end{aligned} \quad (4.45)$$

where y_0 and the y_j corresponding to $\vec{\mathcal{S}}_K^*$ are fixed, while the other y_j are free real parameters that can be varied until the condition $\tilde{\Gamma} \succeq 0$ is fulfilled.

If SdP (4.45) is infeasible, $\tilde{\Gamma} \not\succeq 0$ independently on the free y_j , which proves that there exist a σ such that $l(\vec{\mathcal{S}}_K^*) < 0$. Therefore, infeasibility of (4.45) certifies that $\vec{\mathcal{S}}_K^* \notin \text{CH}(\mathcal{V}) \supseteq \mathbb{P}_K^S$, *i.e.* its nonlocal nature (see the example and Fig. 4.5).

⁴For a detailed proof, see the proof of Theorem 5.1 in [124]

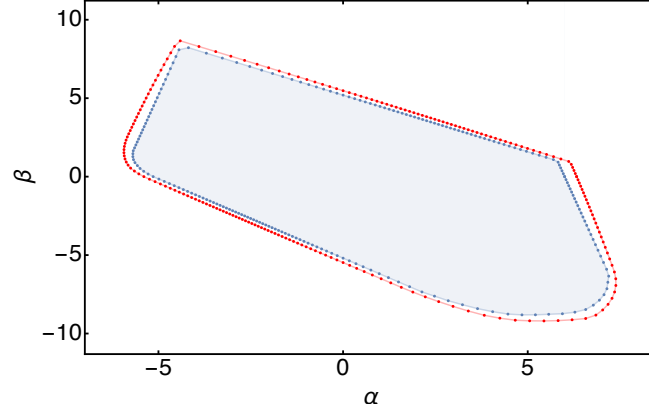


Figure 4.4: For $N = 10$ and $K = 2$, the plane of the symmetric correlations of the form $\alpha\vec{\mathcal{S}}_2^{(1)} + \beta\vec{\mathcal{S}}_2^{(2)}$, with $\vec{\mathcal{S}}_2^{(1)} = (1, -1, 0, -1, 1)^T/\sqrt{4}$ and $\vec{\mathcal{S}}_2^{(2)} = (0, -1, -1, 1, 0)^T/\sqrt{3}$. In blue, the intersection of $\mathbb{P}_2^{\mathcal{S}}$ with the plane, computed with a linear program. In red, the boundary of the feasible set of SdP (4.45) for $\mu = 1$. The gap between the two objects is imputable mainly to the first relaxation, and the small N was chosen also to appreciate its size, which remains of the same order while $\mathbb{P}_2^{\mathcal{S}}$ increases with N (see also Fig. 4.5)

While the output of SdP (4.45) is the answer feasible/infeasible, we can also write a SdP to maximize λ subject to $y_0 = 1$ and $y_j = \lambda(\vec{\mathcal{S}}_K^*)_j$. The dual formulation of this modified SdP results in the dual variables $\alpha_{j_1 \dots j_k}$ associated to $y_1 \dots y_i$, and β_C associated to y_0 , defining a Bell inequality (4.37) that can be used to certify the nonlocality of $\vec{\mathcal{S}}_K^*$ ⁵ (see the example and Fig. 4.5). In addition, maximizing λ along different directions $\vec{\mathcal{S}}_K^*$ results in the points $\lambda_{\max}\vec{\mathcal{S}}_K^*$ that can be used to approximate the boundary of $\mathbb{P}_K^{\mathcal{S}}$, (see Fig. 4.4).

On the other hand, if SdP (4.45) is feasible it means that it does not exist a σ that is s.o.s. of degree 2μ , modulo I , such that $l(\vec{\mathcal{S}}_K^*) < 0$. In this case, we could access a higher level of our hierarchy by increasing μ , which enlarges the class of $l(\vec{\mathcal{S}}_K^*)$ to be tested⁶.

An additional result in [121, 122] ensures that, since the variety \mathcal{V} we want to approximate is compact, our hierarchy converges at least asymptotically to $\text{CH}(\mathcal{V})$. Actually, in all examples we studied, we observed numerically that convergence at $\mu = 1$ was already present.

Example. – In the spirit of [21, 26], we consider $d = K = 2$, giving rise to the set of correlators $\vec{\mathcal{S}}_2 = (\mathcal{S}_0, \mathcal{S}_1, \mathcal{S}_{00}, \mathcal{S}_{01}, \mathcal{S}_{11}) \in \mathbb{R}^5$, and N parties. In this scenario, there are four LDS parameterized by $x_i \geq 0$ and satisfying $\sum_{i=1}^4 v_i = N$. By expressing the

⁵See Section 3.1 of [126] and, for a detailed derivation, Section 4.2 of [123]

⁶Note that the matrix $\tilde{\Gamma}$ for the level μ , is a minor of the matrix $\tilde{\Gamma}'$ for the level $\mu' > \mu$. Therefore, if $\tilde{\Gamma}' \succeq 0$ then necessarily $\tilde{\Gamma} \succeq 0$, while the converse is not always true.

4. Quantum correlations: Theory

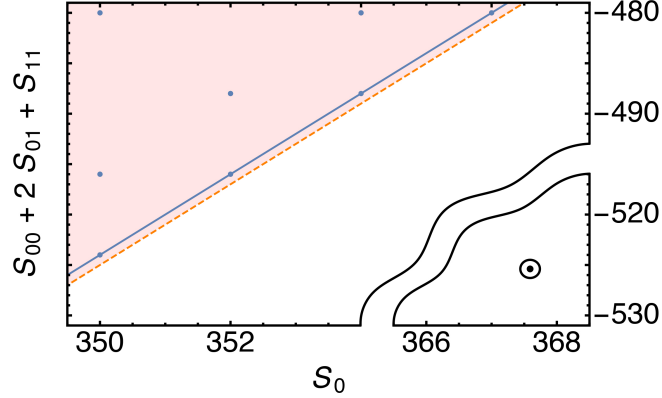


Figure 4.5: Plane generated by $\{S_0, (S_{00} + 2S_{01} + S_{11})\}$. Black circled dot, point $(367.6, -525.4)$ measured experimentally in [26] for $N = 476$. Blue points, projected vertices of \mathbb{P}_2^S . Blue line, bound given by the Bell inequality $-2S_0 + (S_{00} + 2S_{01} + S_{11})/2 + 2N \geq 0$, from [21, 26]. This inequality is tight, meaning that it is also a facet of the projected polytope. Pink region, points where SdP (4.48) gives $\lambda \geq 1$. Orange dashed line, Bell inequality obtained numerically by solving the dual of SdP (4.48). The distance between the blue and the orange lines is 1.000002, meaning that the error of our method compared to the tight classical bound scales as $1/N$, and it is imputable mainly to the first relaxation.

correlators \vec{S}_2 evaluated on a LDS in terms of \vec{v} , we obtain [21]

$$\begin{pmatrix} N \\ S_1 \\ S_0 \\ \mathcal{Z} \end{pmatrix} = \begin{pmatrix} v_1 + v_2 + v_3 + v_4 \\ v_1 + v_2 - v_3 - v_4 \\ v_1 - v_2 + v_3 - v_4 \\ v_1 - v_2 - v_3 + v_4 \end{pmatrix}, \quad (4.46)$$

$$\begin{pmatrix} S_{00} \\ S_{01} \\ S_{11} \end{pmatrix} = \begin{pmatrix} S_0^2 - N \\ S_0 S_1 - \mathcal{Z} \\ S_1^2 - N \end{pmatrix}. \quad (4.47)$$

When N is fixed Eqs. (4.46) are three free parameters, while Eqs. (4.47) define the ideal I , whose $\binom{d+K}{d} - m = 2$ generators $\{f_1(\vec{S}_2), f_2(\vec{S}_2)\} = \{S_{00} - S_0^2 + N, S_{11} - S_1^2 + N\}$ form also a Gröbner basis for I . Inverting Eq. (4.46) we obtain four polynomials in \vec{S}_2 that allow to express the constraints $v_i = g_i(\vec{S}_2) \geq 0$; *e.g.*

$$g_1(\vec{S}_2) = (S_0 + S_1 + (S_0 S_1 - S_{01}) + (S_0^2 - S_{00}))/4 \geq 0.$$

At the first level of our hierarchy, $\mu = 1$, the vector $\vec{b}_1^T = (1, S_0, \dots, S_{11})$ generates the five 6×6 moment matrices Γ_i . Combined together, the Γ_i give a 30×30 block-diagonal moment matrix $\tilde{\Gamma}$, in which N appears as a parameter, and thus not affecting its size.

Considering our experimental data presented in Ref. [26] (see also chapter 5), we can conclude that the measured statistics $(S_0^*, S_{00}^* + 2S_{01}^* + S_{11}^*) = (367.6, -525.4)$

contain Bell correlations because the following SdP gives $\lambda < 1$:

$$\begin{aligned}
& \max_{y_j \in \mathbb{R}} \lambda \\
& \text{s.t. } \tilde{\Gamma} \preceq 0 \\
& \quad y_0 = 1 \\
& (y_1, y_3 + 2y_4 + y_5) = \lambda(\mathcal{S}_0^*, \mathcal{S}_{00}^* + 2\mathcal{S}_{01}^* + \mathcal{S}_{11}^*)
\end{aligned} \tag{4.48}$$

The dual of SdP (4.48) gives as result the dual variables associated to y_0 , y_1 and $y_3 + 2y_4 + y_5$, which correspond respectively to the coefficients of the Bell inequality $\beta_C + \alpha_1 \mathcal{S}_0 + \alpha_2 (\mathcal{S}_{00} + 2\mathcal{S}_{01} + \mathcal{S}_{11}) \geq 0$, (see Fig. 4.5).

As a generalization of this method, it is possible to consider the case where measurements have more outcomes by defining the expectation values as *e.g.* $\langle \mathcal{M}_{x_i}^{(i)} \rangle^{(a)} = 2P_i(a|x) - 1$, where $P_i(a|x)$ is the probability that measurement x on party i gives as outcome a , and the symmetrized correlators as *e.g.* $\mathcal{S}_x^{(a)} = \sum_{i=1}^N \langle \mathcal{M}_{x_i}^{(i)} \rangle^{(a)}$.

To summarize, we presented a method to bound the set of LHM correlations from the outside. Its main advantage, with respect to other techniques, is that there is no scaling with the number of parties, making it particularly suited for the study of Bell correlations in many-body systems. Our approach has several applications, some of which were presented here, such as the characterization of experimentally observed correlations or the derivation of new Bell inequalities. Furthermore, it can be easily generalized to scenarios with more measurements settings and outcomes, potentially enlarging the class of systems and states where Bell correlations could be experimentally detected.

4.5.3 Bell correlations depth

In collaboration with several researcher at ICFO we developed a method to quantify the depth of Bell correlations in a many-body system. In this section we present a summary of what can be found in Ref. [30].

The violation of a Bell inequality signals the presence of Bell correlations. However, as it is the case for entanglement, in multi-partite scenarios the question arise of how different Bell correlated states are classified. To give a partial answer to this question, we propose a method to quantify the depth of nonlocality, *i.e.* the number of particles sharing genuinely nonlocal correlations. This is a challenging task, as known inequalities for genuine nonlocality are based on N -order correlators, they require an individual addressing of parties, and a number of measurement settings scaling exponentially with the number of parties. For this reason, we follow the approach of the previous paragraph, and focus on inequalities with up to two-body permutationally invariant correlators.

To begin with an example, in a system with three particles the nonlocality condition $P(a, b|x, y) \neq \int d\lambda p(\lambda) P(a|x, \lambda) P(b|y, \lambda)$ formulated by Bell is generalized as

$$P(a, b, c|x, y, z) \neq \int d\lambda p(\lambda) P(a|x, \lambda) P(b|y, \lambda) P(c|z, \lambda) . \tag{4.49}$$

However, as Svetlichny pointed out [128], observing a joint probability $P(a, b, c|x, y, z)$ irreducible in the form of Eq. (4.49) still leaves open the possibility of a decomposition

4. Quantum correlations: Theory

in the form of *e.g.*

$$P(a, b, c|x, y, z) = \int d\lambda p(\lambda) P(a, b|x, y, \lambda) P(c|z, \lambda), \quad (4.50)$$

(or with any other cyclic permutation of a, b, c, x, y, z). This expression represents the situation where only two out of the three parties in the system share nonlocal correlations. As a concrete example, the state $(1/\sqrt{2})(|00\rangle + |11\rangle) \otimes |0\rangle$, that is the product of the maximally entangled state of two qubits with some additional state, and the GHZ state $(1/\sqrt{2})(|000\rangle + |111\rangle)$ are both nonlocal, however, while the former has only two-body nonlocality, the latter shows nonlocality among all parties. Observing a negation of all possible decompositions of the form Eq. (4.50) is more demanding than Eq. (4.49), establishing a hierarchy that could serve to characterize nonlocality in a three-body system. Proving that nonlocal correlations exist among all particles in the system is called genuine multipartite nonlocality, and it is the strongest known form of correlation.

This idea has been generalized to multi-partite scenarios, and a number of approaches to classify different types of nonlocality have been proposed [129, 130]. Following the approach of [130], we choose here the notion of nonlocality depth (or k -producibility of nonlocality), which is similar to the approach adopted to quantify multipartite entanglement (see Refs. [131]). In few words, we are looking for inequalities whose violation certify that the observed statistics cannot be explained by groups of k particles sharing some specific resources.

To find inequalities allowing to quantify the depth of nonlocality, we proceed in the following way. We partition the set of parties $I = \{1, \dots, N\}$ into L pairwise-disjoint non-empty subsets \mathcal{A}_i , each containing at most k parties, and call it L_k -partition of I . We call the correlations $\{P(\mathbf{a}|\mathbf{x})\}$ k -producible with respect to the given L_k -partition if they admit the following decomposition

$$P(\mathbf{a}|\mathbf{x}) = \int d\lambda p(\lambda) P_1(\mathbf{a}_{\mathcal{A}_1}|\mathbf{x}_{\mathcal{A}_1}, \lambda) \dots P_L(\mathbf{a}_{\mathcal{A}_L}|\mathbf{x}_{\mathcal{A}_L}, \lambda) \quad (4.51)$$

where $\mathbf{a}_{\mathcal{A}_i}$ and $\mathbf{x}_{\mathcal{A}_i}$ are the respectively the outcomes and the measurements choices corresponding to the parties belonging to \mathcal{A}_i .

The probability distributions $P_i(\mathbf{a}_{\mathcal{A}_i}|\mathbf{x}_{\mathcal{A}_i}, \lambda)$ appearing in Eq. (4.51) must be constrained to the specific resources available to the partitions. In our case, we choose these probabilities to satisfy the no-signaling condition (4.52). No-signaling expresses the notion that faster-than-light communication between different parties is not possible, *i.e.*

$$\sum_{a_i} P(a_1, \dots, a_i, \dots | x_1, \dots, x_i, \dots) = \sum_{a_i} P(a_1, \dots, a_i, \dots | x_1, \dots, x'_i, \dots) \quad (4.52)$$

for all a 's, x 's, x'_i . Concretely, Eq. (4.52) tells that the marginal probability for a set of particles not including the i -th, $P(a_1, \dots, a_{i-1}, a_{i+1}, \dots | x_1, \dots, x_{i-1}, x_{i+1}, \dots)$, does not depend on the measurement setting x_i for particle i , which has to be expected if the latter is space-like separated from the others. Another more restrictive choice would be

to assume that each partition shares quantum correlations, which will be explored in a future work.

The decomposition Eq. (4.51) assumes a specific L_k -partition of the system. However, we would like to know whether the observed probabilities could be explained by any possible L_k -partition with a fixed k . For this reason, we define the probabilities $\{P(\mathbf{a}|\mathbf{x})\}$ to be k -producible if they can be written as a convex combination of correlations that are k -producible with respect to different L_k -partitions, *i.e.*

$$P(\mathbf{a}|\mathbf{x}) = \sum_{l \in \mathcal{L}_k} q_l P_l(\mathbf{a}|\mathbf{x}) \quad (4.53)$$

where \mathcal{L}_k is the set of all L_k -partitions and $P_l(\mathbf{a}|\mathbf{x})$ are correlations that admit the decomposition (4.51) with respect to the k -partition l . The minimal k for which the correlations $\{P(\mathbf{a}|\mathbf{x})\}$ are of the form (4.53) is called nonlocality depth (with respect to nonsignaling resources). Correlations whose nonlocality depth is k are (genuinely) k -partite nonlocal, as there must exist a subset of k parties which share nonsignaling correlations that are genuinely nonlocal [128].

Let us notice that in the particular case of $k = 1$ there is only one, up to permutations, L_1 -partition: each party forms a singleton $\mathcal{A}_i = \{A_i\}$ ($i = 1, \dots, N$), and the definition of fully local correlations is recovered. Then, on the other extreme of $k = N$, we have correlations in which all parties share nonlocality and are thus called genuinely multipartite nonlocal (GMNL).

Geometrically, as in the case of LHV, the sets of k -producible correlations form polytopes which we denote $\mathcal{P}_{N,k}$. Thanks to this fact, in order to detect the nonlocality depth of given correlations one can follow the standard procedure used to reveal nonlocality: construct Bell-like inequalities that constrain $\mathcal{P}_{N,k}$. The violation of one of these implies that $\{P(\mathbf{a}|\mathbf{x})\}$ is at least genuinely $k + 1$ -nonlocal, or, in other words, that these correlations have nonlocality depth of at least $k + 1$. The vertices of $\mathcal{P}_{N,k}$ are product probability distributions of the form

$$P(\mathbf{a}|\mathbf{x}) = P_1(\mathbf{a}_{\mathcal{A}_1}|\mathbf{x}_{\mathcal{A}_1}) \cdot \dots \cdot P_L(\mathbf{a}_{\mathcal{A}_L}|\mathbf{x}_{\mathcal{A}_L}) \quad (4.54)$$

with each $P_i(\mathbf{a}_{\mathcal{A}_i}|\mathbf{x}_{\mathcal{A}_i})$ being a vertex of the corresponding $|\mathcal{A}_i|$ -partite nonsignaling polytope, with $|\mathcal{A}_i| \leq k$ for all i . If for some i , $|\mathcal{A}_i| = 1$, then $P_i(\mathbf{a}_{\mathcal{A}_i}|\mathbf{x}_{\mathcal{A}_i}) \equiv P_i(a_i|x_i)$ is simply a deterministic probability distribution, *i.e.*, $P_i(a_i|x_i) \in \{0, 1\}$ for all values of x_i . In order to construct all vertices of $\mathcal{P}_{N,k}$ one needs to consider all L_k -partitions in Eq. (4.54). It thus follows that one needs to know the vertices of the p -partite nonsignaling polytopes \mathcal{NS}_p for all $p \leq k$.

At this point, following the idea behind Eq. (4.38), we are interested in understanding whether one- and two-body PI correlators, \mathcal{S}_{x_1} and $\mathcal{S}_{x_1 x_2}$, are sufficient to measure the depth of nonlocality in a many-body system. Therefore, we project the polytope $\mathcal{P}_{N,k}$ onto the space of such correlators, and obtain the two-body symmetric polytope of k -producible correlations $\mathcal{P}_{N,k}^{2,S}$. In the scenario with two measurement settings per party, this polytope is constrained by inequalities of the form

$$\mathcal{I} \equiv \alpha \mathcal{S}_0 + \beta \mathcal{S}_1 + \frac{\gamma}{2} \mathcal{S}_{00} + \delta \mathcal{S}_{01} + \frac{\varepsilon}{2} \mathcal{S}_{11} \geq -\beta_C^k. \quad (4.55)$$

4. Quantum correlations: Theory

The constant β_C^k is the maximal value of \mathcal{I} over all correlations belonging to $\mathcal{P}_{N,k}^{2,S}$. In practice, as the latter is a polytope, it is enough to find the minimal value of \mathcal{I} over all its vertices in order to determine β_C^k .

For $k = 1$, Eq. (4.55) reproduces the two-body symmetric Bell inequalities introduced in [21], *e.g.* Eq. (4.38). Our aim here is to go beyond this case, and find inequalities valid for $k > 1$ and any N . Unfortunately, despite the fact that for any k and N the polytope $\mathcal{P}_{N,k}^{2,S}$ lives in a five-dimensional real space, its vertices and facets are unknown.

In Ref. [30] we address this problem, and we introduced a general description of all the vertices of the projected k -nonlocal polytope in the two-body symmetric space, which is in principle valid for any value of N and $k \leq N$. However, this description requires the knowledge of (i) all the vertices of the symmetrized local polytope for p parties, with $p = 1, \dots, k$, and (ii) all the nonlocal vertices of the projections of p -partite nonsignaling polytopes \mathcal{NS}_p onto the two-body symmetric space, for $p = 1, \dots, k$, which we denote $\mathcal{NS}_p^{2,S}$. This is overall a very complicated task, especially for the complexity of computing the vertices of $\mathcal{NS}_p^{2,S}$, and, for this reason, we were not able to go beyond $k = 6$.

With the lists of vertices of $\mathcal{P}_{N,k}^{2,S}$ available, we derived the corresponding complete set of inequalities defining its facets [30]. This can be done by solving the convex hull problem, which is implemented in softwares such as CDD [119]. Thanks to the low dimension of the space, we were able to solve this problem for scenarios involving up to $N = 12$ parties.

In particular, since our inequalities can test against k -producibility with $k \leq 6$, we can identify all the symmetric two-body inequalities that detect genuine multipartite nonlocality (GMNL) for systems of $N \leq 7$ particles (see Ref. [30] for the complete lists). Interestingly, we find that no inequality of such kind can be violated by quantum mechanics in the tripartite case. That is, symmetric two-body correlations provide not enough information to detect GMNL in three-partite quantum states. This is no longer the case with four parties, for which we find an inequality which is violated by quantum mechanics, therefore allowing to detect GMNL.

Of particular interest is the observation that our lists of inequalities sometimes contain also expressions in the form of Eq. (4.38), but with a classical bound that depends on degree of nonlocality depth that one is interested to detect. This implies that nonlocality depth can be inferred from the amount of quantum violation observed in a single inequality, which is appealing for experimental investigations. For this reason, we focus on the expression

$$2\mathcal{S}_0 + \frac{1}{2}\mathcal{S}_{00} + \mathcal{S}_{01} + \frac{1}{2}\mathcal{S}_{11} + \beta_C^k \geq 0, \quad (4.56)$$

and determine β_C^k for different k and any number of parties, such that the inequality is satisfied for all correlations belonging to $\mathcal{P}_{N,k}^{2,S}$. The bounds we find are

k	β_C^k
1	$2N$
2	$2N$
3	$2N$
4	$(2 + \frac{2}{49}) N + \frac{1}{2}$
5	$(2 + \frac{8}{121}) N + \frac{1}{2}$
6	$(2 + \frac{1}{12}) N + \frac{1}{2}$

(4.57)

By performing a numerical check, it is easy to show that these inequalities can be violated by quantum mechanics. The strategy consists in computing the minimal eigenvalue of the Bell operator associated to Eq. (4.56), which can be constructed following the procedure presented in [115].

To summarize, the expression Eq. (4.56), with the bounds given in the table, consists in a set of Bell inequalities allowing to detect k -partite nonlocality. This shows that two-body symmetric correlations are enough to distinguish the depth of Bell correlations for any number of parties.

As a future direction to investigate, it would be interesting to derive inequalities that test for Bell correlation depth higher than 6, as it is already possible for entanglement. In particular, it would be interesting to find inequalities confirming genuine Bell correlations in many-body systems, without relying on parity measurements.

Another possible research direction would be to consider inequalities involving more than two settings per party. The resulting witness could still only involve two measurement directions and provide improved bounds. In particular, it would be interesting to find the k -nonlocality bounds for the family of inequalities in Ref. [29] admitting an arbitrary number of settings.

4.5.4 Witnessing Bell correlations and their depth

To experimentally test the multipartite Bell inequalities we presented one needs to measure terms like $\langle \mathcal{M}_0^{(i)} \mathcal{M}_1^{(j)} \rangle$ entering into *e.g.* S_{01} . In practice, this means that individual addressing of the particles is needed, which is an experimentally challenging task that seems unfeasible for most systems if the number of parties is already above few tens. In fact, in many-body systems it is usually more practical to measure collective observables, like magnetization, and their fluctuations. For this reason, we propose to replace the Bell inequalities, which do not rely on assumptions neither on the state nor on the measurements, by Bell correlation witnesses assuming that the measurements performed in the experiment are (quantum) measurement of the spin projection along some chosen direction. This allows us to formulate criteria involving only measurements of the collective spin, whose violation witnesses the presence of Bell correlations in the system.

4. Quantum correlations: Theory

This approach was developed and published in Ref. [26], where we also report a corresponding experiment (see chapter 5).

The additional assumption of a correct quantum-mechanical description of the measurements may be motivated by the fact that the experimental apparatus is “properly” built and calibrated by the experimenters, and that independent characterizations of it show agreement with the theory, leading us to believe that we understand its operation. We emphasize that no assumption is made on the state of the system we are investigating. Thanks to this, even if the violation of a Bell witness cannot conclusively prove statements like the incompatibility of nature with local realism, its violation still allows us to characterize the state of the system without prior knowledge of this state. Namely, we can conclude that, under the mentioned assumption on the measurements, the state has the resources to violate a Bell inequality.

From Bell inequalities to Bell correlation witnesses

As a first example, we show how to derive a Bell correlation witness from the Bell inequality (4.38). First, we associate each party i with a spin 1/2, on which we assume that the measurement $\mathcal{M}_{\mathbf{d}}^{(i)} = 2\hat{\mathbf{s}}^{(i)} \cdot \mathbf{d}$ of the spin projection along an axis \mathbf{d} is performed, where $2\hat{\mathbf{s}}^{(i)} = \{\hat{\sigma}_x^{(i)}, \hat{\sigma}_y^{(i)}, \hat{\sigma}_z^{(i)}\}$ is the Pauli vector. Then, we define the total spin observable $\hat{S}_{\mathbf{d}} = \mathbf{d} \cdot \sum_{i=1}^N \hat{\mathbf{s}}^{(i)}$ in the direction \mathbf{d} , which can be probed by collective measurements on the entire system.

Setting $\mathcal{M}_0^{(i)} = \mathcal{M}_{\mathbf{n}}^{(i)}$ and $\mathcal{M}_1^{(i)} = \mathcal{M}_{\mathbf{m}}^{(i)}$, with $\mathbf{m} = 2(\mathbf{a} \cdot \mathbf{n})\mathbf{a} - \mathbf{n}$ and $\|\mathbf{a}\| = \|\mathbf{m}\| = \|\mathbf{n}\| = 1$, allows us to express the one- and two-body correlators as

$$\begin{aligned} \mathcal{S}_0 &= 2 \langle \hat{S}_{\mathbf{n}} \rangle \\ \mathcal{S}_{00} + 2\mathcal{S}_{01} + \mathcal{S}_{11} &= 16(\mathbf{a} \cdot \mathbf{n})^2 \langle \hat{S}_{\mathbf{a}}^2 \rangle - 4N(\mathbf{a} \cdot \mathbf{n})^2. \end{aligned} \quad (4.58)$$

With these relations, and the fact that $\hat{S}_{-\mathbf{n}} = -\hat{S}_{\mathbf{n}}$, we transform the Bell inequality (4.38) into the witness observable

$$\hat{W} = - \left| \frac{\hat{S}_{\mathbf{n}}}{N/2} \right| + (\mathbf{a} \cdot \mathbf{n})^2 \frac{\hat{S}_{\mathbf{a}}^2}{N/4} + \frac{\beta_C}{2N} - (\mathbf{a} \cdot \mathbf{n})^2. \quad (4.59)$$

The Bell inequality Eq. (4.38) guarantees that $\langle \hat{W} \rangle \geq 0$ whenever the state of the system is not Bell-correlated. By construction, the Bell correlation witness Eq. (4.59) only involves first and second moments of collective spin measurements along two directions \mathbf{a} and \mathbf{n} , making it well suited for experiments on many-body systems. Although this witness was derived with assumptions about the measurements, it does not make any assumptions about the measured state. In particular, we do not assume that the state is symmetric under particle exchange. Moreover, this witness applies whether the particles are spatially separated or not, similar to entanglement witnesses [132], under the common assumption that particles do not communicate (interact) through unknown channels.

Although such an assumption would be questioned in a Bell test aimed at disproving the locally realist nature of the world, it is a well-satisfied and common assumption in the context of many-body systems, where the goal is to characterize correlations, assuming quantum mechanics to be valid.

The number of particles N , entering in Eq. (4.59), may fluctuate slightly from one experimental run to the next. To take this into account, we replace N in Eq. 4.59 by the observable \hat{N} , and introduce the scaled collective spin $\mathcal{C}_n = \langle 2\hat{S}_n/\hat{N} \rangle$ and the scaled second moment $\zeta_a^2 = \langle 4\hat{S}_a^2/\hat{N} \rangle$. The witness inequality then becomes

$$\mathcal{W} = -|\mathcal{C}_n| + (\mathbf{a} \cdot \mathbf{n})^2 \zeta_a^2 + \frac{\beta_C}{2N} - (\mathbf{a} \cdot \mathbf{n})^2 \geq 0, \quad (4.60)$$

which holds for any two axes \mathbf{a} and \mathbf{n} , and for all non-Bell-correlated states.

The expression Eq. (4.60) depends on the angle ϑ between \mathbf{a} and \mathbf{n} , and therefore its experimental violation relies on the accurate calibration of the measurement directions. To improve the robustness against uncertainties in this angle, we derive a more practical witness through the following consideration. We express $\mathbf{n} = \mathbf{a} \cos(\theta) + \mathbf{b} \sin(\theta) \cos(\phi) + \mathbf{c} \sin(\theta) \sin(\phi)$, with the ortho-normal vectors \mathbf{a} , \mathbf{b} and $\mathbf{c} = \mathbf{a} \times \mathbf{b}$, where \times denotes the vector product. With these definitions, we write Ineq. (4.60) as

$$\zeta_a^2 \geq \frac{\mathcal{C}_a \cos(\theta) + \mathcal{C}_b \sin(\theta) \cos(\phi) + \mathcal{C}_c \sin(\theta) \sin(\phi) - \beta_C/(2N) + \cos^2(\theta)}{\cos^2(\theta)}, \quad (4.61)$$

which is satisfied by all non-Bell-correlated states, for all (θ, ϕ) . For this reason, such states satisfy also

$$\begin{aligned} \zeta_a^2 &\geq Z(\mathcal{C}_{bc}, \mathcal{C}_a) \equiv \max_{\theta \in [0, \pi]} \left[\frac{\mathcal{C}_{bc} \sin(\theta) - \mathcal{C}_a \cos(\theta) - \beta_C/(2N) + \cos^2(\theta)}{\cos^2(\theta)} \right] \\ &\geq Z(\mathcal{C}_b, 0) = \frac{2 - \beta_C/(2N) - \sqrt{[\beta_C/(2N)]^2 - \mathcal{C}_b^2}}{2}, \end{aligned} \quad (4.62)$$

where $\mathcal{C}_{bc} = \sqrt{\mathcal{C}_b^2 + \mathcal{C}_c^2}$ and where we used the monotonicity of the function $Z(\mathcal{C}_{bc}, \mathcal{C}_a)$, which is discussed in more detail in Ref. [26]. Inserting into Eq. (4.62) the classical bound of inequality Eq. (4.38), $\beta_C = 2N$, we obtain the witness inequality

$$\zeta_a^2 \geq \frac{1}{2} \left(1 - \sqrt{1 - \mathcal{C}_b^2} \right), \quad (4.63)$$

which involves the measurements of ζ_a and \mathcal{C}_b , for the two orthogonal directions \mathbf{a} and \mathbf{b} , and is satisfied by all non-Bell-correlated states. In other words, a violation of InEq. (4.63) witnesses that the state is Bell correlated.

In the following chapter we present an experiment showing the violation of inequalities Eq. (4.60) and Eq. (4.63) for a many-body system, which allows us to conclude the presence of Bell correlations among the constituent parties.

4. Quantum correlations: Theory

An interesting observation is that the witness Eq. (4.63) resembles to some extent the criterion to detect entanglement with the Wineland squeezing parameter Eq. (4.24). We will discuss this connection more in detail in the following chapter.

As a second example, we show how to derive a Bell correlation witness from the Bell inequality (4.39). The approach is similar to the one just described, and it is presented in detail in Ref. [29]. We consider m measurement directions $\mathbf{d}_k = \mathbf{a} \cos(\vartheta_k) + \mathbf{b} \sin(\vartheta_k)$, lying in a plane spanned by two orthonormal vectors \mathbf{a} and \mathbf{b} , with the antisymmetric angle distribution $\vartheta_{m-k-1} = -\vartheta_k$. From Eq. (4.39) with even m , we arrive at the family of witnesses

$$\mathcal{W}_m = \mathcal{C}_b \sum_{k=0}^{\frac{m}{2}-1} \alpha_k \sin(\vartheta_k) - (1 - \zeta_a^2) \left[\sum_{k=0}^{\frac{m}{2}-1} \cos(\vartheta_k) \right]^2 + \frac{m^2}{4} \geq 0, \quad (4.64)$$

which are satisfied by all states that are not Bell correlated. These Bell correlation witnesses depend on the $m/2$ angles ϑ_k (that we emphasize are just free variables to be optimized), but they involve just two quantities to be measured experimentally: the scaled collective spin \mathcal{C}_b and the scaled second moment ζ_a^2 , as it is the case for Eq. (4.60).

The tightest constraints on \mathcal{C}_b and ζ_a^2 that allow for a violation of Eq. (4.64) are obtained by minimizing \mathcal{W}_m over the angles ϑ_k . Solving $\frac{\partial \mathcal{W}_m}{\partial \vartheta_k} = 0$ yields the optimal angles [29]

$$\vartheta_k = -\arctan[\lambda_m(m - 2k - 1)], \quad (4.65)$$

$$\frac{\mathcal{C}_b}{2\lambda_m(1 - \zeta_a^2)} = \sum_{k=0}^{\frac{m}{2}-1} \cos(\vartheta_k). \quad (4.66)$$

Equation (4.66) is a self-consistency equation for λ_m that has to be satisfied in order to minimize \mathcal{W}_m .

Inserting these optimal angles, we rewrite Eq. (4.64) as a witness involving the physical parameters \mathcal{C}_b and ζ_a^2 only. Interestingly, for two measurement directions ($m = 2$) we obtain again Eq. (4.63), which was previously derived from the different inequality Eq. (4.38). Increasing the number of measurement directions allows for the detection of Bell correlations in additional states. In the limit $m \rightarrow \infty$, we find [29]

$$\zeta_a^2 \geq Z_\infty(\mathcal{C}_b) = 1 - \frac{\mathcal{C}_b}{\operatorname{arctanh}(\mathcal{C}_b)}. \quad (4.67)$$

Figure 4.6 shows the bounds given by the two witnesses (4.63) and (4.67), together with the one obtained similarly for $m = 4$ settings, in the \mathcal{C}_b - ζ_a^2 plane. Points below the curve Z_m in Fig. 4.6 indicate a violation of the witness Eq. (4.64) obtained from the corresponding m -settings Bell inequality Eq. (4.39). Violation of any such bound reveals the presence of a Bell correlations in the system under investigation.

Note that the curve Z_∞ reaches the point $\mathcal{C}_b = \zeta_a^2 = 1$, therefore allowing in principle for the detection of Bell correlations in presence of arbitrarily low squeezing. It is

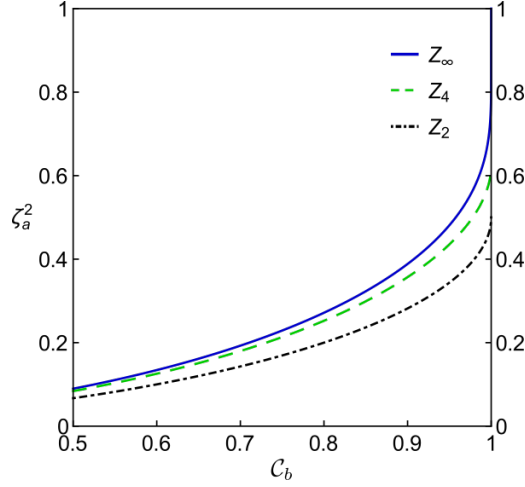


Figure 4.6: Plots of the critical lines $Z_2(C_b) = Z(C_b, 0)$ [Eq. (4.62)], $Z_4(C_b)$ and $Z_{\infty}(C_b)$ [Eq. (4.67)]. The witness obtained from the Bell inequality with $m = 4$ settings already provides a significant improvement over the case of $m = 2$ settings, by allowing to detect Bell correlations in a larger class of states. Figure adapted from [29].

known, however, that some values of C_b and ζ_a^2 can only be reached in the limit of a large number of spins [100]. For any fixed N , a finite amount of squeezing is thus necessary in order to allow for the violation the witness Eq. (4.64), [29].

Witnessing Bell correlation depth

Inequalities allowing to quantify the depth of Bell correlations can also be transformed into witnesses. In the case of Eq. (4.56), we note that the inequality is of the same form as Eq. (4.38), except for the classical bound β_C that is replaced by β_C^k . For this reason, following the calculation used to derive Eq. (4.62), it is straightforward to derive a witness for Bell correlations of depth k . The result is of the same form as Eq. (4.62), but with β_C replaced by β_C^k , namely

$$\zeta_a^2 \geq \frac{2 - \beta_C^k/(2N) - \sqrt{[\beta_C^k/(2N)]^2 - C_b^2}}{2}. \quad (4.68)$$

The violation of Ineq. (4.68), for the β_C^k given in Tab. (4.57), witnesses that the state contains Bell correlations with a depth of (at least) k particles.

Remarkably, the fact that Ineq. (4.68) involves only ζ_a and C_b (for the two orthogonal directions \mathbf{a} and \mathbf{b}) implies that also the depth of Bell correlations can be witnessed in many-body systems with collective measurements, as we will show for the experiment presented in the following chapter. This resembles again the case of entanglement, for which the Wineland criterion as extended by Sørensen and Mølmer in Ref. [100] provides a quantification of its depth. Unfortunately, while for entanglement there is a

4. Quantum correlations: Theory

method to witness any depth k , for Bell correlations we have only the few bounds reported in Tab. (4.57). This is due to the complexity behind the approach we used, which relies on the characterization of non-signaling polytopes, and it might be overcome by approaching the problem with different ideas.

4.5.5 Finite statistics loophole

Observing experimentally the violation of a Bell correlation witness indicates that the system under investigation is Bell-correlated. However, since experiments are always collecting a finite number of measurement results, such conclusion require a detailed statistical investigation. There is in fact the possibility that a finite number of measurements on states that are not Bell-correlated could be responsible for the violation of a witness, which is the so called statistics loophole [133, 134].

To give a concrete example, consider a Bell witness whose quantum violation is bounded from below by $\langle \varphi | \hat{W} | \varphi \rangle = \mathcal{W}_{\min} < 0$, for an optimal state $|\varphi\rangle$, while its largest possible value $\mathcal{W}_{\max} > 0$ is achievable by a product state $|\uparrow\rangle^{\otimes N}$. If a small number of measurements is performed on a system in the state

$$\hat{\rho}(q) = (1 - q)|\varphi\rangle\langle\varphi| + q(|\uparrow\rangle\langle\uparrow|)^{\otimes N}, \quad (4.69)$$

where q is small, then it is likely to obtain a negative estimate for $\langle \mathcal{W} \rangle$, even though $\langle \mathcal{W} \rangle \geq 0$ in the limit of infinitely many measurement rounds [26, 29]. For this reason, the state in Eq. (4.69) imposes a lower bound on the number of measurements required to exclude, through the considered witness, all non-Bell-correlated states with high confidence. This is only a lower bound because, in general, one can think of states that are more pathological than Eq. (4.69) and, therefore, that requires more measurements. For this reason, it is of interest to find instead an upper bound, whose derivation needs a more careful statistical analysis.

In the work presented in Ref. [29] we performed this analysis and provide a number of measurements M sufficient to exclude, with a probability larger than $1 - \epsilon$ and without additional assumptions (*e.g.* that the statistics is Gaussian), that a local states is responsible of the observed witness violation. This corresponds to a p -value lower than a given threshold for the null hypothesis ‘*The measured state is not Bell-correlated*’. Our results are summarized in Figure 4.7, where the required number of experimental runs per spin are plotted as a function of the scaled collective spin \mathcal{C}_b (horizontal axis) and of the scaled second moment ζ_a^2 (curve color). For a confidence level of $1 - \epsilon = 99\%$ in the considered parameter region, the required number of measurement runs per spin is in the range of $\approx 20 \div 500$.

As illustrated in Figure 4.8, we observe that the ratio M/N tends to a constant for large N [29]. This implies that a number of measurements growing linearly with the system size is both necessary and sufficient to detect Bell correlations without the statistical loophole, which is a reasonable scaling when considering systems with a large number of particles. It is important to note that such conclusion cannot follow only by observing a violation of the witness by a fixed number of standard deviations. Indeed,

4.5 Detection of Bell correlations

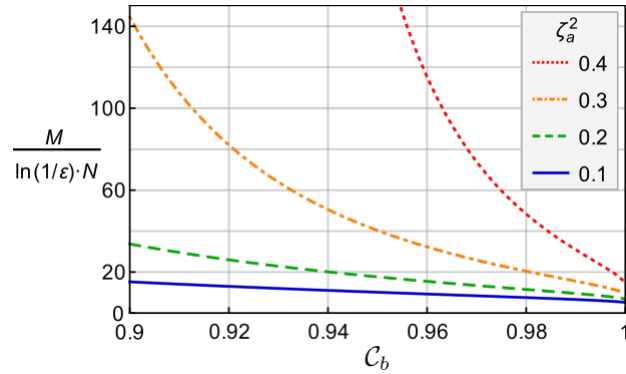


Figure 4.7: Number of experimental runs per spin required to rule out non-Bell-correlated states with a confidence of $1 - \varepsilon$ as a function of C_b (horizontal axis) and ζ_a (curve color). For $C_b = 0.98$ and $\zeta_a^2 = 0.272$ (as reported in [26]), approximately $17 \cdot \ln(100) \simeq 80$ runs per spin are sufficient to reach a confidence level of 99%. Figure taken from [29]

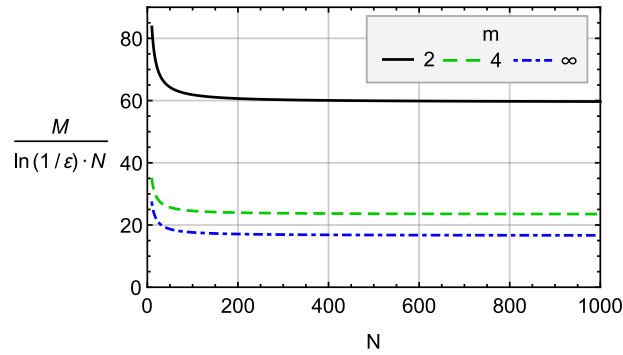


Figure 4.8: Number of experimental runs per spin required to rule out non-Bell-correlated states with a confidence of $1 - \varepsilon$ as a function of the number of spins N . The plots are for the witness Eq. (4.64) with $m = 2, 4, \infty$ measurement settings, and for $\zeta_a^2 = 0.272$ and $C_b = 0.98$ (as reported in [26]). The ratio M/N tends to a constants for larger systems. Figure taken from [29].

standard deviations inform on the precision of a violation, but fail at excluding arbitrary local models [134], including *e.g.* models which may showing non-gaussian statistics with rare events.

Quantum correlations: Experiments

In this Chapter we present the experimental preparation and detection of nonclassical correlations in many-body systems. First, we describe the sequence to prepare BECs in spin-squeezed states, and we recall their connection to entanglement. Then, we demonstrate that collective measurements allow to witness the strongest form of correlations known, namely Bell correlations. To conclude, we show an approach to extract correlations from indistinguishable particles into distinguishable subsystems, which enabled us to observe entanglement strong enough for EPR-steering. These results were published in Refs. [26, 27].

5.1 Spin-squeezing and entanglement in Bose-Einstein condensates

In this section we present our experimental sequence to prepare BECs in a specific family of entangled states, called spin-squeezed states [25]. Such states are particularly relevant in quantum metrology, where quantum correlations are a resource to enhance interferometric sensitivity beyond classical limits [12]. Moreover, their relative robustness against particle losses, when compared with other entangled states such as cat states, is a crucial feature in practical applications. The non-linear dynamics that is required to build up the correlations originates from the collisional interactions among the constituent atoms, which is controllable in our experiments. Moreover, we present the common tools to characterize such spin squeezed states, in terms of their metrological usefulness and depth of entanglement.

Our group originally demonstrated spin squeezing in Ref. [19], the techniques for tomographic state reconstruction in Ref. [52] and the implementation of an atom interferometer with sensitivity beyond the standard quantum limit in Ref. [17]. We present state of the art results of state preparation and characterization, and the review of these tools will motivate the next experiments we are going to present in this chapter.

5. Quantum correlations: Experiments

5.1.1 Experimental preparation of spin-squeezed states

We perform experiments with Bose-Einstein condensates of Rubidium-87 atoms, magnetically trapped on an atom chip [17, 19, 24, 26]. As internal degrees of freedom, we use the two hyperfine states $|F = 1, m_F = -1\rangle \equiv |1\rangle$ and $|F = 2, m_F = 1\rangle \equiv |2\rangle$. One of the advantages is that at the “magic” magnetic field of 3.23 G they have an energy difference to first order insensitive to magnetic field fluctuations, resulting in very good coherence properties [135]. Moreover, because of the nearly identical magnetic moments, state $|1\rangle$ and $|2\rangle$ experience almost the same magnetic (harmonic) confining potential of trap frequencies $f_x = 110$ Hz and $f_y = f_z = 729$ Hz.

To prepare a spin-squeezed state, we start with a BEC of $N \approx 600$ atoms in state $|1\rangle$. Then, we use a Rabi pulse to prepare the system in the coherent spin state $[(|1\rangle + |2\rangle)/\sqrt{2}]^{\otimes N}$, in which the atomic spins are uncorrelated, Fig. 5.1A. At this point, we initiate the squeezing dynamics by controlling the collisional interactions between the two states through a state-dependent microwave near-field potential [24]. A state-selective splitting of the two potential minima by 150 nm induces coherent demixing-remixing dynamics, as described in Refs. [17, 19]. During this process, the coherent spin state evolves in time according to the one-axis twisting [25] Hamiltonian $\hat{H} = \chi \hat{S}_z^2$, resulting in a spin-squeezed state with reduced quantum noise in a certain spin component, Fig. 5.1B. The preparation needs two complete demixing-remixing oscillations (≈ 55 ms in total) to generate ≈ -6 dB of spin squeezing according to the Wineland criterion [99]. Note that, in reality, our squeezed states are (i) not exactly on the equator of the Bloch sphere, due to different particle loss rates in the two states during the preparation, and (ii) tilted by $\approx 10^\circ$ against the horizontal due to the one-axis twisting dynamics, Fig. 5.1B.

After the state preparation, our experiments require the measurement of the collective spin along certain directions. However, because spin projection measurements by absorption imaging are always taken along the $+z$ spin axis, we perform Rabi rotations of the state before the measurement, Fig. 5.1C. In this way, the passive rotations of the spin operators \vec{S} (*i.e.* measurements along different axes for a fixed state) are experimentally replaced by active rotations (*i.e.* measurements along a fixed axis for differently rotated states).

The actual measurement sequence starts by releasing the atoms from the trapping potential by ramping down the magnetic bias field. During their free fall, atoms accelerate away from the chip surface, in the vertical downward direction. After a time-of-flight of a few milliseconds a resonant absorption image of each state is taken. This pair of pictures (together with a reference picture) allow us to count the number of atoms in the two hyperfine states, N_1 and N_2 , as described in chapter 3.

5.1.2 Squeezing sequence with spin echo

In the most recent experiments we introduced a small variation on the sequence just presented in the previous paragraph. To decrease the impact of technical noise and particle losses in the squeezed state preparation, we perform a spin-echo protocol during the squeezing dynamics. Concretely, after the $\pi/2$ Rabi rotation which prepares the BEC

5.1 Spin-squeezing and entanglement in Bose-Einstein condensates

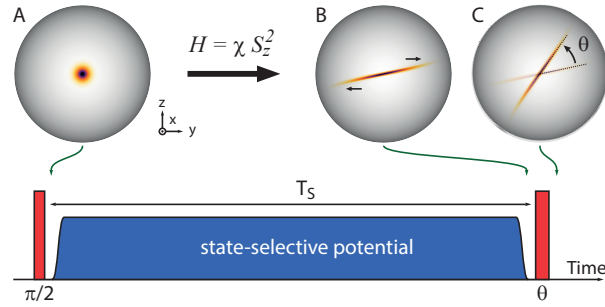


Figure 5.1: Sequence to prepare and characterize a spin-squeezed state. The figure shows Rabi pulses (red) and on-chip microwave pulses (blue). The spheres show the Wigner function of the collective spin state at various stages of the experiment, simulated for $N = 200$ atoms. **(A)** Initial coherent state on the equator, along the $+x$ spin direction. **(B)** Spin squeezed-state resulting from the one-axis twisting Hamiltonian. **(C)** State after the counter-clockwise rotation by an angle θ around its center. Figure adapted from [53]

in a coherent spin state, we turn on the state-selective potential only until the first revival of the demixing-remixing dynamics (≈ 28 ms). Then, we apply a Rabi π -pulse (echo pulse) before a second state-selective potential period, of the same duration as the first, starts.

The addition of a spin echo pulse makes the experimental sequence less sensitive to uncontrolled shot-to-shot fluctuations of the detuning between the atomic transition and the two-photon drive, *e.g.* due a fluctuating microwave potential or fluctuating collisional interactions. Additionally, since the echo effectively inverts the population of $|1\rangle$ and $|2\rangle$, the effect of asymmetric losses from the two states is partially compensated. This results in a state closer to the equatorial plane, and to the fact that clock-shifts are compensated without the need to post-process the data. The latter implies also that the state preparation is less sensitive to drifts in the total atom number. In order to prevent uncontrolled offsets due to fluctuations of the Rabi rotation angle, the spin-echo pulse phase is chosen such that the state is rotated by π around its mean spin value.

With the echo protocol, we observe a spin squeezed state with typically $-3.8(2)$ dB of spin squeezing according to the Wineland criterion. On the one hand, the states prepared in this way are $1 - 2$ dB less squeezed than the typical ones we observe without the echo pulse. The additional noise along the squeezing direction might originate from imperfections in the additional echo pulse, from turning off and on the MW potential in the middle of the sequence, or from other unknown sources. This question will be addressed in detail by future investigations. On the other hand, the antisqueezed quadrature we measure on squeezed states prepared with the echo pulse are typically $10(1)$ dB anti-squeezed, which is ≈ 3 dB less compared to the one in squeezed states prepared without the echo pulse.

5. Quantum correlations: Experiments

5.1.3 Experimental characterization of spin-squeezed states

To characterize the prepared spin squeezed states, we start by measuring the spin variance $\text{Var}[S_{\mathbf{d}}]$ for different directions of the vector $\mathbf{d} = (0, \cos(\theta), \sin(\theta))$ in the yz -plane. This is accomplished with the sequence illustrated in Fig. 5.1: after the spin-squeezed state is prepared with the protocol previously described (Fig. 5.1B), a Rabi pulse which rotates the state by an angle θ around its center is applied (Fig. 5.1C). To get a good estimation of the variance, we take typically ≈ 100 measurements of the spin projection before changing the angle θ . Ideally, if the state is on the equator and the rotation axis is properly calibrated, the mean $\langle S_{\mathbf{d}} \rangle \approx 0$, while the variance $\text{Var}[S_{\mathbf{d}}]$ varies with θ , reflecting the squeezed and anti-squeezed quadratures [19].

To make an insightful comparison, the measured variance is usually normalized by the variance of an ideal coherent state with the same number of particles, which is $N/4$ independent of θ . This suggests to define the number squeezing parameter

$$\xi_n^2 = \frac{4}{N} \text{Var}[S_{\mathbf{d}}] = N \text{Var}[N_{\text{rel}}] , \quad (5.1)$$

where $N_{\text{rel}} = (N_1 - N_2)/N$, to compare the observed spin noise to a binomial distribution [25].

Since displacements of a spin-squeezed state along certain directions can be detected with a better sensitivity than for a coherent state, such states allow to perform quantum-enhanced metrology. To quantify the metrological usefulness of a quantum state, Wineland *et al.* introduced in Ref. [99] the squeezing parameter

$$\xi^2 = \frac{N \text{Var}[S_{\mathbf{d}^*}]}{\langle S_x \rangle^2} , \quad (5.2)$$

where x is the direction of the mean spin, \mathbf{d}^* is the direction perpendicular to x minimizing the spin variance $\text{Var}[S_{\mathbf{d}}]$. A state with $\xi^2 < 1$ allows to improve the interferometric sensitivity by a factor ξ^2 in variance with respect to an ideal coherent state of the same particle number, *i.e.* with respect to the standard quantum limit. It is interesting to note that, contrary to the number squeezing, ξ^2 depends on the spin length $\langle S_x \rangle$, reflecting the fact that a high interferometric contrast, as well as a reduced variance, is required to achieve better sensitivity. We measure $\langle S_x \rangle$ in an independent experiment, by performing Rabi rotations of the state around the y -axis.

In Figure 5.2 we show an example of such state characterization for spin-squeezed BECs with $N = 580 \pm 40$ atoms, prepared as described in paragraph 5.1.1 [dataset 151002#1]. For different directions in the yz -plane, parametrized by the angle θ , Figure 5.2a shows the individual spin projection measurements in terms of N_{rel} . For each angle, the variance of the data distribution gives the number squeezing reported in Figure 5.2b. The effect of detection noise is subtracted from each data point [53], and it corresponds to $\xi_{\text{det}}^2 = -0.55$ dB at the optimal squeezing angle. The observation that for a turning angle of $\theta = 0$ the measured variance is consistent with that of an ideal coherent state confirming that our imaging system is properly calibrated, and that imaging noise is correctly subtracted. For small negative θ , noise lower than the one of a

5.1 Spin-squeezing and entanglement in Bose-Einstein condensates

coherent state is observed. Its minimum is reached for the optimal turning angle of $\theta^* = -11.4^\circ$, when the squeezed direction is aligned with the z -axis. In spin-squeezed states the variance of one spin quadrature is reduced at the expenses of increasing the variance of the orthogonal one, as required by the uncertainty principle. This is shown by the fact that, turning the state 90° from the optimal point aligns the anti-squeezed direction with the z -axis, and the measured noise is far above that of a coherent state. In theory, the amount of noise reduction in the squeezed direction should exactly compensate the noise increase in the anti-squeezed direction. The observation of an imbalance, as in our measurements, indicates the presence of additional noise sources. The interferometric (Rabi) contrast of $\langle S_x \rangle / (N/2) = 0.971(8)$ is obtained from an independent measurement, where the state is rotated around the y axis, Figure 5.2c. In this dataset, we see at the optimal turning angle a number squeezing of $-7.1(4)$ dB and a Wineland squeezing parameter of $\xi^2 = 0.209 = -6.8$ dB.

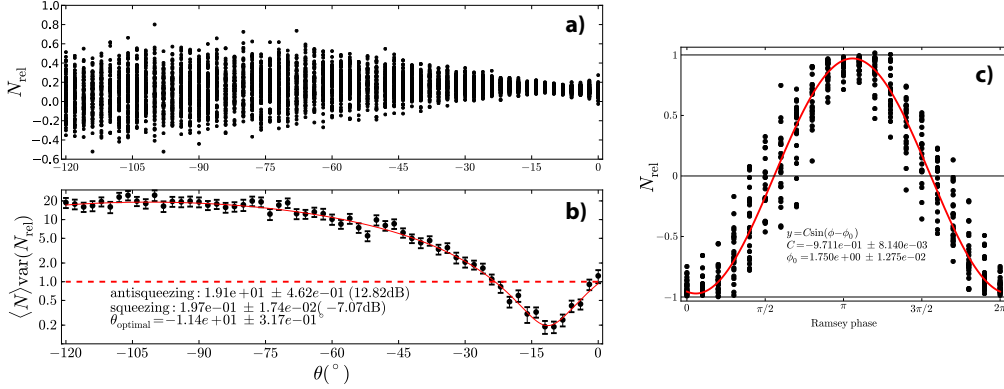


Figure 5.2: Experimental characterization of a spin-squeezed BEC. Measurements taken from BECs with $N = 580 \pm 40$ atoms, prepared in a spin-squeezed state as described in Paragraph 5.1.1. **a)** Individual spin projection measurements for different directions (see Fig. 5.1), in terms of relative atom number. **b)** Number squeezing as a function of the turning angle θ . Error bars indicate statistical uncertainty based on the number of shots used in each data point. The independently measured contribution from imaging noise has been subtracted. At the optimal turning angle of $\theta^* = -11.4^\circ$, we observe $-7.1(4)$ dB of number squeezing. **c)** Measurement of the Rabi contrast. The sinusoidal fit (red curve) gives $0.971(8)$. The Wineland spin-squeezing parameter for this dataset is of $\xi^2 = 0.209 = -6.8$ dB. [dataset 151002#1]

5.1.4 Entanglement in spin-squeezed states

The Wineland squeezing parameter Eq. (5.2), apart from quantifying the metrological usefulness of a state, can be also used to witness entanglement, and its depth (see Paragraph 4.3.2). This result makes a connection between spin-squeezing and entanglement, and it allows to conclude the presence of such correlations in many-body systems with collective measurements. In particular, observing a Wineland parameter $\xi^2 < 1$ implies

5. Quantum correlations: Experiments

that the particles are entangled. Moreover, following the approach presented in Paragraph 4.3.2 we are able to derive a lower bound on the depth of entanglement required to observe the given values of spin contrast and variance [100].

Figure 5.3 shows the measured depth of entanglement for the data presented in the previous paragraph, Fig. 5.2. The red lines illustrate the smallest variance attainable in a k -partite entangled state for a given Rabi contrast, and they have been generated numerically. For large k , an analytic approximation to these curves exists, and it is given in Eq. (4.26). The squeezed states we observed fall on the curve for ≈ 56 -partite entanglement.

It should be noted that in a pure BEC particles are indistinguishable, and therefore that the spin state is restricted to the symmetric subspace. For this reason one expects in an ideal system maximal entanglement depth of N particles for all levels of squeezing. The meaning of entanglement depth in such a system is discussed in Ref. [132], where they say that observing $k < N$ is likely due either to noise or to the fact that the entangled state is only partially useful for parameter estimation.

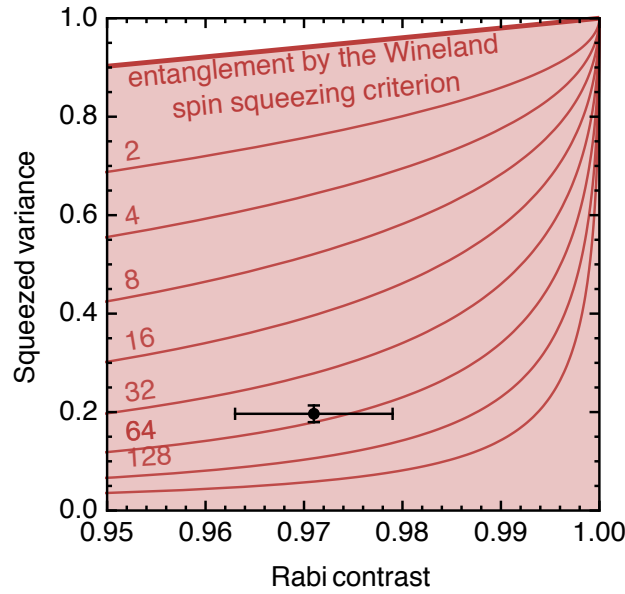


Figure 5.3: Depth of entanglement in a spin-squeezed BEC. Depth of entanglement calculated according to reference [100]. Lines correspond to k -particle entanglement for $k = 2, 4, 8, \dots, 256$. The black data point corresponds to the squeezed states with $N = 580 \pm 40$ atoms of Fig. 5.2, and it falls on the line for $k \approx 56$ [dataset 151002#1]

5.1.5 Conclusions and outlook

In this section we presented our experimental sequence to prepare and characterize BECs in spin-squeezed states. We reviewed known results connecting squeezing with entan-

5.1 Spin-squeezing and entanglement in Bose-Einstein condensates

gument, which show how such correlations, and their depth, can be witnessed in a many-body system by collective measurements. As an example, we applied such tools to our best experimental dataset.

Apart from finding practical applications in quantum metrology, spin-squeezed states are also interesting for fundamental studies. Preparing entangled states of large numbers of particles pushes the quantum world towards macroscopic scales, which is useful to test the validity range of the theory of quantum mechanics.

At this point, interesting questions that might arise are: 1) is it possible to detect in such systems correlations even stronger than entanglement? 2) is it possible to go beyond collective measurements, and observe directly the correlations among the constituent particles? Their answers are found in the next two sections, and constitute the major results of this thesis.

5.2 Bell correlations in a BEC

Measurements performed on the parts of a composite system can show correlations that cannot be explained by any classical theory [5]. These so-called Bell correlations can be confirmed by violating a Bell inequality, and represent the most profound departure of quantum from classical physics.

Bell correlations have been detected between up to fourteen ions [11], four photons [136,137], two neutral atoms [138], two solid-state spin qubits [139], and two Josephson phase qubits [140]. Even though multi-partite Bell inequalities are known [5, 128, 141, 142], their violation in larger systems has remained elusive, due to the lack of suitable measurement schemes that can be implemented with limited detection resolution and acquisition time.

Recently proposed multipartite Bell inequalities [21, 29], which involve only one- and two-body correlators, significantly reduce these difficulties. The reason being that such low-order correlators are relatively easy to be measured experimentally, therefore opening the possibility of detecting Bell correlations in large systems. Importantly, these inequalities can be rewritten in the form of quantum mechanical witnesses, which allows us to detect Bell correlations with collective measurements only. Further theoretical investigations even extended this approach to quantify the depth of such correlations, in analogy to what is done for entanglement [30].

In this section we report experiments violating Bell witness inequalities, therefore detecting Bell correlations between the spins of about 480 atoms in spin-squeezed Bose-Einstein condensates. Moreover, we discuss the statistical significance of the observed violation and quantify the correlation's depth. The experimental results have been published in Ref. [26], and our several further theoretical developments on the subject appeared in Refs. [28–30].

5.2.1 Violation of a Bell correlation witness

In section 4.5.1 we presented the multi-partite Bell inequality found in Ref. [21], involving only one- and two-body correlators. As it was mentioned, this inequality still requires the experimentally challenging task of addressing the parties individually, which seems difficult if the number of parties is already above hundred. For this reason, we discussed the advantages of considering global observables, and in section 4.5.4 we derived from the Bell inequality Eq. (4.38) the Bell correlation witness Eq. (4.59),

$$\mathcal{W} = -|\mathcal{C}_n| + (\mathbf{a} \cdot \mathbf{n})^2 \zeta_a^2 + 1 - (\mathbf{a} \cdot \mathbf{n})^2 \geq 0, \quad (5.3)$$

where $\mathcal{C}_n = \langle 2\hat{S}_n/\hat{N} \rangle$ is the scaled collective spin and $\zeta_a^2 = \langle 4\hat{S}_a^2/\hat{N} \rangle$ is the scaled second moment, thus involving only collective measurements. The violation of this criterion allows us to conclude, under the additional assumption of properly characterized measurements, that the state we are probing has the resources to violate the original Bell inequality Eq. (4.38).

With the following experiment we show that the spin-squeezed state of a BEC with $N \approx 500$ atoms, prepared as explained in paragraph 5.1.1, violates witness Eq. (5.3). This observation allows us to conclude the presence of Bell correlations in a many-body system.

The witness \mathcal{W} requires collective spin measurements along directions \mathbf{a} and \mathbf{n} . As mentioned before, our spin-squeezed states are not exactly on the equator, and they are tilted by $\approx 11^\circ$ against the horizontal direction. Because inequalities (5.3) and (5.4) are most easily violated when \mathbf{a} is the axis that minimizes $\zeta_{\mathbf{a}}^2$, this means that in our case \mathbf{a} should be taken to be the squeezing direction, Fig. 5.4B, and that the state should be placed on the equator of the sphere, where $\mathcal{C}_{\mathbf{a}} = 0$. In a first set of measurements, we thus rotate the squeezed state so that $\mathcal{C}_{\mathbf{a}}$ is as close as possible to zero and $\zeta_{\mathbf{a}}^2$ is minimal. In practice, we scan the phase of the Rabi pulse, keeping its area fixed to 11.0° , and pick the value of the phase that minimizes $|\mathcal{C}_{\mathbf{a}}|$.

In a second experimental run, we measure $\mathcal{C}_{\mathbf{n}(\tau)}$ for many different axes $\mathbf{n}(\tau)$ in the plane defined by the center of the state \mathbf{b} and the vector \mathbf{a} (Fig. 5.4A). For this, after having put the state on the equator with a first Rabi rotation, we apply a second rotation by an angle $\vartheta(\tau)$, where τ is the Rabi pulse duration, with a phase adjusted such that the contrast is maximized. This sequence ensures that the rotation is around an axis perpendicular to the position of the state on the equator. Since in this second run the state has slightly shifted in phase due to experimental drifts, the first rotation does not bring the state exactly onto the equator and we end up with a slightly different $\mathcal{C}_{\mathbf{n}(\tau=0)} \neq \mathcal{C}_{\mathbf{a}}$ even for $\tau = 0$. We simultaneously account for this shift and calibrate the Rabi frequency and its nonlinearity by fitting $\mathcal{C}_{\mathbf{n}(\tau)} = \mathcal{C}_{\mathbf{b}} \sin(\tau_0 + \gamma\tau + \delta\tau^2)$ with $\{\mathcal{C}_{\mathbf{b}}, \tau_0, \gamma, \delta\} = \{0.980(2), -0.030(9), 2.464(15) \text{ ms}^{-1}, -1.6(5) \times 10^{-2} \text{ ms}^{-2}\}$, from which we compute $\vartheta(\tau) = \tau_0 + \gamma\tau + \delta\tau^2 - \arcsin(\mathcal{C}_{\mathbf{a}}/\mathcal{C}_{\mathbf{b}})$ such that $\mathbf{a} \cdot \mathbf{n}(\tau) = \cos[\vartheta(\tau)]$. The measurement of $\mathcal{C}_{\mathbf{n}(\tau)}$ as a function of τ is shown in Fig. 5.4C. Using the above values of $\zeta_{\mathbf{a}}^2$, $\mathcal{C}_{\mathbf{n}(\tau)}$, and $\mathbf{a} \cdot \mathbf{n}(\tau)$, we plot the expectation value \mathcal{W} as a function of τ (see Fig. 5.4E). A sign of a properly calibrated angle $\vartheta(\tau)$ is seen in the four-fold symmetry of Fig. 5.4E. Raw data are corrected for detection noise [53] ($\sigma_{N_1, \text{det}} = 4.5$ and $\sigma_{N_2, \text{det}} = 3.9$), from imaging non-linearities [26, 53], and for added noise due to collisional clock-shift [53], which is correlated with the total atom number N ($\lambda = -6.8(12) \times 10^{-4}$ per atom).

To finally evaluate the Bell correlation witness \mathcal{W} we post-select the data from BECs with a total atom number of $N = 476 \pm 21$, for which we observe $-5.5(6)$ dB of spin squeezing according to the Wineland criterion Eq. (5.2). We find $\zeta_{\mathbf{a}}^2 = 0.272(37)$ and $\mathcal{C}_{\mathbf{b}} = 0.980(2)$, where the quoted uncertainties are statistical standard deviations. From the resulting measurement of $\mathcal{W}(\tau)$ (Fig. 5.4E), we observe a violation of inequality (5.3) over a large range of angles. For $\vartheta = 128^\circ$ we see the strongest violation, confirming the presence of Bell correlations with a statistical significance of 3.8 standard deviations (red square in Fig. 5.4E).

5. Quantum correlations: Experiments

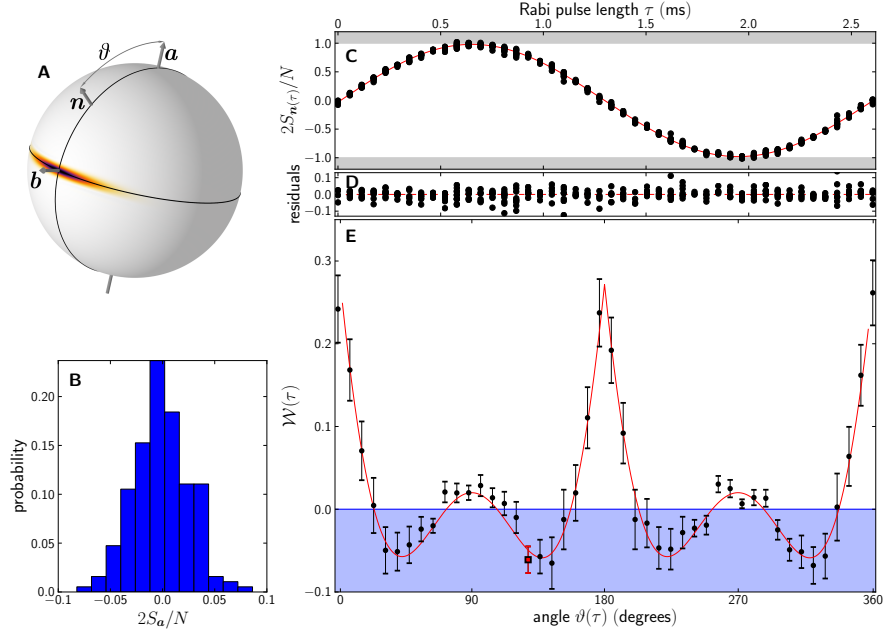


Figure 5.4: Observation of Bell correlations in a BEC with inequality (5.3). **a**, illustration of the spin-squeezed state (Wigner function on the Bloch sphere) and the axes used in the measurement of the Bell correlation witness \mathcal{W} . The vector \mathbf{n} lies in the plane spanned by the squeezing axis \mathbf{a} and the center of the state \mathbf{b} . The squeezing and anti-squeezing planes are indicated with thin black lines. **b**, histogram of measurements of $2S_a/N$ from which we determine ζ_a^2 . **c**, individual measurements of $2S_{\mathbf{n}(\tau)}/N$ as a function of Rabi pulse length τ . The red line is a sinusoidal fit from which we determine the Rabi contrast and $\mathbf{a} \cdot \mathbf{n}(\tau) = \cos[\vartheta(\tau)]$. **d**, residuals of the fit of **c**. **e**, measurement of $\mathcal{W}(\tau)$ as a function of $\vartheta(\tau)$. The red continuous line is the value of $\mathcal{W}(\tau)$ computed from the measurement of ζ_a^2 and the fitted Rabi oscillation (red line in **c**). The blue shaded region indicates Bell correlations. Note that the observed four-fold symmetry of $\mathcal{W}(\tau)$ indicates that $\mathbf{a} \cdot \mathbf{n}(\tau)$ is well calibrated. The red square data point at $\vartheta = 128^\circ$ violates inequality (5.3) by 3.8 standard deviations. Figure taken from Ref. [26].

5.2.2 Connection with entanglement

From the Bell correlation witness Eq. (5.3), we derived in section 4.5.4 a criterion (Eq. (4.63)) that is more robust to uncertainties in the angle ϑ between \mathbf{a} and \mathbf{n} : for any two axes \mathbf{a} and \mathbf{b} perpendicular to each other,

$$\zeta_a^2 \geq \frac{1}{2} \left(1 - \sqrt{1 - C_b^2} \right) \quad (5.4)$$

holds for all non-Bell-correlated states. This expression depends on the scaled collective spin C_n and on the scaled second moment ζ_a^2 , resembling the Wineland squeezing parameter [99], Eq. (5.2), which is a common measure of entanglement. A difference we note is that in the numerator of Eq. (5.2) the squeezed variance $\text{Var}[S_a] = \langle S_a^2 \rangle - \langle S_a \rangle^2$

contains the additional term $\langle S_a \rangle^2$. As an upper bound, and also because our state is oriented to have $\langle S_a \rangle \approx 0$, we can neglect this term and replace the variance by the squeezed second moment $\langle S_a^2 \rangle$. These substitutions allow us to write the Wineland spin-squeezing parameter as

$$\xi^2 \leq \frac{\zeta_a^2}{\mathcal{C}_b^2}, \quad (5.5)$$

which witnesses entanglement if $\xi^2 < 1$ [98].

As both entanglement and Bell correlations can be witnessed by looking at the parameters \mathcal{C}_n and ζ_a^2 , we provide a graphical illustration for the relationship between the two criteria with Fig. 5.5. The red shaded region corresponds to $\xi^2 < 1$, while the blue shaded region to the points also violating Eq. (5.4). For any experimentally measured Rabi contrast and second moment, Fig. 5.5 gives an immediate characterization of the correlations present in the system under study.

In section 4.3.2 we have seen how the parameter ξ^2 allows also for a characterization of the entanglement depth. In particular, $(k+1)$ -particle entanglement is witnessed by measuring squeezed variances (and hence ζ_a^2) below the red k -producibility curves in Fig. 5.5, [100].

Natural questions arising are whether Bell correlations could be concluded from points above the blue curve in Fig. 5.5 by better witnesses, whether the observed violation can be a statistical artifact, or whether the depth of Bell correlations could also be quantified in a similar way as entanglement. In the next paragraphs we are going to give (sometimes partial) answers to these questions.

5.2.3 Many settings witnesses

By looking at Fig. 5.5, we can see that there are entangled states which are not Bell correlated according to the criterion Eq. (5.4). We may therefore ask whether this is the case because such states do not allow for the violation of any Bell inequality, or because our witness is not sensitive enough. The latter possibility motivated us to search for better inequalities, for example by including higher order correlators or, as presented in section 4.5.1, by increasing the number of measurement settings per party m . Remarkably, even considering $m > 2$, under the assumption that these measurements are spin projection measurements we were able to derive Bell witnesses still involving only the two experimentally measured quantities ζ_a^2 and \mathcal{C}_b , Eq. 4.64. The sensitivity of such witnesses increases with m (even if such a parameter is a theoretical quantity, since experimentally one takes measurements only along direction \mathbf{a} or \mathbf{b}), in the sense that for a larger m less squeezing is needed to detect Bell correlations for a given contrast \mathcal{C}_b . In other words, as m increases more Bell correlated states can be detected experimentally. A considerable improvement is obtained by taking the limit $m \rightarrow \infty$, which gives us the criterion

$$\zeta_a^2 \geq 1 - \frac{\mathcal{C}_b}{\operatorname{arctanh}[\mathcal{C}_b]} \quad (5.6)$$

5. Quantum correlations: Experiments

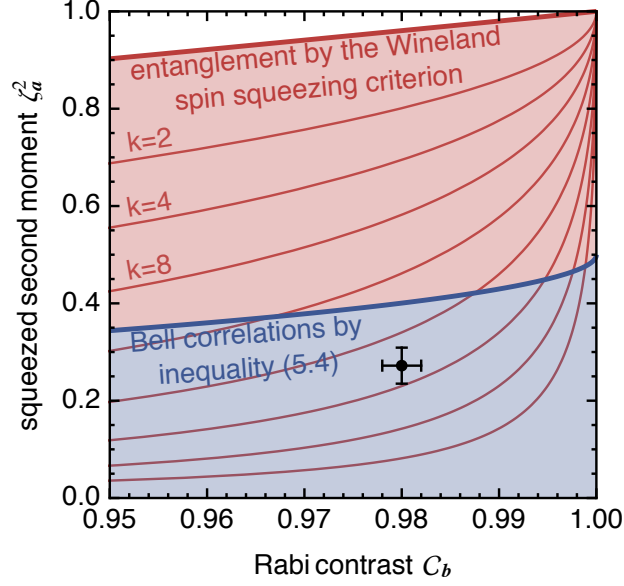


Figure 5.5: Observation of Bell correlations in a BEC with inequality (5.4) and connection to entanglement. Black: the data set of figure 5.4 expressed in terms of the Rabi contrast C_b and the squeezed second moment ζ_a^2 , with 1σ error bars. Blue shaded region: Bell correlations detected by violation of inequality (5.4). Red shaded region: entanglement witnessed by the squeezing parameter (5.5). Red lines: limits on ζ_a^2 below which there is at least $(k + 1)$ -particle entanglement [100], increasing in powers of two up to $k = 256$. According to Gaussian statistics, our data set has a 99% overlap with the area below the limit for $k = 24$ -partite entanglement, and 99.9% overlap with the blue area associated with the presence of Bell correlations. Figure taken from Ref. [26].

satisfied by all non Bell correlated states. In Fig. 5.6 we plot the different bounds corresponding to the witnesses for $m = 2, 4, 6$ and ∞ , to show that they allow for detecting Bell correlations in larger sets of states.

5.2.4 Statistical analysis

The witnesses we presented allow us to conclude the presence of Bell correlation in a quantum state if the measured ζ_a^2 and C_b violate an inequality. However, we have to keep in mind that experimental measurements of the spin moments gives us only an estimation of ζ_a^2 and C_b , which might differ from their true value. Of crucial interest is the case of a finite number of measurement, which always occurs in practice, because it imposes a bound on the confidence of our conclusions. This “statistics loophole” makes it difficult to rule out, without further assumptions, that the violation of a witness originates from an insufficient number of measurements on non-Bell-correlated states, and it can be particularly severe in the case of experiments involving many-body systems.

A first possibility to estimate the likelihood that the measured state is Bell correlated,

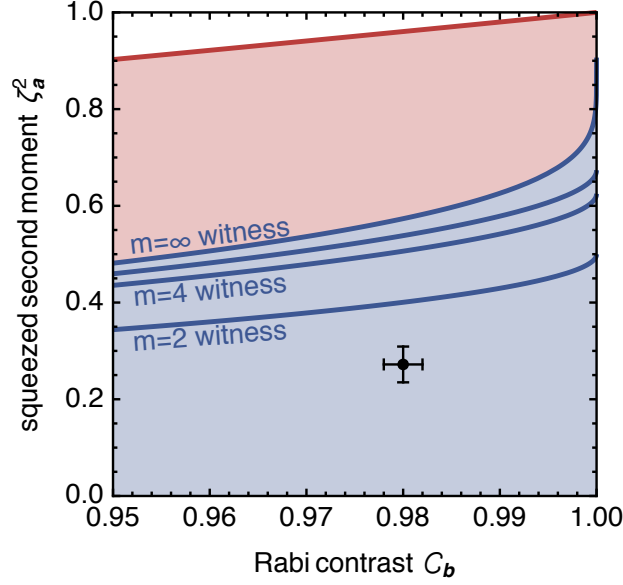


Figure 5.6: Observation of Bell correlations in a BEC with m -setting witnesses. Black: the data set of figure 5.4 expressed in terms of the Rabi contrast C_b and the squeezed second moment ζ_a^2 , with 1σ error bars. Blue shaded region: Bell correlations detected by violation of inequality (5.6). Blue lines: bounds corresponding to the witnesses for $m = 2, 4, 6$ and ∞ settings. Red shaded region: entanglement witnessed by spin squeezing [98, 99]. According to Gaussian statistics, our data set has a $1 - 1.1 \times 10^{-3}$ ($m = 2$), $1 - 1.6 \times 10^{-7}$ ($m = 4$), $1 - 7 \times 10^{-9}$ ($m = 6$), $1 - 2 \times 10^{-10}$ ($m = \infty$) overlap with the blue area below the respective bounds.

from the violation of a witness, consists in assuming Gaussian statistics. Specifically, we assume that C_b is a random variable following a beta distribution on the interval $[-1, 1]$ and ζ_a^2 is an independent random variable following a gamma distribution on $[0, \infty)$, with both mean values and both variances as determined experimentally. This allows us to estimate the likelihood of our conclusion as the overlap of the estimated probability distribution associated to our data set, Fig. 5.7, with the region for which Bell correlations are detected by the witness of interest (blue regions in the Figures). As an example, according to Eq. (5.4) our data set has likelihood of 99.9% of being Bell correlated, Fig. 5.7, while according to the improved witness Eq. (5.6) this is $1 - 2 \times 10^{-10}$. This likelihood can be interpreted as a P value of 10^{-3} , respectively 2×10^{-10} , for rejecting the null hypothesis: “Our data were generated by a state that has no Bell correlations, in the presence of Gaussian noise”.

Using the same approach we can estimate the overlap of our data set with the various k -producibility entanglement areas of Fig. 5.5. We find overlaps of 0.010 for $k = 24$ and 0.046 for $k = 29$, which allow us to rule out 24-producibility at the 1% level and 29-producibility at the 5%-level.

If we do not want to make the additional assumption of Gaussian statistics, the exper-

5. Quantum correlations: Experiments

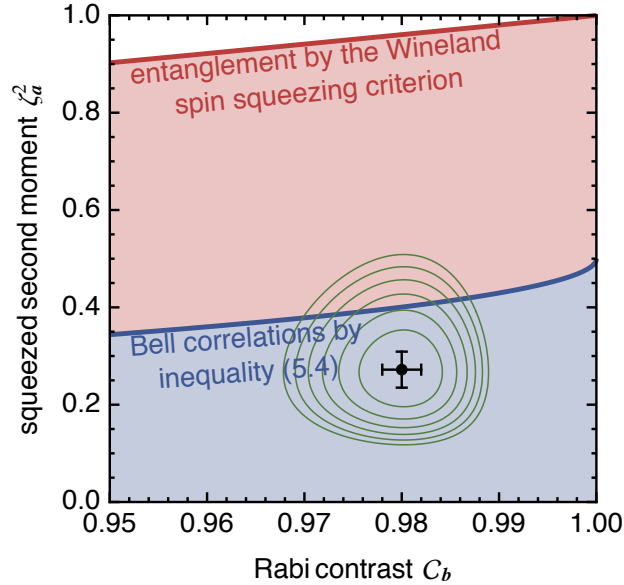


Figure 5.7: Probability distribution compatible with our experimental data set. The green contours contain 90% (innermost), 99%, . . . , 99.9999% (outermost) of the joint probability density for two random variables C_b and ζ_a^2 as described in the text.

imental results may come from any probability distribution compatible with the measurement results. Therefore, the task of estimating the likelihood that a non-Bell-correlated state is responsible for the violation of a witness becomes more difficult, and a limited number of measurements might give no conclusion. In section 4.5.5 we discussed this statistics loophole, and presented a bound on the number of measurement rounds sufficient to exclude with a given confidence non-Bell-correlated states from an observed witness violation. In order to minimize the amount of measurements required to reach our conclusion, we consider the optimal witness among the ones we know, which originates from the inequality Eq. (4.39) with $m \rightarrow \infty$. The statistical analysis we presented show that, for many-body systems ($N \gg 1$), the upper bound on the number of runs M is linear in the number of particles, hence making it reasonable to detect Bell correlations free of the statistical loophole also in systems with a large number of particles. For our experimental parameters, $C_b = 0.98$ and $\zeta_a^2 = 0.272$, a number of measurements per spin of $M/N \approx 80$ is sufficient to reach a confidence level of 99%.

We note once again that the standard deviations of one- and two-body correlation functions decrease instead as the number of particles increases. Therefore, our conclusion does not follow from observing the violation of a witness by a fixed number of standard deviations, as it results from assuming Gaussian statistics. As a concrete example, the experimental point shown in Fig. 5.6 clearly violates the witnesses for $m = 2, 4, \dots, \infty$ by several standard deviations, resulting in an extremely high likelihood

$(1 - 2 \times 10^{-10})$ of having detected Bell correlations under the assumption of Gaussian statistics. However, without this further assumption, the limited number of measurement rounds do not allow us to rule out the possibility that our state is not Bell-correlated with a confidence larger than 14%.

5.2.5 Nonlocality depth

Entangled states can be characterized in terms of their entanglement depth, as presented in section 4.3.2 and shown by the red curves in Fig. 5.5. We may ask whether Bell correlations could be characterized in a similar way, by witnessing their depth. We answered this question in section 4.5.3, where we introduced Bell inequalities for k -partite Bell correlations, and derived from them experimentally accessible witnesses which consist in the inequalities (Eq. (4.56))

$$\zeta_a^2 \geq \frac{2 - \beta_C^k/(2N) - \sqrt{(\beta_C^k/(2N))^2 - C_b^2}}{2}, \quad (5.7)$$

with β_C^k a constant depending on k , whose violation witnesses that the state contains Bell correlations with a depth of (at least) $k + 1$. Note that, once more, Eq. (5.7) involves only the measurements of the two quantities ζ_a^2 and C_b .

We plot in Fig. 5.8 the bounds given by Eq. (5.7), for $k = 1, \dots, 6$, together with the entanglement depth bounds, and the experimentally measured point. A statistical analysis on the (Gaussian) probability distribution estimated experimentally gives a likelihood of 99.9%, 97.5%, 90.3%, 80.8% for 1/2/3-, 4-, 5-, 6-partite Bell correlations, respectively. These likelihoods can be interpreted as, for example, a P value of $1 - 80.8\% = 19.2\%$ for rejecting the null hypothesis: “The experimental data were generated by a state that has no 6-partite Bell correlations, in the presence of Gaussian noise”.

It is clearly of interest to find bounds for higher k 's but, as mentioned in section 4.5.3, the approach we used is likely bound to fail for $k > 6$. The reason is the computational complexity of the task, which might be overcome by taking other routes. Of particular interest is also the question of whether one- and two-body correlators allow for detecting genuine multipartite nonlocality, which we leave as an open problem.

Moreover, it would be interesting to investigate whether better bounds could be obtained by increasing the number of measurement settings per party, in the spirit of what we observe in Fig. 5.6.

5.2.6 Towards a Bell test with a many-body system

We emphasize again that, unlike a Bell inequality, a Bell witness relies on (assuming) the knowledge of the measurements that are performed. Still, if this knowledge is accurate, a violation of the witness certifies that the correlations in the measured state could violate a Bell inequality. For a direct test of the Bell inequalities we discussed, one must be able to address several parties individually. Even if in principle we might want to separate

5. Quantum correlations: Experiments

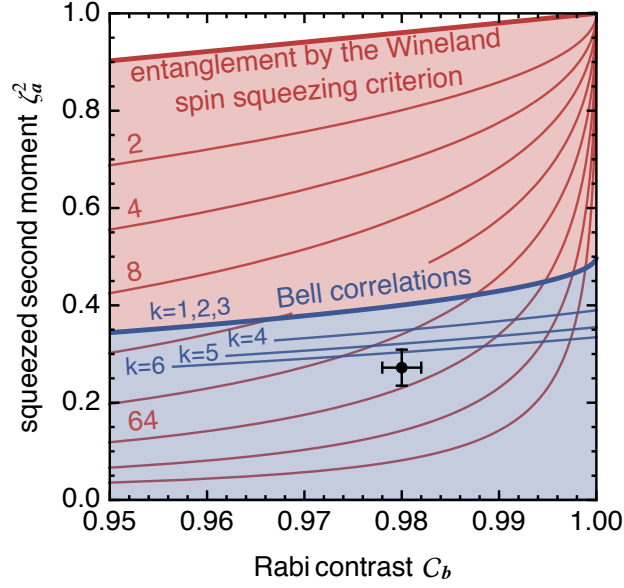


Figure 5.8: Quantification of Bell correlation depth in a spin-squeezed BEC. Black: the data set of figure 5.4 expressed in terms of the Rabi contrast C_b and the squeezed second moment ζ_a^2 , with 1σ error bars. The number of particles is $N = 480$. Blue shaded region: Bell correlations detected by violation of inequality (5.7) for $k = 1$. Red shaded region: entanglement witnessed by spin squeezing [98, 99]. Red lines: limits on ζ_a^2 below which there is at least $(k + 1)$ -particle entanglement [100], increasing in powers of two up to $k = 256$. Blue lines: limits on ζ_a^2 below which there is at least $(k + 1)$ -particle nonlocality, for $k = 1, \dots, 6$.

all spins from each other, already separating the particles into just two well-identifiable groups could in principle already be sufficient to test a bipartite Bell inequality.

In a BEC, for instance, the atoms could be partitioned into two different spatial locations by means of a state-independent potential. An adequate bipartite Bell inequality could then be tested by performing local measurements on these two groups of atoms. If a violation is observed, it would be device-independent, and it would certify that proper measurements have been performed and that the outcome statistics observed could not be described in terms of pre-established agreements (local-hidden-variable model).

Note that for continuous variables (CVs) it was shown that Gaussian measurements on non-Gaussian entangled states allow to violate a Bell inequality [143–145]. Alternatively, a non-deterministic violation of a Bell inequality is allowed by performing non-Gaussian measurements (such as conditioned Gaussian measurements) on Gaussian CV states [145, 146]. However, Bell himself argued that no violation of a Bell inequality can appear by performing Gaussian measurements on Gaussian states [147] (pp. 37 and 198). However, it was shown both theoretically [148] and experimentally [149] that this “no-go” theorem can be circumvented provided one trusts the measurement system, as we have been doing with our Bell correlation witness.

For our current experimental apparatus, the fact that our detection system cannot resolve single atoms implies that we are restricted to Gaussian measurements. Since the typical spin-squeezed states we prepare are close to CV Gaussian states, as the curvature of the Bloch sphere can be neglected for mild squeezing, we conclude that only the violation of a bipartite witness for Bell correlations is possible. This witness would be derived from a Bell inequality, with further assumptions on the measurements. Alternatively, the one-axis twisting Hamiltonian allows to prepare states beyond Gaussian states (*e.g.* over-squeezed states that wrap around the Bloch sphere), if the evolution time is long enough. In this situation we might be in the condition to violate a Bell inequality.

In the situation of a strict Bell test one might be interested in closing the detection loophole, and therefore post-selection of the data would not be allowed. Furthermore, one might still need to rely on the assumption that atoms belonging to different parties do not communicate. This is similar to the assumption that the spins do not communicate while testing a witness. This assumption could be relaxed by separating the parties sufficiently to allow for measurements to be performed at space-like separations.

5.2.7 Conclusions and outlook

With the experiment presented in this section, we have shown the possibility of preparing BECs in spin-squeezed states, where the correlations among the atoms are strong enough to violate a Bell inequality. This conclusion, unprecedented for more than a few particles, has been reached with the help of a Bell correlation witness that requires collective measurement only, which can be applied to other many-body systems as well.

We performed a statistical analysis of the experimental data, and discussed how a finite number of measurements could prevent us from drawing any conclusions about the observed results. To circumvent this statistics loophole, we propose to either introduce the hypothesis that measurements come from a Gaussian distribution, or to perform a much larger number of measurements proportional to the number of parties in the system.

Similarly to entanglement, which can be quantified in terms of k -producibility, our study raises the question of how our witness can be extended to quantify the degree of nonlocality or to detect genuine multipartite nonlocality. We give a partial answer to this question by introducing witnesses able to rule out up to 6-partite nonlocality.

The possibility of applying our method to other physical systems motivates the search for new multipartite Bell inequalities and witnesses, which might be violated by states with a lower amount of squeezing or by completely different states. In this direction, we derived Bell inequalities involving an arbitrary number of measurements per party, and the associated witnesses, to finally show that they outperform previously known inequalities.

In future experiments, we see the possibility of violating a Bell inequality with a many body system. This could be realized, for example, by separating the particles into spatially distinct regions, and then performing local measurements. Cold atoms in optical lattices, or ion crystals [150], might be well-suited systems for such investigations.

5. Quantum correlations: Experiments

Finally, we mention that Bell correlations in many-body systems, apart from being of fundamental interest, might find useful practical applications. In fact, since Bell correlations are a resource more powerful than entanglement, they could allow for quantum information tasks beyond quantum metrology, *e.g.* for certifiable randomness generation. Although Bell-correlation-based randomness has been extracted from two-qubit systems [9], an implementation in a many-body system would considerably increase the amount of randomness per experimental run.

Recently, the Kasevich group reported a violation of our witness inequality Eq. (5.3) with approximately half a million particles [151]. Their experiment was performed on a thermal ensemble of ^{87}Rb atoms at $25\ \mu\text{K}$, also prepared in a spin-squeezed state. Contrary to our case, their atoms are optically trapped inside a cavity, which is used to perform quantum non-demolition measurements of the spin components and the state preparation. This allows them to generate states with around $-15\ \text{dB}$ of noise suppression with respect to a coherent spin state, resulting in a violation of the witness by 124 standard deviations. Remember however that, according to our investigation, to close the statistics loophole the number of measurements required grows linearly with N . In this sense, our experiment, even if dealing with lower squeezing, is (maybe counterintuitively) closer to a violation of the witness without statistic loophole.

5.3 Spatial entanglement patterns and Einstein-Podolsky-Rosen steering in a Bose-Einstein condensate

It is interesting to note that, in the variety of entangled states that are routinely prepared in ultracold atomic systems [12], correlations between particles have almost always been inferred from collective measurements on the entire system [2, 3]. In the case of BECs it is impossible even in principle to address the atoms individually: they are identical particles that occupy the same spatial mode. For this reason, several authors have questioned whether the concept of entanglement in systems of indistinguishable particles is fully legitimate and useful for quantum information tasks beyond metrology (For a brief review of the debate, see Ref. [22]).

A significant result in this context would be to directly detect the correlations present in the system, which would require to spatially separate the atoms, and to perform local measurements on them. To make a step in this direction, we employ an experimental procedure consisting of taking high-resolution images of the atomic density distribution. On these images we can define local spin observables and measure the correlations between them. This allows us to reveal the underlying correlations among the parties of our many-body system. For simplicity, we consider a bipartite scenario and, due to technical limitations, we are restricted to taking the same measurements on the two parties. This scenario is well suited to reveal entanglement and EPR correlations between the two partitions of our many-body system using the criteria presented in section 4.3.1 and 4.4.1

Previously, entanglement (nonseparability) was observed between spatially separated atomic ensembles [95, 152–154] and between individually addressable atoms in optical lattices [155, 156]. On the other hand, EPR steering has been extensively explored with optical systems [4]. With massive particles it has been observed between spin modes without spatial separation [20] and between two individual atoms [10]. Demonstrating the EPR paradox with ensembles of massive particles is interesting as it puts quantum physics to a stringent test in a new regime of increasingly macroscopic systems [4]. Moreover, it opens up new perspectives for applications of such systems in quantum metrology and one-sided device-independent quantum information tasks, which exploit EPR steering as a resource [157].

In this section we report the violation of an entanglement criterion, and of a criterion for EPR steering, by detecting correlations between spatially separated bipartitions of the spins of about 600 atoms in a spin-squeezed Bose-Einstein condensate. This shows also how entanglement of indistinguishable particles can be extracted into distinguishable spatial modes, and used for quantum information tasks beyond metrology. These results have been published in Ref. [27]. Similar experiments were performed by the Oberthaler and Klempt groups and published back-to-back with our work [158, 159].

5. Quantum correlations: Experiments

5.3.1 From indistinguishable particles to distinguishable modes

In this study we want to investigate the correlations among the indistinguishable atoms of a BEC in a spin-squeezed state. As pointed out in the theoretical work of Killoran *et al.* [22], the presence of entanglement in an ensemble of indistinguishable particles can be unambiguously confirmed by extracting it into spatially separated modes.

In order to access spatially separated modes in the BEC, we use the sequence illustrated in Fig. 5.9a. Initially, Fig. 5.9a1, a BEC with $N \approx 600$ atoms is prepared in a spin-squeezed state as explained in paragraph 5.1.2. We obtain typically $-3.8(2)$ dB of spin squeezing according to the Wineland criterion Eq. (5.2) (alternatively, we can prepare the BEC in a coherent spin state, where the atomic internal states are uncorrelated). As mentioned before, the one-axis twisting dynamics result in a spin-squeezed state tilted against the horizontal direction. In order to reduce the sensitivity of the spin-squeezed state to magnetic field fluctuations happening during its expansion, the state is rotated around its center by 13° to align it with the equator (see Fig. 5.9b). Afterwards, the currents for the magnetic trap are ramped down in 0.4 ms, and the cloud is let expanding during its free-fall for 2.2 ms, Fig. 5.9a2. This expansion is nearly spin-independent since collisional interactions are very similar for $|1\rangle$ and $|2\rangle$ and leads to a magnification of the atomic cloud. During time-of-flight, the magnetic field is kept at ≈ 3.23 G to reduce differential phase noise. Next, we set the axis \vec{n} of the spin components to be measured by applying a Rabi rotation pulse to the entire atomic cloud, Fig. 5.9a3. For the $\pm\hat{S}_x$ measurements, the state is rotated by $\pm\pi/2$ around the direction on the equator orthogonal to the mean spin direction (*i.e.* around the y -axis). For the \hat{S}_z measurement, no rotation is applied, and for the \hat{S}_y measurement, a $\pi/2$ rotation around the mean spin direction is applied (*i.e.* around the x -axis). Then, the magnetic field is rotated in 0.2 ms to point along the imaging beam and reduced to ~ 1 G. Immediately thereafter, we record two high-resolution absorption images of the atomic density distributions in states $|2\rangle$ and $|1\rangle$ by illuminating the atomic cloud twice with a resonant laser beam. The imaging pulses project the spin state and simultaneously localize the atoms in well-defined positions. Fig. 5.9c shows typical absorption images taken in this way (the atom number noise levels are $\sigma_{N_{1,\text{det}}} = 3.5$ atoms and $\sigma_{N_{2,\text{det}}} = 3.3$ atoms per whole picture). This experimental sequence is repeated ~ 2500 times, alternating the measurement direction \vec{n} along either x , y or z . To reduce the effect of possible technical long-term drifts the data acquisition is divided into small subsets. In each subset, 4 measurements along $+x$ and 4 measurements along $-x$ give $|\langle\hat{S}_x\rangle|$, followed by 70 measurements along y and 60 measurements along z , which are used to compute variances.

Instead of considering a global collective spin for the entire BEC, as was done in the previous experiments, we aim to construct local observables. We define two regions A and B to be analyzed on all pairs of absorption images, Fig. 5.9c, and we define for each a local collective spin, $\hat{S}_{\vec{n}}^A$ and $\hat{S}_{\vec{n}}^B$ respectively. The two regions are defined by two binary masks, one for state $|1\rangle$ and the other for state $|2\rangle$. These are positioned according to the ensemble average (*i.e.* average over all images) of the two atomic densities, and

5.3 Spatial entanglement patterns and EPR steering in a BEC

then applied to all individual pictures. The counted atom numbers N_1^A and N_2^A in region A constitute a single-shot projective measurement of $\hat{S}_{\vec{n}}^A$. Similarly, the counted atom numbers in region B yield a measurement of $\hat{S}_{\vec{n}}^B$.

Our finite optical resolution and the motion of atoms during the imaging pulses lead to an uncertainty in the atomic position, as discussed in chapter 3. For this reason, spins near the boundary have only partial overlap with the region A or B , which needs to be taken into account [160]. Furthermore, spins overlapping with both A and B lead to detection crosstalk, which we reduce by leaving a gap of typically 1 pixel between the two regions. All these effects complicate the definition of a local collective spin, as we will show in the next paragraph.

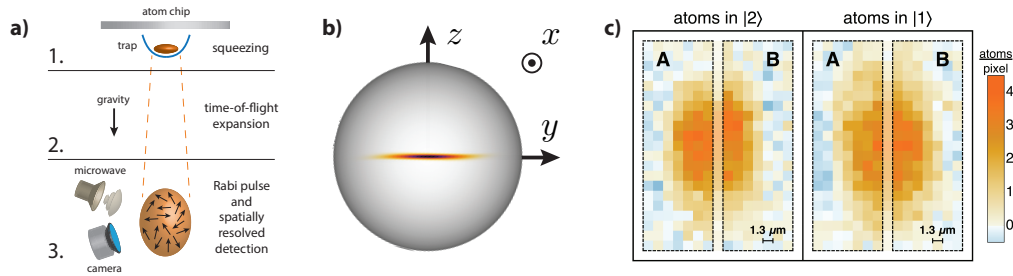


Figure 5.9: Extracting entanglement from spatially separated regions of a BEC. **a:** Experimental sequence. Step 1 consists in the preparation of a BEC in a spin squeezed state on an atom chip. In step 2 the trapping potential is switched off and the BEC expands. In step 3, a Rabi rotation pulse is applied to select the spin quadrature $\hat{S}_{\vec{n}}$ to be measured, followed by recording two high-resolution absorption images of the atomic density distributions in states $|1\rangle$ and $|2\rangle$. **b:** Illustration of the spin-squeezed state on a sphere (Wigner function, representing the quantum fluctuations of the spin) and definition of the axes $\vec{n} \in \{x, y, z\}$ used in the measurement of the entanglement and EPR steering criteria. **c:** Single-shot absorption images of the atomic densities in $|2\rangle$ and $|1\rangle$, showing example regions A and B used to define the collective spins \hat{S}^A and \hat{S}^B entering in the entanglement and EPR steering criteria.

5.3.2 Local collective spins

In considering a region A on the absorption images, we would be tempted to define the local collective spin as $\sum_{i \in A} \vec{s}_i^A$, where the index i runs over all spins contained in A . However, in the case where the detected spin signal has some spatial extent, for example because of the point-spread function of the imaging system, the above definition of local collective spin needs to be corrected because the spin noise gets reduced and the usual spin commutation relations are not satisfied.

This problem has already been observed in experiments relying on atom-light interactions to detect and manipulate collective spin systems [160, 161]. In particular, it has been studied that atoms inside a cavity can couple with different interaction strengths to the optical mode, depending on their position. In this nonuniform scenario, the proper

5. Quantum correlations: Experiments

definition of the collective spin is given by $\vec{S} = \eta_{\text{eff}}^{-1} \sum_i \eta_i \vec{s}_i$, where \vec{s}_i is the spin of the i -th particle, η_i its coupling strength and $\eta_{\text{eff}} = \sum_i \eta_i^2 / \sum_i \eta_i$. Following the same argument, we define our local spin as

$$\vec{S}^A = \frac{1}{\eta_{\text{eff}}^A} \sum_i \eta_i^A \vec{s}_i, \quad (5.8)$$

where η_{eff}^A and η_i^A depend on the density distribution $g(\vec{x}, \vec{x}_i)$ of the i -th atom, and on the probability density function $\rho(\vec{x}_i)$ for its position \vec{x}_i . As the atoms in a BEC occupy the same spatial mode, we take $\rho(\vec{x}_i)$ to be independent on i . In appendix C we show that

$$\eta_i^A = \int_A g(\vec{x}, \vec{x}_i) dx \equiv f^A(\vec{x}_i) \quad \frac{\int_{-\infty}^{+\infty} \rho(\vec{x}_1) (f^A(\vec{x}_1))^2 d\vec{x}_1}{\int_{-\infty}^{+\infty} \rho(\vec{x}_1) f^A(\vec{x}_1) d\vec{x}_1} = \eta_{\text{eff}}^A, \quad (5.9)$$

Following these definitions, a spin projection measurement is given by

$$S_{\vec{\alpha}}^A = \frac{1}{\eta_{\text{eff}}^A} \left(\frac{N_1^A - N_2^A}{2} \right), \quad (5.10)$$

where $\vec{\alpha}$ is the measurement axis along which the spin is projected and $N_{1,2}^A$ are the number of atoms counted in region A . As we prove in appendix C, for a coherent spin state we obtain the expected result

$$\frac{4\text{Var}(S_z^A)}{N} = 1, \quad (5.11)$$

independently of the choice of the region A , showing that the definition Eq. (5.8) allows us to associate local spins to very small regions, in principle even of a single pixel size. This is confirmed by looking at the experimental data in Fig. 5.10.

We evaluate Eq. (5.9) for our experimental situation taking ρ to be the normalized ($\int \rho(\vec{x}) d\vec{x} = 1$) BEC density for one of the states and $g(\vec{x}, \vec{x}_i)$ the Gaussian point spread function of our imaging system. The analytical result is shown in Fig. 5.10, together with experimental data (see also Ref. [158]). Since the mean densities of the two spin states are slightly different, in the analysis we use the one which gives the smallest η_{eff}^A as a conservative value. The same approach is followed to compute η_{eff}^B .

5.3.3 Spatial entanglement patterns

In our experiment, we want to study the correlations between the two collective spins \hat{S}^A and \hat{S}^B , that describe the internal state of atoms in regions A and B , respectively. To detect entanglement we use the criterion of Giovannetti *et al.* [97], who have shown that for all separable states (see also section 4.3.1)

$$\mathcal{E}_{\text{Ent}} = \frac{4 \text{Var}(g_z \hat{S}_z^A + \hat{S}_z^B) \text{Var}(g_y \hat{S}_y^A + \hat{S}_y^B)}{\left(|g_z g_y| |\langle \hat{S}_x^A \rangle| + |\langle \hat{S}_x^B \rangle| \right)^2} \geq 1, \quad (5.12)$$

5.3 Spatial entanglement patterns and EPR steering in a BEC

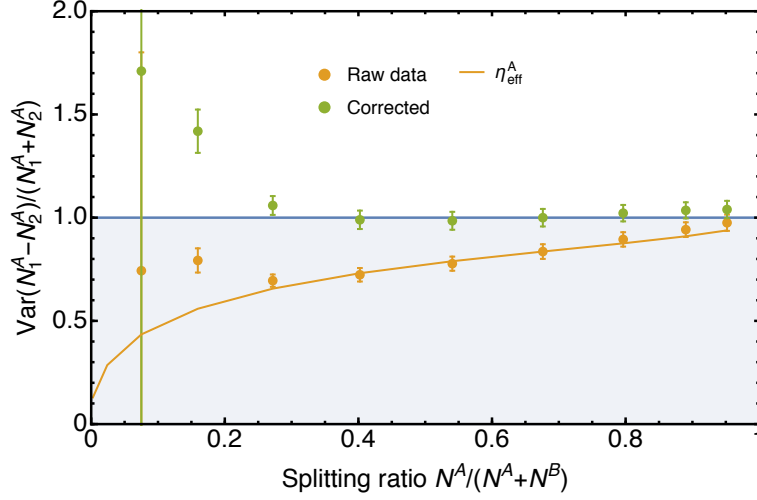


Figure 5.10: Local spin fluctuations for a coherent spin state. Normalized fluctuations of the local spin in region A for different horizontal positions of the gap (see Fig. 5.9c), corresponding to different splitting ratios $N^A/(N^A + N^B)$, where $N^A = N_1^A + N_2^A$ and similarly for N^B . Orange dots: fluctuations evaluated using the measured atom number (raw data). For regions A smaller than the entire cloud (splitting ratios < 1) the fluctuations are suppressed by a factor η_{eff}^A (orange line), as expected from Eq. (5.9). Green dots: the correct definition of the local spin Eq. (5.10) gives the expected fluctuations due to projection noise of uncorrelated atoms, Eq. (5.11). For region B the behavior is similar. For very small regions (splitting ratios < 0.3) technical noise increases the fluctuations above the coherent spin state projection noise.

where $\text{Var}(\cdot)$ denotes the variance and g_z, g_y , are real parameters that can be optimized to minimize \mathcal{E}_{Ent} . Therefore, $\mathcal{E}_{\text{Ent}} < 1$ is a sufficient condition to certify entanglement (nonseparability) between A and B .

The variances in Eq. (5.12) quantify the uncertainty with which an observer in A can predict (infer) the outcome of a spin measurement in B , based on a corresponding measurement on her own system, and are therefore called inferred variances. Since \hat{S}_z and \hat{S}_y do not commute, measuring both inferred variances requires repeated experiments on identically prepared systems.

As described in the previous paragraph, the component $\hat{S}_z^A = \frac{1}{\eta_{\text{eff}}^A} \frac{(\hat{N}_1^A - \hat{N}_2^A)}{2}$ is evaluated from the atom numbers counted in region A , and a similar approach holds for \hat{S}_z^B . Any other spin component is measured by applying appropriate spin rotations before detection. Raw data are not corrected from imaging non-linearities or from clock-shifts (which are compensated by the echo pulse), but only from detection noise as explained in appendix C.4.

To detect entanglement between regions A and B we evaluate Eq. (5.12) for different horizontal positions of the gap (see Fig. 5.9c), corresponding to different splitting ratios $N^A/(N^A + N^B)$, where $N^A = N_1^A + N_2^A$ and similar for N^B (Fig. 5.11a, green dots). For a wide range of splitting ratios we observe a violation of the inequality in Eq. (5.12),

5. Quantum correlations: Experiments

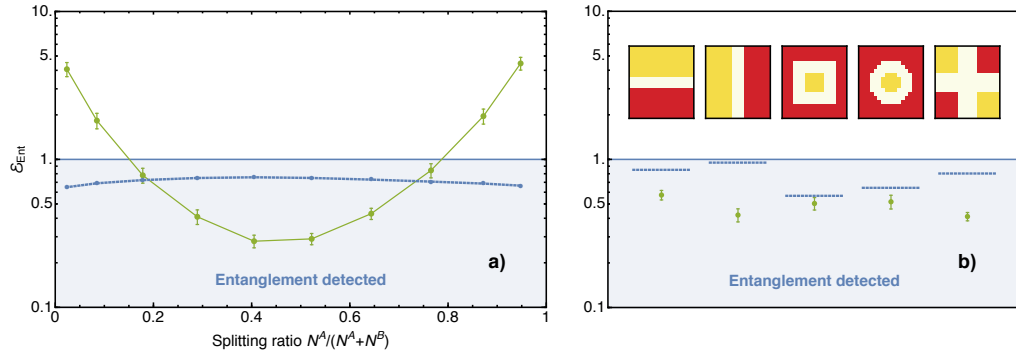


Figure 5.11: Spatial entanglement patterns in the atomic cloud. **a:** Entanglement criterion Eq. (5.12) evaluated for a spin-squeezed BEC (green points) for different horizontal positions of the gap between regions A and B (see Fig. 5.9c), corresponding to different splitting ratios $N^A/(N^A + N^B)$. Lines are a guide to the eye and error bars indicate one standard error of the mean. The blue points show the maximum violation that could be explained by detection crosstalk. **b:** Entanglement between regions of different shapes (A =yellow, B =red) in a spin-squeezed BEC. The pixel pattern used for the analysis is illustrated above the respective data points, and the blue segments show the corresponding maximum violation expected by crosstalk.

which goes far below the value that could be explained by detection crosstalk. This proves that the two local spins \hat{S}^A and \hat{S}^B are entangled. The extracted entanglement derives from the quantum correlations among the indistinguishable atoms in the initial state [22], since the expansion of the cloud, the spin rotation and detection do not create such correlations, as it is confirmed by performing similar measurements with coherent spin states (see section 5.3.6).

An intriguing feature of our approach to extract entanglement [22] from a many-body state is that the subsystems can be defined a posteriori on the images. This is in contrast to other experiments where the subsystems are defined by the experimental setup [95, 152–154] or by the source of the state [4, 104]. We exploit this feature to detect entanglement between regions A and B patterned in a variety of different shapes, see Fig. 5.11b. The fact that we observe entanglement between all such regions reflects the symmetry of the underlying many-body quantum state: the quantum state of the indistinguishable bosons in the condensate has to be totally symmetric under particle exchange. Consequently, each atom is entangled with all other atoms, and the entanglement extends over the entire atomic cloud. In experiments with atoms in optical lattices, entanglement between different spatial bipartitions was observed by measuring entanglement entropy or concurrence, using systems of up to 10 atoms that were individually addressed [155, 156]. By comparison, our experiment reveals entanglement in ensembles of hundreds of atoms using inequalities that apply in the continuous variable limit.

5.3 Spatial entanglement patterns and EPR steering in a BEC

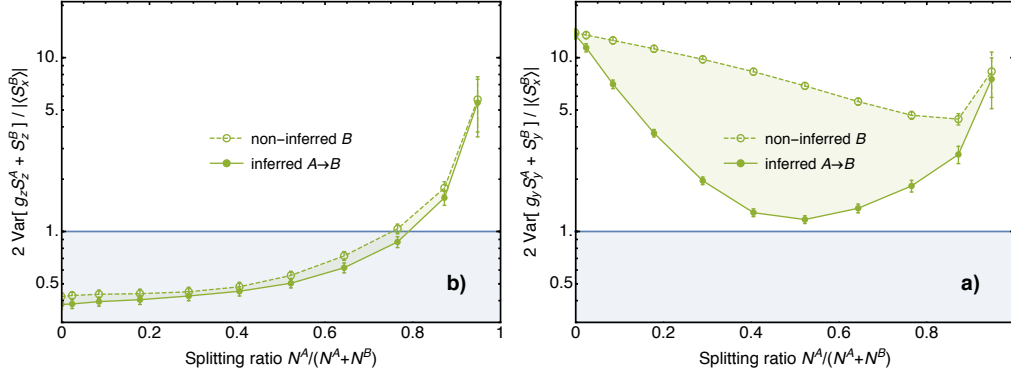


Figure 5.12: Reduction of the normalized inferred variances. **a:** Normalized variance $2 \text{Var}(g_z \hat{S}_z^A + \hat{S}_z^B) / |\langle \hat{S}_x^B \rangle|$, evaluated by non-inferring (empty circles) or by inferring $A \rightarrow B$ (filled circles) in a spin-squeezed BEC, for different horizontal positions of the gap (see Fig. 5.9c), corresponding to different splitting ratios $N^A / (N^A + N^B)$. Lines are a guide to the eye and the shaded regions are the reduction of the uncertainty product in replacing the non-inferred variances with the inferred ones. The vertical blue line is the bound expected for an ideal coherent state. For this quadrature the minimum appears for zero splitting ratio, as the splitting process introduces fluctuations reducing squeezing. **b:** Similar plot as in (a), for the normalized variance $2 \text{Var}(g_y \hat{S}_y^A + \hat{S}_y^B) / |\langle \hat{S}_x^B \rangle|$. For this quadrature the minimum appears for intermediate splitting ratios.

5.3.4 Einstein-Podolsky-Rosen steering

If correlations between the parties A and B are strong enough, an observer in A can predict the result of non-commuting measurements performed by B with a product of the inferred variances below the Heisenberg uncertainty bound for system B , *i.e.* there is a violation of the relation [4] (see also section 4.4.1)

$$\mathcal{E}_{\text{EPR}}^{A \rightarrow B} = \frac{4 \text{Var}(g_z \hat{S}_z^A + \hat{S}_z^B) \text{Var}(g_y \hat{S}_y^A + \hat{S}_y^B)}{|\langle \hat{S}_x^B \rangle|^2} \geq 1. \quad (5.13)$$

Note that if there are no correlations between A and B , the variances in Eq. (5.13) are minimized for $g_z = g_y = 0$, for which the spin uncertainty relation for B is recovered. In the presence of a violation of Eq. (5.13), B must conclude that he is in the paradoxical situation considered by EPR, where A is able to predict his measurement results without any interaction.

Note that a violation of Eq. (5.12) does not imply a violation of Eq. (5.13), while the converse is true. This reflects the fact that entanglement is necessary but not sufficient for EPR steering, and that they are inequivalent types of correlations [1, 85]. Moreover, the asymmetry between A and B present in Eq. (5.13) implies that if A can steer B (denoted $A \rightarrow B$), then not necessarily B can steer A ($B \rightarrow A$), as investigated both theoretically [84, 85, 103] and experimentally [104, 105] in optics.

5. Quantum correlations: Experiments

In Figure 5.12 we separately plot the two inferred variances appearing in Eq. (5.13), normalized by $|\langle \hat{S}_x^B \rangle|/2$ such that they are unity for a coherent spin state. As it can be seen from Fig. 5.12b, inferring plays a major role in reducing the noise along the anti-squeezing direction y . On the contrary, inferring the squeezing direction z has little effect, Fig. 5.12a.

The correlations in our system are strong enough to demonstrate an EPR paradox: Fig. 5.13a shows a measurement of the EPR criterion Eq. (5.13) for horizontal splitting of the cloud and different positions of the gap. We observe EPR steering $A \rightarrow B$ (green data points) for intermediate splitting ratios. For comparison, we evaluate the spin uncertainty relation $4 \text{Var}(\hat{S}_z^B) \text{Var}(\hat{S}_y^B)/|\langle \hat{S}_x^B \rangle|^2 \geq 1$ for system B , illustrating the reduction of the uncertainty product when replacing the non-inferred variances with the inferred ones.

As can be seen in Eq. (5.13), EPR steering is an asymmetric concept. By relabeling region A as B and vice versa, we can invert the roles of the steering and steered systems. This inverted scenario also shows EPR steering $B \rightarrow A$ (red data points in Fig. 5.13a). The asymmetry between the curves indicates the presence of technical noise in our system [84, 104, 162]. For intermediate splitting ratios we observe two-way steering $A \leftrightarrow B$, a necessary (but insufficient) prerequisite for observing the even stronger Bell correlations [85]. We note that we also observe EPR steering if we do not subtract detection noise from the inferred variances, and also for vertical instead of horizontal splitting of the cloud.

Finally, we characterize the robustness of the observed EPR steering $A \rightarrow B$ to a variation of the gap size. We fix the central position of the gap such that the splitting ratio is 0.40 (the ratio maximizing steering $A \rightarrow B$ and $B \rightarrow A$ in Fig. 5.13a) and change the gap width symmetrically with respect to this position (Fig. 5.13c). We observe that EPR steering vanishes for large widths of the gap, where the size of the steered system is considerably reduced (Fig. 5.13b).

We have also performed measurements similar to Fig. 5.11 and Fig. 5.13 with the BEC initially prepared in a coherent spin state, showing no statistically significant violations of Eqs. (5.12) and (5.13) beyond detection crosstalk (see section 5.3.6).

5.3.5 Crosstalk

Limitations in the detection scheme, such as the finite optical resolution or the motion of atoms during imaging, translate into an uncertainty in the atomic position. As a consequence, spins near the boundary between A and B contribute a signal to both regions. This detection crosstalk leads to classical correlations between the two regions, which could result in an apparent violation of the entanglement and EPR criteria.

In particular, for the case of a coherent spin state with equal superposition we evalu-

5.3 Spatial entanglement patterns and EPR steering in a BEC

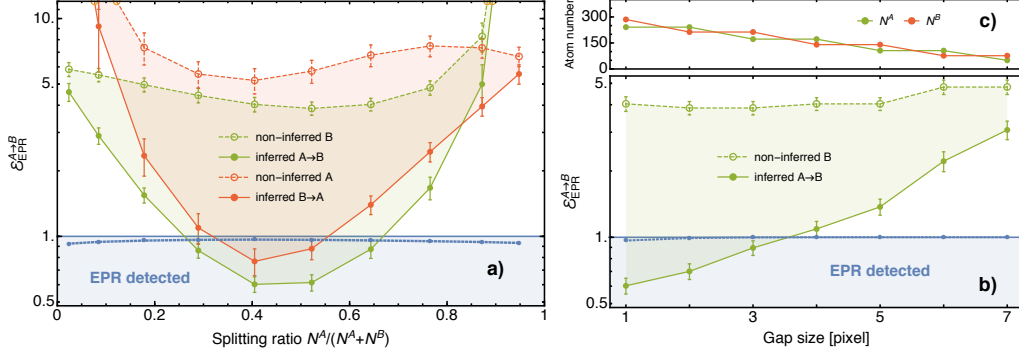


Figure 5.13: Observation of Einstein-Podolsky-Rosen steering. **a:** EPR steering criterion Eq. (5.13), evaluated for steering $A \rightarrow B$ (green filled circles) and $B \rightarrow A$ (red filled circles) in a spin-squeezed BEC, for different horizontal positions of the gap (see Fig. 5.9c), corresponding to different splitting ratios $N^A/(N^A + N^B)$. EPR steering is strongest for intermediate splitting ratios. Empty circles: spin uncertainty relation involving the product of non-inferred variances in region B (green) and A (red). Lines are a guide to the eye and the shaded regions are the reduction of the uncertainty product in replacing the non-inferred variances with the inferred ones. Blue points: maximum violation that could be explained by detection crosstalk. **b:** EPR steering $A \rightarrow B$ for different widths of the gap in Fig. 5.9c. The center of the gap is fixed to the position showing maximum EPR steering in Fig. 5.13a for a width of one pixel. Even for increased gap size we find a significant violation of the bound, confirming that the correlations cannot be explained by detection crosstalk between the regions. Lines and shaded regions as in (a). **c:** Atom number in regions A and B as a function of the gap size.

ate the EPR criterion for the optimal g 's (see appendix C)

$$\begin{aligned}
 & \frac{4 \left(\text{Var}(S_z^B) - \text{Cov}^2(S_z^A, S_z^B)/\text{Var}(S_z^A) \right) \left(\text{Var}(S_y^B) - \text{Cov}^2(S_y^A, S_y^B)/\text{Var}(S_y^A) \right)}{|\langle S_x^B \rangle|^2} = \\
 & = \frac{\left(\left(\int_{-\infty}^{+\infty} \rho(\vec{x}_1) f^A(\vec{x}_1) f^B(\vec{x}_1) d\vec{x}_1 \right)^2 - \int_{-\infty}^{+\infty} \rho(\vec{x}_1) (f^A(\vec{x}_1))^2 d\vec{x}_1 \int_{-\infty}^{+\infty} \rho(\vec{x}_1) (f^B(\vec{x}_1))^2 d\vec{x}_1 \right)^2}{\left(\int_{-\infty}^{+\infty} \rho(\vec{x}_1) (f^A(\vec{x}_1))^2 d\vec{x}_1 \right)^2 \left(\int_{-\infty}^{+\infty} \rho(\vec{x}_1) f^B(\vec{x}_1) d\vec{x}_1 \right)^2}.
 \end{aligned} \tag{5.14}$$

Note that this quantity is independent of N , and the asymmetry between A and B in the denominator. It is important to realize that an apparent violation of the EPR criterion can occur in the presence of crosstalk but also if the fluctuations in the individual regions are not properly estimated, which is already taken into account by the definition of collective spin Eq. (5.8). Since Eq. (5.14) includes both effects, to isolate the apparent EPR violation caused by detection crosstalk, we divide it by $(\eta_{\text{eff}}^B)^2$. For our experimental parameters we estimate that for a gap of one pixel, classical correlations originating from detection crosstalk between the two regions cannot decrease the EPR criterion below 0.94 for the splitting ratios of our interest, see Fig. 5.14. This indicates that this effect is

5. Quantum correlations: Experiments

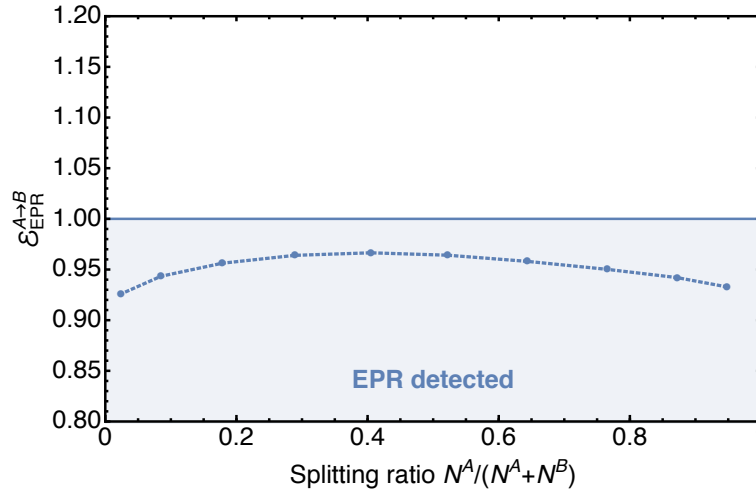


Figure 5.14: EPR violation due to detection crosstalk between regions A and B . Crosstalk for different horizontal positions of the gap (see Fig. 5.9c), corresponding to different splitting ratios $N^A / (N^A + N^B)$. The blue dots correspond to Eq. (5.14) divided by $(\eta_{\text{eff}}^B)^2$.

small compared to the observed EPR steering in Fig. 5.13.

The same idea has been applied to find the apparent violation of the entanglement criterion due to crosstalk. Since this criterion is much more sensitive to correlations between regions A and B than the EPR criterion, detection crosstalk gives a larger apparent violation in this case, see Fig. 5.11. For the measurements performed on a spin-squeezed state, Fig. 5.11 and Fig. 5.13, the observed violation of the entanglement and EPR criteria cannot be explained by classical crosstalk between the regions.

5.3.6 Coherent state measurements

In addition to the data for a spin squeezed state presented in Fig. 5.11 and Fig. 5.13, we have performed measurements with a BEC in a coherent spin state (CSS). This state is prepared by a single $\pi/2$ -pulse in the trap. In contrast to the spin squeezed state, the demixing-remixing sequence is omitted and the atoms are directly released from the trap. The readout of the different spin directions is done in the exact same way as in case of the spin squeezed state. The measured entanglement and EPR steering parameters we find for this state are shown in Fig. 5.15

The coherent state shows no EPR steering. It is also compatible with no entanglement for all splitting ratios, except one which does not have a very large statistical significance (1.7 sigma below the bound).

5.3 Spatial entanglement patterns and EPR steering in a BEC

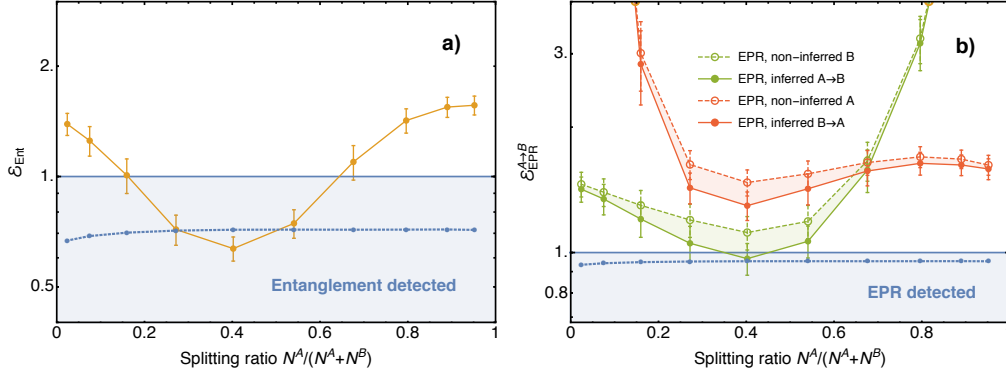


Figure 5.15: Measurement of entanglement and EPR criteria for a BEC in a CSS. a: Entanglement criterion Eq. (5.12) evaluated for a CSS and different horizontal positions of the gap between regions A and B (see Fig. 5.9c), corresponding to different splitting ratios $N^A/(N^A + N^B)$. **b:** EPR steering criterion Eq. (5.13), evaluated for steering $A \rightarrow B$ (green filled circles) and $B \rightarrow A$ (red filled circles) in a CSS, for different splitting ratios $N^A/(N^A + N^B)$. Empty circles: spin uncertainty relation involving the product of non-inferred variances in region B (green) and A (red). Lines are a guide to the eye and the shaded regions are the reduction of the uncertainty product in replacing the non-inferred variances with the inferred ones. Note that this reduction is much smaller than in the case of a spin-squeezed state, Fig. 5.13.

5.3.7 Conclusions and outlook

With the experiments presented in this section we have shown how correlations among indistinguishable particles can be revealed unambiguously by extracting them into spatially distinct modes. This conclusion has been reached by taking images with high spatial resolution of an expanded BEC in a spin-squeezed state, on which local observables can be defined. For pairs of regions, we see that the local collective spins are entangled strongly enough to observe EPR steering.

From a practical perspective, our method can be used for quantum metrology of electromagnetic field patterns. Consider an applied field that shifts the spin components \hat{S}_y^B and \hat{S}_z^B with respect to \hat{S}_y^A and \hat{S}_z^A . The EPR entanglement allows one to detect this shift in the yz -plane with an uncertainty characterized by the product of the inferred variances. The EPR parameter $\mathcal{E}_{\text{EPR}}^{A \rightarrow B} < 1$ quantifies by how much this measurement improves over the Heisenberg uncertainty bound for \hat{S}^B and is thus a direct measure of the metrological enhancement provided by the EPR entanglement. Since our imaging method allows us to define the regions A and B a posteriori in a variety of shapes (see Fig. 5.11), a single dataset could be used to analyze dipole, quadrupole and more complex patterns of the applied field. This is different from other field sensing methods where the pattern is defined by the state preparation [14, 163].

Beyond metrology, EPR steering is a resource for one-sided device-independent quantum information tasks [157]. The asymmetry of the steering concept allows tasks such as quantum teleportation, entanglement swapping, or randomness certification to

5. Quantum correlations: Experiments

be performed in a situation where one of the involved parties can be trusted but not the other. An interesting perspective in this context is to distribute the correlations over macroscopic distances by splitting the atomic cloud with a double- or multi-well potential, exploiting the full control of BEC wavefunctions provided by the atom chip [24].

Furthermore, our study raises the question of whether Bell correlations could also be observed between spatially separated regions. While the EPR paradox can be demonstrated with Gaussian states and measurements and identical measurement settings in A and B , a violation of a Bell inequality would require non-Gaussian states or measurements as well as the ability to measure different spin components in the two regions in a single run of the experiment [5]. This could be achieved by rotating the collective spins \hat{S}^A and \hat{S}^B independently with on-chip microwave near-fields, followed by atomic fluorescence detection with single-atom resolution. In summary, our results open up a variety of new perspectives for quantum science and technology with massive many-body systems.

6

Summary and outlook

In this Chapter we summarize the main experimental and theoretical results presented in this thesis. Finally, we give an outlook on future perspectives and possible interesting research directions.

6.1 Summary

In this thesis I reported the experimental investigation of nonclassical correlations in many-body systems. Our studies have been performed on BECs of $N \approx 600$ Rubidium-87 atoms, trapped on an atom chip. These are prepared in spin-squeezed states showing an interferometrically useful reduction of projection noise up to $\xi^2 \approx -7$ dB in variance compared to the SQL (Wineland criterion).

As it is already known, observing $\xi^2 < 0$ witnesses entanglement among the particles. Moreover, measurements of the spin contrast and of the squeezed variance allow to bound the depth of entanglement, *i.e.* how many particles in the system are genuinely entangled with each other. Using this technique we infer a depth of entanglement of ≈ 56 particles from our data.

In a similar spirit, we derived a criterion witnessing Bell correlations involving only collective measurements of the spin contrast and of the squeezed variance. Observing $\mathcal{W} < 0$ allows to conclude that the correlations among the particles are strong enough to violate a multipartite Bell inequality. In addition, we also derived criteria to quantify the depth k of Bell correlations, and performed a statistical analysis to estimate how many measurements are needed to rule out the possibility that an insufficient number of measurements is responsible for observing $\mathcal{W} < 0$. We tested such criteria on BECs with $N = 476 \pm 21$ atoms prepared in a state with $\xi^2 \approx -5.5(6)$ dB of spin squeezing according to the Wineland criterion. Our measurements show the presence of Bell correlations, under the assumption of Gaussian statistics, with a depth of at least $k = 6$ particles.

The use of collective observable to investigate correlations offers a great simplification for many-body systems. However, it also poses conceptual challenges, as the subsystems are not individually resolved. For this reason, it was debated whether entanglement witnessed by collective spin measurement was a fully legitimate concept and re-

6. Summary and outlook

ally useful for quantum information tasks beyond metrology. To study this problem, we implemented a protocol to extract the correlations among the indistinguishable atoms of a BEC into spatially separated, and therefore distinguishable, regions. We let the atomic cloud expand in time-of-flight, and then take high-resolution absorption images of the atomic density distribution. Upon imaging, atoms get localized in different spatial locations, and correlations can be investigated among them. We performed our experiments on BECs with $N = 590 \pm 30$ atoms prepared in a state with $\xi^2 \approx -3.8(2)$ dB of spin squeezing according to the Wineland criterion. Our measurements show entanglement between bi-partitions of the atomic density distribution. Moreover, for some bipartitions we observed entanglement strong enough for two-way EPR-steering.

6.2 Outlook

In this section, I discuss several experiments that could be performed with our apparatus in the near future. In addition, I also discuss further theoretical investigations that could be relevant for future experiments.

6.2.1 Nonclassical correlations between two BECs

With our experiments, we have shown that the correlations among the atoms of a BEC in a spin-squeezed state can be extracted into spatially separated regions. In the specific, we observed entanglement and EPR steering between different parts of an atomic ensemble. Of particular interest would be to prepare and detect quantum correlations between two separate BECs that can be split by a larger distance and individually manipulated.

Entanglement has already been observed between two macroscopic samples of 10^{12} Cesium atoms at room temperature, separated by few centimeters [95]. However, the observation of stronger correlations, namely EPR steering and Bell correlations, is still lacking in such scenarios.

In our experimental apparatus we could develop different strategies to prepare correlations between a pair of BECs. Two possibilities are to begin with two independent BECs and then to use state-dependent double-well potentials to control the collisional interactions among them, Fig. 6.1A and B. These sequences have been investigated in detail in Refs. [164, 165]. Another strategy would be to start with a BEC in a spin squeezed state, and then split it into two BECs by transforming the harmonic trapping potential into double well potential, Fig. 6.1C.

Apart from the experimental implementation of a protocol preparing pairs of entangled BECs, appropriate measurements are needed to investigate the correlations among them. Ideally, independent Rabi rotations for both BECs are desirable in order to measure different spin components. To this end, magnetic field gradients might be used to obtain different Rabi frequencies at the two sites, which would allow individual manipulation.

Conveniently, entanglement and EPR steering can be concluded by measuring on both BECs the same spin quadratures, as we have seen in the previous chapter. For

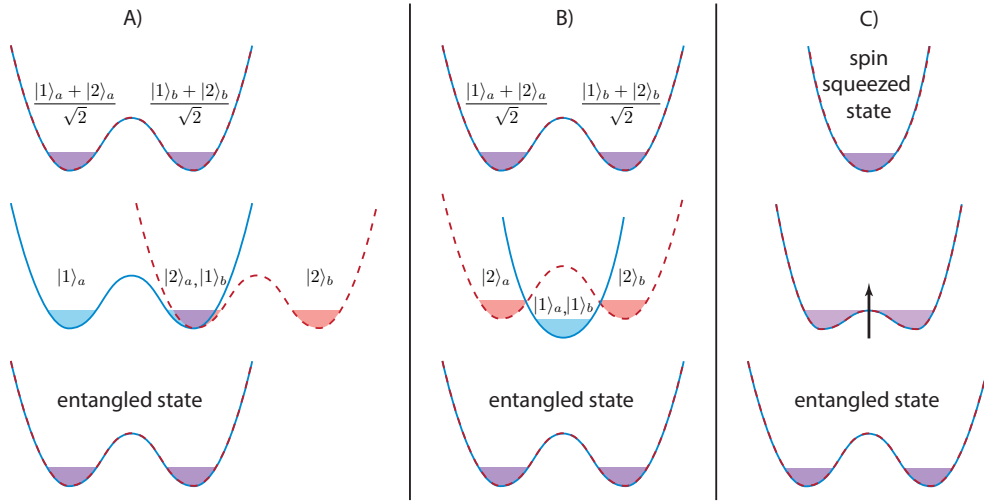


Figure 6.1: Strategies to prepare correlations between two BECs. Panel A shows the approach presented in Ref. [164]. Initially, a coherent spin state is prepared in each well. Then, the potential for state $|2\rangle$ is shifted spatially such that $|2\rangle_a$ and $|1\rangle_b$ overlap. Finally, the traps are overlapped again at their initial position. Panel B shows the approach presented in Ref. [165]. Initially, a coherent spin state is prepared in each well. Then, the potential for state $|1\rangle$ is turned into a single harmonic trap such that $|1\rangle_a$ and $|1\rangle_b$ overlap dynamically. Finally, the harmonic trap is turned back into a double well potential. Panel C shows the approach presented in the text. Initially, a spin squeezed state is prepared in a single well. Then, the potential for both states is turned into a double well such that the BEC is split into two subsystems.

this reason, collective Rabi rotations might already be a sufficient tool. Note that this is not straightforward to implement, as the spatial separation between the two BECs might already result in experiencing position-dependent (near-field) Rabi fields.

To test a Bell inequality, independent measurements are necessary. However, witnesses for Bell correlations might be found, which involve identical measurement settings on both BECs [166].

6.2.2 Schrödinger kitten states

Beyond squeezed states, the one-axis twisting evolution allows to prepare interesting non-Gaussian states. In particular, a coherent spin state can evolve into a superposition of two coherent spin states with opposite phases, called Schrödinger cat state [167, 168].

On the one hand, cat states are maximally entangled states that are optimal for quantum metrology. The Wigner function of a N -atom cat state present a band of N fringes of size $\text{Var}[S_z] \sim 1/N^2$, which allow the best possible sensitivity for parameter estimation [12]. On the other hand, they are the most fragile states to particle losses: losing a single particle already collapses the state to a coherent state. Apart from this, their preparation and detection require exceptional atom number stability and single-atom resolution.

6. Summary and outlook

Interestingly, there are similar highly entangled states that could be accessible with less stringent experimental requirements. The so-called Schrödinger kitten states are superpositions of two coherent spin states, separated by an angle smaller than π . Key features are their robustness against fluctuations in total N , in the loss of few particles, and that the larger fringes ($\text{Var}[S_z] > 1/N^2$) in the Wigner function can be observed without single-atom resolution. We investigated theoretically this possibility in Ref. [168], and show the feasibility of kitten states with $N \approx 150$ and an angle of $\pi/8$ between the two coherent states, corresponding to ≈ 6 atoms.

As the preparation of Schrödinger cat and kitten states requires evolution times longer than the one needed to prepare squeezed states (≈ 150 ms instead of ≈ 50 ms), a better understanding of the BEC phase coherence might be useful. In particular, in Ref. [168] we have shown that finite temperature effects also play an important role in the final state fidelity.

6.2.3 More multipartite Bell inequalities

So far, many-body Bell correlations have been detected only in spin-squeezed states [26, 151], for which the witnesses we developed are best suited [169]. However, experiments with atomic ensembles allow to prepare other nonclassical states [12], where observing Bell correlations would be of particular interest.

For Dicke states, for example, the known Bell inequality involving only up to two-body correlators [21] shows a quantum violation decreasing with the number of parties. This makes challenging, if not unrealistic, to use such a criterion experimentally. Instead, we observed that introducing fourth-order correlators could suffice to derive robust inequalities with a quantum violation increasing with N . These are currently under study, and will be presented in a future publication.

For spin-1 systems, it is relevant to look for Bell inequalities where parties have three outcomes, corresponding to the spin projections $-1, 0, +1$. Due to the complexity of this scenario, a full characterization of the (2-body, symmetric) local polytope is unfeasible already for $N > 8$. For this reason, we are currently investigating this problem with the SDP hierarchy presented in this thesis [28].

Appendix A

BEC ground state

A.1 Derivation of the Gross-Pitaevskii equation

We give here a detailed derivation of the time-independent Gross-Pitaevskii equation.

The Hamiltonian operator for a (non-relativistic) quantum particle of mass m in a potential $V(\mathbf{x})$ is

$$h(\mathbf{x}) = -\frac{\hbar^2}{2m}\nabla_{\mathbf{x}}^2 + V(\mathbf{x}) . \quad (\text{A.1})$$

This can be diagonalized in the basis of eigenfunctions $\phi_n(\mathbf{x})$, associated to the eigenvalues ϵ_n , meaning that

$$h(\mathbf{x})\phi_n(\mathbf{x}) = \epsilon_n\phi_n(\mathbf{x}) \quad \forall n \in \mathbb{N} . \quad (\text{A.2})$$

For a system of N identical non-interacting particles, the total Hamiltonian is the sum of single-particle Hamiltonians Eq. (A.1), namely

$$H(\mathbf{x}_1, \dots, \mathbf{x}_N) = \sum_{i=1}^N h(\mathbf{x}_i) , \quad (\text{A.3})$$

This operator can be diagonalized as

$$H\Phi_{\mathbf{n}} = E_{\mathbf{n}}\Phi_{\mathbf{n}} \quad \forall \mathbf{n} \in \mathbb{N}^N , \quad (\text{A.4})$$

where we omitted the $\mathbf{x}_1, \dots, \mathbf{x}_N$ dependencies for brevity, and where $\Phi_{\mathbf{n}}$ are tensor products of single-particle eigenfunctions and $E_{\mathbf{n}}$ are sums of single-particle eigenenergies.

As an example, the ground state of the system corresponds to the situation where each particle is in its lowest energy state

$$\Phi_0(\mathbf{x}_1, \dots, \mathbf{x}_N) = \phi_0(\mathbf{x}_1)\dots\phi_0(\mathbf{x}_N) \quad \text{and} \quad E_0 = N\epsilon_0 . \quad (\text{A.5})$$

Then, the first excited state corresponds to the situation where $(N-1)$ particles are in ϕ_0 and one particle is in ϕ_1 . This state is degenerate since there are N of such combinations

A. BEC ground state

(depending on which particle is in ϕ_1) having all the same energy $(N - 1)\epsilon_0 + \epsilon_1$. Excited states with higher energy are derived in a similar way, and their degeneracy usually increases.

In the case where additional constraints are imposed on the total wavefunction of the system, such as symmetry or anti-symmetry under particle relabeling, the degeneracies of the excitations can be altered.

If we include now interactions between the particles, the total Hamiltonian takes the form

$$H(\mathbf{x}_1, \dots, \mathbf{x}_N) = \sum_{i=1}^N h(\mathbf{x}_i) + \frac{1}{2} \sum_{\substack{i,j=1 \\ i \neq j}}^N U(\mathbf{x}_i, \mathbf{x}_j), \quad (\text{A.6})$$

where $U(\mathbf{x}_i, \mathbf{x}_j)$ is the interaction potential between particle i and j . In general, this term makes the Hamiltonian not separable, meaning that its eigenfunctions will not simply be products of single-particle eigenfunctions.

Depending on the number of particles N , on the dimensionality of the system (1D, 2D, 3D, ...), on the trapping potential V , and on the type and strength of the interactions U , many exact and non-exact solutions have been found.

Among the approximations proposed to obtain solutions describing special parameter regimes, the one of particular interest for us is the Hartree approximation. This is well suited to treat weakly interacting bosons, and it consists in assuming that the many-body wavefunction is a symmetrized product of single-particle wavefunctions (but not necessarily eigenfunctions). If all particles occupy the same single-particle state, as in a BEC, the many-body wavefunction in the Hartree approximation corresponds to the ansatz

$$\Phi(\mathbf{x}_1, \dots, \mathbf{x}_N) = \phi(\mathbf{x}_1) \dots \phi(\mathbf{x}_N) \quad (\text{A.7})$$

where the single-particle wavefunction $\phi(\mathbf{x})$, satisfying the normalization condition $\int d\mathbf{x} |\phi(\mathbf{x})|^2 = 1$, is unknown and it must be determined in a self-consistent way as we will show shortly.

We now look for the ground state wavefunction, *i.e.* the wavefunction which minimizes the energy of the system. To this end, we express the expectation value of the energy, using the Hartree approximation Eq. (A.7), which after a simple calculation takes the form

$$\begin{aligned} \langle \Phi | H | \Phi \rangle &= N \int d\mathbf{x} \phi^*(\mathbf{x}) h(\mathbf{x}) \phi(\mathbf{x}) + \frac{1}{2} N(N-1) \int d\mathbf{x} d\mathbf{x}' \phi^*(\mathbf{x}) \phi^*(\mathbf{x}') U(\mathbf{x}, \mathbf{x}') \phi(\mathbf{x}) \phi(\mathbf{x}') \\ &= N \int d\mathbf{x} \phi^*(\mathbf{x}) h(\mathbf{x}) \phi(\mathbf{x}) + \frac{1}{2} N(N-1) \int d\mathbf{x} d\mathbf{x}' |\phi(\mathbf{x})|^2 U(\mathbf{x}, \mathbf{x}') |\phi(\mathbf{x}')|^2 \end{aligned} \quad (\text{A.8})$$

Note that Eq. (A.8) arises from the indistinguishability of the particles (which allows to relabel the \mathbf{x}_i) and from the Hartree approximation (which allows to collect all the ϕ in $N\phi$). We now treat Eq. (A.8) as an energy functional (a scalar function of a function),

A.1 Derivation of the Gross-Pitaevskii equation

and minimize it with respect to ϕ , imposing the normalization constraint $\int d\mathbf{x} |\phi(\mathbf{x})|^2 = 1$ using the method of Lagrange multipliers. This means that we look for a solution of

$$\begin{aligned} \frac{\delta}{\delta\phi^*(\mathbf{x})} \left[\langle \Phi | H | \Phi \rangle - \epsilon N \left(\int d\mathbf{x} |\phi(\mathbf{x})|^2 - 1 \right) \right] &\stackrel{!}{=} 0 \\ \frac{\delta}{\delta\phi(\mathbf{x})^*} \left[N \int d\mathbf{x} \phi^*(\mathbf{x}) h(\mathbf{x}) \phi(\mathbf{x}) + \frac{1}{2} N(N-1) \int d\mathbf{x} d\mathbf{x}' |\phi(\mathbf{x})|^2 U(\mathbf{x}, \mathbf{x}') |\phi(\mathbf{x}')|^2 - \right. \\ &\quad \left. - \epsilon N \left(\int d\mathbf{x} |\phi(\mathbf{x})|^2 - 1 \right) \right] &\stackrel{!}{=} 0 \\ \left[N \int d\mathbf{x} \left(h(\mathbf{x}) + (N-1) \int d\mathbf{x}' U(\mathbf{x}, \mathbf{x}') |\phi(\mathbf{x}')|^2 - \epsilon \right) \phi(\mathbf{x}) \right] &\stackrel{!}{=} 0 \end{aligned} \quad (\text{A.9})$$

where ϵ is the Lagrange multiplier (which appears multiplied by N for later convenience), a real number that we will relate to a physical quantity. Carrying out the derivative gives the Hartree equation for bosons

$$\left[h(\mathbf{x}) + (N-1) \int d\mathbf{x}' U(\mathbf{x}, \mathbf{x}') |\phi(\mathbf{x}')|^2 \right] \phi(\mathbf{x}) = \epsilon \phi(\mathbf{x}), \quad (\text{A.10})$$

where $(N-1) \int d\mathbf{x}' U(\mathbf{x}, \mathbf{x}') |\phi(\mathbf{x}')|^2 = U_{\text{mf}}(\mathbf{x})$ is a mean-field potential which depends on $\phi(\mathbf{x})$. Note here that Eq. (A.10) is a (integro-differential) nonlinear Schrödinger equation for the single-particle state, where the eigenvalue ϵ/N is not the energy per particle as it is for the usual (linear) Schrödinger equation.

In the case of a contact inter-particle potential, $U(\mathbf{x}, \mathbf{x}') = g\delta(\mathbf{x} - \mathbf{x}')$, the mean-field potential is

$$(N-1) \int d\mathbf{x}' U(\mathbf{x}, \mathbf{x}') |\phi(\mathbf{x}')|^2 = (N-1) \int d\mathbf{x}' g\delta(\mathbf{x} - \mathbf{x}') |\phi(\mathbf{x}')|^2 = (N-1)g|\phi(\mathbf{x})|^2, \quad (\text{A.11})$$

and the Hartree equation Eq. (A.10) becomes the Gross-Pitaevskii equation (GPE)

$$\left[h(\mathbf{x}) + g(N-1)|\phi(\mathbf{x})|^2 \right] \phi(\mathbf{x}) = \epsilon \phi(\mathbf{x}). \quad (\text{A.12})$$

For atoms in dilute gases, where s -wave scattering is a good approximation of the interaction process and the scattering length a_s is much less than the mean interparticle spacing, this short-range potential is motivated with

$$g = \frac{4\pi a_s \hbar^2}{m}, \quad (\text{A.13})$$

where a_s is the s -wave scattering cross-section. Therefore, Eq. (A.12) accurately describes the zero-temperature properties of Bose gases.

A.2 ϵ as the chemical potential

We are interested here in relating the Lagrange multiplier ϵ appearing in the GPE Eq. (A.12) to a quantity of physical significance. To this end, we start by computing the chemical potential of the system, which in statistical mechanics is defined as

$$\mu = \frac{\partial E}{\partial N}. \quad (\text{A.14})$$

For the case we are considering, N indistinguishable bosons with contact interaction, the total energy

$$E = N \int d\mathbf{x} \phi^*(\mathbf{x}) h(\mathbf{x}) \phi(\mathbf{x}) + \frac{1}{2} N(N-1)g \int d\mathbf{x} |\phi(\mathbf{x})|^4 \quad (\text{A.15})$$

can be easily derived with respect to N by noticing that to first order $\partial\phi(\mathbf{x})/\partial N = 0$. This gives us

$$\mu = \int d\mathbf{x} \phi^*(\mathbf{x}) h(\mathbf{x}) \phi(\mathbf{x}) + \frac{1}{2} (2N-1)g \int d\mathbf{x} |\phi(\mathbf{x})|^4. \quad (\text{A.16})$$

To obtain an expression for ϵ , we multiply the GPE Eq. (A.12) by $\phi(\mathbf{x})^*$ from the left, and integrate. This gives

$$\epsilon = \int d\mathbf{x} \phi^*(\mathbf{x}) h(\mathbf{x}) \phi(\mathbf{x}) + (N-1)g \int d\mathbf{x} |\phi(\mathbf{x})|^4. \quad (\text{A.17})$$

Now, let us take a moment to compare Eqs. (A.15), (A.16) and (A.17). First, it is now evident that (if $g \neq 0$)

$$\frac{E}{N} \neq \epsilon, \quad (\text{A.18})$$

meaning that, in the interacting case, ϵ is not the mean energy per particle. On the other hand, in the limit $N \gg 1$ we can say that

$$\epsilon \approx \mu \approx \int d\mathbf{x} \phi^*(\mathbf{x}) h(\mathbf{x}) \phi(\mathbf{x}) + Ng \int d\mathbf{x} |\phi(\mathbf{x})|^4, \quad (\text{A.19})$$

meaning that the Lagrange multiplier appearing in the GPE Eq. (A.12) can be interpreted as the chemical potential of the system (Koopmans theorem).

Interestingly, if one defines the chemical potential to be the energy difference between having N and $N-1$ particles in the system, *i.e.*

$$\mu = E_N - E_{N-1}, \quad (\text{A.20})$$

then one finds for any N

$$\epsilon = \mu = \int d\mathbf{x} \phi^*(\mathbf{x}) h(\mathbf{x}) \phi(\mathbf{x}) + (N-1)g \int d\mathbf{x} |\phi(\mathbf{x})|^4. \quad (\text{A.21})$$

In this sense, the chemical potential can be thought as “the energy needed to add one particle from the system”.

Appendix B

Derivation of phase noise due to losses

Here we give a detailed derivation of Eq. (2.45), which describes the contrast decay due to phase noise originating from particle losses.

As we have seen from Eq. (2.40), the interference contrast is related to the phase noise as

$$C(t) \simeq e^{-\frac{1}{2} \text{Var}[\delta\theta(t)]} . \quad (\text{B.1})$$

On the other hand, the contrast can be expressed as

$$C(t) = \frac{2}{N} \sqrt{\langle \hat{S}_x \rangle^2 + \langle \hat{S}_y \rangle^2} = \frac{2}{N} |\langle \hat{a}_2^\dagger \hat{a}_1 \rangle| . \quad (\text{B.2})$$

In Ref. [49] (see Eq. (125) there) is given the analytical expression for the quantum average $\langle \hat{a}_2^\dagger \hat{a}_1 \rangle$ in the two-mode approximation with asymmetric one-body losses. For a coherent spin state with N atoms equally split among the two components this reads

$$\langle \hat{a}_2^\dagger \hat{a}_1 \rangle_N = \frac{N}{2} e^{-2iv(N)t} e^{-\frac{1}{2}(\gamma_1 + \gamma_2)t} L^{N-1} , \quad (\text{B.3})$$

where

$$v(N) = \frac{1}{2\hbar} [(\mu_1 - \mu_2) - \hbar\chi(\bar{N}_1 - \bar{N}_2) + \hbar\tilde{\chi}(N - \bar{N})] , \quad (\text{B.4})$$

and

$$L = \frac{1/2}{\gamma_1 + i(\chi + \tilde{\chi})} \left[\gamma_1 e^{i\tilde{\chi}t} + i(\chi + \tilde{\chi}) e^{-(\gamma_1 + i\chi)t} \right] + \frac{1/2}{\gamma_2 - i(\chi - \tilde{\chi})} \left[\gamma_2 e^{i\tilde{\chi}t} - i(\chi - \tilde{\chi}) e^{-(\gamma_2 - i\chi)t} \right] . \quad (\text{B.5})$$

If the initial number of atoms N fluctuates according to a Poissonian distribution with mean value \bar{N} , the ensemble average is

$$\langle \hat{a}_2^\dagger \hat{a}_1 \rangle_{\text{ens.}} = \sum_{N=0}^{\infty} \frac{\bar{N}^N}{N!} e^{-\bar{N}} \langle \hat{a}_2^\dagger \hat{a}_1 \rangle_N \quad (\text{B.6})$$

$$= \frac{\bar{N}}{2} e^{-2iv(1)t} e^{-\frac{1}{2}(\gamma_1 + \gamma_2)t} e^{(e^{-i\tilde{\chi}t} L - 1)\bar{N}} . \quad (\text{B.7})$$

B. Derivation of phase noise due to losses

From this expression, and the identity $|e^a| = \sqrt{e^{a^*} e^a} = e^{\Re[a]}$, we write

$$|\langle \hat{a}_2^\dagger \hat{a}_1 \rangle_{\text{ens.}}| = \frac{\bar{N}}{2} e^{-\frac{1}{2}(\gamma_1 + \gamma_2)t} e^{\Re[(e^{-i\tilde{\chi}t} L - 1)\bar{N}]} . \quad (\text{B.8})$$

Here, the term $e^{-\frac{1}{2}(\gamma_1 + \gamma_2)t}$ describes the loss of contrast due to a decrease in the atom number, which is not related to phase noise. This effect can be compensated by measuring the maximum single-shot contrast at time t , *i.e.* the visibility $\mathcal{V}(t) = \frac{\bar{N}}{2} e^{-\frac{1}{2}(\gamma_1 + \gamma_2)t}$, and then considering $C'(t) = C(t)/\mathcal{V}(t)$. For this reason, in the following we will consider this new contrast $C'(t)$, which allows us to focus on the phase noise due to particle losses.

Finally, from Eqs. (B.1,B.2,B.8), we obtain Eq. (2.45) presented in the main text

$$\begin{aligned} \text{Var} [\delta\theta(t)] &\simeq -2 \log \left[\frac{2}{\bar{N}} e^{\frac{1}{2}(\gamma_1 + \gamma_2)t} |\langle \hat{a}_2^\dagger \hat{a}_1 \rangle_{\text{ens.}}| \right] \\ &\simeq -2 \log \left[e^{\Re[(e^{-i\tilde{\chi}t} L - 1)\bar{N}]} \right] \\ &\simeq 2 \Re \left[\bar{N} (1 - e^{-i\tilde{\chi}t} L) \right] . \end{aligned} \quad (\text{B.9})$$

Appendix C

Local collective spins

C.1 Definition of local collective spins

In this section we present the details behind the definition of local collective spins used in chapter 5, and it is based on Ref. [27].

C.2 Naive definition

In considering a region A on the absorption images, we would be tempted to define the local collective spin as $\sum_{i \in A} \vec{s}_i^A$, where the index i runs over all spins contained in A . However, in the case where the spins have some spatial extent, for example because of the point-spread function of the imaging system, the above definition of local collective spin needs to be corrected because the spin noise gets reduced and the usual spin commutation relations are not satisfied. To see this, imagine N atoms where the i -th has a density distribution $g(\vec{x}, \vec{x}_i)$ centered at \vec{x}_i . A spin projection measurement corresponds to counting in a single experimental realization

$$\frac{N_1^A - N_2^A}{2} = \frac{1}{2} \int_A \left(\sum_{i=1}^{N_1} g(\vec{x}, \vec{x}_i) - \sum_{i=N_1+1}^N g(\vec{x}, \vec{x}_i) \right) d\vec{x}. \quad (\text{C.1})$$

Here, and in what follows, we assume for simplicity that the distribution $g(\vec{x}, \vec{x}_i)$, the region A , and the distribution of the \vec{x}_i , are independent of the internal state of the atom. The spin expectation value is the ensemble average of this quantity over all possible positions x_i and all possible partitions of N into N_1 and $N_2 = N - N_1$, denoted $\langle \cdot \rangle_{N_1}$. If all the \vec{x}_i come from the same probability density function ρ we can write

$$\begin{aligned} \left\langle \left(\frac{N_1^A - N_2^A}{2} \right) \right\rangle &= \left\langle \int_{-\infty}^{+\infty} \rho(\vec{x}_1) \dots \rho(\vec{x}_N) \frac{1}{2} \int_A \left(\sum_{i=1}^{N_1} g(\vec{x}, \vec{x}_i) - \sum_{i=N_1+1}^N g(\vec{x}, \vec{x}_i) \right) d\vec{x} d\vec{x}_1 \dots d\vec{x}_N \right\rangle_{N_1} \\ &= \left\langle \left(\frac{N_1 - N_2}{2} \right) \int_{-\infty}^{+\infty} \rho(\vec{x}_1) \int_A g(\vec{x}, \vec{x}_1) d\vec{x} d\vec{x}_1 \right\rangle_{N_1} \\ &= \left\langle \left(\frac{N_1 - N_2}{2} \right) \right\rangle_{N_1} \int_{-\infty}^{+\infty} \rho(\vec{x}_1) f^A(\vec{x}_1) d\vec{x}_1, \end{aligned} \quad (\text{C.2})$$

C. Local collective spins

where in going from the first to the second line we exchanged the order of the sum and the integrals, we used the fact that $\int_{-\infty}^{+\infty} \rho(\vec{x}_i) d\vec{x}_i = 1$, and that atoms can be relabeled. In the last line we introduced

$$f^A(\vec{x}_i) = \int_A g(\vec{x}, \vec{x}_i) d\vec{x} \quad (\text{C.3})$$

representing the ‘‘mode overlap’’ between an atom centered in \vec{x}_i and the region A . Similarly, for the total atom number in region A we have

$$\begin{aligned} \langle (N_1^A + N_2^A) \rangle &= \left\langle \int_{-\infty}^{+\infty} \rho(\vec{x}_1) \dots \rho(\vec{x}_N) \int_A \left(\sum_{i=1}^N g(\vec{x}, \vec{x}_i) \right) d\vec{x} d\vec{x}_1 \dots d\vec{x}_N \right\rangle_{N_1} \\ &= N \int_{-\infty}^{+\infty} \rho(\vec{x}_1) f^A(\vec{x}_1) d\vec{x}_1, \end{aligned} \quad (\text{C.4})$$

We now go through the same steps for the fluctuations. We consider the regions $U, V \in \{A, B\}$ and we calculate

$$\begin{aligned} \left\langle \left(\frac{N_1^U - N_2^U}{2} \right) \left(\frac{N_1^V - N_2^V}{2} \right) \right\rangle &= \quad (\text{C.5}) \\ &= \left\langle \frac{1}{4} \int_{-\infty}^{+\infty} \rho(\vec{x}_1) \dots \rho(\vec{x}_N) \times \right. \\ &\quad \left. \times \int_U \left(\sum_{i=1}^{N_1} g(\vec{x}, \vec{x}_i) - \sum_{i=N_1+1}^N g(\vec{x}, \vec{x}_i) \right) \int_V \left(\sum_{j=1}^{N_1} g(\vec{y}, \vec{x}_j) - \sum_{j=N_1+1}^N g(\vec{y}, \vec{x}_j) \right) d\vec{x} d\vec{y} d\vec{x}_1 \dots d\vec{x}_N \right\rangle_{N_1} \\ &= \left\langle \frac{1}{4} \int_{-\infty}^{+\infty} \rho(\vec{x}_1) \dots \rho(\vec{x}_N) \times \right. \\ &\quad \left. \times \left(\sum_{i=1}^{N_1} f^U(\vec{x}_i) - \sum_{i=N_1+1}^N f^U(\vec{x}_i) \right) \left(\sum_{j=1}^{N_1} f^V(\vec{x}_j) - \sum_{j=N_1+1}^N f^V(\vec{x}_j) \right) d\vec{x}_1 \dots d\vec{x}_N \right\rangle_{N_1} \\ &= \left\langle \frac{1}{4} \int_{-\infty}^{+\infty} \rho(\vec{x}_1) \dots \rho(\vec{x}_N) \left(\sum_{i=1}^N f^U(\vec{x}_i) f^V(\vec{x}_i) + \sum_{i=N_1+1}^{N-1} \sum_{j=i+1}^N \left(f^U(\vec{x}_i) f^V(\vec{x}_j) + f^U(\vec{x}_j) f^V(\vec{x}_i) \right) \right. \right. \\ &\quad \left. \left. + \sum_{i=1}^{N_1-1} \sum_{j=i+1}^{N_1} \left(f^U(\vec{x}_i) f^V(\vec{x}_j) + f^U(\vec{x}_j) f^V(\vec{x}_i) \right) - \sum_{i=1}^{N_1} \sum_{j=N_1+1}^N \left(f^U(\vec{x}_i) f^V(\vec{x}_j) + f^U(\vec{x}_j) f^V(\vec{x}_i) \right) \right) d\vec{x}_1 \dots d\vec{x}_N \right\rangle_{N_1} \\ &= \left\langle \frac{1}{4} \int_{-\infty}^{+\infty} \rho(\vec{x}_1) \dots \rho(\vec{x}_N) \left(N f^U(\vec{x}_1) f^V(\vec{x}_1) + \right. \right. \\ &\quad \left. \left. + \frac{1}{2} \left((N_1^2 - N_1) + (N_2^2 - N_2) - 2N_1 N_2 \right) \left(f^U(\vec{x}_1) f^V(\vec{x}_2) + f^U(\vec{x}_2) f^V(\vec{x}_1) \right) \right) d\vec{x}_1 \dots d\vec{x}_N \right\rangle_{N_1} \\ &= \frac{N}{4} \int_{-\infty}^{+\infty} \rho(\vec{x}_1) f^U(\vec{x}_1) f^V(\vec{x}_1) d\vec{x}_1 + \frac{1}{4} \left(\langle (N_1 - N_2)^2 \rangle_{N_1} - N \right) \int_{-\infty}^{+\infty} \rho(\vec{x}_1) \rho(\vec{x}_2) f^U(\vec{x}_1) f^V(\vec{x}_2) d\vec{x}_1 d\vec{x}_2, \end{aligned} \quad (\text{C.6})$$

which allows us to evaluate variances and covariances.

Example:

In the case of a coherent spin state on the equator $\langle (N_1 - N_2)^2 \rangle_{N_1} = N$ (this can be seen also from the fact that the average $\langle h(N_1) \rangle_{N_1}$ is given by the binomial distribution $\sum_{N_1=0}^N \binom{N}{N_1} p^{N_1} (1-p)^{N-N_1} h(N_1)$, with $p = 1/2$.) This means that, from Eq. (C.4) and Eq. (C.6), the ratio

$$\frac{\text{Var}(N_1^A - N_2^A)}{\langle N_1^A + N_2^A \rangle} = \frac{\int_{-\infty}^{+\infty} \rho(\vec{x}_1) (f^A(\vec{x}_1))^2 d\vec{x}_1}{\int_{-\infty}^{+\infty} \rho(\vec{x}_1) f^A(\vec{x}_1) d\vec{x}_1} = \eta_{\text{eff}}^A \leq 1, \quad (\text{C.7})$$

where $\eta^A = 1$ if and only if for all \vec{x}_1 where $\rho(\vec{x}_1) \neq 0$, $f^A(\vec{x}_1)$ is either 0 or 1. This can happen if either A is the entire space, for which $f^A(\vec{x}_1) = 1 \forall \vec{x}_1$, or $g(\vec{x}, \vec{x}_1) = \delta(\vec{x} - \vec{x}_1)$, for which $f^A(\vec{x}_1) = 1 \forall \vec{x}_1 \in A$. This means that a collective spins is properly defined if either we count atoms over all space or if atoms are properly localized.

We can evaluate Eq. (C.7) for our experimental situation taking ρ to be the normalized BEC density for one of the states and $g(\vec{x}, \vec{x}_1)$ the Gaussian point spread function of our imaging system. The analytical result is shown in Fig. 5.10 together with experimental data. See also Ref. [158].

C.3 Proper definition

The problem illustrated by Eq. (C.7) has already been observed in experiments relying on atom-light interactions [160, 161]. In particular, it has been studied that atoms inside a cavity can couple with different interaction strengths to the optical mode, depending on their position. In this nonuniform scenario, the proper definition of the collective spin is given by $\vec{S} = \eta_{\text{eff}}^{-1} \sum_i \eta_i \vec{s}_i$, where \vec{s}_i is the spin of the i -th particle, η_i its coupling strength and $\eta_{\text{eff}} = \sum_i \eta_i^2 / \sum_i \eta_i$. Following the same argument, we define our local spin as

$$\vec{S}^A = \frac{1}{\eta_{\text{eff}}^A} \sum_i \eta_i^A \vec{s}_i, \quad (\text{C.8})$$

where $\eta_i^A = \int_A g(\vec{x}, \vec{x}_i) dx = f^A(\vec{x}_i)$, and $\eta_{\text{eff}}^A = \langle (\eta^A)^2 \rangle / \langle \eta^A \rangle$ is given by Eq. (C.7). This definition allows us to define local spins for very small regions, in principle even of a single pixel size.

A spin projection measurement is given by

$$S_{\vec{\alpha}}^A = \frac{1}{\eta_{\text{eff}}^A} \left(\frac{N_1^A - N_2^A}{2} \right), \quad (\text{C.9})$$

where $\vec{\alpha}$ is the measurement axis along which the spin is projected and $N_{1,2}^A$ are the number of atoms counted in region A .

Note that with this definition, for a coherent state we have (using Eq. (C.7))

$$\frac{4 \text{Var}(S_z^A)}{N} = \frac{\text{Var}((\eta_{\text{eff}}^A)^{-1} (N_1^A - N_2^A))}{(\eta_{\text{eff}}^A)^{-1} \langle N_1^A + N_2^A \rangle} = \frac{\eta_{\text{eff}}^A}{\eta_{\text{eff}}^A} = 1, \quad (\text{C.10})$$

C. Local collective spins

independently of the definition of the region A . This is confirmed by comparison with the data in Fig. 5.10. We compute η_{eff}^A from the mean detected atom densities by discrete numerical integration, according to Eq. (C.7). Since the mean densities of the two spin states are slightly different, we use the one which gives the smallest η_{eff}^A as a conservative value. The same approach is followed to compute η_{eff}^B .

C.4 Imaging noise subtraction

In the experiment we measure $N_1^A + \delta_1^A$ and $N_2^A + \delta_2^A$, where δ_i^A is due to imaging noise in region A for state i . Therefore, our measured effective spin is $\tilde{S}_\alpha^A = S_\alpha^A + \Delta^A$, where $\Delta^A = (\eta_{\text{eff}}^A)^{-1}(\delta_1^A - \delta_2^A)/2$. The variance entering the entanglement and the EPR criteria is

$$\begin{aligned} \text{Var} \left(g_z \tilde{S}_z^A + \tilde{S}_z^B \right) &= \text{Var} \left(g_z (S_z^A + \Delta^A) + (S_z^B + \Delta^B) \right) = \\ &= \text{Var} \left(g_z S_z^A + S_z^B \right) + \text{Var} \left(g_z \Delta^A + \Delta^B \right) + 2\text{Cov}(\dots, \dots), \end{aligned} \quad (\text{C.11})$$

where we assume the covariance to be zero because imaging noise is uncorrelated with the spin projection. This allows us to subtract imaging noise from the criteria by writing the numerator as

$$\begin{aligned} \text{Var} \left(g_z S_z^A + S_z^B \right) \text{Var} \left(g_y S_y^A + S_y^B \right) &= \\ &= \left(\text{Var} \left(g_z \tilde{S}_z^A + \tilde{S}_z^B \right) - \text{Var} \left(g_z \Delta^A + \Delta^B \right) \right) \left(\text{Var} \left(g_y \tilde{S}_y^A + \tilde{S}_y^B \right) - \text{Var} \left(g_y \Delta^A + \Delta^B \right) \right). \end{aligned} \quad (\text{C.12})$$

Note that the optimal g 's minimizing Eq. (C.12) are

$$g_z^* = - \frac{\text{Cov} \left(\tilde{S}_z^A, \tilde{S}_z^B \right)}{\text{Var} \left(\tilde{S}_z^A \right) - \text{Var} \left(\Delta^A \right)}, \quad (\text{C.13})$$

and similarly for g_y^* .

We estimate the contribution of imaging noise, $\text{Var}(\delta_i^A)$, from the photon shot noise on the actual absorption image. This estimate is conservative in the sense that additional noise sources such as dark counts, photon shot noise on the reference images and other sources of noise are neglected. However, in our case these sources give only a very small contribution to the noise.

We obtain the conversion factor from the CCD counts to photon number by a calibration routine with flat-field correction. This number allows us to directly estimate the noise contribution of each pixel by the observed counts assuming Poissonian statistics of the photon numbers. By using error propagation this noise is converted into an effective atom number noise on the pixel.

For the subtraction of imaging noise from the observed spin variances we take the mean of this noise on the respective set of images.

C.5 Unbiased sample estimate of inferred variances

The unbiased sample estimate of inferred variances is:

$$\text{Var} \left(g_z \hat{S}_z^A + \hat{S}_z^B \right) = \frac{1}{m-2} \sum_{j=1}^m \left[\left(\bar{g}_z s_{z,j}^A + s_{z,j}^B \right) - \left(\bar{g}_z \bar{s}_z^A + \bar{s}_z^B \right) \right]^2 \quad (\text{C.14})$$

where m is the number of measurements, \bar{g}_z is the optimal g_z for the given subset, $s_{z,j}^K$ ($K = A, B$) are individual spin measurement results and \bar{s}_z^K ($K = A, B$) are the usual sample means. The normalization factor $m - 2$ is necessary to take into account the additional degree of freedom originating from the inferring. This can be seen as the estimation of the variance of residuals in linear regressions.

Appendix D

Derivation of the Sørensen entanglement criterion

We present here the calculation for deriving the entanglement criterion by Sørensen *et al.* of Ref. [98], which was introduced in Eq. (4.23).

D.1 Original derivation

For a multipartite scenario, the N -body density matrix ρ is separable if it can be expressed in the form

$$\rho = \sum_k p_k \rho_k^{(1)} \otimes \rho_k^{(2)} \otimes \cdots \otimes \rho_k^{(N)}, \quad (\text{D.1})$$

where the coefficients k satisfy $0 \leq p_k \leq 1$ and $\sum_k p_k = 1$, and where $\rho_k^{(i)}$ is a density matrix for the i th particle.

We now derive a number of inequalities, valid for all separable states, that will be

D. Derivation of the Sørensen entanglement criterion

used to obtain the desired result. First, consider the variance

$$\text{Var}[S_z] = \langle S_z^2 \rangle - \langle S_z \rangle^2 \quad (\text{D.2})$$

$$= \left\langle \sum_i (s_z^{(i)}) \sum_j (s_z^{(j)}) \right\rangle - \left\langle \sum_i s_z^{(i)} \right\rangle^2 \quad (\text{D.3})$$

$$= \left\langle \sum_{i=j} s_z^{(i)} s_z^{(j)} \right\rangle + \left\langle \sum_{i \neq j} s_z^{(i)} s_z^{(j)} \right\rangle - \left\langle \sum_i s_z^{(i)} \right\rangle^2 \quad (\text{D.4})$$

$$= \left\langle \sum_i \frac{1}{4} \right\rangle + \sum_{i \neq j} \langle s_z^{(i)} \rangle \langle s_z^{(j)} \rangle - \left\langle \sum_i s_z^{(i)} \right\rangle^2 \quad (\text{D.5})$$

$$= \frac{N}{4} + \sum_{i \neq j} \langle s_z^{(i)} \rangle \langle s_z^{(j)} \rangle - \left\langle \sum_i s_z^{(i)} \right\rangle^2 + \underbrace{\sum_i \langle s_z^{(i)} \rangle^2 - \sum_i \langle s_z^{(i)} \rangle^2}_{=0} \quad (\text{D.6})$$

$$= \frac{N}{4} - \sum_i \langle s_z^{(i)} \rangle^2 \quad \text{using } \left\langle \sum_i s_z^{(i)} \right\rangle^2 = \sum_i \langle s_z^{(i)} \rangle^2 + \sum_{i \neq j} \langle s_z^{(i)} \rangle \langle s_z^{(j)} \rangle. \quad (\text{D.7})$$

This expression can be used to derive the relation

$$\langle S_z^2 \rangle = \sum_k p_k \langle S_z^2 \rangle_k \quad (\text{D.8})$$

$$= \sum_k p_k \left(\text{Var}[S_z]_k + \langle S_z \rangle_k^2 \right) \quad (\text{D.9})$$

$$= \sum_k p_k \left(\left(\frac{N}{4} - \sum_i \langle s_z^{(i)} \rangle_k^2 \right) + \langle S_z \rangle_k^2 \right) \quad (\text{D.10})$$

$$= \frac{N}{4} - \sum_k p_k \sum_i \langle s_z^{(i)} \rangle_k^2 + \sum_k p_k \langle S_z \rangle_k^2, \quad (\text{D.11})$$

meaning that

$$\text{Var}[S_z] = \langle S_z^2 \rangle - \langle S_z \rangle^2 \quad (\text{D.12})$$

$$= \left(\frac{N}{4} - \sum_k p_k \sum_i \langle s_z^{(i)} \rangle_k^2 + \sum_k p_k \langle S_z \rangle_k^2 \right) - \langle S_z \rangle^2. \quad (\text{D.13})$$

Then, we note that

$$\langle S_z \rangle^2 = \left(\sum_k p_k \langle S_z \rangle_k \right)^2 \quad (\text{D.14})$$

$$= \left(\sum_k \sqrt{p_k} \sqrt{p_k} \langle S_z \rangle_k \right)^2 \quad (\text{D.15})$$

$$\leq \left(\sum_k \sqrt{p_k^2} \right) \left(\sum_k (\sqrt{p_k} \langle S_z \rangle_k)^2 \right) \quad (\text{D.16})$$

$$= \sum_k p_k \langle S_z \rangle_k^2. \quad (\text{D.17})$$

where the inequality sign comes from the use of the Cauchy-Schwarz inequality

$$\left| \sum_i u_i v_i^* \right|^2 \leq \left(\sum_i |u_i|^2 \right) \left(\sum_i |v_i|^2 \right). \quad (\text{D.18})$$

Using the fact that for a single spin-1/2

$$0 \leq \langle s_x^{(i)} \rangle_k^2 + \langle s_y^{(i)} \rangle_k^2 + \langle s_z^{(i)} \rangle_k^2 \leq \frac{1}{4}, \quad (\text{D.19})$$

we obtain $\langle s_z^{(i)} \rangle_k^2 \leq \frac{1}{4} - \langle s_x^{(i)} \rangle_k^2 - \langle s_y^{(i)} \rangle_k^2$, and therefore

$$- \sum_k p_k \sum_i \langle s_z^{(i)} \rangle_k^2 \geq \sum_k p_k \sum_i \left(\langle s_x^{(i)} \rangle_k^2 + \langle s_y^{(i)} \rangle_k^2 - \frac{1}{4} \right) \quad (\text{D.20})$$

$$= \sum_k p_k \sum_i \left(\langle s_x^{(i)} \rangle_k^2 + \langle s_y^{(i)} \rangle_k^2 \right) - \frac{N}{4}. \quad (\text{D.21})$$

Finally, starting from Eq. (D.17) for an arbitrary direction \mathbf{v} , we have

$$\langle S_{\mathbf{v}} \rangle^2 \leq \sum_k p_k \langle S_{\mathbf{v}} \rangle_k^2 \quad (\text{D.22})$$

$$= \sum_k p_k \left(\sum_i \langle s_{\mathbf{v}}^{(i)} \rangle_k \right)^2 \quad (\text{D.23})$$

$$= \sum_k p_k \left(\sum_i 1 \langle s_{\mathbf{v}}^{(i)} \rangle_k \right)^2 \quad (\text{D.24})$$

$$\leq \sum_k p_k \left(\sum_i 1^2 \right) \left(\sum_i \langle s_{\mathbf{v}}^{(i)} \rangle_k^2 \right) \quad \text{using Cauchy-Schwarz} \quad (\text{D.25})$$

$$= \sum_k p_k N \left(\sum_i \langle s_{\mathbf{v}}^{(i)} \rangle_k^2 \right). \quad (\text{D.26})$$

D. Derivation of the Sørensen entanglement criterion

At this point, by making use of the previous results, it is straightforward to see that for all separable states

$$\begin{aligned}
 \xi^2 &= \frac{N \text{Var}[S_z]}{\langle S_x \rangle^2 + \langle S_y \rangle^2} && \text{(D.27)} \\
 &= \frac{N \left(\frac{N}{4} - \sum_k p_k \sum_i \langle s_z^{(i)} \rangle_k^2 + \sum_k p_k \langle S_z \rangle_k^2 - \langle S_z \rangle^2 \right)}{\langle S_x \rangle^2 + \langle S_y \rangle^2} && \text{using Eq. (D.13)} \\
 &\geq \frac{N \left(\frac{N}{4} - \sum_k p_k \sum_i \langle s_z^{(i)} \rangle_k^2 \right)}{\langle S_x \rangle^2 + \langle S_y \rangle^2} && \text{using Eq. (D.17)} \\
 &\geq \frac{N \left(\frac{N}{4} + \sum_k p_k \sum_i \left(\langle s_x^{(i)} \rangle_k^2 + \langle s_x^{(i)} \rangle_k^2 \right) - \frac{N}{4} \right)}{\langle S_x \rangle^2 + \langle S_y \rangle^2} && \text{using Eq. (D.21)} \\
 &\geq \frac{N \left(\sum_k p_k \sum_i \left(\langle s_x^{(i)} \rangle_k^2 + \langle s_x^{(i)} \rangle_k^2 \right) \right)}{\sum_k p_k N \left(\langle s_x^{(i)} \rangle_k^2 \right) + \sum_k p_k N \left(\langle s_y^{(i)} \rangle_k^2 \right)} && \text{using Eq. (D.26)} \\
 &= 1, && \text{(D.28)}
 \end{aligned}$$

which proves the relation in the main text.

D.2 Derivation from the spin uncertainty relation

An interesting alternative derivation of Eq. (4.23) starts from the spin uncertainty relation.

First, as for a single spin-1/2 the variance is constrained to be $\text{Var} [s_y^{(i)}] \leq \frac{1}{4}$, the Heisenberg uncertainty relation $\text{Var} [s_z^{(i)}] \text{Var} [s_y^{(i)}] \geq \frac{1}{4} |\langle s_x^{(i)} \rangle|^2$ implies

$$\text{Var} [s_z^{(i)}] \geq |\langle s_x^{(i)} \rangle|^2. \quad (\text{D.29})$$

Then, for a separable state we have (added terms equal to unity have been highlighted in blue and lines 5 and 9 derive from the Cauchy-Schwarz inequality)

$$\begin{aligned} \text{Var} [S_z] &\geq \sum_k p_k \text{Var} [S_z]_k \\ &= \sum_k p_k \sum_i \text{Var} [s_z^i]_k \\ &\geq \sum_k p_k \sum_i |\langle s_x^{(i)} \rangle_k|^2 \\ &= \sum_i \left(\sum_k p_k |\langle s_x^{(i)} \rangle_k|^2 \right) \left(\sum_k p_k \right) \\ &\geq \sum_i \left| \sum_k p_k \langle s_x^{(i)} \rangle_k \right|^2 \\ &= \sum_i |\langle s_x^{(i)} \rangle|^2 \\ &= N \sum_i \frac{1}{N} |\langle s_x^{(i)} \rangle|^2 \\ &= N \left(\sum_i \frac{1}{N} |\langle s_x^{(i)} \rangle|^2 \right) \left(\sum_i \frac{1}{N} \right) \\ &\geq N \left| \sum_i \frac{1}{N} \langle s_x^{(i)} \rangle \right|^2 \\ &\geq \frac{1}{N} |\langle S_x \rangle|^2, \end{aligned} \quad (\text{D.30})$$

which proves again the relation in the main text.

Appendix E

Correlations in systems with fluctuating number of particles

We prove here that correlations can also be detected in many-body systems with shot-to-shot fluctuations in the total number of particles. In particular, we show that the criteria for entanglement and for Bell correlations we introduced in Eq. (4.23) and Eq. (4.59) respectively, can be rewritten in a convenient form where the number of particles N is replaced by the operator \hat{N} to take into account these fluctuations.

E.1 Theoretical framework

The state of a system with shot-to-shot fluctuations in the number of particles (statistical mixture) can be described by the block-diagonal density matrix

$$\hat{\rho} = \bigoplus_{N \geq 1} p_N \hat{\rho}^{(N)}, \quad (\text{E.1})$$

where $p_N = \text{Tr}(\mathbb{1}^{(N)} \hat{\rho} \mathbb{1}^{(N)})$ is the probability of having N particles ($\sum_N p_N = 1$) and $\hat{\rho}^{(N)} = (\mathbb{1}^{(N)} \hat{\rho} \mathbb{1}^{(N)})/p_N$ is the normalized ($\text{Tr}(\hat{\rho}^{(N)}) = 1$) N -particle component of the density matrix $\hat{\rho}$, with $\mathbb{1}^{(N)}$ the identity operator on the space with particle number N .

Now, note that the operator \hat{S}_n is block-diagonal in terms of the particle number, *i.e.*

$$\hat{S}_n = \bigoplus_{N \geq 1} \hat{S}_n^{(N)} \quad (\text{E.2})$$

where $\hat{S}_n^{(N)}$ denotes the action of the spin operator \hat{S}_n on the subspace with particle number N . In the same basis, the particle number operator takes the form

$$\hat{N} = \bigoplus_{N \geq 1} N \cdot \mathbb{1}^{(N)}. \quad (\text{E.3})$$

E. Correlations in systems with fluctuating number of particles

For a general operator \hat{O} we define its N -particle expectation value as

$$\langle \hat{O} \rangle_N = \text{Tr}(\hat{O}\hat{\rho}^{(N)}) = \text{Tr}(\hat{O}^{(N)}\hat{\rho}). \quad (\text{E.4})$$

The fact that the collective spin operator is block-diagonal in the atom number basis implies that its expectation value is independent on whether there is a coherent superposition of different $\hat{\rho}^{(N)}$ or not. Therefore, criteria based on measurements of \hat{S}_n and \hat{N} are insensitive on whether the system is in a coherent superposition of states with different particle numbers or in a statistical mixture of these, Eq. (E.1).

Using the above relations we see that for an arbitrary direction \mathbf{n}

$$\begin{aligned} \left\langle \frac{\hat{S}_n^p}{(\hat{N}/2)^q} \right\rangle &= \left\langle \left(\bigoplus_{N \geq 1} \hat{S}_n^{(N)} \right)^p \cdot \left(\bigoplus_{N \geq 1} N/2 \cdot \mathbb{1}^{(N)} \right)^{-q} \right\rangle \\ &= \left\langle \left(\bigoplus_{N \geq 1} (\hat{S}_n^{(N)})^p \right) \cdot \left(\bigoplus_{N \geq 1} (N/2)^{-q} \cdot \mathbb{1}^{(N)} \right) \right\rangle \\ &= \sum_N p_N \langle \hat{S}_n^p \rangle_N \frac{1}{(N/2)^q}. \end{aligned} \quad (\text{E.5})$$

For what follows, consider the relation derived from the Cauchy-Schwarz inequality

$$\begin{aligned} - \left(\sum_N p_N \left\langle \frac{\hat{S}_n}{N/2} \right\rangle_N \right)^2 &= - \left(\sum_N \sqrt{p_N} \sqrt{p_N} \left\langle \frac{\hat{S}_n}{N/2} \right\rangle_N \right)^2 \\ &\geq - \left(\sum_N \sqrt{p_N^2} \right) \left(\sum_N \sqrt{p_N^2} \left(\left\langle \frac{\hat{S}_n}{N/2} \right\rangle_N \right)^2 \right) \\ &= - \left(\sum_N p_N \left(\left\langle \frac{\hat{S}_n}{N/2} \right\rangle_N \right)^2 \right). \end{aligned} \quad (\text{E.6})$$

We now use Eqs. (E.5) and (E.6) to show that

$$\begin{aligned}
 \text{Var} \left[\frac{\hat{S}_n}{\hat{N}/2} \right] &= \left\langle \left(\frac{\hat{S}_n}{\hat{N}/2} \right)^2 \right\rangle - \left\langle \frac{\hat{S}_n}{\hat{N}/2} \right\rangle^2 \\
 &= \left(\sum_N p_N \left\langle \left(\frac{\hat{S}_n}{N/2} \right)^2 \right\rangle_N \right) - \left(\sum_N p_N \left\langle \frac{\hat{S}_n}{N/2} \right\rangle_N \right)^2 \\
 &\geq \left(\sum_N p_N \left\langle \left(\frac{\hat{S}_n}{N/2} \right)^2 \right\rangle_N \right) - \left(\sum_N p_N \left(\left\langle \frac{\hat{S}_n}{N/2} \right\rangle_N \right)^2 \right) \\
 &= \sum_N p_N \left(\left\langle \left(\frac{\hat{S}_n}{N/2} \right)^2 \right\rangle_N - \left(\left\langle \frac{\hat{S}_n}{N/2} \right\rangle_N \right)^2 \right) \\
 &= \sum_N p_N \text{Var} \left[\frac{\hat{S}_n}{N/2} \right]_N
 \end{aligned} \tag{E.7}$$

E.2 Entanglement criterion

Using the fact that for all separable states with a fixed number of atoms N it holds

$$\text{Var} \left[\frac{\hat{S}_n}{N/2} \right]_N \geq \frac{1}{N} \left| \left\langle \frac{\hat{S}_x}{N/2} \right\rangle_N \right|^2 \quad (\text{E.8})$$

we have

$$\begin{aligned} \langle \hat{N} \rangle \text{Var} \left[\frac{\hat{S}_z}{\hat{N}/2} \right] &\geq \langle \hat{N} \rangle \left(\sum_N p_N \text{Var} \left[\frac{\hat{S}_n}{N/2} \right]_N \right) && \text{using Eq. (E.7)} \\ &\geq \left(\sum_N p_N N \right) \left(\sum_N p_N \frac{1}{N} \left| \left\langle \frac{\hat{S}_x}{N/2} \right\rangle_N \right|^2 \right) && \text{using Eq. (E.8)} \\ &\geq \left| \sum_N \sqrt{p_N N} \sqrt{p_N \frac{1}{N}} \left\langle \frac{\hat{S}_x}{N/2} \right\rangle_N \right|^2 && \text{using Cauchy-Schwarz} \\ &= \left| \sum_N p_N \left\langle \frac{\hat{S}_x}{N/2} \right\rangle_N \right|^2 \\ &= \left| \left\langle \frac{\hat{S}_x}{\hat{N}/2} \right\rangle \right|^2. \end{aligned} \quad (\text{E.9})$$

This proves that for all separable states it holds

$$\frac{\langle \hat{N} \rangle \text{Var} \left[\frac{\hat{S}_z}{\hat{N}/2} \right]}{\left| \left\langle \frac{\hat{S}_x}{\hat{N}/2} \right\rangle \right|^2} \geq 1. \quad (\text{E.10})$$

If no component $\hat{\rho}^{(N)}$ is entangled, then Eq. (E.8) is satisfied for all N , and consequently Eq. (E.10) is satisfied. Conversely, a violation of Eq. E.10 proves that at least one component $\hat{\rho}^{(N)}$ of the system's state is entangled.

A similar idea was used in Ref. [170]. Moreover, the Sørensen-Mølmer criterion for k -particle entanglement [100] presented in Section 4.3.2 can also be extended to systems with a fluctuating number of particles, as it is done in Ref. [132].

E.3 Bell correlation witness

Using the fact that for all non-Bell-correlated states with a fixed number of atoms N it holds

$$-\left| \frac{\langle \hat{S}_n \rangle_N}{N/2} \right| + (\mathbf{a} \cdot \mathbf{n})^2 \frac{\langle \hat{S}_a^2 \rangle_N}{N/4} + 1 - (\mathbf{a} \cdot \mathbf{n})^2 \geq 0 \quad (\text{E.11})$$

we also have

$$\begin{aligned}
 & - \left| \left\langle \frac{\hat{S}_{\mathbf{n}}}{\hat{N}/2} \right\rangle \right| + (\mathbf{a} \cdot \mathbf{n})^2 \left\langle \frac{\hat{S}_{\mathbf{a}}^2}{\hat{N}/4} \right\rangle + 1 - (\mathbf{a} \cdot \mathbf{n})^2 = \\
 & = \sum_N p_N \left[- \left| \frac{\langle \hat{S}_{\mathbf{n}} \rangle_N}{N/2} \right| + (\mathbf{a} \cdot \mathbf{n})^2 \frac{\langle \hat{S}_{\mathbf{a}}^2 \rangle_N}{N/4} + 1 - (\mathbf{a} \cdot \mathbf{n})^2 \right] \geq 0. \quad (\text{E.12})
 \end{aligned}$$

If no component $\hat{\rho}^{(N)}$ is Bell-correlated, then every term in this sum is nonnegative according to Eq. E.11, and consequently Eq. E.12 is satisfied. Conversely, a violation of Eq. E.12 proves that at least one component $\hat{\rho}^{(N)}$ of the system's state is Bell-correlated.

Appendix F

Spin expectation values

F.1 One-axis twisting

We list here the analytical expression for the first and second moments for the collective spin of a spin squeezed state of $N = 2S$ particles, prepared by evolving a coherent state pointing along the x -axis according to the one-axis twisting Hamiltonian $\chi \hat{S}_z^2$ for a time $t = \mu/(2\chi)$. Considering the vector $\mathbf{v} = (x, y, z)$, we have

$$\langle \hat{S}_v \rangle = xS \cos^{2S-1} \left(\frac{\mu}{2} \right), \quad (\text{F.1})$$

$$\begin{aligned} \langle \hat{S}_v^2 \rangle = \frac{S}{4} & \left((2S-1) \left((x^2 - y^2) \cos^{2S-2}(\mu) + 4yz \sin \left(\frac{\mu}{2} \right) \cos^{2S-2} \left(\frac{\mu}{2} \right) \right) + \right. \\ & \left. + (2S+1) (x^2 + y^2) + 2z^2 \right). \end{aligned} \quad (\text{F.2})$$

These formulae allow to compute every variance or covariance, for example using

$$\begin{aligned} \langle \hat{S}_u \hat{S}_v + \hat{S}_v \hat{S}_u \rangle &= \frac{1}{2} \left\langle \left(\hat{S}_u + \hat{S}_v \right)^2 - \left(\hat{S}_u - \hat{S}_v \right)^2 \right\rangle \\ &= \frac{1}{2} \left(\langle \hat{S}_{u+v}^2 \rangle - \langle \hat{S}_{u-v}^2 \rangle \right). \end{aligned} \quad (\text{F.3})$$

The angle θ^* maximizing the second moment along the direction $\mathbf{v} = (0, \cos \theta, \sin \theta)$ is

$$\theta^* = \frac{1}{2} \arctan \left(\frac{4 \sin \left(\frac{\mu}{2} \right) \cos^{2S-2} \left(\frac{\mu}{2} \right)}{1 - \cos^{2S-2}(\mu)} \right). \quad (\text{F.4})$$

F.2 Squeezing and splitting

We consider here an initial coherent spin state of $N = 2S$ particles, pointing along the x -axis, that evolved according to the one-axis twisting Hamiltonian $\chi \hat{S}_z^2$ for a time $t = \mu/(2\chi)$. After the evolution, the resulting state is then split by a two-port beam splitter with a spin-independent splitting ratio set by θ_{BS} , see Ref. [171] for details. Experimentally, this model corresponds to the scenario where the particles in state $|1\rangle$ and $|2\rangle$ are independently distributed into two modes, A and B , according to a binomial distribution, *i.e.* interactions during the splitting process are neglected.

Considering the vector $\mathbf{v} = (x, y, z)$, the analytical expression for the first and second moments of the two collective spins are

$$\langle \hat{S}_v^A \rangle = xS \cos^2 \left(\frac{\theta_{\text{BS}}}{2} \right) \cos^{2S-1} \left(\frac{\mu}{2} \right), \quad (\text{F.5})$$

$$\langle \hat{S}_v^B \rangle = xS \cos^2 \left(\frac{\theta_{\text{BS}}}{2} \right) \sin^{2S-1} \left(\frac{\mu}{2} \right), \quad (\text{F.6})$$

$$\begin{aligned} \left\langle \left(\hat{S}_v^A \right)^2 \right\rangle &= \frac{S}{4} \cos^2 \left(\frac{\theta_{\text{BS}}}{2} \right) \left((2S-1) \cos^2 \left(\frac{\theta_{\text{BS}}}{2} \right) \left((x^2 - y^2) \cos^{2S-2}(\mu) + \right. \right. \\ &\quad \left. \left. + 4yz \sin \left(\frac{\mu}{2} \right) \cos^{2S-2} \left(\frac{\mu}{2} \right) \right) + \right. \\ &\quad \left. + \frac{1}{2} (3 + 2S + (2S-1) \cos(\theta_{\text{BS}})) (x^2 + y^2) + 2z^2 \right) \quad (\text{F.7}) \end{aligned}$$

$$\begin{aligned} \left\langle \left(\hat{S}_v^B \right)^2 \right\rangle &= \frac{S}{4} \sin^2 \left(\frac{\theta_{\text{BS}}}{2} \right) \left((2S-1) \sin^2 \left(\frac{\theta_{\text{BS}}}{2} \right) \left((x^2 - y^2) \cos^{2S-2}(\mu) + \right. \right. \\ &\quad \left. \left. + 4yz \sin \left(\frac{\mu}{2} \right) \cos^{2S-2} \left(\frac{\mu}{2} \right) \right) + \right. \\ &\quad \left. + \frac{1}{2} (3 + 2S - (2S-1) \sin(\theta_{\text{BS}})) (x^2 + y^2) + 2z^2 \right) \quad (\text{F.8}) \end{aligned}$$

$$\begin{aligned} \left\langle \hat{S}_{v_A}^A \hat{S}_{v_B}^B \right\rangle &= \frac{S}{16} (2S-1) \sin^2(\theta_{\text{BS}}) \left(\cos^{2S-2}(\mu) (x_A x_B - y_A y_B) + \right. \\ &\quad \left. + 2 \sin \left(\frac{\mu}{2} \right) \cos^{2S-2} \left(\frac{\mu}{2} \right) (z_A y_B + y_A z_B) + x_A x_B + y_A y_B \right). \quad (\text{F.9}) \end{aligned}$$

Appendix G

Convex optimization

A vast number of problems can be formulated as the task of maximizing or minimizing a function subject to a set of constraints. Convex optimization is the specific situation where a convex function has to be optimized over a convex set. Two important examples belonging to this category are linear programs and semidefinite programs, which have been used in chapter 4. In the following we are going to give an overview of these problems, for a detailed exposition see for example Ref. [172].

G.1 Linear program

A linear program (LP) is a method to maximize or minimize a linear objective function, subject to linear equality and linear inequality constraints defining the feasible set which is a polytope. More precisely, for given $A \in \mathbb{R}^{n \times m}$, $b \in \mathbb{R}^m$ and $c \in \mathbb{R}^n$, our task is to find the optimal point $x^* \in \mathcal{X} = \{x \in \mathbb{R}^n \mid Ax \geq b \text{ and } x \geq 0\}$ which *minimizes* the (real) objective function $f(x) = c^T x$ (note that the inequalities are taken component-wise). Here, we immediately see that c defines the objective function, while A and b define the feasible set \mathcal{X} .

In general a LP might be infeasible, if there are inconsistent constraints, or its solution might be unbounded, if the feasible set is also unbounded. If the feasible set is bounded and if a feasible solution exists, then the optimum value is always attained on the boundary of the feasible set (and it is a global optimum), as the objective function is linear. In the case of problems with distinct optimal solutions (*e.g.* if the objective function is a constant), then every convex combination of the solutions is also a solution.

The duality principle states that every LP, referred to as a primal problem, is associated to a dual LP. In our case, the dual problem consists in finding the optimal point $y^* \in \mathcal{Y} = \{y \in \mathbb{R}^m \mid A^T y \leq c \text{ and } y \geq 0\}$ which *maximizes* the objective function $g(y) = b^T y$. The dual of a dual LP is the original primal LP.

Crucially, every feasible solution to a LP gives a bound on the solution to its dual. Let us call the optimal feasible solutions $p^* = \inf_{x \in \mathcal{X}} c^T x = f(x^*)$ for the primal, and $d^* = \sup_{y \in \mathcal{Y}} b^T y = g(y^*)$ for the dual. The weak duality theorem states that the optimal feasible solution to the primal (minimization) problem is always larger or equal

G. Convex optimization

to its dual (maximization) problem, *i.e.* $p^* \geq d^*$. The difference between the solutions of the primal and the dual problem is called duality gap, and it is necessarily greater or equal than zero. In case the duality gap is zero, then strong duality is said to hold, and $c^T x^* = b^T y^*$. Moreover, weak duality implies that if the primal LP is unbounded then its dual is infeasible. Likewise, if the dual is unbounded, then the primal must be infeasible. However, it is also possible for both the dual and the primal to be infeasible. In the case of LPs strong duality only fails if both programs are infeasible [172].

To summarize, we define the primal LP and its dual as

Primal program	Dual program
minimise $c^T x$	maximise $b^T y$
subject to $Ax \geq b$	subject to $A^T y \leq c$
$x \geq 0$	$y \geq 0$

In this thesis, LPs are mainly be used to prove that certain vectors can be written as convex combination of others. In the context of Bell correlations a LP can be used to check whether the vector of observed correlations can be written as a convex combination of the vectors of correlations originating from local deterministic strategies. Geometrically, in the space of correlators, this corresponds to checking if a point is inside the local polytope. As the number of vertices of the local polytope grows rapidly with the system size, using a LP to verify the presence of Bell correlations is typically impractical in the multipartite scenario.

As a final note, we show a convenient redefinition of the feasibility region. Auxiliary non-negative variables, called slack variables, can be introduced to write the inequality constraints $Ax \geq b$ and $A^T y \leq c$ as equalities. The observation is based on the fact that, for some linear function h_i , $h_i(x) \leq 0$ if and only if there exists a $s_i \geq 0$ such that $h_i(x) + s_i = 0$. Because of this we can write

Primal program	Dual program
minimise $c^T x$	maximise $b^T y$
subject to $Ax - s = b$	subject to $A^T y + s = c$
$x \geq 0$	$y \geq 0$
$s \geq 0$	$s \geq 0$

G.2 Integer program

An integer program (IP) is a LP where the unknown variables are required to be integers, *i.e.* $x \in \mathbb{Z}^n$ and $y \in \mathbb{Z}^m$. While a LP can be solved efficiently in polynomial time, IP are often NP-hard.

IP can be useful in finding the classical bound of a multipartite permutationally-invariant Bell inequality in the following way. First, one expresses the inequality in terms of auxiliary variables counting how many parties are following each of the local deterministic strategies. Then, for a fixed number of parties N , the IP is used to minimize the Bell inequality over all possible partitions of the integer N into the auxiliary variables.

G.3 Semidefinite program

A semidefinite program (SDP) is a method to optimize a linear objective function over the convex cone¹ of positive semidefinite² matrices, subject to linear equality and linear inequality constraints defining the feasible set which is a spectrahedron. More precisely, for given $A_k \in \mathbb{R}^{n \times n}$ with $k = 1, \dots, m$, $b \in \mathbb{R}^m$ and $C \in \mathbb{R}^{n \times n}$, our task is to find the optimal point $X^* \in \mathcal{X} = \left\{ X \in \mathbb{S}^n \mid \text{Tr} \left[A_k^\dagger X \right] \geq b_k \ \forall k = 1, \dots, m \text{ and } X \succeq 0 \right\}$, where \mathbb{S}^n is the space of all $n \times n$ real symmetric matrices and $X \succeq 0$ means positive semidefinite, which *minimizes* the (real) objective function $f(x) = \text{Tr} [C^\dagger X] = \sum_{i,j} C_{ij} X_{ij}$. Here, we immediately see that C defines the objective function, while A_k and b define the feasible set \mathcal{X} . It is interesting to note that all LPs can be expressed as SDPs. As for LPs, a general SDP might be infeasible or its solution might be unbounded.

The duality principle also applies to SDPs. In our case, the dual problem consists in finding the optimal point $y^* \in \mathcal{Y} = \{y \in \mathbb{R}^m \mid \sum_k A_k y_k \preceq C\}$ which *maximizes* the objective function $g(y) = b^\text{T} y$. The dual of a dual SDP is the original primal SDP.

Let us call the optimal feasible solutions $p^* = \inf_{X \in \mathcal{X}} \text{Tr} [C^\dagger X] = f(X^*)$ for the primal, and $d^* = \sup_{y \in \mathcal{Y}} b^\text{T} y = g(y^*)$ for the dual. Again, every feasible solution to a SDP gives a bound on the solution to its dual, *i.e.* $p^* \geq d^*$, as the weak duality theorem applies. However, contrary to LPs, strong duality does not always hold for SDPs. Sufficient conditions for having a zero duality gap (*i.e.* strong duality) are known as Slater's conditions. These read

- If p^* is finite, $X^* \succ 0$ and $\text{Tr} \left[A_k^\dagger X \right] \geq b_k \ \forall k$ (*i.e.* the primal is strictly feasible), then $p^* = d^*$ and there exists a $y^* \in \mathcal{Y}$ such that $d^* = \sup_{y \in \mathcal{Y}} b^\text{T} y = g(y^*)$
- If d^* is finite and $\sum_k A_k y_k \preceq C$ (*i.e.* the dual is strictly feasible), then $p^* = d^*$ and there exists a $X^* \in \mathcal{X}$ such that $p^* = \inf_{X \in \mathcal{X}} \text{Tr} [C^\dagger X] = f(X^*)$

To summarize, we define the primal SDP and its dual as

¹A convex cone is a subset of a vector space that is closed under linear combinations with positive coefficients. More rigorously, A subset C of a vector space V is a cone if for each x in C and positive scalars α , the product αx is in C . A cone C is a convex cone if $\alpha x + \beta y$ belongs to C , for any positive scalars α, β , and any $x, y \in C$. The set of positive semidefinite matrices is a cone.

²A $n \times n$ real symmetric matrix M is said to be positive semidefinite if $x^\text{T} M x \geq 0$ for all $x \in \mathbb{R}^n$. This implies that all the eigenvalues of M are non-negative. An important equivalent definition is that M is positive semidefinite if and only if it can be written as a Gram matrix, *i.e.* as a matrix where the entries $m_{ij} = x_i \cdot x_j$ are scalar products of n vectors $\{x_i\}_{i=1, \dots, n} \in \mathbb{R}^n$. A similar definition holds for the complex case.

G. Convex optimization

Primal program

$$\begin{aligned} &\text{minimise} && \text{Tr} [C^\dagger X] \\ &\text{subject to} && \text{Tr} [A_k^\dagger X] \geq b_k \quad \forall k \\ &&& X \succeq 0 \end{aligned}$$

Dual program

$$\begin{aligned} &\text{maximise} && b^\text{T} y \\ &\text{subject to} && \sum_k A_k y_k \preceq C \end{aligned}$$

SDPs find many applications in the field of quantum information theory. As an example, they have been successfully used to define hierarchies bounding the set of quantum correlations from the outside [126], and for entanglement detection [125]. In this thesis SDPs have been used in chapter 4 to bound the set of classical correlations projected on the space of symmetrized one- and two-body correlators.

Bibliography

- [1] H. M. Wiseman, S. J. Jones, and A. C. Doherty, *Steering, entanglement, non-locality, and the Einstein-Podolsky-Rosen paradox*, Phys. Rev. Lett. **98**, 140402 (2007).
- [2] O. Gühne and G. Tóth, *Entanglement detection*, Physics Reports **474**, 1 (2009).
- [3] L. Amico, R. Fazio, A. Osterloh, and V. Vedral, *Entanglement in many-body systems*, Rev. Mod. Phys. **80**, 517 (2008).
- [4] M. D. Reid, P. D. Drummond, W. P. Bowen, E. G. Cavalcanti, P. K. Lam, H. A. Bachor, U. L. Andersen, and G. Leuchs, *Colloquium: The Einstein-Podolsky-Rosen paradox: From concepts to applications*, Rev. Mod. Phys. **81**, 1727 (2009).
- [5] N. Brunner, D. Cavalcanti, S. Pironio, V. Scarani, and S. Wehner, *Bell nonlocality*, Rev. Mod. Phys. **86**, 419 (2014).
- [6] V. Giovannetti, S. Lloyd, and L. Maccone, *Quantum metrology*, Phys. Rev. Lett. **96**, 010401 (2006).
- [7] C. H. Bennett, G. Brassard, C. Crépeau, R. Jozsa, A. Peres, and W. K. Wootters, *Teleporting an unknown quantum state via dual classical and Einstein-Podolsky-Rosen channels*, Phys. Rev. Lett. **70**, 1895 (1993).
- [8] A. K. Ekert, *Quantum cryptography based on Bell's theorem*, Phys. Rev. Lett. **67**, 661 (1991).
- [9] S. Pironio, A. Acín, S. Massar, A. B. de la Giroday, D. N. Matsukevich, P. Maunz, S. Olmschenk, D. Hayes, L. Luo, T. A. Manning, and C. Monroe, *Random numbers certified by Bell's theorem*, Nature **464**, 1021 (2010).
- [10] E. Hagley, X. Maître, G. Nogues, C. Wunderlich, M. Brune, J. M. Raimond, and S. Haroche, *Generation of Einstein-Podolsky-Rosen Pairs of Atoms*, Physical Review Letters **79**, 1 (1997).

BIBLIOGRAPHY

- [11] B. P. Lanyon, M. Zwerger, P. Jurcevic, C. Hempel, W. Dür, H. J. Briegel, R. Blatt, and C. F. Roos, *Experimental violation of multipartite Bell inequalities with trapped ions*, Phys. Rev. Lett. **112**, 100403 (2014).
- [12] L. Pezzè, A. Smerzi, M. K. Oberthaler, R. Schmied, and P. Treutlein, *Quantum metrology with nonclassical states of atomic ensembles*, Rev. Mod. Phys. **90**, 035005 (2018).
- [13] V. Giovannetti, S. Lloyd, and L. Maccone, *Advances in quantum metrology*, Nature Photonics **5**, 222 (2011).
- [14] C. Gross, T. Zibold, E. Nicklas, J. Estève, and M. K. Oberthaler, *Nonlinear atom interferometer surpasses classical precision limit*, Nature **464**, 1165 (2010).
- [15] A. Louchet-Chauvet, J. Appel, J. J. Renema, D. Oblak, N. Kjaergaard, and E. S. Polzik, *Entanglement-assisted atomic clock beyond the projection noise limit*, New Journal of Physics **12**, 065032 (2010).
- [16] I. D. Leroux, M. H. Schleier-Smith, and V. Vuletić, *Orientation-dependent entanglement lifetime in a squeezed atomic clock*, Phys. Rev. Lett. **104**, 250801 (2010).
- [17] C. F. Ockeloen, R. Schmied, M. F. Riedel, and P. Treutlein, *Quantum metrology with a scanning probe atom interferometer*, Phys. Rev. Lett. **111**, 143001 (2013).
- [18] I. Bloch, J. Dalibard, and W. Zwerger, *Many-body physics with ultracold gases*, Rev. Mod. Phys. **80**, 885 (2008).
- [19] M. F. Riedel, P. Böhi, Y. Li, T. W. Hänsch, A. Sinatra, and P. Treutlein, *Atom-chip-based generation of entanglement for quantum metrology*, Nature **464**, 1170 (2010).
- [20] J. Peise, I. Kruse, K. Lange, B. Lücke, L. Pezzè, J. Arlt, W. Ertmer, K. Hammerer, L. Santos, A. Smerzi, and C. Klempt, *Satisfying the Einstein-Podolsky-Rosen criterion with massive particles*, Nature Communications **6**, 8984 EP (2015).
- [21] J. Tura, R. Augusiak, A. B. Sainz, T. Vértesi, M. Lewenstein, and A. Acín, *Detecting nonlocality in many-body quantum states*, Science **344**, 1256 (2014).
- [22] N. Killoran, M. Cramer, and M. B. Plenio, *Extracting entanglement from identical particles*, Phys. Rev. Lett. **112**, 150501 (2014).
- [23] J. Reichel and V. Vuletić (editors), *Atom chips*, (Wiley-VCH, Weinheim, Germany) (2011).
- [24] P. Böhi, M. F. Riedel, J. Hoffrogge, J. Reichel, T. W. Hänsch, and P. Treutlein, *Coherent manipulation of Bose-Einstein condensates with state-dependent microwave potentials on an atom chip*, Nat. Phys. **5**, 592 (2009).

-
- [25] M. Kitagawa and M. Ueda, *Squeezed spin states*, Phys. Rev. A **47**, 5138 (1993).
- [26] R. Schmied, J.-D. Bancal, B. Allard, M. Fadel, V. Scarani, P. Treutlein, and N. Sangouard, *Bell correlations in a Bose-Einstein condensate*, Science **352**, 441 (2016).
- [27] M. Fadel, T. Zibold, B. Décamps, and P. Treutlein, *Spatial entanglement patterns and Einstein-Podolsky-Rosen steering in Bose-Einstein condensates*, Science **360**, 409 (2018).
- [28] M. Fadel and J. Tura, *Bounding the set of classical correlations of a many-body system*, Phys. Rev. Lett. **119**, 230402 (2017).
- [29] S. Wagner, R. Schmied, M. Fadel, P. Treutlein, N. Sangouard, and J.-D. Bancal, *Bell correlations in a many-body system with finite statistics*, Phys. Rev. Lett. **119**, 170403 (2017).
- [30] F. Baccari, J. Tura, M. Fadel, A. Aloy, J.-D. Bancal, N. Sangouard, M. Lewenstein, A. Acín, and R. Augusiak, *Bell correlations depth in many-body systems*, preprint at arXiv:1802.09516 (2018).
- [31] F. Dalfovo, S. Giorgini, L. P. Pitaevskii, and S. Stringari, *Theory of Bose-Einstein condensation in trapped gases*, Rev. Mod. Phys. **71**, 463 (1999).
- [32] A. J. Leggett, *Bose-Einstein condensation in the alkali gases: Some fundamental concepts*, Rev. Mod. Phys. **73**, 307 (2001).
- [33] W. Ketterle, D. S. Durfee, and D. M. Stamper-Kurn, *Making, probing and understanding Bose-Einstein condensates*, in M. Inguscio, S. Stringari, and C. E. Wieman (editors), *Bose-Einstein condensation in atomic gases, Proceedings of the International School of Physics “Enrico Fermi”, Course CXL*, pp. 67–176 (IOS Press, Amsterdam) (1999).
- [34] S. N. Bose, *Quantentheorie des einatomigen idealen Gases. Zweite Abhandlung*, Z. Physik **26**, 178 (1924).
- [35] A. Einstein, *Quantentheorie des einatomigen idealen Gases. Zweite Abhandlung*, Sitzung der physikalisch-mathematischen Klasse vom 8. Januar 1925 (1925).
- [36] M. H. Anderson, J. R. Ensher, M. R. Matthews, C. E. Wieman, and E. A. Cornell, *Observation of Bose-Einstein condensation in a dilute atomic vapor*, Science **269**, 198 (1995).
- [37] C. C. Bradley, C. A. Sackett, J. J. Tollett, and R. G. Hulet, *Evidence of Bose-Einstein condensation in an atomic gas with attractive interactions*, Phys. Rev. Lett. **75**, 1687 (1995).

BIBLIOGRAPHY

- [38] K. B. Davis, M.-O. Mewes, M. R. Andrews, N. J. van Druten, D. S. Durfee, D. M. Kurn, and W. Ketterle, *Bose-Einstein condensation in a gas of sodium atoms*, Phys. Rev. Lett. **75**, 3969 (1995).
- [39] S. Giorgini, L. P. Pitaevskii, and S. Stringari, *Condensate fraction and critical temperature of a trapped interacting bose gas*, Phys. Rev. A **54**, R4633 (1996).
- [40] W. Hänsel, P. Hommelhoff, T. W. Hänsch, and J. Reichel, *Bose-Einstein condensation on a microelectronic chip*, Nature **413**, 498 EP (2001).
- [41] T. Schumm, S. Hofferberth, L. M. Andersson, S. Wildermuth, S. Groth, I. Bar-Joseph, J. Schmiedmayer, and P. Krüger, *Matter-wave interferometry in a double well on an atom chip*, Nature Physics **1**, 57 EP (2005).
- [42] R. Szmuk, V. Dugrain, W. Maineult, J. Reichel, and P. Rosenbusch, *Stability of a trapped-atom clock on a chip*, Phys. Rev. A **92**, 012106 (2015).
- [43] T. van Zoest, N. Gaaloul, Y. Singh, H. Ahlers, W. Herr, S. T. Seidel, W. Ertmer, E. Rasel, M. Eckart, E. Kajari, S. Arnold, G. Nandi, W. P. Schleich, R. Walser, A. Vogel, K. Sengstock, K. Bongs, W. Lewoczko-Adamczyk, M. Schiemangk, T. Schuldt, A. Peters, T. Könnemann, H. Müntinga, C. Lämmerzahl, H. Dittus, T. Steinmetz, T. W. Hänsch, and J. Reichel, *Bose-Einstein condensation in microgravity*, Science **328**, 1540 (2010).
- [44] Y. Castin, *Bose-einstein condensates in atomic gases: Simple theoretical results*, in R. Kaiser, C. Westbrook, and F. David (editors), *Coherent atomic matter waves*, pp. 1–136 (Springer Berlin Heidelberg, Berlin, Heidelberg) (2001).
- [45] A. Muñoz Mateo and V. Delgado, *Ground-state properties of trapped Bose-Einstein condensates: Extension of the Thomas-Fermi approximation*, Phys. Rev. A **75**, 063610 (2007).
- [46] A. Muñoz Mateo and V. Delgado, *Extension of the Thomas-Fermi approximation for trapped Bose-Einstein condensates with an arbitrary number of atoms*, Phys. Rev. A **74**, 065602 (2006).
- [47] M. Egorov, B. Opanchuk, P. Drummond, B. V. Hall, P. Hannaford, and A. I. Sidorov, *Measurement of s-wave scattering lengths in a two-component Bose-Einstein condensate*, Phys. Rev. A **87**, 053614 (2013).
- [48] D. S. Hall, M. R. Matthews, J. R. Ensher, C. E. Wieman, and E. A. Cornell, *Dynamics of component separation in a binary mixture of Bose-Einstein condensates*, Phys. Rev. Lett. **81**, 1539 (1998).
- [49] Y. Li, P. Treutlein, J. Reichel, and A. Sinatra, *Spin squeezing in a bimodal condensate: spatial dynamics and particle losses*, European Physical Journal B **68**, 365 (2009).

- [50] B. Lücke, M. Scherer, J. Kruse, L. Pezzé, F. Deuretzbacher, P. Hyllus, O. Topic, J. Peise, W. Ertmer, J. Arlt, L. Santos, A. Smerzi, and C. Klempt, *Twin matter waves for interferometry beyond the classical limit*, *Science* **334**, 773 (2011).
- [51] J. P. Dowling, G. S. Agarwal, and W. P. Schleich, *Wigner distribution of a general angular-momentum state: Applications to a collection of two-level atoms*, *Phys. Rev. A* **49**, 4101 (1994).
- [52] R. Schmied and P. Treutlein, *Tomographic reconstruction of the Wigner function on the Bloch sphere*, *New J. Phys.* **13**, 065019 (2011).
- [53] C. F. Ockeloen, *Quantum Metrology with a Scanning Probe Atom Interferometer*, Ph.D. thesis, University of Basel (2014).
- [54] E. A. Burt, R. W. Ghrist, C. J. Myatt, M. J. Holland, E. A. Cornell, and C. E. Wieman, *Coherence, correlations, and collisions: What one learns about Bose-Einstein condensates from their decay*, *Phys. Rev. Lett.* **79**, 337 (1997).
- [55] J. Söding, D. Guéry-Odelin, P. Desbiolles, F. Chevy, H. Inamori, and J. Dalibard, *Three-body decay of a rubidium Bose-Einstein condensate*, *Appl. Phys. B* **69**, 257 (1999).
- [56] Y. Castin and A. Sinatra, *Spatial and Temporal Coherence of a Bose-Condensed Gas*, pp. 315–339 (Springer Berlin Heidelberg, Berlin, Heidelberg) (2013).
- [57] A. Sinatra and Y. Castin, *Binary mixtures of Bose-Einstein condensates: Phase dynamics and spatial dynamics*, *The European Physical Journal D* **8**, 319 (2000).
- [58] A. Sinatra, Y. Castin, and E. Witkowska, *Coherence time of a Bose-Einstein condensate*, *Phys. Rev. A* **80**, 033614 (2009).
- [59] A. Sinatra, Private communication.
- [60] P. Treutlein, *Coherent manipulation of ultracold atoms on an atom chip*, Ph.D. thesis, Ludwigs-Maximilians-Universität, München (2008).
- [61] P. A. Böhi, *Coherent manipulation of ultracold atoms with microwave near-fields*, Ph.D. thesis, Ludwig-Maximilians-Universität, München (2010).
- [62] M. F. Riedel, *Multi-particle entanglement on an atom chip*, Ph.D. thesis, Ludwig-Maximilians-Universität, München (2010).
- [63] C. Enesa, *offser frequency stabilisation of a laser diode for ultra cold atoms experiments*, Master’s thesis, University of Basel (2014).
- [64] G. Reinaudi, T. Lahaye, Z. Wang, and D. Guéry-Odelin, *Strong saturation absorption imaging of dense clouds of ultracold atoms*, *Opt. Lett.* **32**, 3143 (2007).

BIBLIOGRAPHY

- [65] C. F. Ockeloen, A. F. Tauschinsky, R. J. C. Spreeuw, and S. Whitlock, *Detection of small atom numbers through image processing*, Phys. Rev. A **82**, 061606 (2010).
- [66] M. A. Joffe, W. Ketterle, A. Martin, and D. E. Pritchard, *Transverse cooling and deflection of an atomic beam inside a Zeeman slower*, J. Opt. Soc. Am. B **10**, 2257 (1993).
- [67] A. Einstein, B. Podolsky, and N. Rosen, *Can quantum-mechanical description of physical reality be considered complete?*, Physical Review **47**, 777 (1935).
- [68] N. Bohr, *Can quantum-mechanical description of physical reality be considered complete?*, Phys. Rev. **48**, 696 (1935).
- [69] E. Schrödinger, *Discussion of Probability Relations between Separated Systems*, Proceedings of the Cambridge Philosophical Society **31**, 555 (1935).
- [70] E. Schrödinger, *Probability relations between separated systems*, Proceedings of the Cambridge Philosophical Society **32**, 446 (1936).
- [71] J. S. Bell, *On the Einstein-Podolsky-Rosen paradox*, Physics **1**, 195 (1964).
- [72] B. Hensen, H. Bernien, A. E. Dréau, A. Reiserer, N. Kalb, M. S. Blok, J. Ruitenberg, R. F. L. Vermeulen, R. N. Schouten, C. Abellán, W. Amaya, V. Pruneri, M. W. Mitchell, M. Markham, D. J. Twitchen, D. Elkouss, S. Wehner, T. H. Taminiau, and R. Hanson, *Loophole-free Bell inequality violation using electron spins separated by 1.3 kilometres*, Nature **526**, 682 EP (2015).
- [73] L. K. Shalm, E. Meyer-Scott, B. G. Christensen, P. Bierhorst, M. A. Wayne, M. J. Stevens, T. Gerrits, S. Glancy, D. R. Hamel, M. S. Allman, K. J. Coakley, S. D. Dyer, C. Hodge, A. E. Lita, V. B. Verma, C. Lambrocco, E. Tortorici, A. L. Migdall, Y. Zhang, D. R. Kumor, W. H. Farr, F. Marsili, M. D. Shaw, J. A. Stern, C. Abellán, W. Amaya, V. Pruneri, T. Jennewein, M. W. Mitchell, P. G. Kwiat, J. C. Bienfang, R. P. Mirin, E. Knill, and S. W. Nam, *Strong loophole-free test of local realism*, Phys. Rev. Lett. **115**, 250402 (2015).
- [74] M. Giustina, M. A. M. Versteegh, S. Wengerowsky, J. Handsteiner, A. Hochrainer, K. Phelan, F. Steinlechner, J. Kofler, J.-A. Larsson, C. Abellán, W. Amaya, V. Pruneri, M. W. Mitchell, J. Beyer, T. Gerrits, A. E. Lita, L. K. Shalm, S. W. Nam, T. Scheidl, R. Ursin, B. Wittmann, and A. Zeilinger, *Significant-loophole-free test of Bell's theorem with entangled photons*, Phys. Rev. Lett. **115**, 250401 (2015).
- [75] W. Rosenfeld, D. Burchardt, R. Garthoff, K. Redeker, N. Ortegel, M. Rau, and H. Weinfurter, *Event-ready Bell test using entangled atoms simultaneously closing detection and locality loopholes*, Phys. Rev. Lett. **119**, 010402 (2017).

- [76] J. Handsteiner, A. S. Friedman, D. Rauch, J. Gallicchio, B. Liu, H. Hosp, J. Kofler, D. Bricher, M. Fink, C. Leung, A. Mark, H. T. Nguyen, I. Sanders, F. Steinlechner, R. Ursin, S. Wengerowsky, A. H. Guth, D. I. Kaiser, T. Scheidl, and A. Zeilinger, *Cosmic Bell test: Measurement settings from milky way stars*, Phys. Rev. Lett. **118**, 060401 (2017).
- [77] C. Abellán, A. Acín, A. Alarcón, O. Alibart, C. K. Andersen, F. Andreoli, A. Beckert, F. A. Beduini, A. Bendersky, M. Bentivegna, P. Bierhorst, D. Burchardt, A. Cabello, J. Cariñe, S. Carrasco, G. Carvacho, D. Cavalcanti, R. Chaves, J. Cortés-Vega, A. Cuevas, A. Delgado, H. de Riedmatten, C. Eichler, P. Farrera, J. Fuenzalida, M. García-Matos, R. Garthoff, S. Gasparinetti, T. Gerrits, F. Ghafari Jouneghani, S. Glancy, E. S. Gómez, P. González, J. Y. Guan, J. Handsteiner, J. Heinsoo, G. Heinze, A. Hirschmann, O. Jiménez, F. Kaiser, E. Knill, L. T. Knoll, S. Krinner, P. Kurpiers, M. A. Larotonda, J. Å. Larsson, A. Lenhard, H. Li, M. H. Li, G. Lima, B. Liu, Y. Liu, I. H. López Grande, T. Lunghi, X. Ma, O. S. Magaña-Loaiza, P. Magnard, A. Magnoni, M. Martí-Prieto, D. Martínez, P. Mataloni, A. Mattar, M. Mazzera, R. P. Mirin, M. W. Mitchell, S. Nam, M. Oppliger, J. W. Pan, R. B. Patel, G. J. Pryde, D. Rauch, K. Redeker, D. Rieländer, M. Ringbauer, T. Roberson, W. Rosenfeld, Y. Salathé, L. Santodonato, G. Sauder, T. Scheidl, C. T. Schmiegelow, F. Sciarrino, A. Seri, L. K. Shalm, S. C. Shi, S. Slussarenko, M. J. Stevens, S. Tanzilli, F. Toledo, J. Tura, R. Ursin, P. Vergyris, V. B. Verma, T. Walter, A. Wallraff, Z. Wang, H. Weinfurter, M. M. Weston, A. G. White, C. Wu, G. B. Xavier, L. You, X. Yuan, A. Zeilinger, Q. Zhang, W. Zhang, J. Zhong, and T. B. B. T. Collaboration, *Challenging local realism with human choices*, Nature **557**, 212 (2018).
- [78] A. Einstein, M. Born, and H. Born, *The Born-Einstein letters : correspondence between Albert Einstein and Max and Hedwig Born from 1916 to 1955* (Macmillan London) (1971).
- [79] N. Bohr, *On the notions of causality and complementarity*, Dialectica **2**, 312 (1948).
- [80] J. S. Bell, *On the Einstein Podolsky Rosen paradox*, Physics **1**, 195 (1964).
- [81] S. J. Freedman and J. F. Clauser, *Experimental test of local hidden-variable theories*, Phys. Rev. Lett. **28**, 938 (1972).
- [82] A. Aspect, P. Grangier, and G. Roger, *Experimental realization of Einstein-Podolsky-Rosen-Bohm Gedankenexperiment: A new violation of Bell's inequalities*, Phys. Rev. Lett. **49**, 91 (1982).
- [83] S. J. Jones, H. M. Wiseman, and A. C. Doherty, *Entanglement, Einstein-Podolsky-Rosen correlations, Bell nonlocality, and steering*, Phys. Rev. A **76**, 052116 (2007).

BIBLIOGRAPHY

- [84] Q. Y. He, Q. H. Gong, and M. D. Reid, *Classifying directional gaussian entanglement, Einstein-Podolsky-Rosen steering, and discord*, Phys. Rev. Lett. **114**, 060402 (2015).
- [85] M. T. Quintino, T. Vértesi, D. Cavalcanti, R. Augusiak, M. Demianowicz, A. Acín, and N. Brunner, *Inequivalence of entanglement, steering, and Bell non-locality for general measurements*, Phys. Rev. A **92**, 032107 (2015).
- [86] N. Gisin, *Bell's inequality holds for all non-product states*, Physics Letters A **154**, 201 (1991).
- [87] A. Acín, N. Gisin, and B. Toner, *Grothendieck's constant and local models for noisy entangled quantum states*, Phys. Rev. A **73**, 062105 (2006).
- [88] A. Peres, *Separability criterion for density matrices*, Phys. Rev. Lett. **77**, 1413 (1996).
- [89] R. Augusiak, M. Demianowicz, and A. Acín, *Local hidden-variable models for entangled quantum states*, Journal of Physics A: Mathematical and Theoretical **47**, 424002 (2014).
- [90] J. Krivine, *Constantes de Grothendieck et fonctions de type positif sur les sphères*, Advances in Mathematics **31**, 16 (1979).
- [91] F. Hirsch, M. T. Quintino, T. Vértesi, M. Navascués, and N. Brunner, *Better local hidden variable models for two-qubit Werner states and an upper bound on the Grothendieck constant $K_G(3)$* , Quantum **1**, 3 (2017).
- [92] Q. Y. He, P. D. Drummond, and M. D. Reid, *Entanglement, EPR steering, and Bell-nonlocality criteria for multipartite higher-spin systems*, Phys. Rev. A **83**, 032120 (2011).
- [93] M. D. Reid, Q.-Y. He, and P. D. Drummond, *Entanglement and nonlocality in multi-particle systems*, Frontiers of Physics **7**, 72 (2012).
- [94] Q. Y. He and M. D. Reid, *Genuine multipartite Einstein-Podolsky-Rosen steering*, Phys. Rev. Lett. **111**, 250403 (2013).
- [95] B. Julsgaard, A. Kozhekin, and E. S. Polzik, *Experimental long-lived entanglement of two macroscopic objects*, Nature **413**, 400 (2001).
- [96] F. Fröwis, P. C. Strassmann, A. Tiranov, C. Gut, J. Lavoie, N. Brunner, F. Bussières, M. Afzelius, and N. Gisin, *Experimental certification of millions of genuinely entangled atoms in a solid*, Nature Communications **8**, 907 (2017).
- [97] V. Giovannetti, S. Mancini, D. Vitali, and P. Tombesi, *Characterizing the entanglement of bipartite quantum systems*, Phys. Rev. A **67**, 022320 (2003).

-
- [98] A. Sørensen, L.-M. Duan, J. I. Cirac, and P. Zoller, *Many-particle entanglement with Bose-Einstein condensates*, *Nature* **409**, 63 (2001).
- [99] D. J. Wineland, J. J. Bollinger, W. M. Itano, and D. J. Heinzen, *Squeezed atomic states and projection noise in spectroscopy*, *Phys. Rev. A* **50**, 67 (1994).
- [100] A. S. Sørensen and K. Mølmer, *Entanglement and extreme spin squeezing*, *Phys. Rev. Lett.* **86**, 4431 (2001).
- [101] D. Bohm, *Quantum theory*, (Prentice-Hall) (1951).
- [102] Q. Y. He and M. D. Reid, *Towards an Einstein-Podolsky-Rosen paradox between two macroscopic atomic ensembles at room temperature*, *New Journal of Physics* **15**, 063027 (2013).
- [103] S. L. W. Midgley, A. J. Ferris, and M. K. Olsen, *Asymmetric Gaussian steering: When Alice and Bob disagree*, *Physical Review A* **81**, 022101 (2010).
- [104] V. Händchen, T. Eberle, S. Steinlechner, A. Sambrowski, T. Franz, R. F. Werner, and R. Schnabel, *Observation of one-way Einstein-Podolsky-Rosen steering*, *Nat Photon* **6**, 596 (2012).
- [105] S. Wollmann, N. Walk, A. J. Bennet, H. M. Wiseman, and G. J. Pryde, *Observation of Genuine One-Way Einstein-Podolsky-Rosen Steering*, *Physical Review Letters* **116**, 160403 (2016).
- [106] A. Fine, *Hidden variables, joint probability, and the Bell inequalities*, *Phys. Rev. Lett.* **48**, 291 (1982).
- [107] L. Babai, L. Fortnow, and C. Lund, *Non-deterministic exponential time has two-prover interactive protocols*, *computational complexity* **1**, 3 (1991).
- [108] D. Avis, H. Imai, T. Ito, and Y. Sasaki, *Deriving tight Bell inequalities for 2 parties with many 2-valued observables from facets of cut polytopes* (2004), arXiv: quant-ph/0404014.
- [109] D. Rosset, J.-D. Bancal, and N. Gisin, *Classifying 50 years of Bell inequalities*, *Journal of Physics A: Mathematical and Theoretical* **47**, 424022 (2014).
- [110] J. F. Clauser, M. A. Horne, A. Shimony, and R. A. Holt, *Proposed experiment to test local hidden-variable theories*, *Phys. Rev. Lett.* **23**, 880 (1969).
- [111] S. Pironio, *All Clauser-Horne-Shimony-Holt polytopes*, *Journal of Physics A: Mathematical and Theoretical* **47**, 424020 (2014).
- [112] I. Pitowsky and K. Svozil, *Optimal tests of quantum nonlocality*, *Phys. Rev. A* **64**, 014102 (2001).

BIBLIOGRAPHY

- [113] C. Śliwa, *Symmetries of the Bell correlation inequalities*, Physics Letters A **317**, 165 (2003).
- [114] J.-D. Bancal, N. Gisin, and S. Pironio, *Looking for symmetric Bell inequalities*, Journal of Physics A: Mathematical and Theoretical **43**, 385303 (2010).
- [115] J. Tura, R. Augusiak, A. B. Sainz, B. Lücke, C. Klempt, M. Lewenstein, and A. Acín, *Nonlocality in many-body quantum systems detected with two-body correlators*, Annals of Physics **362**, 370 (2015).
- [116] J. Tura, A. B. Sainz, T. Vértesi, A. Acín, M. Lewenstein, and R. Augusiak, *Translationally invariant multipartite Bell inequalities involving only two-body correlators*, Journal of Physics A: Mathematical and Theoretical **47**, 424024 (2014).
- [117] J. Tura, G. D. las Cuevas, R. Augusiak, M. Lewenstein, A. Acín, and J. I. Cirac, *Energy as a detector of nonlocality of many-body spin systems* (2016), arXiv:1607.06090.
- [118] T. Christof and A. Loebel, *Polyhedron representation transformation algorithm (porta)*, <http://porta.zib.de/> (1997).
- [119] K. Fukuda, *CDD Double Description Method*, https://www.inf.ethz.ch/personal/fukudak/cdd_home/ (2016).
- [120] B. Chazelle, *An optimal convex hull algorithm in any fixed dimension*, Discrete & Computational Geometry **10**, 377 (1993).
- [121] J. Gouveia, P. A. Parrilo, and R. R. Thomas, *Theta bodies for polynomial ideals*, SIAM Journal on Optimization **20**, 2097 (2010).
- [122] J. Gouveia and R. R. Thomas, *Semidefinite Optimization and Convex Algebraic Geometry, Chapter 7: Spectrahedral Approximations of Convex Hulls of Algebraic Sets*, pp. 293–340 (MOS-SIAM Series on Optimization) (2012).
- [123] J. B. Lasserre, *Moments, Positive Polynomials and Their Applications*, , Series on Optimization and Its Applications Series (Imperial College Press) (2009).
- [124] M. F. Anjos and J. B. Lasserre, *Handbook on Semidefinite, Conic and Polynomial Optimization*, , International Series in Operations Research & Management Science (Springer US) (2012).
- [125] F. Baccari, D. Cavalcanti, P. Wittek, and A. Acín, *Efficient device-independent entanglement detection for multipartite systems* (2016), arXiv:1612.08551.
- [126] M. Navascués, S. Pironio, and A. Acín, *A convergent hierarchy of semidefinite programs characterizing the set of quantum correlations*, New Journal of Physics **10**, 073013 (2008).

- [127] B. Buchberger, *Phd thesis (1965): An algorithm for finding the basis elements of the residue class ring of a zero dimensional polynomial ideal*, Journal of Symbolic Computation **41**, 475 (2006).
- [128] G. Svetlichny, *Distinguishing three-body from two-body nonseparability by a Bell-type inequality*, Phys. Rev. D **35**, 3066 (1987).
- [129] J.-D. Bancal, C. Branciard, N. Gisin, and S. Pironio, *Quantifying multipartite nonlocality*, Phys. Rev. Lett. **103**, 090503 (2009).
- [130] F. J. Curchod, N. Gisin, and Y.-C. Liang, *Quantifying multipartite nonlocality via the size of the resource*, Phys. Rev. A **91**, 012121 (2015).
- [131] O. Gühne, G. Tóth, and H. J. Briegel, *Multipartite entanglement in spin chains*, New Journal of Physics **7**, 229 (2005).
- [132] P. Hyllus, L. Pezzé, A. Smerzi, and G. Tóth, *Entanglement and extreme spin squeezing for a fluctuating number of indistinguishable particles*, Phys. Rev. A **86**, 012337 (2012).
- [133] R. D. Gill, *Statistics, causality and Bell's theorem*, Statist. Sci. **29**, 512 (2014).
- [134] Y. Zhang, S. Glancy, and E. Knill, *Asymptotically optimal data analysis for rejecting local realism*, Phys. Rev. A **84**, 062118 (2011).
- [135] P. Treutlein, P. Hommelhoff, T. Steinmetz, T. W. Hänsch, and J. Reichel, *Coherence in microchip traps*, Phys. Rev. Lett. **92**, 203005 (2004).
- [136] M. Eibl, S. Gaertner, M. Bourennane, C. Kurtsiefer, M. Żukowski, and H. Weinfurter, *Experimental observation of four-photon entanglement from parametric down-conversion*, Phys. Rev. Lett. **90**, 200403 (2003).
- [137] Z. Zhao, T. Yang, Y.-A. Chen, A.-N. Zhang, M. Żukowski, and J.-W. Pan, *Experimental violation of local realism by four-photon Greenberger-Horne-Zeilinger entanglement*, Phys. Rev. Lett. **91**, 180401 (2003).
- [138] J. Hofmann, M. Krug, N. Ortegel, L. Gérard, M. Weber, W. Rosenfeld, and H. Weinfurter, *Heralded entanglement between widely separated atoms*, Science **337**, 72 (2012).
- [139] W. Pfaff, T. H. Taminiau, L. Robledo, H. Bernien, M. Markham, D. J. Twitchen, and R. Hanson, *Demonstration of entanglement-by-measurement of solid-state qubits*, Nat. Phys. **9**, 29 (2013).
- [140] M. Ansmann, H. Wang, R. C. Bialczak, M. Hofheinz, E. Lucero, M. Neeley, A. D. O'Connell, D. Sank, M. Weides, J. Wenner, A. N. Cleland, and J. M. Martinis, *Violation of Bell's inequality in Josephson phase qubits*, Nature **461**, 504 (2009).

BIBLIOGRAPHY

- [141] P. D. Drummond, *Violations of Bell's inequality in cooperative states*, Phys. Rev. Lett. **50**, 1407 (1983).
- [142] M. Żukowski and Č. Brukner, *Bell's theorem for general N -qubit states*, Phys. Rev. Lett. **88**, 210401 (2002).
- [143] A. Gilchrist, P. Deuar, and M. D. Reid, *Contradiction of quantum mechanics with local hidden variables for quadrature phase amplitude measurements*, Phys. Rev. Lett. **80**, 3169 (1998).
- [144] W. J. Munro, *Optimal states for bell-inequality violations using quadrature-phase homodyne measurements*, Phys. Rev. A **59**, 4197 (1999).
- [145] R. García-Patrón, J. Fiurášek, N. J. Cerf, J. Wenger, R. Tualle-Brouiri, and P. Grangier, *Proposal for a loophole-free Bell test using homodyne detection*, Phys. Rev. Lett. **93**, 130409 (2004).
- [146] H. Nha and H. J. Carmichael, *Proposed test of quantum nonlocality for continuous variables*, Phys. Rev. Lett. **93**, 020401 (2004).
- [147] J. S. Bell and A. Aspect, *Speakable and Unspeakable in Quantum Mechanics: Collected Papers on Quantum Philosophy*, (Cambridge University Press), 2nd edition (2004).
- [148] T. C. Ralph, W. J. Munro, and R. E. S. Polkinghorne, *Proposal for the measurement of Bell-type correlations from continuous variables*, Phys. Rev. Lett. **85**, 2035 (2000).
- [149] O. Thearle, J. Janousek, S. Armstrong, S. Hosseini, M. Schünemann (Mraz), S. Assad, T. Symul, M. R. James, E. Huntington, T. C. Ralph, and P. K. Lam, *Violation of Bell's inequality using continuous variable measurements*, Phys. Rev. Lett. **120**, 040406 (2018).
- [150] J. G. Bohnet, B. C. Sawyer, J. W. Britton, M. L. Wall, A. M. Rey, M. Foss-Feig, and J. J. Bollinger, *Quantum spin dynamics and entanglement generation with hundreds of trapped ions*, Science **352**, 1297 (2016).
- [151] N. J. Engelsen, R. Krishnakumar, O. Hosten, and M. A. Kasevich, *Bell correlations in spin-squeezed states of 500,000 atoms*, Phys. Rev. Lett. **118**, 140401 (2017).
- [152] C. W. Chou, H. de Riedmatten, D. Felinto, S. V. Polyakov, S. J. van Enk, and H. J. Kimble, *Measurement-induced entanglement for excitation stored in remote atomic ensembles*, Nature **438**, 828 (2005).
- [153] D. N. Matsukevich, T. Chanelière, S. D. Jenkins, S. Y. Lan, T. A. B. Kennedy, and A. Kuzmich, *Entanglement of Remote Atomic Qubits*, Physical Review Letters **96**, 030405 (2006).

- [154] J. Simon, H. Tanji, S. Ghosh, and V. Vuletić, *Single-photon bus connecting spin-wave quantum memories*, *Nature Physics* **3**, 765 (2007).
- [155] R. Islam, R. Ma, P. M. Preiss, M. Eric Tai, A. Lukin, M. Rispoli, and M. Greiner, *Measuring entanglement entropy in a quantum many-body system*, *Nature* **528**, 77 (2015).
- [156] T. Fukuhara, S. Hild, J. Zeiher, P. Schauß, I. Bloch, M. Endres, and C. Gross, *Spatially Resolved Detection of a Spin-Entanglement Wave in a Bose-Hubbard Chain*, *Physical Review Letters* **115**, 035302 (2015).
- [157] D. Cavalcanti and P. Skrzypczyk, *Quantum steering: a review with focus on semidefinite programming*, *Reports on Progress in Physics* **80**, 024001 (2017).
- [158] P. Kunkel, M. Prüfer, H. Strobel, D. Linnemann, A. Frölian, T. Gasenzer, M. Gärtner, and M. K. Oberthaler, *Spatially distributed multipartite entanglement enables epr steering of atomic clouds*, *Science* **360**, 413 (2018).
- [159] K. Lange, J. Peise, B. Lücke, I. Kruse, G. Vitagliano, I. Apellaniz, M. Kleinmann, G. Tóth, and C. Klempt, *Entanglement between two spatially separated atomic modes*, *Science* **360**, 416 (2018).
- [160] J. Hu, W. Chen, Z. Vendeiro, H. Zhang, and V. Vuletić, *Entangled collective-spin states of atomic ensembles under nonuniform atom-light interaction*, *Phys. Rev. A* **92**, 063816 (2015).
- [161] R. McConnell, H. Zhang, J. Hu, S. Čuk, and V. Vuletić, *Entanglement with negative Wigner function of almost 3,000 atoms heralded by one photon*, *Nature* **519**, 439 (2015).
- [162] K. Wagner and et. al., *Asymmetric epr entanglement in continuous variable systems*, *J. Phys. B: At. Mol. Opt. Phys.* **47**, 225502 (2014).
- [163] W. Muessel, H. Strobel, D. Linnemann, D. B. Hume, and M. K. Oberthaler, *Scalable Spin Squeezing for Quantum-Enhanced Magnetometry with Bose-Einstein Condensates*, *Physical Review Letters* **113**, 103004 (2014).
- [164] H. Kurkjian, K. Pawłowski, A. Sinatra, and P. Treutlein, *Spin squeezing and Einstein-Podolsky-Rosen entanglement of two bimodal condensates in state-dependent potentials*, *Phys. Rev. A* **88**, 043605 (2013).
- [165] P. Treutlein, T. W. Hänsch, J. Reichel, A. Negretti, M. A. Cirone, and T. Calarco, *Microwave potentials and optimal control for robust quantum gates on an atom chip*, *Phys. Rev. A* **74**, 022312 (2006).
- [166] H. Tanji, J. Simon, S. Ghosh, and V. Vuletić, *Simplified measurement of the Bell parameter within quantum mechanics*, preprint at arXiv:0801.4549.

BIBLIOGRAPHY

- [167] B. Yurke and D. Stoler, *Generating quantum mechanical superpositions of macroscopically distinguishable states via amplitude dispersion*, Phys. Rev. Lett. **57**, 13 (1986).
- [168] K. Pawłowski, M. Fadel, P. Treutlein, Y. Castin, and A. Sinatra, *Mesoscopic quantum superpositions in bimodal bose-einstein condensates: Decoherence and strategies to counteract it*, Phys. Rev. A **95**, 063609 (2017).
- [169] M. Fadel and J. Tura, *Bell correlations at finite temperature*, under evaluation (2018), 1805.00449.
- [170] P. Hyllus, L. Pezzé, and A. Smerzi, *Entanglement and sensitivity in precision measurements with states of a fluctuating number of particles*, Phys. Rev. Lett. **105**, 120501 (2010).
- [171] Y. Jing, M. Fadel, V. Ivannikov, and T. Byrnes, *Split spin-squeezed Bose-Einstein Condensates* (2018), 1808.10679.
- [172] S. Boyd and L. Vandenberghe, *Convex Optimization* (Cambridge University Press, New York, NY, USA) (2004).

Curriculum Vitae

Matteo Fadel

Born: December 11, 1989 in Pordenone, Italy

Education

- 2014 – 2018 PhD in Experimental Physics, University of Basel, Switzerland
Thesis: *Many-particle entanglement, Einstein-Podolsky-Rosen steering and Bell correlations in Bose-Einstein condensates.*
- 2011 – 2013 MSc in Physics, ETH Zürich, Switzerland
Thesis: *Cryogenic setup for fast manipulation of the quantum motional states of trapped ions.*
- 2008 – 2011 BSc in Physics, University of Padova, Italy
Thesis: *The black hole information loss problem.*

Publications

- “*Bell correlations at finite temperature*”
M. Fadel and J. Tura
preprint at arXiv:1805.00449
- “*Spatial entanglement patterns and Einstein-Podolsky-Rosen steering in Bose-Einstein condensates*”
M. Fadel, B. Décamps, T. Zibold and P. Treutlein
Science **360**, 409 (2018)
- “*Bell correlations depth in many-body systems*”
F. Baccari, J. Tura, M. Fadel, A. Aloy, J.-D. Bancal, N. Sangouard, M. Lewenstein, A. Acín and R. Augusiak
preprint at arXiv:1802.09516
- “*Bounding the set of classical correlations of a many-body system*”
M. Fadel and J. Tura
Phys. Rev. Lett. **119**, 230402 (2017)

BIBLIOGRAPHY

- “*Bell correlations in a many-body system with finite statistics*”
S. Wagner, R. Schmied, M. Fadel, P. Treutlein, N. Sangouard, J.-D. Bancal
Phys. Rev. Lett. **119**, 170403 (2017)
- “*Mesoscopic quantum superpositions in bimodal Bose–Einstein condensates: decoherence and strategies to counteract it*”
K. Pawłowski, M. Fadel, P. Treutlein, Y. Castin and A. Sinatra
Phys. Rev. A. **95**, 063609 (2017)
- “*Self-testing Dicke states*”
M. Fadel
Preprint at arXiv:1707.01215
- “*Bell correlations in a Bose–Einstein condensate*”
R. Schmied, J.-D. Bancal, B. Allard, M. Fadel, V. Scarani, P. Treutlein and N. Sangouard
Science **352**, 441 (2016)
- “*Sideband Rabi spectroscopy of finite-temperature trapped Bose gases*”
B. Allard, M. Fadel, R. Schmied and P. Treutlein
Phys. Rev. A. **93**, 043624 (2016)
- “*Generation of large coherent states by bang–bang control of a trapped-ion oscillator*”
J. Alonso, F. M. Leupold, Z. U. Solèr, M. Fadel, M. Marinelli, B. C. Keitch, V. Negnevitsky and J. P. Home
Nature Communication **7**, 11243 (2016)

Acknowledgements

This thesis would not have been possible without the contribution of other people. All the results presented here are fruits of collaborations with several colleagues, which deserve all my gratitude and proper acknowledgement.

First, I'm grateful to my supervisor, Philipp Treutlein, for his constant support, inspiration and motivation. He gave me innumerable opportunities to learn, to explore and to make experiences.

The experimental setup used for this thesis work has been built and developed by many people, who all put great efforts and thoughts in its design. Among these, I want to particularly thank my predecessor, Caspar Ockeloen, who left behind a well working machine, significantly simplifying my job.

From the experimental point of view, I'm indebted to Baptiste Allard, Tilman Zibold and Boris Décamps. They put constant effort in keeping the experiment running at its best, improving its performance, as well as in data acquisition and analysis. I acquired many experimental skills from them.

From the theoretical point of view, I'm particularly grateful to Roman Schmied, who encouraged my mathematical inclinations and stimulated philosophical discussions, and to Jordi Tura, for all the Skype calls about nonlocality in the middle of the night.

The investigations of BEC phase coherence were motivated and supported by Alice Sinatra and Krzysztof Pawłowski, and they are still an ongoing project.

The results on Bell correlations presented here have been obtained in collaborations with the theory groups of Nicolas Sangouard, Toni Acín and Maciej Lewenstein. I learned a lot working together with their talented team members.